

Study of biomass burning pollution over the Amazon using modelling and satellite data

Laura Gonzalez Alonso



Submitted to

the University of Sheffield

for the degree of

Doctor of Philosophy

Department of Chemical and Biological Engineering

May 2019

Abstract

Significant ozone levels are observed every year in the Amazon during the burning season, with potential risks for populations and ecosystems. The dynamics that govern the distribution of biomass burning pollution across the region and hence, the impact on surface ozone are still unknown. Fire activity is predicted to increase, due to its strong dependence on global warming and droughts. Thus, understanding the vertical distribution of biomass burning emissions in the Amazon is crucial to determine and quantify the impacts. For that, this work used satellite observations, aircraft and ground-based measurements and ozonesondes, combined with an Earth system model.

The first part of this work characterised the vertical distribution of Amazonian smoke plumes from satellite observations and analysed major factors of variability. The statistical analysis of smoke plume characteristics combined with an extensive dataset on the main drivers in smoke plume dynamics revealed that most smoke concentrates below 2.5 km and plume heights depend largely on biome type, fire properties, and atmospheric and drought conditions. Specifically, droughts enhanced fire activity, favoured lower smoke plume heights and larger emissions, which may result in poor regional air quality with important implications in the future, when more severe and extended droughts are expected.

To improve the vertical distribution of biomass burning pollution across the Amazon in Earth system models, an injection height scheme derived using observations of smoke plumes in the Amazon was applied. The simulation showed better

performance at representing ozone compared to observations, particularly close to the fires. Furthermore, results evidenced a significant impact of biomass burning emissions on ozone levels, and a considerable decline in air quality across populated and vegetated areas. These outcomes highlighted the necessity of including improved representation of the vertical distribution of biomass burning emissions in future air quality studies and provided insights of the magnitude of biomass burning impact on air quality, enhancing scientific understanding of the significance of biomass burning in the Amazon.

Dedication

To the memory of Armando and my Dad.

Declaration

I, Laura Gonzalez Alonso, hereby declare that I am the sole author of this thesis and that, except where specific reference is made to the work of others, the contents of this research is the result of my own work, unless otherwise acknowledged in the text. I confirm that this dissertation is original and has not been submitted for any other degree, diploma or other qualifications to this university or any other institution.

Acknowledgements

I would like to express enormous gratitude to my supervisor, Maria Val Martin. First, for believing in me by giving me this invaluable and challenging opportunity, and second, for guiding and supporting me throughout all my research. I can never really express how grateful I am to you. I am also thankful to Ralph A. Kahn, who contributed to the interpretation of my results in chapter 3 and provided insightful comments and advice.

I would also like to thank to the Atmospheric Chemistry Observations & Modeling group, at the National Center for Atmospheric Research, and Dr. Merritt Deeter for hosting me during my visit as a graduate student. To Dr. Benjamin Gaubert for his help, camaraderie, technical support and inspiration during my visit at NCAR, as well as Dr Simon Tilmes and Dr Louisa Emmons, who also contributed to my research. Finally, I would also like to mention my appreciation to Daniel Ziskin for his kindness, support and friendship at NCAR.

I am thankful to my friends. For looking after me, for visiting me, for taking me out, for calling me, for making me laugh. Because you painted this journey with bright colours. Adri, Cris, Palo, Patri, Bea, Inga, Jen, Marco and Lorena. Also, I could not have done this without my second family. For their unconditional support, jokes, fun and hard moments shared. For all the experiences lived together that made us grow and become what we are. You are part of me, and I have a part of you in me: Ale, Alex, Juanlu, Luisiana and Maitane.

Finally, I am extremely grateful to my family. Mum and dad, you have been my

biggest supporters and made this happen. Dad, I will always be in debt with you, for giving me such an example for life. I hope I can live up to your expectations. Mum, you are the bravest, my admiration to you is infinite as well as my love. To Sara and Vega, my little mermaids. Thanks for giving me hope. I love you both more than words can describe. My utmost thanks go to Nathan, for your patience, for your songs, for being my friend, my family and my love.

To all, I give you my deepest and sincere thanks.

Laura

Contents

Abstract	i
Dedication	iii
Declaration	v
Acknowledgements	vii
1 Introduction	1
1.1 Background	1
1.2 Motivation, research objectives and approach	13
1.3 Dissertation overview	15
2 MISR and MINX: Developing a biomass burning smoke plume climatology across the Amazon	17
2.1 Introduction	17
2.2 MISR Instrument and products	19
2.3 MODIS Instrument and products	22
2.4 MINX Software	23
2.4.1 MINX Stereo retrieval algorithm	27
2.4.2 Digitalization of smoke plumes with MINX	31
2.4.3 Summary of MINX outputs	34
2.4.4 MINX Additional tools	41
2.4.5 Interpreting wind direction	44
2.4.6 Other applications of MINX	45
2.5 MINX Limitations and biases	48
3 Biomass burning smoke heights over the Amazon observed from space	51

3.1	Introduction	51
3.2	Data and Methods	54
3.2.1	MINX overview	54
3.2.2	MINX smoke plume database	58
3.2.3	Land cover unit data	60
3.2.4	Atmospheric conditions	60
3.2.5	Drought conditions	61
3.2.6	CALIOP observations	61
3.3	Results and discussion	65
3.3.1	Smoke plume height observations	65
3.3.2	Effect of atmospheric and fire conditions on smoke plumes	68
3.3.3	Seasonality of smoke plumes heights	71
3.3.4	Interannual variability of smoke plumes and drought conditions	74
3.3.5	CALIOP smoke plume observations	80
3.4	Conclusions	84
4	Biomass burning influence on CO and ozone over the Amazon: sensitivity to vertical smoke distribution and source contributions	89
4.1	Introduction	89
4.2	Modelling Framework	93
4.2.1	Model description	94
4.2.2	Biomass burning injection height parametrisation	95
4.2.3	Experimental setup	97
4.2.4	CO Tags	97
4.3	Observational datasets for model evaluation	98
4.3.1	CO Observations	98
4.3.2	Ozone Observations	100
4.4	Model performance with the smoke injection height parametrisation	101
4.4.1	Impact of the smoke injection height scheme on simulated CO	101
4.4.2	Impact of smoke injection height scheme on simulated O ₃	108
4.5	Large scale impacts of biomass burning on CO and O ₃	115
4.5.1	Source attribution of CO	115
4.5.2	Contribution of biomass burning in the Amazon to CO and O ₃	117
4.6	Impact of biomass burning in the Amazon on surface O ₃ and air quality O ₃ standards	119

4.7	Conclusions	126
5	Summary and Conclusions	131
5.1	Vertical distribution of biomass burning emissions over the Amazon .	131
5.2	Factors of variability on the vertical distribution of biomass burning over the Amazon	132
5.3	Impacts of Amazonian biomass burning on surface ozone levels across the Amazon	133
5.4	Summary of conclusions and future research	134
A	Supplementary information	137
B	Supplementary information	145
C	Contributions and co-authors	153
	Bibliography	153

List of Figures

1.1	Image of the arc of deforestation	11
2.1	TERRA satellite with MISR aboard	20
2.2	MODIS thermal anomalies	23
2.3	MISR nine multi-angle images of a plume	25
2.4	Comparison of wind-corrected and zero-wind stereo-height	27
2.5	MISR view, parallax and features in motion	29
2.6	MODIS parameters to configure in MINX	33
2.7	Image of a smoke plume successfully digitised with MINX	34
2.8	Image of the location of MISR orbit and path by MINX	35
2.9	MINX heights and winds profiles	38
2.10	MINX aerosol histograms	39
2.11	Example of features in MINX-plumes ascii files	40
2.12	MINX camera registration tool	42
2.13	Dialog box with parameters to digitise	43
2.14	MINX cloud mask tool	44
2.15	Volcanic ash plume digitised with MINX	46
2.16	Dust plume digitised with MINX	47
3.1	CALIOP smoke plume characterisation	64
3.2	Locations of the MISR plumes in the Amazon	66
3.3	Time series of the MISR Amazon smoke-plume-height climatology	67
3.4	Vertical distribution of MISR stereo-height by atmospheric stability conditions	70
3.5	Seasonal cycle of MISR smoke plumes, MODIS FRP, atmospheric stability and MISR AOD	72
3.6	Seasonal variation of Amazon plume injection above the PBL	74

3.7	Interannual variability of MISR maximum plume heights, MODIS FRP and MISR AOD per biome	76
3.8	Interannual relationship of MODIS DSI and MISR maximum plume height, MODIS FRP and MISR AOD per biome	77
3.9	Time series of the CALIOP smoke plumes	81
3.10	Average CALIOP and MISR plume heights per biome, time of the season and climatic conditions	82
4.1	Vertical distribution of biomass burning emissions	96
4.2	Relative differences in simulated CO mixing ratios	103
4.3	Vertical profiles of CO mixing ratios from aircraft campaigns, CAMvert and CAMsurf	105
4.4	Mean MOPITT and simulated CO total column for September 2012 .	107
4.5	Averaged MOPITT CO mixing ratios and relative bias of CAMsurf and CAMvert for September 2012	108
4.6	Monthly averages of CO total columns for MOPITT, CAMsurf, CAMvert and CAMzeroBB in 2012	109
4.7	Relative differences (%) [(CAMvert – CAMsurf)/CAMsurf	111
4.8	Monthly mean O ₃ mixing ratios across the Equatorial and Atlantic/African regions for ozonesonde observations, CAMsurf and CAMvert	112
4.9	Monthly averages of O ₃ mixing ratios at the Amazon TT34 and Porto Velho from observations CAMvert, CAMsurf and CAMzeroBB	114
4.10	Monthly relative contributions to primary CO in 2012	116
4.11	Simulated averaged CO and O ₃ columns by CAMvert and CAMzeroBB and relative changes between CAMvert and CAMzeroBB in September 2012	118
4.12	Simulated MDA8, M12 and AOT40 and fire-induced changes during the 2012 burning season	120
4.13	Estimated number of days with fire-induced exceedances of MDA8 O ₃	121
4.14	Cumulative probability distributions of estimated O ₃ MDA8 at some cities for CAMvert, CAMsurf and CAMzeroBB	123
4.15	Simulated fire-induced surface O ₃ AOT40 and M12 for quinoa, wheat, tobacco and tropical forest	126
A1	Percentage of MISR plumes by year, month, biome and drought conditions	139
A2	Vertical distribution of individual MISR stereo-height retrievals per biome	140
A3	Relationship between MISR maximum plume heights and MODIS FRP	141

A4	Interannual variability of MISR plume maximum heights, MODIS FRP and MISR AOD by biome	142
A5	Location of the CALIOP plumes in the Amazon	143
A6	Examples of CALIOP vertical extinction profiles	143
B1	Fire regions of tagged CO	146
B2	Location of the ozone observational dataset for evaluation	147
B3	MODIS active fires and FINNv1.5 CO and NO _x emissions	148
B4	CAMsurf and CAMvert simulated CO for March and September 2012	149
B5	Averaged MOPITT CO mixing ratios and relative bias of CAMsurf and CAMvert for March 2012	149
B6	CAMsurf and CAMvert simulated O ₃ for March and September 2012	150
B7	Monthly averages of O ₃ mixing ratios from TOAR observations, CAMvert, CAMsurf and CAMzeroBB	151
B8	Simulated averaged CO and O ₃ columns by CAMvert and CAMzeroBB and relative changes between CAMvert and CAMzeroBB in March 2012	152

List of Tables

1.1	Summary of observational studies on smoke heights across the globe	8
1.2	Summary of ozone metrics for air quality	9
1.3	Summary of ozone standards for human health	9
1.4	Summary of ozone standards for vegetation	10
2.1	Summary of MISR and MODIS products used by MINX	26
3.1	Summary of instruments and products	55
3.2	Summary of MISR smoke plumes over the Amazon	59
3.3	Statistical summary for main parameters	67
3.4	Summary of the main atmospheric parameters at the plumes per year	75
4.1	Summary of emissions per sectors	95
4.2	Vegetation-specific statistical summary of estimated O ₃ AOT40 and M12	125
A1	Statistical summary for main smoke plume and drivers of variability	138
B1	Summary of the TOAR stations	146
C1	Summary of contributions and co-authors	153

Chapter 1

Introduction

1.1 Background

Biomass burning is the combustion of living and dead vegetation, including natural and anthropogenic burning. Every year, vegetation fires burn around 3 million km² of land globally ([Giglio et al., 2010](#)), which constitutes a significant primary source of gases and particles ([Crutzen and Andreae, 1990](#), [Andreae and Merlet, 2001](#), [Ito and Penner, 2004](#), [van der Werf et al., 2006](#), [Wiedinmyer et al., 2010](#)), equivalent to about 20% of global emissions from fossil fuels ([Denman et al., 2007](#)), and contributes to the formation of secondary pollutants ([Val Martin et al., 2006](#), [Alvarado et al., 2010](#), [Akagi et al., 2011](#), [Jaffe and Wigder, 2012](#)). Gases released by fires include greenhouse gases i.e., carbon dioxide (CO₂), methane (CH₄) and nitrous oxide (N₂O), reactive trace gases i.e., sulfur oxides (SO_x) and ammonia (NH₃), some of which are precursors of tropospheric ozone (O₃), i.e., carbon monoxide (CO), volatile organic compounds (VOC), nitrogen oxides (NO_x). Fine and coarse particulate matter (PM) are also largely produced by fires ([Goode et al., 2000](#), [Andreae and Merlet, 2001](#)), including black and organic carbon.

Biomass burning emissions significantly influence the chemical composition of the atmosphere (e.g., [Yurganov et al., 2004](#), [Lapina et al., 2006](#), [Simpson et al.,](#)

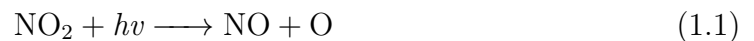
2006), with the potential to degrade air quality, being detrimental to human health and ecosystems, as well as to reduce visibility (e.g., [Lippmann, 1993](#), [Fiscus et al., 2005](#), [Felzer et al., 2007](#), [Jaffe et al., 2008](#), [Ainsworth et al., 2012](#), [Marais et al., 2014](#), [Reddington et al., 2015](#)). For instance, in a recent comprehensive 20-year modelling study, [Jacobson \(2014\)](#) suggested that biomass burning may be responsible for around 250,000 premature deaths per year. In addition, fire emissions alter weather and climate from regional to global scales (e.g., [Ramanathan et al., 2001](#), [Yurganov et al., 2004](#), [Langmann et al., 2009](#)) directly, via emitting greenhouse gases and aerosols, and increasing the amount of solar radiation absorbed or reflected to space ([Ramanathan and Carmichael, 2008](#)), and indirectly, via secondary effects on atmospheric chemistry (e.g., ozone and secondary organic aerosols formation) or changes in cloud microphysics, precipitation regimes and albedo, from aerosol emissions (e.g., [Twomey, 1977](#), [Albrecht, 1989](#), [Sitch et al., 2007](#)). Thus, emissions from biomass burning have been suggested to cause a 20-year global warming of 0.4 K ([Jacobson, 2014](#)).

Biomass burning contributes substantially to global CO, NO_x and O₃ budgets (32%, 21% and 3.5%, respectively) ([Andreae, 1991](#), [Jaffe and Wigder, 2012](#)). CO and NO_x play an important role in atmospheric chemistry. CO acts as the dominant sink for the hydroxyl radical (OH), the main tropospheric oxidant, with 90-95% of CO and about 75% of OH removal ([Novelli et al., 1998](#)). In addition, CO oxidation provides a source for O₃ formation in the presence of NO_x (e.g., [Levy, 1971](#), [Crutzen, 1973](#), [Logan et al., 1981](#)). NO_x promote substantial changes in the chemical production and loss rates of O₃ and CH₄ ([Andreae and Merlet, 2001](#)). Therefore, emissions of CO and NO_x have the potential to influence air quality and climate by altering CH₄ and other radiatively important gases that are removed by OH, and by affecting tropospheric O₃ itself (e.g., [Mickley et al., 1999](#)).

Tropospheric O₃ is an important oxidant ([Seinfeld and Pandis, 1998](#)) and source of OH. In addition, O₃ is the third most important greenhouse gas ([IPCC, 2007](#)) and a major air pollutant harmful to human health and plants. Inhaled O₃ can cause

decreases in lung function, aggravation of asthma, throat irritation and cough, chest pain and shortness of breath, inflammation of lung tissue, higher susceptibility to respiratory infection and premature mortality (e.g., [Bell et al., 2004, 2006](#), [Kheirbek et al., 2013](#), [Liu et al., 2018](#)). Exposure to ozone can also cause a range of effects on vegetation, including visible leaf injury (e.g., [Fumagalli et al., 2001](#)), growth and yield reductions, and altered sensitivity to abiotic and biotic stresses, such as droughts and fungi, respectively (e.g., [Fuehrer and Achermann, 1994](#), [Ashmore and Marshall, 1998](#), [Benton et al., 2000](#)). For instance, increases in tropospheric O₃ due to fire emissions have been found to reduce global forest net primary production by 0.7% per year, considerably larger than reductions from droughts (0.1% per year) ([Yue and Unger, 2018](#)). Exposure to O₃ has also been found to produce crops yield losses (e.g., [Avnery et al., 2011](#)), resulting in substantial economic costs and posing a risk to global food security ([Van Dingenen et al., 2009b](#), [Avnery et al., 2011](#), [Ghude et al., 2014](#)). O₃ forms from the photochemical reaction through the oxidation of CO, CH₄ and VOCs, controlled and catalyzed by NO_x (NO_x denotes the sum of NO and NO₂) ([Jonson et al., 2006](#)). In urban areas, NO_x is mainly emitted by the combustion of fossil fuels, whereas in rural areas NO_x is produced by biomass burning, peroxyacetyl nitrate (PAN) decomposition and soils ([Jaeglé et al., 2005](#)). Most of the direct emission of NO_x is in the form of NO, which is rapidly transformed into NO₂ (~5 min) ([Seinfeld and Pandis, 1998](#)). VOCs are mainly produced by plants and to a lesser extent, by a range of industrial activities, road traffic and fires ([Lerdau et al., 1997](#)).

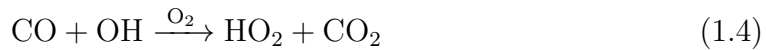
Ozone production starts with the photolysis of NO₂ (Reaction 1.1) and subsequent reaction of the oxygen atom with molecular oxygen (Reaction 1.2).



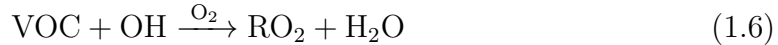
Once formed, ozone reacts with NO to form NO₂.



Reactions 1.1, 1.2 and 1.3 constitute a net zero ozone production cycle. However, in the presence of ozone precursors such as CO, VOC and hydrocarbons, net ozone production occurs. The chemistry leading to O₃ production starts with the oxidation of CO by the OH radical, forming the peroxy radical (HO₂) (Reaction 1.4). The formed HO₂ converts NO to NO₂ (Reaction 1.5), and photolysis of NO₂ forms O₃ (Reactions 1.1 and 1.2).



In the case of VOC reactions are



and subsequent Reactions 1.5, 1.1 and 1.2 to form O₃.

The ratio of VOCs to NO_x is particularly important in ozone formation. In VOCs-limited environments (e.g. urban areas or polluted remote areas), increases in VOCs leads to higher O₃ production, but lower O₃ production if NO_x mixing ratio increases above 300 ppt (NO_x-titration) ([Sillman, 1999](#)). In NO_x-limited environments (e.g. the Amazon), O₃ production increases with increasing NO_x and shows relatively little change in response to increased VOC.

In biomass burning plumes O₃ formation is complex, non-linear and highly variable, depending on many factors, such as photochemical conditions, ageing and dilution/mixing ([Jaffe and Wigder, 2012](#)). Some studies have shown rapid production

of O_3 in plumes (Baylon et al., 2015), whereas others have shown no enhancement or even depletion (Alvarado et al., 2010, Akagi et al., 2011, Baylon et al., 2015, Verma et al., 2009). One reason for the difference in O_3 formation rates in plumes is the variability in NO_x/CO ratios among fires. This ratio is lower (higher) for fires with dominant smouldering (flaming) combustion (Lobert and Warnatz, 1993, Yokelson et al., 1997, Goode et al., 2000) however, O_3 production in the plume can be enhanced downwind in the presence of additional sources of NO_x , as the plume encounters polluted air from urban areas (Singh et al., 2010). Another reason for differences in O_3 production in plumes is the presence of aerosols (Baylon et al., 2018), which can reduce O_3 photochemical reactions due to aerosol absorption and scattering of solar radiation (Xing et al., 2017).

The atmospheric impacts of biomass burning, e.g., O_3 production, depend on many factors: the amount of emissions released for each species, meteorological conditions, topography, factors related to fire behaviour (fire intensity, fuel availability, fuel characteristics, i.e., type, loading, moisture) and injection height, i.e., the altitude at which fire emissions are released. A key factor in biomass burning emissions is the combustion process, which is directly related to the type and amount of species emitted and their vertical distribution. Combustion can be divided into several stages: distillation or drying, pyrolysis, flaming combustion and smouldering combustion (Benkoussas et al., 2007), which in vegetation fires usually occur simultaneously and in the immediate surroundings. In terms of fire emissions, combustion is mainly divided into flaming and smouldering combustion and their ratios in a fire vary over time. Typically, flaming dominates in the earlier stage of a fire, whereas smouldering occurs in a later stage (Andreae and Merlet, 2001). Flaming combustion is characterised by intense flames, higher rates of spread, and high temperatures ($\sim 1500^\circ\text{C}$) (Rein, 2016), which produce gas-phase emissions dominated by highly oxidised compounds (i.e., CO_2 , NO_x) (Lobert et al., 1991, Yokelson et al., 1997, Radke et al., 1991, Reid et al., 2005, Chen, 2007). Temperate forest, tropical savannas and grassland fires are typically dominated by flaming combustion. On the

other hand, smouldering combustion is the slow, persistent, low-heat (450–700°C) flameless burning (Rein, 2016), which releases incomplete combustion products (i.e., CO). Areas with soil rich in organic matter and high moisture content, i.e. boreal forest, tropical forest and peatland, are mainly dominated by smouldering fires.

The injection height is another important factor in the atmospheric impacts of biomass burning. It is directly linked to the combustion stage and determines the lifetime and behaviour of the emitted species (Freitas et al., 2006, Paugam et al., 2016). Low-intensity smouldering fires tend to produce weaker buoyant smoke plumes than intense flaming fires (Val Martin et al., 2010, Amiridis et al., 2010). When a fire is in its flaming combustion stage, the intense heat released from the burning creates fire-induced convection above the fire, and a buoyant smoke plume originates, which interacts with the ambient atmosphere and transports fire emissions vertically. Most fire plumes concentrate below the planetary boundary layer (PBL), where emissions are well-mixed (Trentmann et al., 2002) and their impacts extend on a local to regional scale. However, a significant fraction of smoke can reach the free troposphere (FT) (e.g., Kahn et al., 2008, Val Martin et al., 2010), extending the lifetime of the emitted species and the spatial scale of their impact, due to faster downwind transport (Fromm et al., 2004). Injection heights in smoke plumes are highly variable. Atmospheric conditions and the energy released by the fire are the main drivers of the variability associated with smoke plume heights (Kahn et al., 2007, Paugam et al., 2016). For example, the thermal stratification of the atmosphere can promote or suppress the plume rise. That is, if the atmospheric temperature at a certain level is lower than the plume's, the plume tends to ascend. Furthermore, in the case of energetic fires, and in the presence of water vapour condensation and latent heat release, the vertical transport within the plume can be invigorated, and occasionally form pyro-cumulus clouds that inject large amounts of biomass burning emissions into the FT, even reaching the lower stratosphere (Fromm et al., 2010).

Plume-rise models (PRM) and semi-empirical parametrisations use atmospheric

profiles of meteorological variables combined with satellite observations related to the fire, i.e., fire size, fire radiative power (FRP) to predict the evolution of a plume (Paugam et al., 2016, Rémy et al., 2017). They are usually included in chemical transport models (CTM) and provide results on the injection heights, but simulations are computationally expensive and poorly validated, particularly for PRM (Val Martin et al., 2012). Satellite observations, ground-based and aircraft measurements provide more accurate data on the vertical distribution of smoke. This information is commonly used to evaluate results from PRM, as well as to constrain the vertical distribution of biomass burning emissions in CTM. Across the globe, many studies have sought to characterise smoke plume heights. Table 1.1 presents a summary of the most relevant to this study.

Many pollutants released or produced in fires are regulated due to their negative effects on human health and ecosystems, including O₃ (Felzer et al., 2007, Wegesser et al., 2009, Haikerwal et al., 2016, Crippa et al., 2016, Schweizer and Cisneros, 2017). O₃ standards and regulations vary substantially depending on the country and region, and provide guidelines and limit values to safeguard human health and ecosystems based on some metrics. Some of the most commonly used metrics for O₃ air quality regulations are summarised in Table 1.2. O₃ exposure risks for human health are typically assessed with MDA8 as the basic metric. MDA8 can be applied in combination with a number of exceedances that are allowed before violation of O₃ standards occurs (Fleming et al., 2018). For instance, the European Commission (under Directive 2008/50/EU) has a target value for MDA8 ozone concentrations of 60 ppb not to be exceeded on more than 25 days per calendar year. A summary of the main O₃ exposure standards for human health, including those relevant to this study, are presented in Table 1.3. Previous studies that used some of these standards to assess air quality, suggested that intense biomass burning periods can significantly increase the frequency of O₃ standards exceedances (Jaffe et al., 2008, Pfister et al., 2008, Chalbot et al., 2013, Rubio et al., 2015, Brey and Fischer, 2016). However, most of these studies have focused on fire-induced exceedances across the

Table 1.1: Summary of the most relevant observational studies on smoke heights across the globe.

Parameter ^a	Smoke height ^b	Temporal coverage	Spatial coverage ^c	Instrument/Product ^d	Reference
Att. bck.	<PBL	Jul-Aug 2006	GFR	CALLIOP L1	Labonne et al. (2007)
Plume	0.7–5.2 km	Jun-Sep 2004	North America	MISR/MODIS	Mazzoni et al. (2007)
Plume	0.18–4.5 km	summer 2004	Alaska-Yukon	MISR/MINX	Kahn et al. (2008)
CO	10–20% FT	Jun-Oct 2006	GFR	TES /MLS	Gonzi and Palmer (2010)
AI/Att. bck.	AI>9; >5 km	2006–2009	Globe	OMI/CALLIOP L2	Guan et al. (2010)
Plume	0.7–1 km	2002/2004-2007	North America	MISR/MINX	Val Martin et al. (2010)
Att. bck.	1.6–5.9 km	2006-2008	SW Russia/E Europe	CALLIOP L1	Amiridis et al. (2010)
Plume	26%>PBL	Dec2000/Nov2002	Australia	MISR/MINX	Mims et al. (2010)
Plume	0.7 km	2001–2009	Borneo/Sumatra	MISR/MINX	Tosca et al. (2011)
Ext. coef.	0.5–4 km	2006–2009	Borneo	CALLIOP L1	Tosca et al. (2011)
Att. bck./Ext. coef.	<2/3–5 km	Jul–Nov 2008	Manaus, BR	Raman lidar	Baars et al. (2012)
Plume	45%>1 km	2001-2010	SE Asia	MISR/MINX	Jian and Fu (2014)
AOD	1.6–4 km	2007-2012	GFR	CALLIOP L2	Huang et al. (2015)
Extinction	2–5 km	2007–2012	South America	CALLIOP L2	Bourgeois et al. (2015)
Att. bck.	0.8–5.3 km	2005–2012	Asia	CALLIOP L1	Vadrevu et al. (2015)
Ext. coef.	1–1.5/4–6 km	16–29 Sep 2012	6 flighttracks, BR	ALS-450 lidar	Marenco et al. (2016)
Plume/AOD	<2 km	2008–2010	Globe	MISR/MINX	Val Martin et al. (2018b)

^aAtt. bck.: Attenuated backscatter; AI: aerosol index; Ext. coef.: extinction coefficient; AOD: aerosol optical depth.

^bSmoke height is given as a range of heights where smoke concentrates, as a percentage above or below the PBL or the FT. / is used to separate between smoke layers, when observed more than one.

^cGFR: global fire regions; BR: Brazil.

^dCALLIOP: Cloud-Aerosol Lidar with Orthogonal Polarization; L1: level 1; L2: level 2; MISR: The Multi-angle Imaging SpectroRadiometer; MODIS: Moderate Resolution Imaging Spectroradiometer; MINX: MISR Interactive eXplorer; TES: The Tropospheric Emission Spectrometer; MLS: the Microwave Limb Sounder; OMI: Ozone Monitoring Instrument.

northern hemisphere (NH). In addition to human health standards, O₃ metrics for vegetation i.e., AOT40, W126 and M12, are used to determine levels above which adverse effects on sensitive vegetation may occur. Table 1.4 summarises some of the most relevant. Studies on the global impact on crops yield of current and future exposure to elevated concentrations of ozone suggested substantial yield reductions, depending on crop and metric (3-16%), enhanced under future scenarios (by >10%) (Van Dingenen et al., 2009b, Avnery et al., 2011, Tai et al., 2014). As in the case of ozone impacts on human health, most of these studies are based on dose-response functions for agricultural and horticultural crops in the NH.

Table 1.2: Summary of metrics relevant to ozone standards for air quality. n is the number of hours in the growing season, $[O_3]$ is the hourly ozone concentration from 08:00–19:59 hours and i is the hour index.

Metric	Definition	Unit	Application
MDA8	maximum daily 8-h mean	ppb	human health
AOT40	$\sum_{i=1}^n [[O_3] - 0.04]_i$ for $[O_3] \geq 0.04$ ppm h	ppm h	vegetation
W126	$\sum_{i=1}^n \left[\frac{[O_3]}{1 + 4403 \exp(-0.126 \times [O_3])} \right]_i$ for $[O_3] \geq 0$ ppm h	ppm h	vegetation
M12	$\frac{1}{n} \sum_{i=1}^n [O_3]_i$	ppb	vegetation

Table 1.3: Summary of relevant ozone standards for human health. (Adapted from Fleming et al. (2018)).

Region ^a	Metric ^b	Value [ppb]	Reference
WHO	MDA8	55	WHO (2008)
EU	MDA8	60 ^c	CLRTAP (2017)
USA	4MDA8	70	EPA (2016)
AMAZON	MDA8	40–80 ^d	National environmental agencies ^e

^a WHO: world Health Organization; AMAZON: Bolivia, Brazil, Colombia, Chile, Ecuador, French Guiana, Peru, Venezuela.

^b 4MDA8: annual 4th highest MDA8.

^c not to be exceeded on more than 25 days per calendar year.

^d MDA8 standards range across the Amazon region.

^e <http://www.cleanairinstitute.org>; <https://www.minambiente.gov.co/>; <http://www.leychile.cl>; <http://www.mma.gov.br>

Intense biomass burning in the Amazon contributes to the global fire emissions by approximately 15% (Van der Werf et al., 2010, Mishra et al., 2015), so the Amazon

Table 1.4: Summary of ozone main standards for vegetation. (Adapted from [Mills et al. \(2018\)](#)).

Metric	Period	Standard	Vegetation type	Effect/Reduction	Reference
AOT40	3-months	3000 ppb h	Agricultural	Grain yield (5% ^a)	CLRTAP (2017)
	3-months	8000 ppb h	Horticultural	Fruit yield (5% ^b)	
	6-months	5000 ppb h	Forest	Biomass (5% ^c)	
	3-months	3000 ppb h	Annuals	Biomass (10%)	
	6-months	5000 ppb h	Perennials	Biomass (10%)	
W126	Highest consecutive 3-months	15000 ppb h	Crops	Prevent loss >5%	US Federal Register (2015)
		17000 ppb h	Tree Plants	Improve protection	
		10000 ppb h		Reduce foliar injury	
		7000 ppb h	Ecosystems	Limit loss <2%	

^a Based on wheat.

^b Based on tomato.

^c Based on beech and birch.

is one of the most important biomass burning regions in the world. With one of the largest global deforestation rates ([Artaxo et al., 2002](#), [Malhi et al., 2008](#)), every year, thousands of fires burn in the Amazon basin. Most fires are of anthropogenic origin, i.e., for preparation of agricultural or pastoral lands, and burn during the burning season, from July to November, across the arc of deforestation ([Andreae et al., 2012](#)) (see Figure 1.1), with dominant burning of savanna and tropical forest (94% of the fires) ([Gonzalez-Alonso et al., 2019](#)). Furthermore, the Amazon basin covers an area of about 35.5% of South America and comprises the countries of Bolivia, Brazil, Colombia, Ecuador, Guyana, Peru, Suriname and Venezuela, with a population of 25 million people ([Davidson et al., 2012](#)), including indigenous communities, unique biodiversity and a rich agriculture-based economy (i.e., cocoa, coffee, quinoa). Thus, a large portion of this population suffers regularly from high level of pollutants from biomass burning emissions ([Brito et al., 2014](#)). At the same time, the Amazon basin contains the world's largest rainforest ([Laurance et al., 2001](#), [Aragao et al., 2014](#)), which is a key component of the Earth System. It provides about a fifth of all of the freshwater inputs to the global oceans ([Marengo and Espinoza, 2016](#), [Nobre et al., 2016](#)), which makes it the single, largest source of fresh water on the Earth. The Amazon rainforest stores approximately 120 billion tonnes of carbon ([Malhi et al., 2006](#), [Saatchi et al., 2011](#)), equivalent to approximately 9–14 decades of

current global anthropogenic carbon emissions (Canadell et al., 2007), and absorbs about 1 billion tonnes of carbon per year (more than 10% of annual anthropogenic CO₂ emissions) (Marengo et al., 2018). In addition, moisture exchanges in the Amazon forest play a crucial role in the climate system, contributing to atmospheric circulation and to the water, energy and carbon cycles (Zemp et al., 2014, Spracklen and Garcia-Carreras, 2015, Nobre et al., 2016). However, climate variability and anthropogenic activities, i.e., deforestation fires, have become important agents of disturbance in the Amazon basin (Davidson et al., 2012).

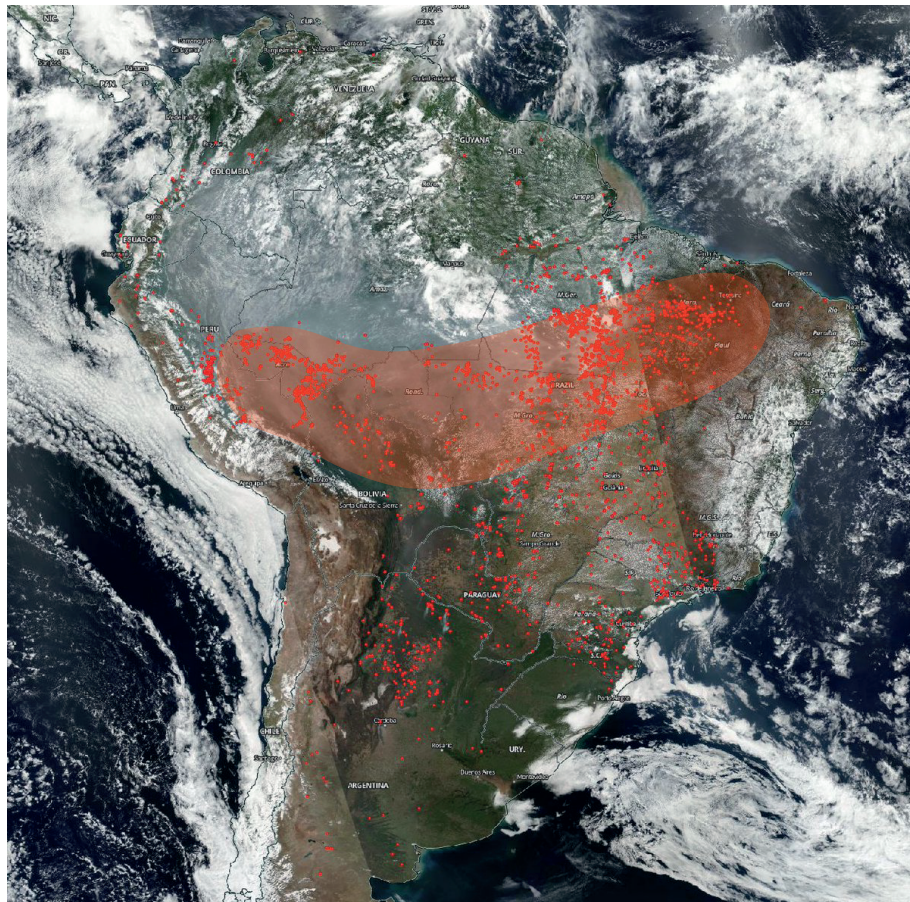


Figure 1.1: Satellite image collected by the Moderate Resolution Imaging Spectroradiometer (MODIS) aboard the Terra satellite on August 18, 2015. Actively burning areas, detected by MODIS, are outlined in red and the arc of deforestation shaded in red; Image adapted from <https://www.nasa.gov/image-feature/goddard/el-ninos-effects-bring-more-wildfires-to-brazil>.

Previous studies have sought to understand the impact of biomass burning emissions in the Amazon from local to hemispheric scales (Andreae et al., 1988, Kirchoff

et al., 1989, Zhang et al., 2008, Ignotti et al., 2010, de Andrade Filho et al., 2013, Kolusu et al., 2015, de Oliveira Alves et al., 2015, Reddington et al., 2015, Archer-Nicholls et al., 2016, Martin et al., 2016, Giangrande et al., 2017). For instance, a few studies on smoke height across the Amazon have determined that smoke tends to concentrate under 2.5 km although they also found the presence of a persistent haze layer at around 4–6 km (Table 1.1). These studies are based on limited observations for short periods of time or specific locations, that may be influenced by specific weather conditions. Because of the lack of resources and complexities of such a complex, vast and undeveloped area, in-situ sampling in the region is scarce. Therefore, studies on biomass burning across the region have typically used satellite observations (i.e., MOPITT, MAPS and TOMS), ozonesondes and ground-based observations, combined with global and regional CTMs supplied with meteorological data and fire emission estimations. In addition, aircraft campaigns across the region have been designed to overcome the scarcity of observations, by providing with high temporal and spatial resolution data on biomass burning pollution, but limited to flight tracks. These include ABLE 2A (Harriss et al., 1988), CITE 3 (Hoell Jr et al., 1993), TRACE A (Fishman et al., 1996b), BARCA (Andreae et al., 2012), and more recently, SAMBBA (Allan et al., 2014) and GoAmazon (Martin et al., 2016). Overall, these observational and modelling studies have revealed that emissions from biomass burning in the Amazon are a large contributor to CO and O₃ budgets and their interannual variability in the southern hemisphere (SH), as well as they have shown high mixing ratios of both gases in the mid-upper troposphere over the region (e.g., Reichle et al., 1986, Andreae et al., 1988, Kirchhoff and Rasmussen, 1990, Watson et al., 1990, Fishman et al., 1996a, Galanter et al., 2000, Thompson et al., 2001, Edwards et al., 2006, Deeter et al., 2018). Substantially high surface CO and O₃ mixing ratios of 400 ppb (Andreae et al., 2012) and 40–60 ppb (Bela et al., 2015), respectively, have also been reported during the burning season, even reaching maximum daily surface O₃ mixing ratios as large as 100 ppb (Artaxo et al., 2002, Kirkman et al., 2002). The ozone levels found are well above the critical level known to be hazardous to human health and plants (40 ppb) (Ainsworth et al.,

2012). Furthermore, [Pacífico et al. \(2015\)](#) assessed the impact of fire-induced ozone exposure on the Amazonian tropical forest productivity and suggested enhancements of 15 ppb in O_3 mixing ratios, due to biomass burning, which resulted in mean reductions in forest productivity of 15%. Nevertheless, modelling studies across the Amazon have reported some systematic quantitative differences compared to observations, which seemed to be related to poor representation of biomass burning emissions and smoke injection heights, as well as convective and long-range transport in the models ([Andreae et al., 2012](#), [Bela et al., 2015](#)).

Despite the large influence of biomass burning from the Amazon on the atmosphere budget, and the critical levels of ozone found each year during the burning season, no studies have yet comprehensively investigated the smoke plume dynamics governing the region, or assessed biomass burning impacts on surface ozone levels, with implications for human health and crops productivity. Future projections suggest an increase in fire activity over the Amazon region ([Cochrane and Barber, 2009](#)), exacerbated by more frequent droughts, as a consequence of climate change and human activities ([Bowman et al., 2009](#)). Under this scenario, increases of fire emissions are expected, which may lead to large, more frequent and extended episodes of ozone pollution, compromising larger population's health and food security. To fully understand the factors that drive smoke plume dynamics and the transport and distribution of pollution produced in a fire is crucial to accurately predict and help mitigate impacts on air quality and climate, from local to global scales, as well as minimise the risks to human population and ecosystems.

1.2 Motivation, research objectives and approach

By 2015, an estimated area of 66% of the total Brazilian Amazonia had been deforested ([INPE, 2016](#)). Extensive deforestation leads to changes in Amazon forest dynamics with the potential to affect the concentration of atmospheric CO_2 and modify precipitation, among other parameters (i.e., albedo, temperature, surface

roughness, stomatal resistance, soil moisture). All these changes have significant consequences on global climate, i.e., air cooling and changes in large-scale circulation (Nobre et al., 1991, Marengo and Nobre, 2001, Werth and Avissar, 2002). Furthermore, deforestation fires in combination with global warming and more frequent and severe droughts may increase biomass burning emissions and the Amazon forest may become in the near future, a source of carbon rather than a sink (Davidson et al., 2012).

In view of the importance of the Amazon as a global stabiliser and the large contribution of local biomass burning emissions to the global and regional atmospheric budget, it is crucial to have a better understanding of the drivers that control the transport and distribution of biomass burning pollution over the Amazon, its contribution to the atmospheric composition and its global and regional impacts. This project seeks to characterise smoke plume dynamics across the region, which will help represent the best modelling approach to study biomass burning over the Amazon, assess the contribution of biomass burning to the ground ozone levels and associated impacts on air quality. For this purpose, satellite observations, ozonesondes, and aircraft and ground-based measurements combined with a global Earth System Model (ESM) are employed. Specifically, this study seeks to answer the following scientific questions:

What is the vertical distribution of biomass burning emissions over the Amazon? Determining the height at which fires inject pollutants in the atmosphere will allow understanding of how and in which degree biomass burning in the Amazon impacts the atmospheric composition, air quality and climate, from regional to global scales. Despite the importance of fire emissions from the Amazon in the global atmospheric budget, little is known about the processes that control fire pollution and plume dynamics over this region, mostly due to the lack of smoke plume height observations. This study proposes the use of a combination of satellite data during the burning seasons of 2005-2012 to develop a climatology of smoke plume heights over the Amazon. The information obtained from this analysis will help better

represent the vertical distribution of Amazonian fire emissions in ESMs.

Which are the main factors that control the vertical distribution of biomass burning emissions over the Amazon? Biomass burning in the Amazon is influenced by complex interactions among meteorology, climate, topography and human activities. Identifying main drivers of variability in fire plume dynamics across the Amazon is key to define future trends and make decisions to responsibly manage air quality and climate. On that respect, this project will evaluate the main aspects that affect smoke plume dynamics. This includes an extensive evaluation of fire properties, plume characteristics, weather and climatic conditions from 2005 to 2012.

What is the influence of biomass burning on surface O₃ levels and its impact on air quality over the Amazon? Exploring the contribution of Amazonian biomass burning emissions on surface ozone levels and its potential toxicity and phytotoxicity is crucial to understanding the regional and large-scale implications on air quality. For this, results from scientific questions 1 and 2 will provide information to better represent the vertical distribution of biomass burning emissions in an ESM, and assess the potential contribution of biomass burning to surface ozone levels and the impacts on air quality. This work will implement a novel fire injection height parametrisation, based on satellite observations, into an ESM and evaluate results with a combination of satellite observations, ozonesondes, aircraft and ground-based measurements. Finally, results from the modelling experiments will help widen the understanding of the impacts of fire-induced ozone on human health and vegetation across the region.

1.3 Dissertation overview

The following chapters include data, methods, analyses, results and conclusions that address the research objectives of this study. Chapter 2 presents an overview of the main features, settings, performance and limitations of the software used

to develop a climatology of smoke plumes across the Amazon for 2005-2012. This chapter addresses the first research objective. Chapter 3 presents an analysis of the climatology of smoke plume heights derived from satellite observations and assesses the main drivers of variability on smoke plume heights across the region, which directly addresses first and second research objectives. This chapter is included as a manuscript that was published on February 8th, 2019 in the Atmospheric Chemistry and Physics journal (ACP). Chapter 4 presents a modelling analysis of the impact of the vertical distribution of biomass burning on ozone and its precursors and assess the influence of Amazonian biomass burning on surface ozone and air quality over the Amazon region. This chapter is inserted as a manuscript to be submitted to ACP. Chapter 5 provides conclusions from all the analyses conducted in this work and recommendations for future research. Appendix A includes supplementary information for chapter 3. Appendix B includes supplementary information for chapter 4. Appendix C presents a summary of the chapters with contributions.

Chapter 2

MISR and MINX: Developing a biomass burning smoke plume climatology across the Amazon

2.1 Introduction

Remote sensing techniques allow observing the spatial and temporal distribution of aerosols in the atmosphere, which is crucial to study their impacts on climate and air quality. Passive remote sensing techniques detect the natural radiation reflected or emitted by features under cloud-free conditions. They provide high spatial and temporal coverage, but limited accuracy on the vertical aerosols distribution. These passive techniques include Radiometry, Imaging Radiometry, Spectrometry and Spectroradiometry. The latter is used by the Multi-angle Imaging SpectroRadiometer (MISR) combined with multi-image matching stereoscopic techniques, based on the principle of parallax ([Diner et al., 1998](#)). An important advantage of this technique is that it relies uniquely on geometry and no calibration is needed, but its major limitation is its low sensitivity to thin aerosol features without a well-defined contour that is not clearly discernible from the background. On the

other hand, active remote sensing techniques send a pulse of energy and receive the radiation reflected. These techniques include Radar, Scatterometry, Laser altimetry and LIDAR, such as the Cloud-Aerosol Lidar with Orthogonal Polarization (CALIOP), on board the CALIPSO satellite. CALIOP provides high accurate aerosol scattering profiles (Winker et al., 2009) but extremely low spatial coverage due to its narrow path (~ 60 m).

MISR and CALIOP have been widely used in the study of the vertical distribution of aerosol plumes and clouds in the atmosphere over several regions (Val Martin et al., 2010, Amiridis et al., 2010, Jian and Fu, 2014, Huang et al., 2015). For instance, over North America, Val Martin et al. (2010) developed an extensive 5-year climatology of smoke plume heights based on height-retrievals derived using MISR imagery. Similarly, Jian and Fu (2014) and Tosca et al. (2011) characterised smoke plume heights during the burning seasons of 2001–2009/2010, over tropical regions in Asia and Mims et al. (2010), over grassland fires in Australia. Using observations made by CALIOP, Huang et al. (2015) examined the most probable height of dust and smoke layers over six fire impacted regions and Amiridis et al. (2010) investigated aerosols vertical distribution and smoke top heights from agricultural burning in Europe. All these studies showed the large variability in smoke plumes across biome, season and region, as well as demonstrated that although most smoke concentrates in the boundary layer, where it is well-mixed, a variable but significant percentage of generally, low-density smoke reaches the free troposphere, as a result of favourable fire and local weather conditions, and can be transported long-range distances. MISR and CALIOP performance and sensitivity are disparate. Specifically MISR provides near-source constraints on the vertical distribution of smoke and allows to study smoke plume dynamics on a plume-by-plume case.

The Amazon region is a major fire region, which contributes largely to the global fire emissions (Van der Werf et al., 2010). However, despite its important role in the distribution and transport of global biomass burning products, no study has yet developed a climatology of smoke plume heights over the region. The present study

aims at improving the vertical distribution of biomass burning emissions represented in Earth system models (ESM) over the Amazon. For that, MISR capabilities are exploited to develop a large dataset of smoke plume heights during the burning seasons (July to November) from 2005–2012. This is the first time that such a comprehensive study of the vertical distribution of biomass burning emissions has ever been done over the Amazon. The smoke plume database developed over the Amazon presented in Chapter 3 (Gonzalez-Alonso et al., 2019) was created with the MINX interactive tool (Nelson et al., 2008b, 2013), using the MISR imagery and MODIS thermal anomalies (Diner et al., 1998, Giglio et al., 2003). Because the use of MINX requires some understanding of the software and algorithms used, this chapter describes the principal features of the MISR instrument and performance of MINX, with focus on the Amazon smoke plume climatology.

2.2 MISR Instrument and products

The Multi-angle Imaging SpectroRadiometer (MISR) is a spaceborne instrument that measures atmospheric and surface properties, designed to study cloud, aerosols and the Earth surface. MISR flies on board the Terra satellite (launched in December 1999) and since February 2000 has been acquiring images of the Earth at nine different fixed angles (from -70° to 70°) (Diner et al., 1998). This multi-angle imagery provides stereoscopic retrievals of aerosol plumes and clouds heights at 275 m to 1.1 km of resolution. MISR is integrated in the NASA Earth Observing System (EOS) fleet, with a near-polar orbit at an altitude of 705 km and about 380 km of swath common to all cameras. The descending node crosses the Equator at around 10:30 a.m. local time and provides global coverage every 9 days at the equator and every two days near the poles.

The nine push-broom cameras are designated as An, for the nadir camera and A, B, C and D followed by "a" or "f", depending of their viewing, being "a" for aft-viewing and "f" for forward-viewing (i.e., Aa, Ba, Ca, Da and Af, Bf, Cf, Df;

Figure 2.1). The camera viewing angles differ in approximately 7 min from each other and 70.5° (D), 60.0° (C), 45.6° (B), and 26.1° (A) from the nadir. Images are acquired in four spectral channels for each camera at blue, green, red and near-infrared wavelengths (446.4 ± 41.9 ; 557.5 ± 28.6 ; 671.7 ± 21.9 and 866.4 ± 39.7 nm, respectively). More information about the MISR instrument can be found in Diner et al. (1998) and at <https://misr.jpl.nasa.gov/Mission/misrInstrument/>.

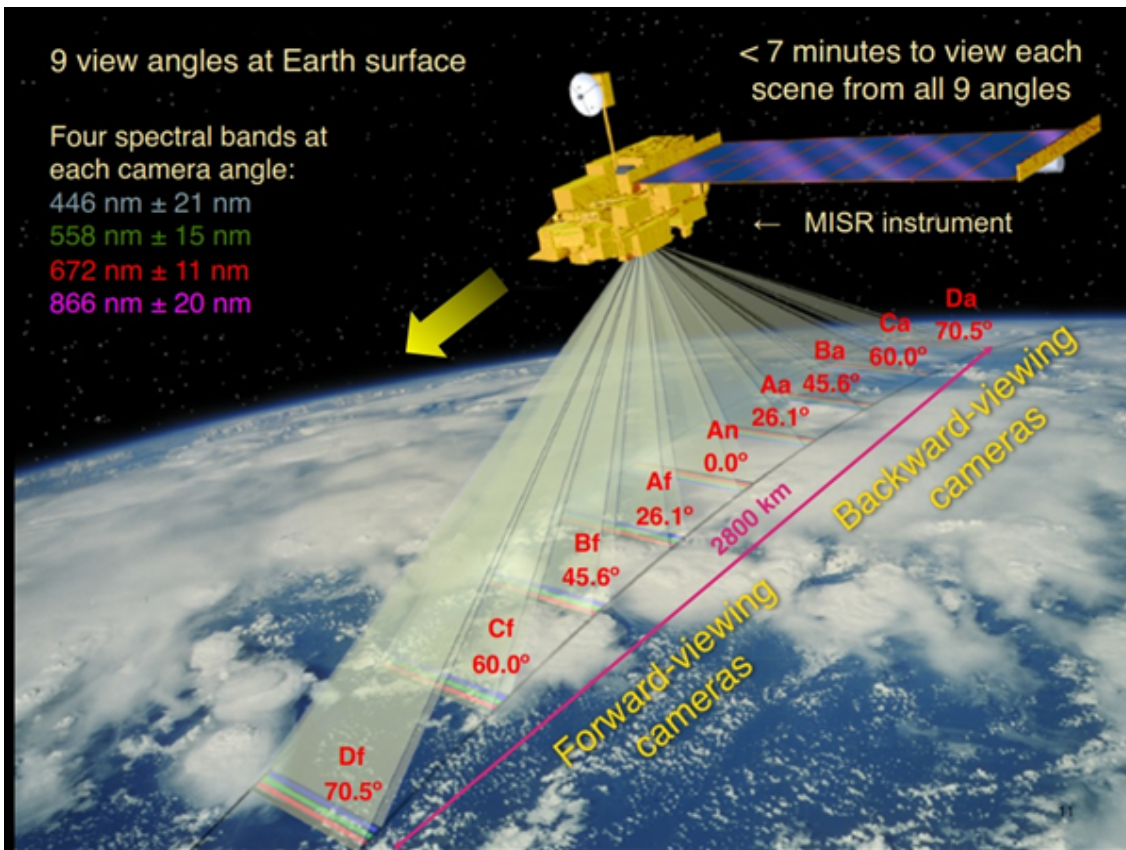


Figure 2.1: TERRA satellite with MISR aboard, and the four-spectral-band multi-angle nine cameras; https://github.com/nasa/MINX/blob/master/webdoc/MINX_Doc1.pdf.

MISR data are freely downloadable from the Earth Data website¹, following registration and logging in. Data include three level products and ancillary data. The Levels 1 and 2 products are in swaths of 180 blocks of 140.8 km along track for each MISR orbit. Level 1 products have been processed and calibrated radiometrically and geometrically to remove many of the instrument effects. Level 2

¹<https://urs.earthdata.nasa.gov>; last access 14/02/2019

products are geophysical measurements derived from the instrument data. They include Level 2 Top-of-Atmosphere/Cloud product, with cloud heights and winds, cloud texture, top-of-atmosphere albedos and other related parameters, and Level 2 Aerosol/Surface product, with tropospheric aerosol optical depth, aerosol composition and size, among other parameters. Level 3 product consists of monthly, seasonally, and annually averaged maps for various parameters from Level 2. The NASA Langley Atmospheric Science Data Center² distributes the MISR products in hierarchical data format (HDF). Detailed description of the algorithms used for each data product and specifications of the HDF files can be found in the Atmospheric Science Data Center (ASDC) website³.

The stereo-matching algorithms in the operational MISR Level 2 cloud product use MISR multi-angle ellipsoid-referenced images to automatically retrieve heights and winds of clouds, and other aerosol features above the ground using a stereoscopic method (Moroney et al., 2002a). For that, MISR needs a previous set of some fixed processing parameters, which will be applied equally to all scenes (Muller et al., 2002) to speed-up processing time. If all cameras measured high-resolution radiances, MISR data would be prohibitive. For this reason, only the nadir camera data and the red channels for the off-nadir cameras (12 of the 36 channels) are kept at the highest resolution (275 m), while data on the other channels are at 1.1 km resolution. This operational mode is the default and is called global mode (GM), useful for global studies of cloud heights and winds. However, MISR can also be configured to achieve high resolution for all the channels (36 channels) for a limited period of time and specific domains. This capability is known as the local mode (LM) and it is scheduled upon request from the user community.

The MISR operational product retrieves two types of stereo-heights. The zero-wind heights assume that disparity in the same feature between camera views is

²<https://eosweb.larc.nasa.gov/>; last access 10/02/2019

³https://eosweb.larc.nasa.gov/sites/default/files/project/misr/guide/MISR_Science_Data_Product_Guide.pdf; https://eosweb.larc.nasa.gov/project/misr/misr_table; last access 14/02/2019

caused by parallax. Parallax is the difference in location of a projected feature on the ground due to different viewing angles (Moroney et al., 2002a). Smallest parallax is obtained from the nadir image (An) and is used as the reference camera. Wind-corrected heights are calculated after separating the contribution of the wind and the parallax to that disparity. They need the wind speed along-track and across-track components to be computed and applied to the zero-wind cloud-top heights to produce wind-corrected heights at a horizontal resolution of 1.1 km. The wind direction and the along-track component of the wind speed are extracted using the Df/Da ($\pm 70^\circ$) and Bf/Ba ($\pm 46^\circ$) cameras imagery (Davies et al., 2007). Wind-corrected heights provide more accurate results, but are computationally expensive and at low spatial coverage, unlike the zero-wind heights, which offer excellent coverage (Kahn et al., 2007).

2.3 MODIS Instrument and products

The MODIS instrument is also aboard the NASA Terra satellite and observes the same scenes as MISR. MODIS detects from its far-infrared imagery, under cloud-free conditions, thermal anomalies at 1 km spatial resolution, named "fire pixels", (Figure 2.2). The detection method is based on an algorithm (Giglio et al., 2003) that exploits the strong emission of mid-infrared radiation from fires (Dozier, 1981, Matson and Dozier, 1981) and offers automated daily global fire information. In addition, MODIS provides estimates of the fire radiative power (FRP) for each fire pixel detected, a parameter used as a proxy of fire intensity. FRP is calculated from the differences in the radiance of each fire pixel and its background (Giglio et al., 2003). Two MODIS products are assimilated by MINX:

1. The Level 2 MOD14 Thermal Anomalies at a 1 km resolution, which includes FRP.
2. A global biome classification grid at 500 m of spatial resolution derived from

the MODIS Level 3 land cover product MCD12Q1 Land Cover Product⁴ (Friedl et al., 2010). This MCD12Q1 product classifies the land cover associated with each smoke plume in 17 International Geosphere-Biosphere Programme (IGBP) land cover classes and has an annual temporal resolution.

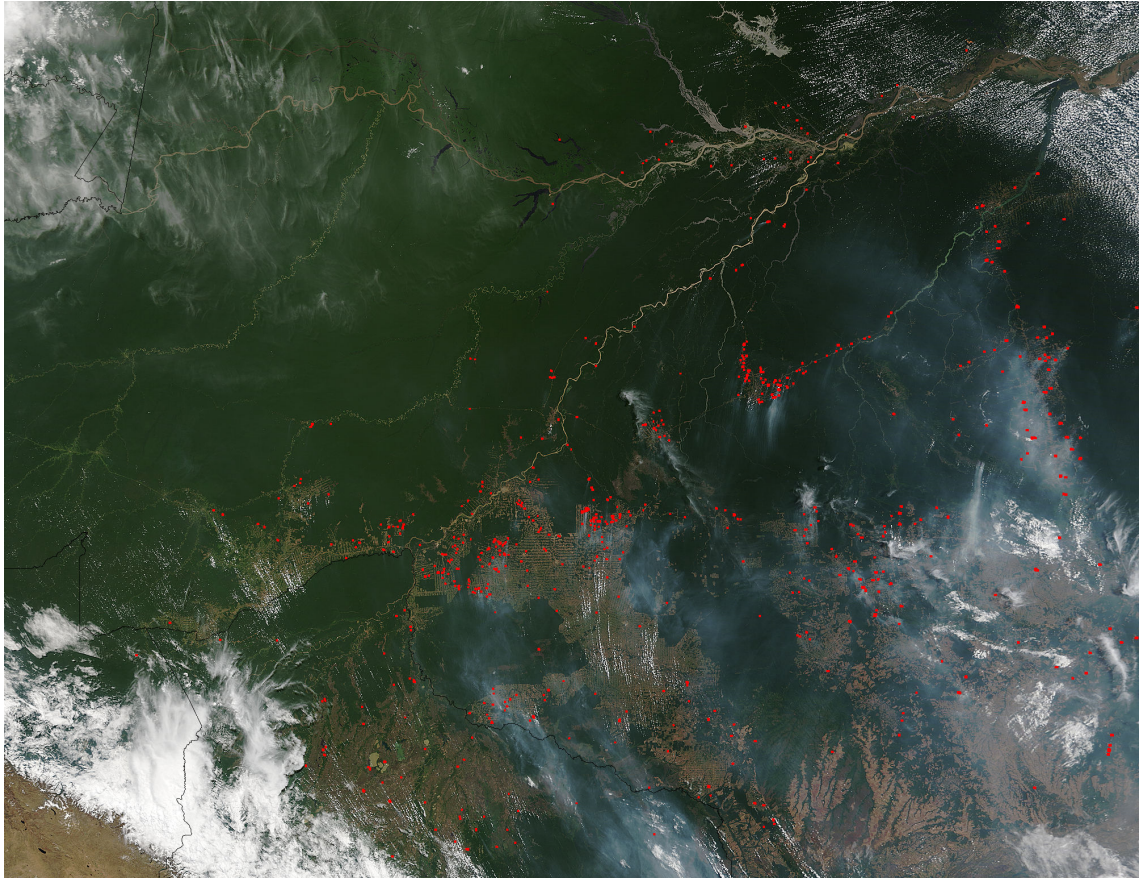


Figure 2.2: Natural-colour image collected by the Terra satellite across the Amazon on September 10, 2015. Actively burning areas, detected by MODIS's thermal bands, in red. <https://www.nasa.gov/image-feature/goddard/wildfires-in-amazonian-region-of-brazil>.

2.4 MINX Software

The MINX visualization and analysis interactive tool complements the MISR Level 2 operational stereo product for detailed studies of smoke, dust and volcanic ash.

⁴<https://search.earthdata.nasa.gov/search?q=MCD12Q1%20V006>; last access 14/02/2019

The MINX stereo-height algorithm was developed to overcome the limitations of the MISR operational product, as it enables the user to retrieve clouds, aerosols plume heights and winds at higher spatial resolution and better precision. Plumes are defined as regions of dense aerosol, with a well-defined discernible contour above the terrain and downwind of its source (Nelson et al., 2013), allowing to determine the direction of transport. Clouds, on the other hand, are not associated with any source and the direction of transport is not evident. MINX is written in the Interactive Data Language (IDL) and it can be downloaded from Github⁵, available for Mac OS X, MS Windows, and Linux platforms. Since the development of MINX, several versions have been released. The latest version is MINXv4, with substantial improvements that provide better quality smoke height retrievals. MINX has been used for the MISR Plume Height Climatology Projects (MPHCP)⁶. MPHCP aims at creating an aerosol injection height climatology to support wildfire, climate change, and air quality studies (Nelson et al., 2008b). In addition, MINX uses have been extended to many detailed studies of smoke plume heights over specific regions in the world (Val Martin et al., 2010, Mims et al., 2010, Tosca et al., 2011), studies of ash clouds from volcanic eruptions (Scollo et al., 2012, Kahn and Limbacher, 2012) and dust plumes from deserts (Kalashnikova and Kahn, 2008).

MINX interface allows the user to display the multi-angle nine camera images one by one or as an animated loop (Figure 2.3). This method enables the user to study plume and cloud dynamics, as it provides a similar 3D effect of the scene that could not be possible with a single image or multiple same-angle images. MINX requires all nine camera terrain-referenced imagery files (GRP_TERRAIN product) to derive accurate heights and winds over land (Jovanovic et al., 1998), and the geometric parameters product (GP_GMP), with zenith and azimuth viewing angles, which are both from MISR Level 1. An additional product is needed to perform stereo retrievals, the MISR Ancillary Geographic Product (AGP) at 1.1 km spatial

⁵<https://github.com/nasa/MINX>; last access 12/02/2019

⁶<https://misr.jpl.nasa.gov/getData/accessData/MisrMinxPlumes2/>; last access 09/02/2019

resolution, which contains the Digital Elevation Model (DEM) and surface feature IDs. Additionally, MISR Level 2 aerosol parameters (AS_AEROSOL) are used to obtain aerosol data, i.e., AOD, and TC_CLASSIFIERS to identify different types of aerosols (e.g., smoke or ash). All the cited products can be downloaded from the Earth data website⁷ after logging in. Table 2.1 summarises the MISR and MODIS products and files necessary to process smoke plume heights with MINX.

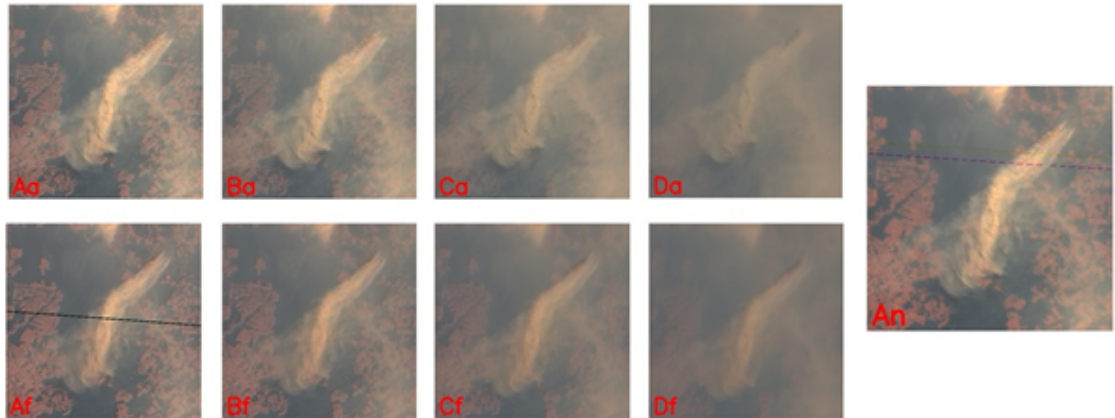


Figure 2.3: MISR nine camera views of a smoke plume on the 22nd of August 2010, in the Amazon

As the MISR operational product, MINX stereo-height algorithm provides zero-wind and wind-corrected height values (Figure 2.4). MINX calculates the wind speed necessary to retrieve wind-corrected plume heights with an accuracy of 250 m by supplying the wind direction in the plume. For each grid in a plume, heights and winds are computed combining each of the six nearest camera neighbours to the nadir camera, used as a reference. Whenever the results of at least three camera pairs are similar, the retrieval is considered successful. In addition, if the MISR aerosol standard products are loaded in MINX, aerosol properties within the plume (e.g. Angstrom exponent, single-scattering albedo) will be extracted at 17.6 km of resolution.

⁷<https://search.earthdata.nasa.gov/search>

Table 2.1: Summary of MISR and MODIS files and products used to digitise smoke plumes with MINX.

Product	Files	Description
MODIS MOD14 ^a	MODIS/Terra Thermal Anomalies/Fire 5-Min L2 Swath 1km V005	fire pixels at 1 km and FRP in MW/pixel
MHB2T ^b	level 1 GRP_TERRAIN (terrain-referenced)	radiance files
MIB2GEOP ^b	level 1 GP_GMP	camera and sun geometry
MIANCAGP ^b	AGP – ancillary geographic	digital elevation data and surface type masks
MI12ASAE ^c	level 2 AS_AEROSOL	aerosol data: AOD, single-scatter albedo etc.
MI12TCCL ^a	level 2 TC_CLASSIFIERS	smoke/cloud mask files

^aOptional files

^bRequired files

^cRequired only for plume studies

2.4.1 MINX Stereo retrieval algorithm

The retrieval process starts by matching images of camera pairs with the nadir camera and measuring the disparities within a plume. When the user determines the wind direction for each camera pair a height, wind-across-track and wind-along-track solution is achieved. This process is done for all camera pairs at the same point, and a maximum of eight heights and wind values are obtained depending on the number of camera pairs selected for matching and the number of successful retrievals. Then, the MINX stereo retrieval algorithm determines the more similar height and wind value among camera pairs for each point.

Height retrievals for static and in movement features

During Terra overpass, each MISR camera observes a feature in the atmosphere within seven-minute difference. The shift in the location of a feature between two cameras is its disparity, and consists of an along-track displacement parallel to the ground, and an across-track displacement in the orthogonal direction. The measure-

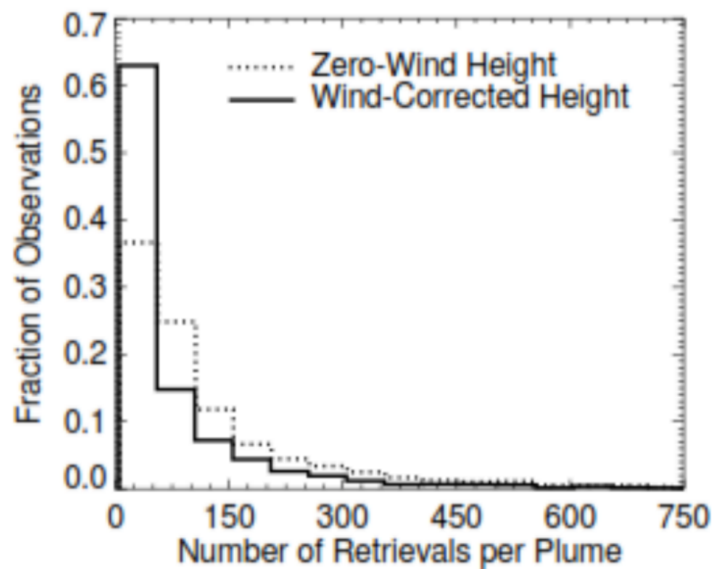


Figure 2.4: Comparison of wind-corrected and zero-wind stereo-height pixels per plume in a smoke plume climatology over North America. (Adapted from [Val Martin et al. \(2010\)](#))

ments of these two components provide the primary information to compute stereo heights and winds (Moroney et al., 2002a).

In the case of static features in the atmosphere, the along and across-track disparities due to motion are zero, the across-track disparity due to parallax is zero and the along-track disparity is only due to parallax. Therefore, its height can be determined by knowing this parallax disparity and the angle of the non-nadir camera (Moroney et al., 2002b)(Figure 2.5). This is called the zero-wind height. The zero-wind height can also be performed for features in movement however, errors range from tens of meters to kilometres, depending on the height of the feature, the wind and the camera pair used.

If the feature is not stationary, then the height, the wind speed in the along- and across-track directions are unknown for a camera pair, assuming no vertical motion. In the MISR operational product this is solved by adding a third camera pair (D) and making some assumptions (Zong et al., 2002) (Section 2.2). In MINX, there are two cases to perform the stereo height retrieval. The case in which the feature moves only in the across-track wind component and the case in which the feature moves in both components, along and across-track. In the first case, the along-track disparity due to motion is zero and the height is determined in the same way as the zero-wind height performance, assuming that the along-track disparity is only due to parallax. The across-track wind speed can then be determined by converting the across-track disparity to map distance and dividing by the time between the two camera viewing angles. To compute this height the Earth's curvature, terrain height and other factors need to be considered. When a feature is moving in the two components, the across-track wind component will be determined using the method described above but the along-track component includes the contribution of the parallax and the real displacement due to the along-track wind. In this case, the height and the along-track wind components need to be determined, knowing only the along-track disparity.

The MINX stereo-height retrieval algorithm allows the user to provide the wind

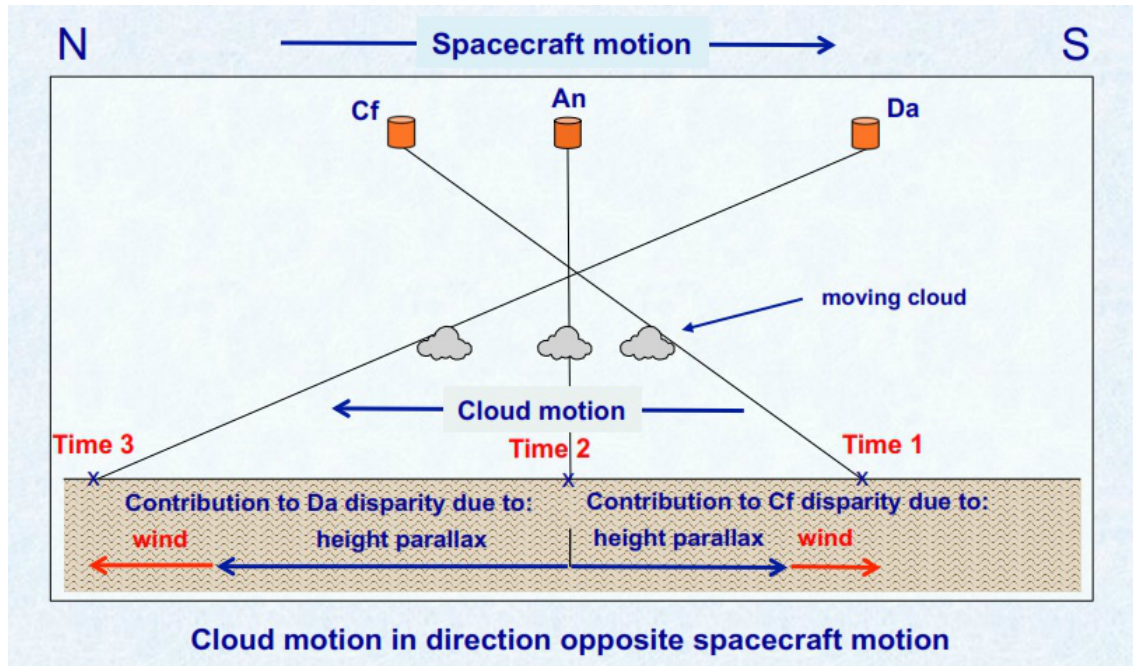


Figure 2.5: MISR view with respect to features in the atmosphere, disparities produced by parallax and due to motion of the MISR instrument and the feature. (Image adapted from https://github.com/nasa/MINX/blob/master/webdoc/MINX_Doc5.pdf).

direction when digitising (Section 2.4.2). For any point in the user-supplied wind direction, the wind direction can be calculated as the slope of the digitised line, which is the ratio of the along- and across-track distances and the ratio of the wind speed in the along- and across-track components. If one of the wind speeds is known, the other can be calculated from the slope of the line and the along-track wind, and height can be determined at high resolution using a camera pair. This stereo retrieval method is applied to each point of the digitised plume using all camera pairs and the nadir camera as reference.

Image matching

The image matching process consists of finding a feature in a non-nadir image that corresponds to that feature in the nadir image and measuring its disparity. During the MINX stereo height retrievals, all cameras selected for image matching should be paired with the nadir camera. Meaning that whenever a feature is not visible

in the nadir camera but visible in any of the off-nadir cameras, MINX will fail at performing the stereo retrieval. This process uses a square template-based reference image in the red-band, centred on the pixel of study in the nadir view. The match is performed when a target pixel in the comparison image is found to best correlate to the reference template. This method provides more accurate matcher results applied to features that extend through the template than to a single pixel at the centre. The image matching process requires intense use of the CPU, and processing times depend on the hardware and the area to perform the match. Larger templates require longer processing times and can improve the retrieval coverage, but the smaller are usually more successful for fine spatial detail when plumes have small variations in height. The matcher template size is defined by the user. In the case of the Amazon climatology of smoke plumes, the default option (medium size) was chosen, which provides enough detail at reasonable processing times.

Determination of height and wind

Once the successful matches for the camera pairs produce the retrieved results for a sample point, these results are then evaluated to determine a consensus height and wind for all camera pairs matching. The mean heights and winds are calculated for those camera pairs retrievals that are more similar to the median values, used to soften the effects of the outliers. Heights and wind results are discarded if they do not fall into a threshold distance from the media, where the threshold distances are calculated dynamically.

Spectral band

The red band is the high-resolution band in the global mode of the MISR operational product because of its larger contrast between atmospheric features over ocean and land (Diner *et al.*, 1998). However, over bright surfaces like grasslands or deserts, or in the case of low-dense features stereo-height retrievals in red band is not pre-

ferred (Mims et al., 2010). Increases in wavelength lead to decreases on atmospheric scattering and smoke will be more transparent, allowing to see the terrain through it. If in the reference image the terrain is seen through the smoke plume, the image matching will be more difficult to process, performing less successful height retrievals. Therefore, blue band retrievals generally offer greater sensitivity to thin aerosol layers and over bright surfaces.

Before the release of MINXv4 the default spectral band option was red. However, the user could select the blue band if applicable to the characteristics of the plume and background. This should be configured by the user manually at the start of digitising each plume, which entails additional time into the digitising process. Since MINXv4, two plume height retrievals are performed for each plume. One retrieval using red-band data and the other using blue-band data. Each retrieval is treated as a different plume, but they share the same aerosol properties, from the MISR aerosol product, and the same plume coded name in exception of a letter, "R" or "B", depending on the spectral band ("R" for red and "B" for blue band). This new capability allows the user to choose between the best quality height retrieval plume, but it doubles the number of plumes created.

2.4.2 Digitalization of smoke plumes with MINX

MINX can be used to digitise and study a single plume or to create a large climatology of smoke plumes observed by MISR. The files generated by MINX include among other parameters the location and time of the plume, different statistics for smoke plume heights based on the individual height retrievals, the radiative power of the associated fires, the direction of transport of plumes and aerosol properties.

MISR files are large (~ 2 Gbytes/orbit) and tedious to download for projects that cover large periods of time or areas, like this study. The MINX "Plume Utilities" is a tool designed to limit the amount of MISR data to download and process, reducing considerably processing time and computing space. This tool allows the user to

select only the MISR orbits and blocks where it is likely to find smoke plumes, rather than download and visually inspect all MISR images for the time range and area of study. In the case of smoke plumes from wildfires, MINX uses the MODIS Terra thermal anomalies product, as mentioned in Section 2.3. By loading the fire pixels, MINX generates a list of the MISR orbits and blocks with coincident active fire pixels. To do so, the user needs to provide the geographic bounds and the time range for the study when ordering the MODIS MOD14 thermal anomalies. The "Plume Utilities" tool reduces the number of MISR files to download by a factor of 100 or more (Nelson et al., 2008b). In addition, the MODIS thermal anomalies files are read by MINX and displayed as a layer of red dots on MISR imagery (Figure 2.2), which helps the user identify plumes, and allows MINX to compute the approximate total FRP for each plume.

Once the necessary MODIS fire pixels and MISR Level 1 and 2 files are downloaded (Table 2.1), MINX is ready to process them, display and compute stereo heights of smoke plumes. Before digitising, the user needs to load and link the MODIS fire pixels to the MISR orbits and paths images. This step includes specifying some parameters as the minimum number of fire pixels to consider or their confidence level. For the specific case of the Amazon climatology, the default options were selected as presented in Figure 2.6. Following this, MINX loads the MODIS thermal anomalies on the MISR images (Figure 2.2). At this point, the user inspects the MISR multi-imagery block by block with the coincident fire pixels superimposed and identifies smoke plumes. The ability to visualise each plume in nearly 3D is decisive to study its structure and dynamics.

The digitising process starts by drawing with the mouse the contour of the plume, starting at the fire source, and the direction of transport. Plumes direction can be digitised with as many points as necessary, being common to draw only two points in the case of a quite linear plume. It is important to make sure that all fire pixels associated with the same plume are contained within the digitised area, as MINX computes the total FRP for each plume and if any fire pixel is not included, it

Only those fire pixels that satisfy all the filtering criteria specified here will be included in the output files.
Fire power is fire radiative power measured in megawatts.

Project Name:
(no spaces or underscores)

Date range (YYYY-MM-DD)
Begin: End:

MISR block range (1-180)
First Block: Last Block:

MISR path range (1-233)
Eastern Path: Western Path:
To span path 233, put larger path in East

Max number of MISR blocks your computer can load into MINX - this defines the block-group size (1-20):

Minimum MODIS confidence level (in %) needed to accept a fire pixel (1-100):

Minimum fire power needed to accept a fire pixel (1-999 MWatt):

Minimum cumulative fire power needed to accept a MISR block (1-999 MWatt):

Minimum cumulative fire power needed to accept a block-group (1-999 MWatt):

Minimum number of fire pixels needed to accept a block-group (1-999):

Figure 2.6: MODIS fire pixel parameters to configure when loading in MINX

will not be summed to the total. Once the contour and direction of transport in a plume are digitised, the MINX stereo-height retrieval algorithm automatically starts, and the drawn plume area is filled in with colour-coded pixels, where colours correspond to the magnitude of the MINX-computed wind-corrected heights. This is achieved only if stereo-heights and winds are successfully retrieved. Figure 2.7 shows the digitising process of a plume observed on the 22nd of August 2010 in the Amazon (O56797-B99-SPWR11). On the left panel, the MINX nadir camera image is displayed with the overlaid red dots representing active fire pixels from the MODIS thermal anomalies product, and the mouse-digitised contour (blue) and wind directions (yellow) of the plume. On the right panel, the retrieved wind-corrected smoke plume heights are displayed on the MISR image in a colour scale, where blue represents low and red high smoke plume heights.

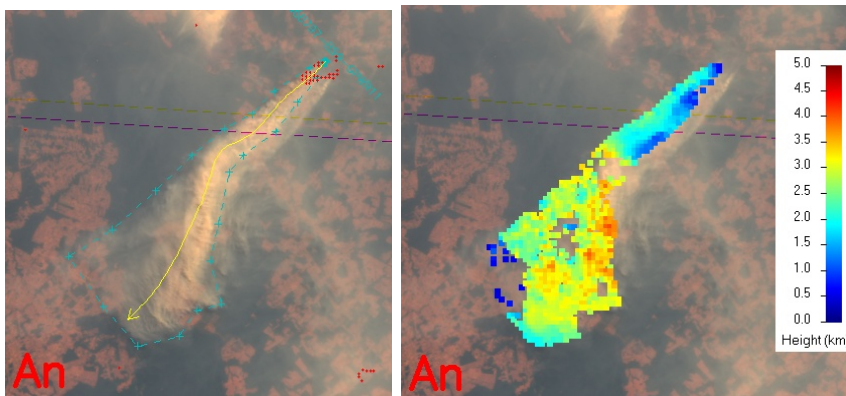


Figure 2.7: MISR nadir image of a smoke plume on the 22nd of August 2010 in the Amazon and MINX smoke wind-corrected height retrievals computed within the plume.

2.4.3 Summary of MINX outputs

MINX automatically generates some outputs for each plume successfully digitised and provides its location in the MISR orbit (Figure 2.8). Firstly, MINX generates a plume name which will be unique and common to all the output files associated with that plume. The name convention follows some rules that are briefly explained below. To illustrate the outputs, Plume O56797-B99-SPWR11, in Figure 2.7, is used as example.

- 56797 is the orbit number and correspond to the 2-7 characters in the name. The minimum value is 000995 and the maximum 999999.
- 99 is the block number where the first point was digitised and corresponds to the 11-12 characters. The minimum value is 001 and the maximum 180.
- S is the 14th character and defines the type of aerosol. S is for smoke, D is for dust, V is for volcanic ash and W is for water (clouds/snow).
- P is the 15th character and defines the geometry of the digitised feature. Being P for polygon and L for line.
- W is the 16th character and is used to define if the direction of the wind was provided or not. Therefore, W will be assigned to plumes, where wind

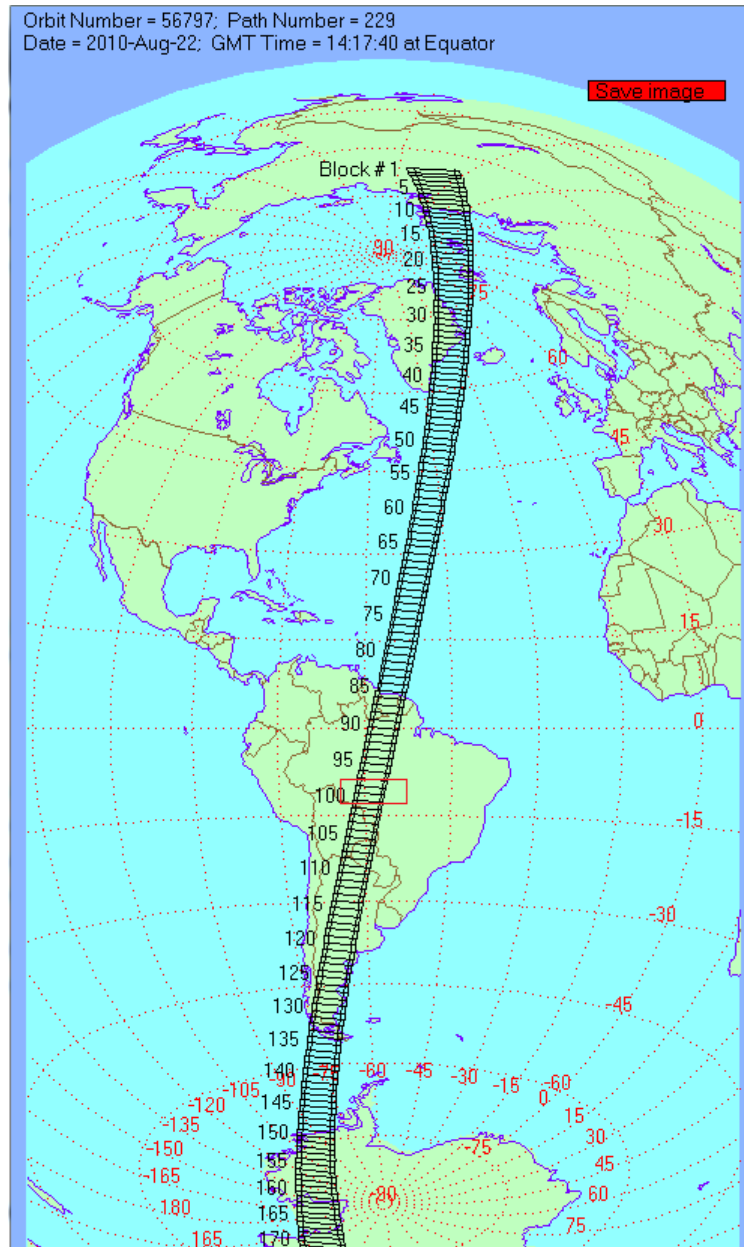


Figure 2.8: Location of the Plume O56797-B99-SPWR11 in the MISR orbit and path. Block 99 in the orbit 56797 is shown with a red square

direction is digitised and zero-wind heights, wind speeds and wind-corrected heights are retrieved. On the contrary, when no wind direction is supplied the letter N is assigned. This is the case of clouds.

- R defines the band used in the height retrieval. It is the 17th character and it can be either R or B, for red or blue band, respectively.

- 11 corresponds to the last characters (18-19) and it refers to the sequenced number of plumes digitised for that block. The minimum value is 01 and the maximum 99.

Immediately after digitising a smoke plume MINX generates a series of outputs that are displayed automatically in the screen. These outputs include:

- **Height Profiles**

The height profiles are plots where the x-axis represents the distance from the first point digitised, usually coincident with the MODIS fire source pixel, and the y-axis represents the height in meters above sea level of each point successfully retrieved and coloured in red (zero-wind) and blue (wind-corrected) (Figure 2.9). Terrain elevation is also represented for each point (green colour). It is typical to find more zero-wind corrected points than wind-corrected points (Figure 2.4, Section 2.4). Stereo-height retrieval profiles display more data whenever the number of successfully retrieved heights is increased and the area of the digitised plume is large, as many points will be at the same distance from the source. However, there are situations in which due to the characteristics of the plume (generally low dense plumes) the number of successful retrievals is low and only a few points will be represented in the profile. This is reflected in the quality of the plume, determined by MINX. In the case of a feature with no apparent direction or movement (smoke clouds), only zero-wind heights are represented. For plumes digitised in both blue and red bands (only MINXv4), MINX creates two different profiles, one for each plume/band.

- **Wind Profiles**

As in the case of the heights profile, wind-corrected profiles are represented by the successful retrieval points from the source fire pixel. Points are split into the across-track and the along-track components of the wind represented in green and red colours, respectively. Wind speed is positive if directed

towards the north and east (top and right directions on MISR images). If the along-track component of wind is directed toward the north, then the wind-corrected height will be less than the zero-wind height. Wind retrievals and wind-corrected heights are less reliable when the wind direction is more aligned to the MISR along-track direction because the along-track motion of the satellite becomes more difficult to separate from the plume motion. MINX determines a quality flag of the retrieval taking this into account. Figure 2.9 shows the MINX vertical height and wind profiles for the same plume on the 22nd of August 2010 (O56797-B99-SPWR11). For this example, the wind-corrected height increases from about 2 km above sea level (asl) in the first 40 km from the origin to a maximum height of ~ 4 km. Median smoke plume height is around 3 km. The along-track wind component shows high variability from the first 40 km, within a range of -18 to -1 m/s, whilst the across-track ranges from -6 to -2 m/s. The sum of these speeds yields around -6 m/s.

- **Aerosol Histograms**

The MISR standard aerosol product provides aerosol data at 17.6 km of resolution whenever the optical depth is lower than 2.0, free of cloud contamination and the terrain is not abrupt. MINX extracts aerosol data from MISR however, results in a single small entire plume may be the same for the whole plume due to the coarse aerosol product pixel. The aerosols histograms created by MINX include optical depth, single-scatter albedo and the tau fraction by particle-type (Figure 2.10). Both optical depth and single-scatter albedo contain spectral data, represented by the colours of the bars. The tau fraction by particle-type histogram represents the fraction of the green-band optical depth value that corresponds to small, medium and large particle sizes and to spherical particles.

In addition to these outputs, for each plume, MINX processes and stores detailed information of each retrieved point in an ASCII file (Figure 2.11). The header of this file contains general information about the plume, i.e., the orbit, path and

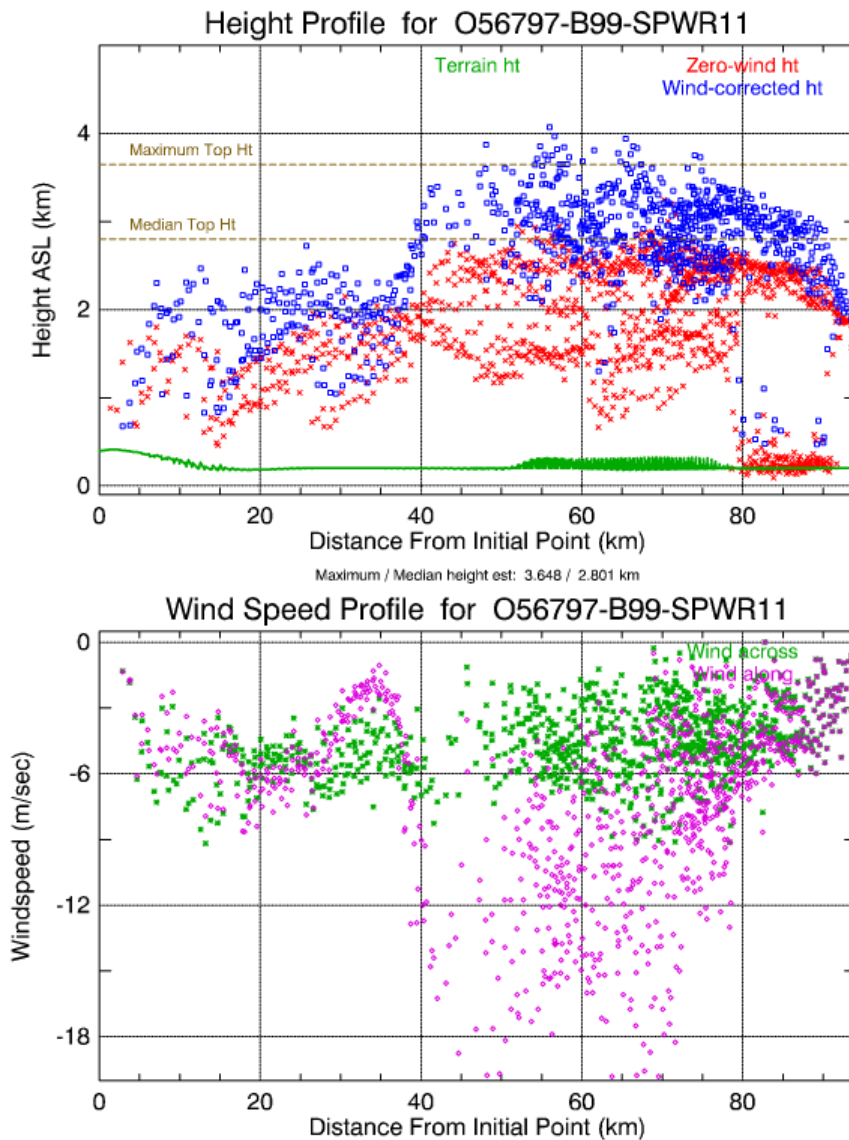


Figure 2.9: Height and wind profiles for the Plume O56797-B99-SPWR11.

block number, date acquired, UTC time, MINX version, user name, date digitised, plume name, aerosol and geometry type, band of retrieval, first point latitude, first point longitude, perimeter, area, mean terrain elevation, retrieval quality, biome (only in MINXv4), MISR product files loaded in MINX, etc (Figure 2.11, top left panel). Following the header, there are three tables, the first two tables contain the coordinates of the points that define the area of the digitised polygon and wind direction (Figure 2.11, top right panel), and the third table contains one data point

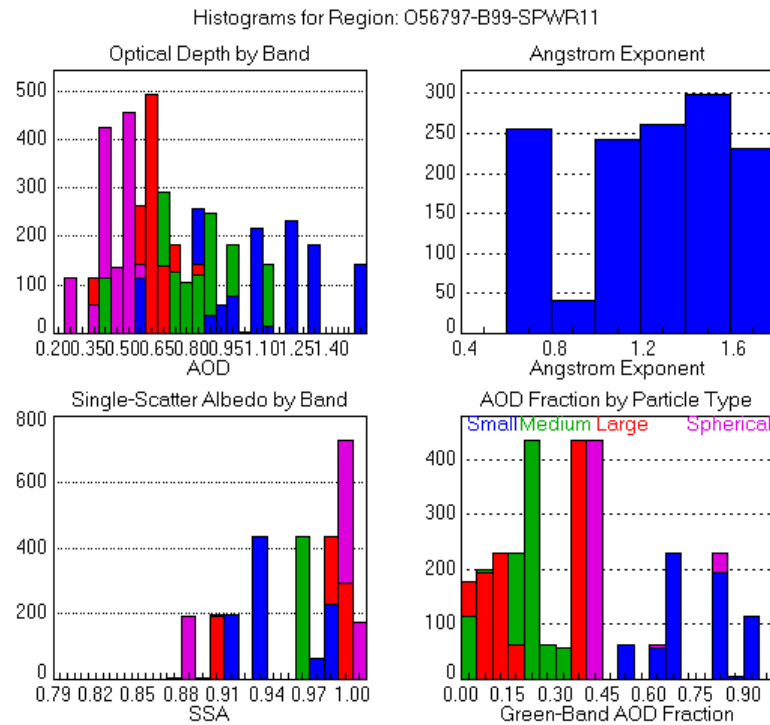


Figure 2.10: Aerosol histograms for the plume O56797-B99-SPWR11 on the 22nd of August 2010.

per row and several columns of parameters (Figure 2.11, bottom panel), where each data point corresponds to the location where MINX retrieves data. Some of the information contained in the file is presented in Figure 2.11 and the most relevant are defined below.

- Retrieved with matcher: specifies the size of the image matcher used in the retrieval.
- Retrieved with cameras: specifies the set of MISR cameras used in the retrieval.
- Power of fire: is the cumulative fire radiative power (FRP) in MW, for all the MODIS fire pixels contained in the digitised polygon that represents a plume.
- Best median and top height: these parameters provide the best estimates for the median and the maximum height, in meters above sea level, in which outliers are removed following different smoothing techniques (Kahn et al.,

```

Drbit number : 56797
Path number : 229
Block number : 99
Date acquired : 2010-08-22
UTC time : 14:19:54
MINX version : V3.0
User name : Laura
Date digitized : 2014-12-23

Region name : 056797-B99-SPWR11
Region aerosol type : Smoke
Region geometry type : Polygon
Region wind dir type : Direction provided
Retrieved with band : Red
Match blue in an only? : No
Retrieved with matcher : Medium
Retrieved with cameras : A B C
Retrieval precision : Medium
Images in "true color" : No

First point longitude : -57.80167
First point latitude : -10.60747
Perimeter length (km) : 228
Area (sq km) : 1633
Area per point (sq km) : 1.210
Wind-corrected points : 962
Percent area covered : 71
Best median ht (m ASL) : 2801
Best top ht (m ASL) : 3648
StdDev metric, corrht : 242
|windDir-AlongDir| (deg) : 35
Power of fire in mw : 3336.7
Retrieval quality : GOOD

Level 1 radiance file : MISR_AM1_GRP_TERRAIN_GM_P229_0056797_AN_F03_0024.hdf
Terrain elevation file : MISR_AM1_GRP_P229_F01_24.hdf
Cam/Sun geometry file : MISR_AM1_GRP_GMP_P229_0056797_F03_0013.hdf
SWM classifiers file : MISR_AM1_TC_CLASSIFIERS_P229_0056797_F01_0012.hdf
Aerosol product file : MISR_AM1_AS_AEROSOL_P229_0056797_F12_0022.hdf

POLYGON: 22 points in this table define the digitized bounding polygon if present.
-----
Pt# Long- itude Lat- itude Blk Samp Line
-----
1 -57.802 -10.607 99 1551 182
2 -57.843 -10.619 99 1535 188
3 -57.938 -10.672 99 1499 212
4 -57.997 -10.725 99 1477 235
5 -58.070 -10.757 99 1449 250
6 -58.156 -10.818 99 1411 277
7 -58.255 -10.900 99 1380 313
8 -58.373 -10.988 99 1336 352
9 -58.489 -11.047 99 1292 379
10 -58.411 -11.180 99 1327 430
11 -58.331 -11.180 99 1362 470
12 -58.223 -11.269 99 1404 460
13 -58.173 -11.208 99 1422 434
14 -58.111 -11.193 99 1446 427
15 -58.131 -11.084 99 1435 383
16 -58.104 -10.994 99 1443 346
17 -58.066 -10.867 99 1454 294
18 -58.028 -10.827 99 1468 277
19 -57.940 -10.774 99 1501 253
20 -57.880 -10.704 99 1523 223
21 -57.825 -10.648 99 1543 199
22 -57.802 -10.607 99 1551 182

DIRECTION: 13 points in this table define the digitized direction line if present.
-----
Pt# Long- itude Lat- itude Blk Samp Line
-----
1 -57.802 -10.607 99 1551 182
2 -57.845 -10.644 99 1535 198
3 -57.898 -10.680 99 1515 214
4 -57.933 -10.710 99 1502 227
5 -57.985 -10.761 99 1483 249
6 -58.032 -10.790 99 1465 262
7 -58.079 -10.809 99 1447 271
8 -58.108 -10.836 99 1437 291
9 -58.139 -10.929 99 1427 321
10 -58.174 -10.996 99 1415 349
11 -58.215 -11.068 99 1401 379
12 -58.280 -11.152 99 1378 415
13 -58.350 -11.217 99 1352 443

RESULTS: 1290 points in this table are samples where Nownd heights or fire power were retrieved.
-----
optical Depth by Band Long- Lat- Single-Scattering Albedo Tau Fraction by Particle Type Ang Power Refl Albedo by Band BB TOA
Pt# itude itude Blk Samp Line Pt 1 Rel N Elev Nownd w/wnd Fltrd Xcross Along Total Blue Green Red NIR Small Medium Large Spher Exp Mwatt 0->1 Deg K Deg K Deg K Deg K
-----
1 -57.802 -10.607 99 1551 182 0.0 0.27 396 -99 -99 -99 -99.9 -99.9 -99.9 0.30 0.24 0.21 0.25 0.19
0.968 0.758 0.626 0.497 0.914 0.905 0.894 0.872 0.891 0.061 0.048 1.000 0.959 -99.9 -9.999 -999.9 -999.9 -999.9
2 -58.479 -11.055 99 1296 382 89.1 229 201 516 -99 -99 -99.9 -99.9 -99.9 0.26 0.20 0.18 0.28 0.19
0.965 0.725 0.574 0.431 0.977 0.991 0.997 0.998 0.535 0.269 0.197 0.600 1.206 -99.9 -9.999 -999.9 -999.9 -999.9
3 -58.468 -11.046 99 1300 378 87.6 229 202 155 -99 -99 -99.9 -99.9 -99.9 0.26 0.21 0.17 0.29 0.19
0.965 0.725 0.574 0.431 0.977 0.991 0.997 0.998 0.535 0.269 0.197 0.600 1.206 -99.9 -9.999 -999.9 -999.9 -999.9
4 -58.469 -11.056 99 1300 382 88.3 229 201 275 -99 -99 -99.9 -99.9 -99.9 0.26 0.20 0.18 0.28 0.19
0.965 0.725 0.574 0.431 0.977 0.991 0.997 0.998 0.535 0.269 0.197 0.600 1.206 -99.9 -9.999 -999.9 -999.9 -999.9
5 -58.470 -11.066 99 1300 386 88.9 229 199 581 -99 -99 -99.9 -99.9 -99.9 0.26 0.21 0.18 0.28 0.19
1.062 0.775 0.589 0.408 -9.999 -9.999 -9.999 -9.999 -9.999 -9.999 -9.999 1.447 -99.9 -9.999 -999.9 -999.9 -999.9
6 -58.471 -11.076 99 1300 390 89.6 229 198 278 -99 -99 -99.9 -99.9 -99.9 0.26 0.21 0.20 0.29 0.19
1.063 0.775 0.589 0.408 0.000 0.000 0.000 0.000 0.000 0.000 0.000 0.000 1.447 00.0 0.000 0.000 0.000 0.000

```

Figure 2.11: MINX ascii file for the plume O56797-B99-SPWR11, observed on the 22nd of August 2010.

2007, Nelson et al., 2013).

- Data quality: specifies the quality of the plume height retrievals based on the number of heights successfully retrieved in a plume, the percentage of the plume's area filled with successful heights, the standard deviation of the mean of the successful heights and the wind direction. This flag can adopt three values, "GOOD", "FAIR" or "POOR", and no value, when the number of retrieved points with wind-corrected heights is too small. Only smoke plumes classified as "FAIR" or "GOOD" should be included in studies of smoke plumes. However, this selection does not guarantee that the wind-corrected heights have the highest accuracy. If the plume was digitised with a wrong wind direction, then the retrieved heights will be less accurate. For the Amazon climatology, 51% of the plumes had low quality and were discarded from the original dataset.

The climatology of smoke plumes over the Amazon consists of 1.21 TB (75232 files and 474 folders), including the required files from MISR and MODIS. In total, 10858 plumes were digitised with different versions of MINX (v2–4), of which only 5393 plumes were included in [Gonzalez-Alonso et al. \(2019\)](#) (Chapter 3). The climatology contains eight years of smoke plumes observed during the burning seasons (July–November), from 2005 to 2012, across the Amazon domain, defined by the coordinates 80°W–40°W of longitude and 25°S–5°N latitude.

The inspection of the plumes via animation and the digitising process in MINX, although both are quite straightforward, are time-consuming and memory and CPU-intensive. Furthermore, the time required to read MISR files is proportional to the number of MISR blocks selected to load. Loading all nine camera images for only five blocks of MISR data over a fast network (there are usually 144 blocks of valid data per MISR orbit) requires 35 seconds on a 2.2 gigahertz windows 7 system with Intel Core i7 processor and 4 gigabytes of memory ([Nelson et al., 2008a](#)).

2.4.4 MINX Additional tools

MINX offers other utilities, which can be very useful depending on the project objectives and the degree of detail required in the study. Some of these utilities have been applied in the development of the smoke plume height database over the Amazon (Chapter 3). The most commonly used are:

I Camera registration correction

Before image matching is performed, images for each camera pair must be geometrically registered to improve stereo height retrieval accuracy. This is achieved by reducing errors in camera-to-camera geometric registration ([Davies et al., 2007](#)). Errors in one pixel (275 m) of co-registration can entail differences in the range of 160 m to 560 m of the height retrievals ([Zong et al., 2002](#)), depending on the cameras pair selected for matching, but mean geometric co-registration error for all cameras is less than 275 m ([Jovanovic et al., 2007](#)).

These errors must be avoided before digitising. For that, the user can superimpose a "fixed grid" over the MISR imagery and focus on a fixed feature on the terrain (Figure 2.12). If the feature is displaced with respect to the fixed grid when displaying the nine angle-views, correction should be applied. Registration errors due to failures in the Digital Elevation Model (DEM) from the MISR Ancillary Geographic Product (AGP) files cannot be corrected.

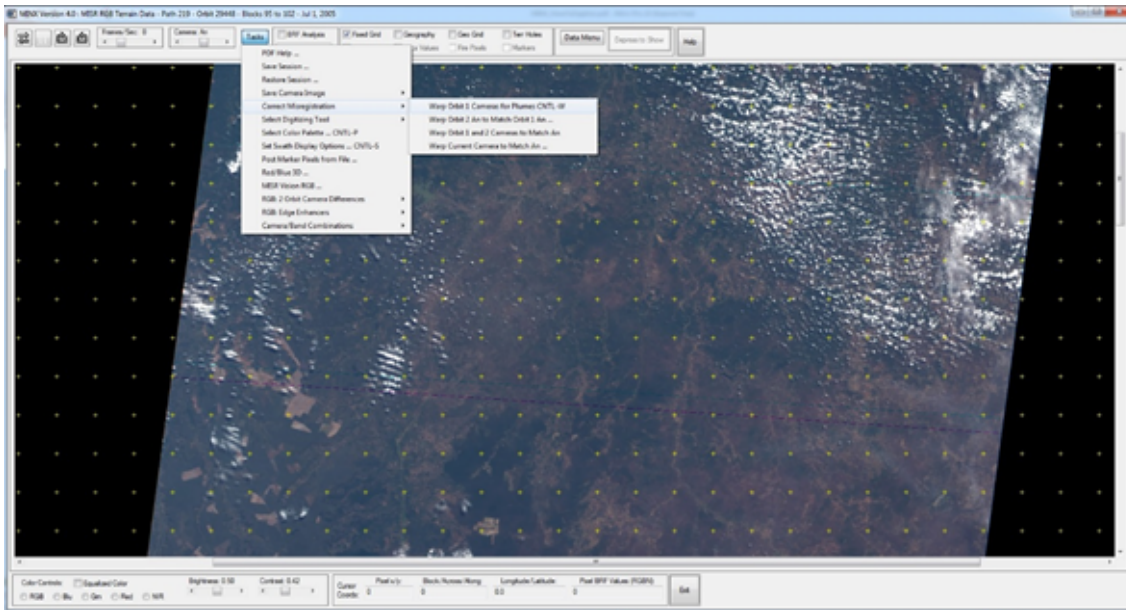


Figure 2.12: MINX camera registration correction. Fixed grid in yellow is displayed superimposed on MISR imagery

II digitising options

When the user starts to digitise a dialog box pops at the MINX interface where the user can select different options according to the study and desired results (Figure 2.14). First, the type of aerosol for which height retrievals will be processed, either smoke, dust, ash or water/ice. Then, the user needs to choose other options, i.e., a line or polygon to retrieve heights, provide wind direction or not (for clouds), select camera pairs for matching, etc. In the case of the Amazonian climatology, the setting was configured for smoke polygons with wind direction and default MINX options (Figure 2.14 depicts the setting selection for the Amazon smoke plumes). Depending on the user's selection,

the digitised feature will have coded letters allocated for those specifications and they will be part of the digitised feature name (Section 2.4.3).

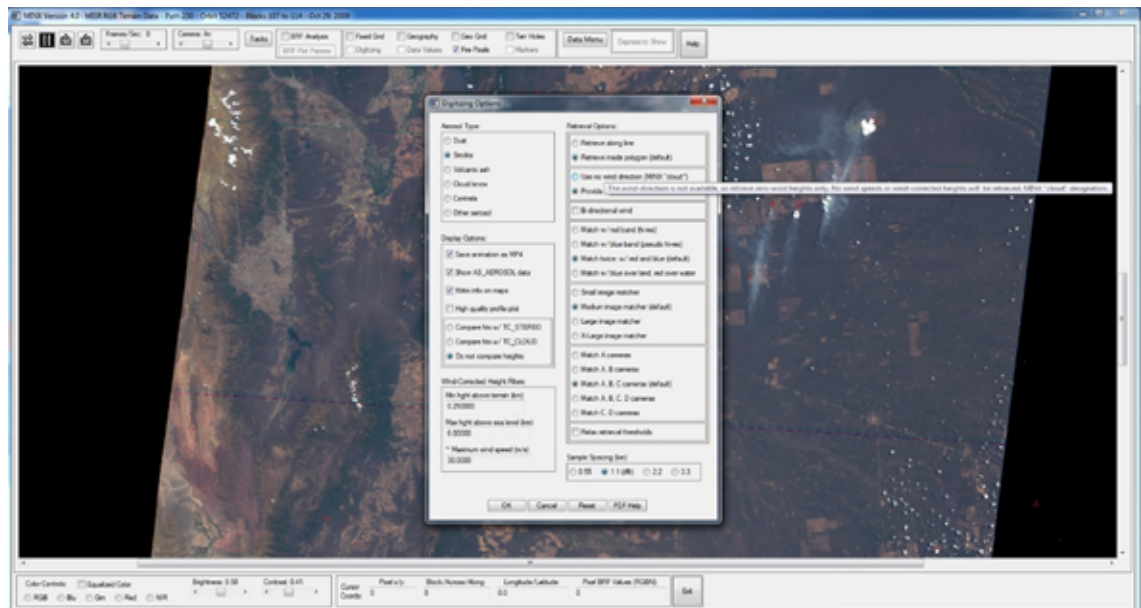


Figure 2.13: Dialog box to set the parameters to digitise a feature in MINX.

III Masks

There are four support vector machine (SVM) masks: cloud, smoke, land and dust masks, which are only available if the MISR standard Level 2 TC_CLASSIFIERS product is loaded at digitising (Table 2.1). Masks are only visible if the user presses the button in the MINX interface (Figure 2.14). The SVM masks provide within a confidence level the probability of each pixel to be or not to be that mask type and assist the user to identify features as a specific type (e.g. cloud or smoke).

IV Re-digitise, Delete

MINX offers the possibility to re-digitise or delete plumes already digitised whenever retrievals are not satisfactory or when after inspecting the height and wind profiles, better results are possible. This capability is very useful as sometimes it is complex to understand the dynamic of the smoke and trying different shapes, reducing the area digitised or changing the wind direction, can lead to more successful retrievals.

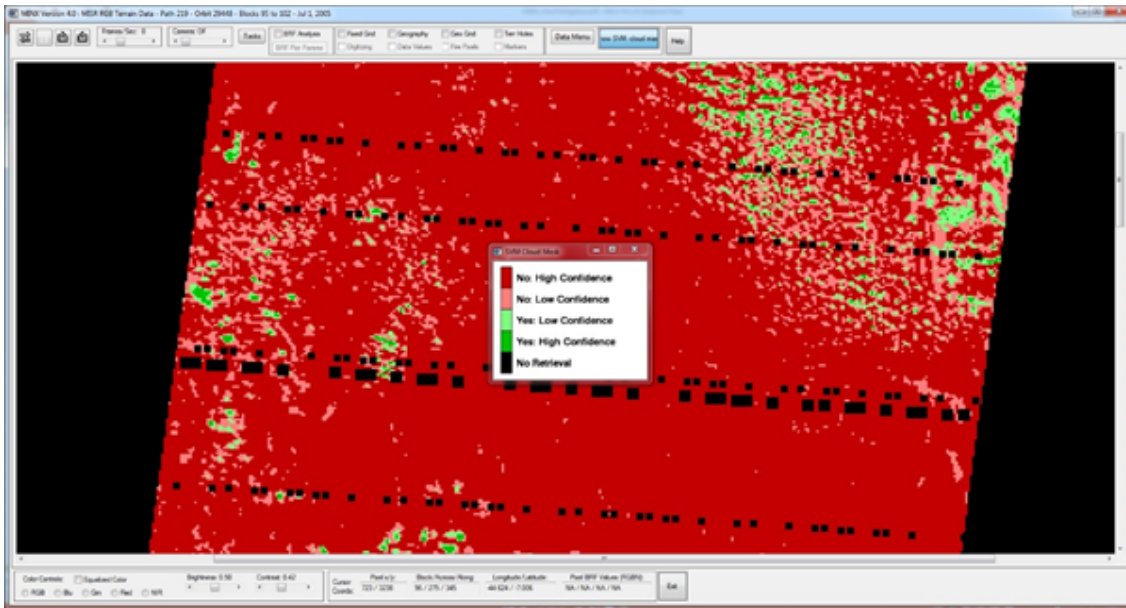


Figure 2.14: Cloud mask tool with black (no value), dark red (high confidence pixel is not mask type), light red (low confidence pixel is not mask type), light green (low confidence pixel is mask type) and dark green (high confidence pixel is mask type).

2.4.5 Interpreting wind direction

Determining the wind direction in the process of digitising is one of the most important tasks for the user. Although it can look trivial, wrong determination of the wind direction can be translated in errors of several kilometres in the wind-corrected heights for fast moving plumes. The direction of motion can usually be determined by investigating the scene, i.e., see the direction of shadows over the terrain or observe the direction of the contiguous plumes. However, there are some cases in which the direction is not so obvious and detailed inspection of the plumes and scenes is required. This is the case for low dense plumes over bright surfaces with not well-defined contour, plumes with a column of air ascending very fast in the vertical, where the convection at the fire is stronger than winds advection, or smoke plumes with two directions, where the plume seems to bifurcate.

2.4.6 Other applications of MINX

In addition to smoke plumes, MINX can be used to study volcanic and dust plumes, as well as hurricanes and boundary layer clouds. For example, [Scollo et al. \(2012\)](#) used MISR multi-year observations from explosive events at Mt. Etna and assessed the height of the volcanic aerosol plume with MINX stereo matching technique. They also used MISR aerosol product to distinguish between the sulphate and/or water vapour dominated volcanic plumes and those dominated by ash, indicative of eruption strength to constrain some parameters in volcanic ash dispersion models. Figure 2.15 represents the 2001 Flank Eruption, on the 22nd of July from [Scollo et al. \(2012\)](#). The explosive activity originated from two craters at 2550 m asl and the eruption extended 24 days, from the 17th of July to the 9th of August, 2001 and it is recorded as one of the most unusual and complex eruptions of Mt. Etna in the last 300 years⁸, causing 3.1 USD million damage, including losses in tourism and agriculture⁹. The ash plumes were captured by MISR on the 20, 22, and 29th of July, and using MINX, wind-corrected heights were determined. In particular, in Figure 2.15 the ash plume was dispersed toward the SE and reached ~ 6 km of altitude.

MINX has also been used to characterise the transport and aerosol optical depth of dust plumes across different regions ([Kalashnikova and Kahn, 2008](#), [Flower and Kahn, 2017](#), [Li and Sokolik, 2018](#)). An example of MINX dust height retrievals is depicted in Figure 2.16, along the Red Sea coast of Sudan ([Nelson et al., 2013](#)), on the 24th of July 2010, where strong onshore winds (20 m/s) lofted dust from the dry riverbeds in the Red Sea to an altitude of 1.4 km. Maximum wind-corrected heights and wind speed are observed within 5–10 km and 100 km, respectively, downwind from the source.

⁸<http://www.ct.ingv.it/en/11-notizie/news/406-10-years-ago-the-july-august-2001-eruption-of-etna.html>; last access 27/02/2019

⁹https://earth.esa.int/web/earth-watching/natural-disasters/volcanoes/content/-/asset_publisher/NBxzsX91cE11/content/etna-volcano-italy-2001; last access 27/02/2019

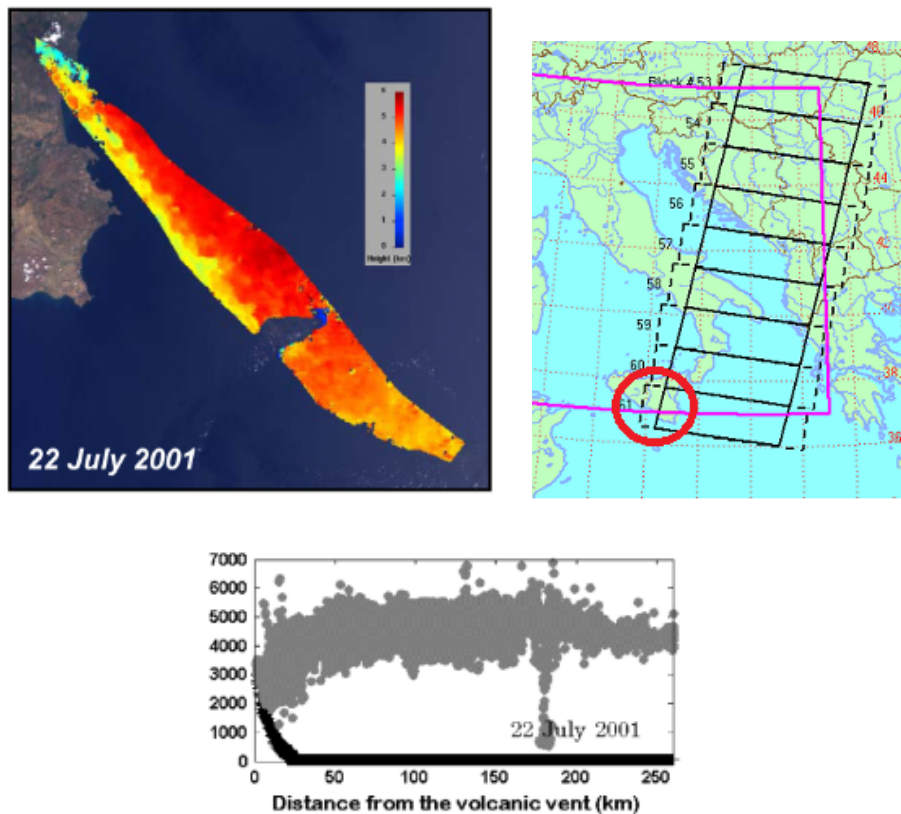


Figure 2.15: The 22nd July 2001, eruption of Mt. Etna in Italy on orbit 8476, block 61. Image from the MISR nadir view with the wind-corrected heights retrieved by MINX (top left panel), wind-corrected height profile (gray points) (bottom panel), (both adapted from [Scollo et al. \(2012\)](#)) and location of the block and MISR orbit (in red circle; top left panel)

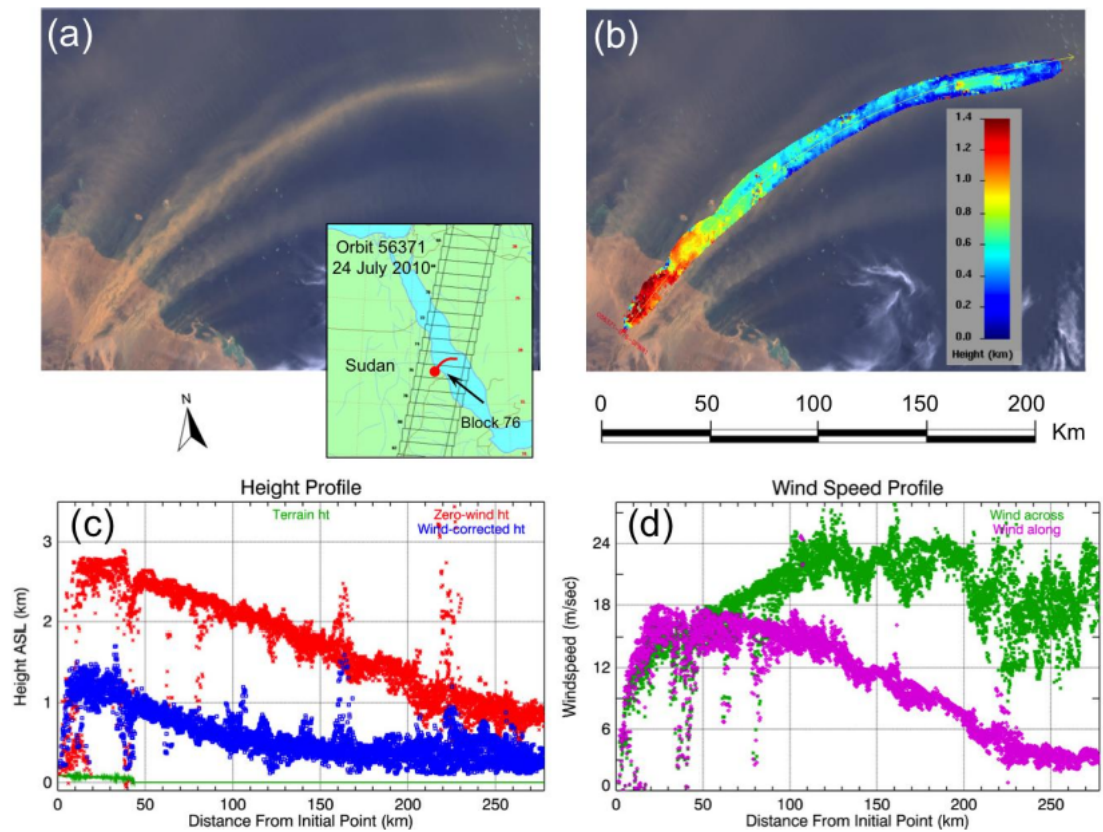


Figure 2.16: Dust over the Red Sea on MISR orbit 56371, block 75–76, from 24 July 2010: (a) MISR nadir image; (b) MINX wind-corrected heights over the MISR nadir image; (c) MINX height profile; (d) MINX wind speed profile. (Image adapted from Nelson et al. (2013)). In this case, the plume descends as it approaches the sea, as the Marine Atmospheric Boundary Layer (MABL) is shallower.

2.5 MINX Limitations and biases

Despite being a powerful software to study plume dynamics, there are some limitations in MINX that need to be taken into account to avoid errors and biases during the digitising process (Nelson et al., 2013). Errors and biases considered during the development of the smoke plume climatology over the Amazon are summarised below:

- Low quality of height retrievals due to low optical depth aerosols: MINX stereo height retrieval algorithm needs first to identify features common to the multiple cameras to perform a cross-correlation between pairs of camera images. If the feature is not texturally discernible from the background, then the algorithm performs the matching with the surface and only zero-wind heights close to the ground are computed. This is typical of low-dense plumes, where the terrain surface can be seen through the smoke, enhanced over high terrain reflectivity, like grassland or thin forests. In particular, for the Amazon climatology, this bias does not have a big impact because the retrieval quality for low dense smoke plumes was poor and therefore, those plumes were discarded.
- Low quality of height retrievals for homogeneous aerosols: MINX fails at retrieving both zero-wind and wind-corrected heights, whenever the smoke plumes or clouds are texturally homogeneous. This bias should be considered specifically for clouds, usually more homogeneous than smoke plumes.
- Contamination by water clouds: MINX users need to pay attention to the presence of clouds in a scene. If clouds are included in the digitised area, height retrievals will be biased high. To avoid this bias, MINX offers the mask tool from the MISR aerosol product, which allows the user to overlay a cloud mask layer to show the confidence to which aerosols in the image pixels are water clouds or not. However, if the user is not sure if a cloud is present in the scene, it is better to avoid digitising it. Over the Amazon, the presence of clouds is quite common, especially during the wet season and plumes were

digitised under cloud-free conditions whenever applicable, avoiding to include them in the digitised area.

- Digitising margins of smoke plumes: In the periphery of the plumes there is a potential bias towards lower quality or lower heights because smoke is more diffuse. For this reason, it is convenient to reduce the area of the plume, excluding the margins. Plumes over the Amazon are usually small and reducing the digitised plume area leads sometimes in a lack of successful retrievals. However, the conservative approach was followed and the area of the plume was reduced to the core as much as possible.
- Pyro-cumulus clouds associated with plumes: Pyro-cumulus constitute a type of clouds generated by intense fires associated with large buoyancy above the fire, which can reach substantially high altitudes. Digitising pyro-cumulus entails a bias towards higher smoke plume heights and they should be excluded at digitising. However, excluding them may translate in a decrease in the number of smoke plumes above the boundary layer. Over the Amazon, pyro-cumulus are not common, but they were excluded whenever present.
- Incorrect wind direction: If the user provides a wrong direction of the plume, motion errors in the wind-corrected height retrievals occur and the quality of the retrieval can be affected. This is a common problem, as sometimes the direction is not evident as mentioned in section [2.4.5](#). For this reason, inspecting the scene with caution is required and it is recommended to digitise the plume providing multiple solutions to the wind direction to finally select the best result for a plume. This strategy was followed when constructing the Amazon smoke plume data.
- Plume wind direction along-track: If the plume direction is parallel to the motion of MISR (along-track), MINX fails at separating the component of motion due to the wind from parallax error and it translates in low-quality retrieval. This is considered by MINX in the quality flag and plumes with low

quality were excluded from the Amazon climatology.

An additional bias arises due to the use of different versions of MINX. As mentioned before, the climatology of smoke plumes across the Amazon was created with different versions of MINX(v2-4). Plumes digitised with versions earlier than v4 had the red-band retrieval as default. The number of successful retrievals in red band is lower compared to blue band, particularly over bright surfaces and for low optical depth smoke plumes, as it is usually the case over the Amazon. Since MINXv4 all plumes are digitised in dual-band and MINXv4 determines the best option for each plume. This functionality allows the user to choose the best quality plume between both options, translating into a larger number of successfully retrieved plumes. For the climatology of Amazonian smoke plumes, blue-band plume retrievals were 60% more successful compared to 36% for the red-band retrievals.

Chapter 3

Biomass burning smoke heights over the Amazon observed from space[†]

3.1 Introduction

Fires burn across the Amazon region every year, releasing large amounts of trace gases and aerosols into the atmosphere (e.g., [Andreae and Merlet, 2001](#)). The majority of these fires are of anthropogenic origin: for deforestation, preparation of agriculture fields, conversion of cropland to pasture or road and city expansion ([Cochrane, 2003](#)). Between 1976 and 2010, deforestation fires destroyed more than 15% of the original Amazonian forest ([Aragao et al., 2014](#)). Most of these fires burn in the so-called arc of deforestation, along the eastern and southern borders of the Amazon forest, during the dry season (typically from July to November) ([Malhi et al., 2008](#)). However, significant variability exists, caused by changes in meteorology, drought

[†]This chapter is based on material previously published as Gonzalez-Alonso, L., Val Martin, M., and Kahn, R. A.: Biomass-burning smoke heights over the Amazon observed from space, *Atmos. Chem. Phys.*, 19, 1685-1702, <https://doi.org/10.5194/acp-19-1685-2019>, 2019. Authors copyright 2019.

and land-management policies (e.g., [Nepstad et al., 2006](#), [Van der Werf et al., 2010](#), [Alencar et al., 2011](#)). Amazon fires can contribute up to about 15% of the total global biomass burning emissions ([Van der Werf et al., 2010](#)). These emissions have important implications for air quality, atmospheric composition, climate and ecosystem health (e.g., [Ramanathan et al., 2001](#), [Johnston et al., 2012](#), [Pacifico et al., 2015](#)). For example, air pollution from deforestation fires is estimated to cause on average about 3,000 premature deaths per year across South America ([Reddington et al., 2015](#)) and may decrease the net primary productivity in the Amazon forest as a result of increases in surface ozone ([Pacifico et al., 2015](#)).

Fires are also an important source of buoyancy locally, which in combination with other atmospheric properties determines the vertical distribution of fire emissions in the atmosphere near the fire source (i.e., injection height). The altitude to which smoke is injected is critical, as it determines the lifetime of the pollutant, its downwind transport dispersion pathway, and the magnitude of its environmental impact (e.g., [Jian and Fu, 2014](#), [Archer-Nicholls et al., 2015](#), [Paugam et al., 2016](#), [Zhu et al., 2018](#)). Space-borne observations have been used to study smoke injection heights across the world. Using Multi-angle Imaging Spectro Radiometer (MISR) stereo-height retrievals, smoke plume heights have been assessed across North America ([Kahn et al., 2008](#), [Val Martin et al., 2010](#)), Indonesia ([Tosca et al., 2011](#)), Australia ([Mims et al., 2010](#)), southeast Asia ([Jian and Fu, 2014](#)), and Europe ([Sofiev et al., 2013](#)). For example, [Val Martin et al. \(2010\)](#), using a 5-year climatology of smoke fire plumes and smoke clouds observed by MISR across North America, showed that wildfire smoke can reach altitudes from a few hundred meters above the ground to about 5 km, and that 5–30% of the smoke plumes are injected into the free troposphere (FT), depending on the biome and year. Related work also demonstrated the important effect that fire radiative power, i.e., a proxy of fire intensity, and atmospheric conditions have on the initial rise of fire emissions ([Freitas et al., 2007](#), [Kahn et al., 2007](#), [Val Martin et al., 2012](#)). [Tosca et al. \(2011\)](#) reported that less than 4% of smoke plumes reach the free troposphere, based on a MISR 8-year climatology

from tropical forest and peatland fires over Borneo and Sumatra, and found that the greatest plume heights were recorded during an El Niño year over Borneo.

Smoke plume heights have also been determined using space-borne lidar observations from CALIOP ([Labonne et al., 2007](#), [Huang et al., 2015](#)), aerosol index from the TOMS and OMI instruments ([Guan et al., 2010](#)), and CO observations from TES and MLS ([Gonzi and Palmer, 2010](#)). [Huang et al. \(2015\)](#) used a multi-year record of CALIOP vertical aerosol distributions to study smoke and dust layer heights over six high-aerosol-loading regions across the globe. Specifically over the Amazon, they found that on a broad scale, smoke layers are typically located above boundary layer clouds, at altitudes of 1.6–2.5 km. Consistent with the smoke altitudes detected by CALIOP, an analysis of injection heights using CO observations from TES and MLS estimated that about 17% of fire plumes over South America reached the free troposphere in 2006 ([Gonzi and Palmer, 2010](#)).

Numerous studies have sought to understand the impact of biomass burning in the Amazon on local to hemispheric scales. In particular, during the past decade, several aircraft campaigns have been designed to study the effect of biomass burning on greenhouse gases, aerosols loading, clouds, regional weather and/or climate over the Amazon [e.g., BARCA ([Andreae et al., 2012](#)), SAMBBA ([Allan et al., 2014](#)) and GoAmazon ([Martin et al., 2016](#))]. For example, modelling studies during SAMBBA showed the importance of the vertical representation of aerosols from biomass burning over the region ([Archer-Nicholls et al., 2015](#)), as biomass burning can modify local weather ([Kolusu et al., 2015](#)) and regional climate ([Thornhill et al., 2017](#)). Based on lidar observations taken in six research flights during SAMBBA (September 16–29, 2014), [Marenco et al. \(2016\)](#) reported the presence of two distinct smoke aerosol layers, a fresh smoke layer extending from the surface to an altitude of 1–1.5 km, and an elevated and persistent layer of aged smoke at 4–6 km. During the 2008 dry biomass season, continuous raman lidar measurements of optical properties taken in Manaus (2.5°S, 60°W) also detected biomass burning layers at 3–5 km heights, although most of smoke was confined below 2 km ([Baars](#)

[et al., 2012](#)). Whilst the results from these aircraft and in-situ lidar observations are significant, there are no analyses yet that seek to quantify the long-term average vertical distribution of smoke from fires across the Amazon, and to identify the key factors that control plume rise over this region.

We present here an 8-year climatology of smoke plume heights over the Amazon, derived from observations by the MISR and CALIOP instruments on board the NASA Terra and CALIPSO satellites, respectively. These data are analysed in combination with measurements of Fire Radiative Power (FRP) from NASA MODerate resolution Imaging Spectroradiometer (MODIS) instruments, assimilated meteorological data from MERRA-2 and drought condition indicators from the MODIS Drought Severity Index (DSI). The objectives of this work are to characterise the magnitude and variability of smoke heights from biomass burning across the Amazon, and to assess the influence of biome type, fire intensity, local atmospheric conditions, and regional drought on smoke vertical distribution as well as aerosol loading.

3.2 Data and Methods

We use a combination of remote sensing data from multiple sources to build a comprehensive climatology of smoke plume heights and characterise the vertical distribution of smoke across the Amazon. We provide below a summary of main datasets and tools used in the analysis and compile their main features in Table 3.1.

3.2.1 MINX overview

The MISR Interactive Explorer (MINX) software is an application written in Interactive Data Language (IDL) that is used to analyse the physical properties of smoke plumes and to study plume dynamics ([Nelson et al., 2013](#)). MINX can use MODIS thermal anomalies to locate active fires, and MINX then computes the smoke plume

Table 3.1: Summary of main features for instruments and products used in the study.

Parameter	Instrument/ Product	Satellite ^a / Model	Level/ Version	Spatial Resolution		Temporal Res.	Main reference
				Horizontal	Vertical		
Smoke Height	MISR	Terra	Level 1 & 2	275–500 m	1.1 km	variable	Diner et al. (1998)
Aerosol Extinction	CALIOP	CALIPSO	Level 2/v4	30–60 m	333 m	variable	Winker et al. (2013)
Active Fires	MOD14/MYD14	Terra & Aqua	v6	1 km x 1 km		daily	Giglio et al. (2006)
Land Cover	MOD12Q1	Terra & Aqua	v5.1	500 m x 500 m		annual	Friedl et al. (2010)
PBL	MERRA-2	GEOS-5 DAS	v5.12.4	0.625° x 0.5°	42	hourly	Bosilovich et al. (2015)
Atm. Stab.	MERRA-2	GEOS-5 DAS	v5.12.4	0.625° x 0.5°	42	6-hourly	Bosilovich et al. (2015)
Drought (DSI)	MOD16/MOD13	Terra & Aqua		0.05° x 0.05°		8-day	Mu et al. (2013)

^a Satellite swaths are 380 km (MISR), 2330 km (MODIS) and 70 m (CALIOP), with overpass times over the Amazon as 10–11 LT (AM/PM) (Terra), 1–2 LT (AM/PM) (Aqua) and 1:30 LT (AM/PM) (CALIPSO)

or cloud heights from MISR stereo imagery. MINX also collects particle property results from the MISR Standard aerosol retrieval algorithm (Martonchik et al., 2009). MODIS and MISR are both aboard the NASA Terra satellite, which crosses the equator in the descending node at around 10:30 a.m. local time. These instruments allow temporally and spatially coincident detection of active fires and their associated smoke plumes (Kahn et al., 2008).

MODIS has a cross-track swath of 2330 km that provides global coverage every one to two days. The instrument has 36 spectral channels with wavelengths between 0.4 μm and 14.2 μm , and detects thermal anomalies at 1 km spatial resolution (at nadir), under cloud-free conditions. MODIS reports fire radiate power based on a detection algorithm that uses brightness temperature differences in the 4 μm and the 11 μm channels (Giglio et al., 2003); this FRP parameter is used as an indicator of fire location and qualitative intensity. We use MODIS Collection 6 (Table 3.1). We note that MINX provides FRP values in MW, although they are actually in MW per 1-km pixel, which corresponds to W/m^2 , except toward the edges of the swath.

MISR has nine push-broom cameras placed at viewing angles spanning -70.5 to 70.5 relative to nadir in the satellite along-track direction (Diner et al., 1998). The cameras each provide imagery in four spectral bands (446, 558, 672, and 867 nm), which makes it possible to distinguish aerosol types qualitatively (Kahn and Gaitley, 2015) and surface structure from the change in reflectance with view angle. This passive stereoscopic imagery method produces cloud and aerosol plume heights, along with cloud-tracked winds aloft. MISR has a swath of 380 km common to all cameras, so global coverage is obtained every nine days at the Equator and every two days at the poles (Diner et al., 1998). The MISR Standard stereo-height product provides vertical resolution of 275–500 meters and horizontal resolution of 1.1 km (Moroney et al., 2002a, Muller et al., 2002).

MINX has a graphical user interface that displays the nine MISR multi-angle images. They can be visualised one by one or as an animated loop, providing a 3-D view of the plume that can help in assessing its structure and dynamical

behaviour. In addition, MODIS thermal anomalies can be superimposed, which helps identify the locations of smoke sources from active fires. A user needs to digitise the boundaries of the plume, starting at the source point, and to indicate the direction of smoke transport. The MINX stereoscopic algorithm also calculates wind speed from the displacement of plume contrast elements, which is used subsequently to compute wind-corrected heights, accounting for displacement due to the proper motion of the plume elements between camera views. As with the MISR Standard stereo-height product, MINX automatically retrieves smoke plume heights and wind speed at a horizontal resolution of 1.1 km and vertical resolution of 250–500 m, but with greater accuracy for the plume itself, due to the user inputs (Nelson et al., 2013). MINX plume heights are reported above the geoid, which correspond to the level of maximum spatial contrast in the multi-angle imagery, typically near the plume top, but actually offering a distribution of heights in most cases, because aerosol plumes are rarely uniform (Flower and Kahn, 2017). Additionally, MINX provides local terrain height from a digital elevation map (DEM) product. Here we report heights above the terrain, by taking account of the DEM values. Further information from the MISR Standard Aerosol product about aerosol amount and type is collected and reported, along with FRP from MODIS (Nelson et al., 2013). MINX has been successfully used to investigate fire smoke plume heights over many regions across the world (eg, Kahn et al., 2008, Val Martin et al., 2010, Tosca et al., 2011, Jian and Fu, 2014).

There are several limitations to the MISR-MINX approach that must be considered when studying smoke plume heights. For example, MISR obtains global coverage only about once per week, and the Terra overpass time in late morning does not coincide with the typical, late-afternoon peak of fire intensity. MODIS does not observe FRP under cloud and dense smoke, and the MINX operator must decide whether to include any pyro-cumulus clouds in the plume-height retrieval. These are the key limitations; they and others are discussed further in the literature (eg, Kahn et al., 2007, Val Martin et al., 2010, Nelson et al., 2013). In addition, three

MINX versions were used to generate the data in this study, which might introduce an additional bias. MINXv2 and v3 included only MISR red-band plume height retrievals, whereas MINXv4 considers both red and blue-band images. Over land, digitalisation with the blue band usually provides higher quality retrievals, especially for optically thin plumes over bright surfaces. In contrast, red-band provides higher vertical resolution over dark surfaces and sometimes performs better for optically dense smoke layers (Nelson et al., 2013). We take these limitations into account throughout our analysis.

3.2.2 MINX smoke plume database

We limited our study to the burning season (July–November) for the period of 2005–2012. Using MINX, we developed a climatology of plume heights across the Amazon, consisting of 10,858 smoke plumes in the region (25°S – 5°N latitude and 80°W – 40°W longitude). Over this domain, the NASA Terra satellite overpass is every 4–8 days at 10:00–11:00 local time. Table 3.2 summarises the number of smoke plumes in each year and the digitising source. The climatology includes a combination of smoke plumes extracted from different projects and created with different versions of MINX (v2–4): plumes for August–September in years 2006 and 2007 are from the MISR Plume Height Project (Nelson et al., 2013); plumes in year 2008 are from the global digitalisation effort made for the AeroCom project (MPHP2 and Val Martin et al. (2018a)); and the five remaining years and additional months are digitised as a part of the current project.

MINX computes several plume heights that describe the altitude that smoke reaches in the atmosphere. In this work, we use the best estimate maximum and median smoke plume heights, which represent the distribution of stereo heights, obtained at the level of maximum spatial contrast over the plume area (Nelson et al., 2013). In addition, as in previous studies, we remove smoke plumes with poor-quality retrieval flags. This screening leaves a total of 5393 plumes, about 56% of

Table 3.2: Summary of MISR smoke plumes over the Amazon domain (2005–2012)

Year	Total	Number of Plumes ^a		MINX version	Reference
		Blue Band	Red Band		
2005	927	122	805	v3/v4	This study
2006	513	501	12	v2/v4	MPHP ^b /This study
2007	858	670	188	v2/v4	MPHP ^b /This study
2008	889	889	0	v3.1	MPHP2 ^c
2009	150	55	95	v3/v4	This study
2010	1373	0	1373	v3	This study
2011	320	320	0	v4	This study
2012	363	30	333	v3/v4	This study
2005–2012	5393	2587	2806		

^aTotal number of plumes, and number of plumes digitised with blue/red band retrievals

^bMISR Plume Height Project; data from <https://mISR.jpl.nasa.gov/getData/accessData/MisrMinxPlumes/>

^cMISR Plume Height Project2; data from <https://mISR.jpl.nasa.gov/getData/accessData/MisrMinxPlumes2/>

the original database, with 77% and 23% plumes digitised in the red and blue bands, respectively. Our final dataset includes plumes digitised in years with intense fire activity associated with severe drought conditions (e.g., 2005, 2007 and 2010) (Chen et al., 2011), in years with low fire intensity and considerable precipitation (2009 and 2011) (Marengo et al., 2013) and in one year when land-management policy measures limited deforestation (2006) (Nepstad et al., 2006). Thus, our climatology is intended to capture smoke plumes variability under diverse conditions.

As mentioned in section 3.2.1, the MISR colour band image used by the MINX algorithm to compute smoke plume heights influences the quality of the plume height and wind speed retrievals. A large majority of the fires detected across our domain have optically thin smoke plumes. Thus, blue band plume retrievals are more successful, with about 60% of the smoke plumes receiving good or fair quality flags, compared to 36% for the red band retrievals. In our dataset overall, most of the plumes were digitised from red band images, as it was the default option for MINX v2–3. However, whenever both band retrievals are available for a plume, blue band is preferred in this study. The choice of the band colour for the retrievals does not affect significantly the results presented here, as the difference in heights for smoke

plumes digitised with both bands is negligible (~ 60 m), lower than the ± 250 m MINX uncertainty.

3.2.3 Land cover unit data

We use the MODIS Level 3 land cover product MCD12Q1 (Friedl et al., 2010) to determine the type of land cover associated with each of our fire smoke plumes. This product contains 17 International Geosphere-Biosphere Programme (IGBP) land cover classes, at a horizontal resolution of 500 m and annual temporal resolution, from 2001 to present day. It is available from the Land Processes Distributed Active Archive Center¹. We merge land cover classes having similar characteristics into four land types representing the main biomes across the Amazon: tropical forest, savanna, grassland and crops.

3.2.4 Atmospheric conditions

To assess the role of atmospheric conditions on the final elevation of smoke plumes across the Amazon, we analyse data from the second Modern Era Retrospective-analysis for Research and Applications (MERRA-2) reanalysis model simulation (Bosilovich et al., 2015). We focus on the height of the planetary boundary layer (PBL) and the atmospheric stability at the location of our fires. As in previous studies (eg, Kahn et al., 2007, Val Martin et al., 2010), we define the atmospheric stability as the vertical gradient of potential temperature. We use data from MERRA-2 at a horizontal resolution of 0.625° longitude by 0.5° latitude, with 42 levels vertical pressure-levels between the surface and 0.01 hPa. MERRA-2 provides hourly PBL height above ground level and potential temperature profiles every 6 hours (0:00, 06:00, 12:00 and 18:00 UTM), so we linearly interpolate these data to the time and location of each fire plume origin.

¹https://lpdaac.usgs.gov/get_data

3.2.5 Drought conditions

To determine the presence and magnitude of droughts over the Amazon during our study period, we use the MODIS Drought Severity Index (DSI). The DSI is a global drought index derived by combining the MODIS16 Evapotranspiration (e.g., [Mu et al., 2007](#)) and the MODIS13 vegetation index (NDVI) data products ([Huete et al., 2002](#)). DSI provides drought conditions at global scale for all vegetated areas at 8-day and annual temporal resolutions and 0.5 or 0.05° horizontal spatial resolution for 2000–2011 ([Mu et al., 2013](#)). In this work, we use the 8-day temporal resolution DSI and interpolate the data to the time and location of our fire smoke plumes. Following [Mu et al. \(2013\)](#), we further define drought conditions as: "Extreme-Severe" ($DSI \leq -1.2$), "Mild-Moderate" ($-1.2 \leq DSI < -0.29$), "Normal" ($-0.29 > DSI > 0.29$) and "Wetter than Normal" ($DSI \geq 0.29$).

3.2.6 CALIOP observations

We also use extinction profiles derived from the CALIOP instrument to provide an independent assessment of the vertical smoke distribution across the Amazon. CALIOP is a space-borne two-wavelength polarisation lidar (532 and 1064 nm) that flies aboard the CALIPSO satellite ([Winker et al., 2013](#)). CALIPSO was launched in 2006 into a sun-synchronous polar orbit of 705 km altitude as a part of the "A-Train" constellation, with an orbit repeat cycle of 16 days. CALIOP collects backscatter and depolarization data that constrain the vertical structure and some properties of aerosols and clouds around the globe ([Vaughan et al., 2004](#), [Liu et al., 2009](#)). In addition, CALIOP provides a characterisation of the aerosol type (i.e. dust, polluted dust, marine, clean continental, pollution and biomass burning) based on externally determined surface type along with measured depolarisation ratios, integrated backscatter altitude and colour ratio ([Omar et al., 2009](#)). This aerosol-type classification can be used to indicate the likely sources that contribute to aerosol mass loading at specific locations and times where the instrument has coverage.

We use CALIOP Level 2 version 4 day and night data (CAL_LID_L2_05kmAPro-Standard-V4-10) over the Amazon for the July to November burning season, from 2006–2012. In this work, we filter the data following [Ford and Heald \(2012\)](#). This filtering approach uses cloud-aerosol distinction scores, extinction uncertainty values, atmospheric volume descriptors, extinction quality control flags and total column optical depths, and assumes that extinction observations classified as 'clear air' have zero aerosol extinction (rather than the fill value). CALIOP daytime retrievals can be biased low due to the noise from scattered solar radiation ([Winker et al., 2009](#), [Rogers et al., 2011](#)). However, we analyse both day (i.e., early afternoon, $\sim 13:30$ LT equator crossing time) and night profiles to identify any differences in smoke heights, as well as to allow a better comparison with the MISR smoke plumes, which are retrieved during the late morning.

The CALIOP "swath" is ~ 100 m wide, so sampling is effectively a curtain. To obtain a climatology of CALIOP smoke plumes as in MISR, we developed an approach to identify individual smoke plumes in the CALIOP data. We first grid all CALIOP aerosol extinction profiles classified as smoke (day and night) at a horizontal resolution of $0.5^\circ \times 0.5^\circ$ over the Amazon region, and a vertical resolution of 250 m, from the surface to 12 km. We chose this horizontal resolution to optimise computing processing time. Within each grid cell, we then determine the vertical distribution of smoke extinction. We define the maximum smoke plume height in each grid cell as the maximum altitude reached by the extinction classified as smoke. Similar to the MINX definition of median plume height, we consider the median of the CALIOP vertical extinction distribution as the height where most of the smoke is probably concentrated. Smoke does tend to concentrate either in the PBL or in thin layers in the FT ([Kahn et al., 2007](#), [Val Martin et al., 2010](#)).

To ensure we do not introduce a bias in the CALIOP plume heights due to the $0.5^\circ \times 0.5^\circ$ horizontal resolution, we also retrieved the smoke plumes for the 2017 burning season at a horizontal resolution of $0.1^\circ \times 0.1^\circ$, and find no significant differences. For this subset, our $0.5^\circ \times 0.5^\circ$ method returns 131 plumes, with an

average altitude of 3.65 km for the maximum plume heights, whereas the $0.1^\circ \times 0.1^\circ$ method returns 149 plumes, with an average altitude of 3.74 km.

To identify CALIOP smoke plumes associated with active fires, we select only those CALIOP-derived grid cells that contain at least two MODIS Collection 6 fire pixels (Giglio et al., 2003), at 80% confidence level or higher, at the time of CALIOP overpass. We also use the mean terrain elevation across each grid cell to reference the maximum and median heights to ground level, as CALIOP provides observations above sea level. We estimate the mean terrain elevation using terrain elevation from the CALIOP digital elevation map. Figure 3.1 shows an example of our approach for the CALIOP observation of September 25th, 2010 at 06:25 UTC. For this example, we identify a CALIOP smoke plume with 1.7 km median and 4.5 km maximum height above ground level. A total of 2460 plumes are characterised with our approach over the Amazon for the months of July to November, from 2006–2012; about 65% of these plumes are linked to active fires with some confidence (i.e., having a clear connection to a MODIS fire pixel), and we only consider those in our analysis, a total of 1600 plumes.

Previous studies used other CALIOP products to determine the vertical distribution of smoke plumes. The Level 2 Aerosol Layer product is commonly used to analyse smoke plume heights from CALIOP, as it reports the top and base heights of aerosol layers. Tosca et al. (2011) used their smoke layer top altitudes and extinction coefficient profiles over Borneo for September–October 2006. Using the CALIOP Level 1 attenuated backscatter profiles at 532 nm, Amiridis et al. (2010) estimated smoke injection heights from agricultural fires over Europe. They selected only those profiles of constant attenuated backscatter coefficient with height, without strong convection, and that were collocated with MODIS active fire pixels from the Aqua satellite. Recently, Huang et al. (2015) used six years of the CALIOP Level 2 vertical feature mask (VFM) data and aerosol layer products over six regions to investigate the Most Probable Height (MPH) of dust and smoke layers. They used two approaches to obtain MPH: one based on the probability distribu-

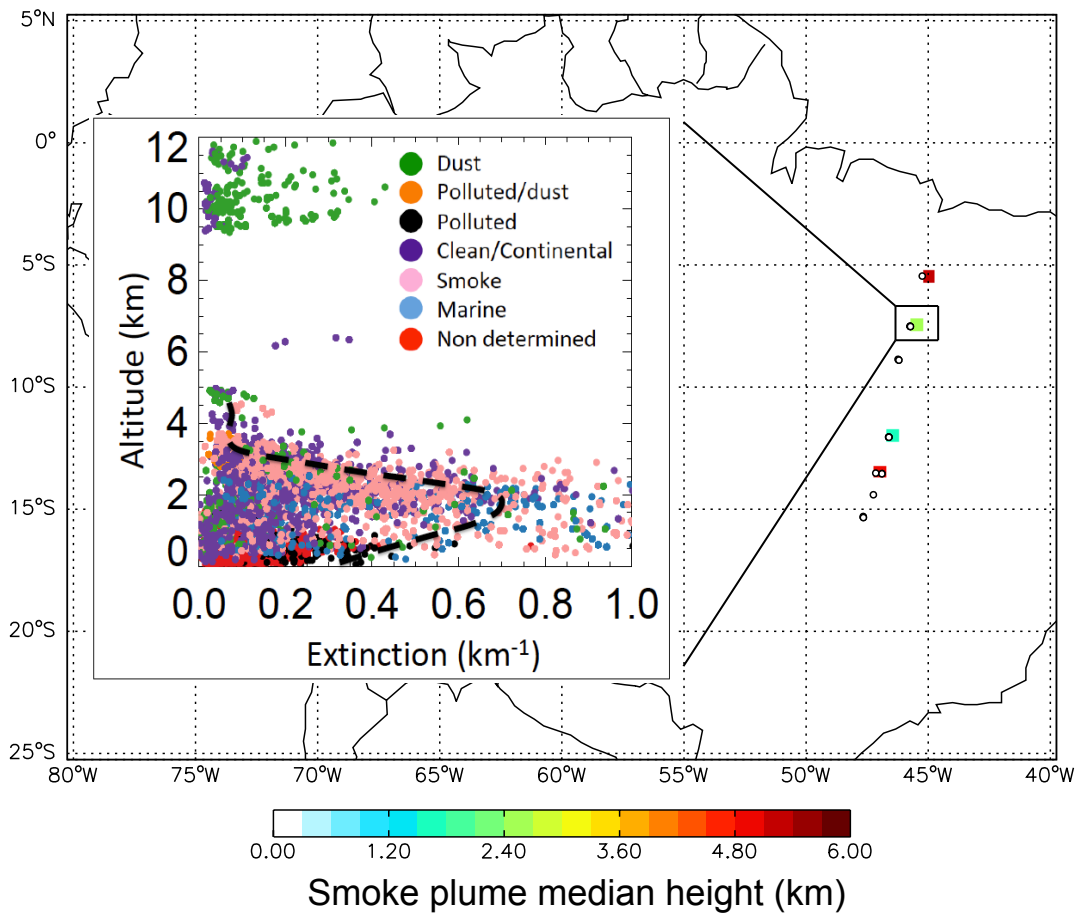


Figure 3.1: Example of the approach followed for the CALIOP smoke plume characterisation. The map shows estimated smoke plume median heights (gridded at 0.5×0.5 horizontal resolution) for September 25th, 2010 at 06:25 UTC. MODIS active fire pixels associated with the CALIOP smoke plumes are represented with open circles. The insert displays the vertical distribution of aerosol extinction for a specific smoke plume in the map, with extinction values coloured by classified aerosol types. Dashed black line represents the averaged extinction profile for the aerosols classified as smoke (pink dots). In this profile, the CALIOP smoke plume has a median height of ~ 2 km (green colour in the smoke plume median height scale) and a maximum height of 4.5 km above the terrain.

tion of the vertical profiles of Occurrence Frequency (OF) (i.e., ratio of number of samples classified as dust or smoke by the VFM to the total samples per grid) and the other as the probability distribution of the aerosol optical depth (AOD) vertical profiles. So MPH_OF and MPH_AOD correspond to the altitude with the largest OF and mid-visible AOD for a certain type of aerosol. Our definition of CALIOP median plume height is most similar to their MPH_AOD. However, [Huang et al.](#)

(2015) analysed vertical profiles over large-scale regions (e.g., the entire Amazon or Sahara), whereas in the current work, we analysed and then aggregated the heights for individual smoke plumes.

Our initial objective was to compare the CALIOP with the MISR plumes to assess the diurnal smoke evolution, as CALIOP has a later sampling time than MISR over the Amazon (14:00–15:00 LT versus 10:00–11:00 LT). However, despite our effort to develop a comprehensive CALIOP climatology, none of the CALIOP plumes coincide with the MISR plumes. As previous studies discuss (eg, Kahn et al., 2008, Tosca et al., 2011), CALIOP and MISR, in addition to having different sampling times, also have different swath widths (380 km versus 70 m). These differences make it difficult to observe the same fire on the same day, but they make CALIOP and MISR observations complementary: MISR provides late-morning near-source constraints of aerosol plume vertical distribution, whereas CALIOP in general offers more regional constraints, later in the day (Kahn et al., 2008). Some differences between the products are thus expected.

3.3 Results and discussion

3.3.1 Smoke plume height observations

Figure 3.2 maps the biomes of the Amazon region for which the MISR plume climatology was developed. Figure 3.3 presents the time series of the smoke plume heights for the biomass burning seasons (July–November) during the 2005–2012 study years. We also include a statistical summary of the number of plumes within the time series by year, month, biome and drought conditions in Figure A1. The largest number of plumes is recorded in 2010, with about 25% of the total plumes in the database, whereas the smallest is in 2009 (3%). These two years are the driest and the wettest in the climatology, respectively. Most of the plumes were observed in August and September (85%), at the peak of the burning season in most vegetated locations, in

the dominant biomes of savanna (48%) and tropical forest (46%), and during dry conditions (76%). We find important interannual variability in the type of fires, with fires over tropical forest dominant in 2005 (65%) and 2010 (47%), two of the three drought years in our database as shown in Section 3.3.4 below, and the majority of fires in savanna (54–65%) for the rest of the years. We note that a large fraction of the plumes were observed in 2008 (17%) even though it was not a drought year. The majority of plumes in the 2008 record are digitised with blue band retrievals (Table 3.2), which produce higher quality results in many situations, especially for optically thin plumes over land surfaces.

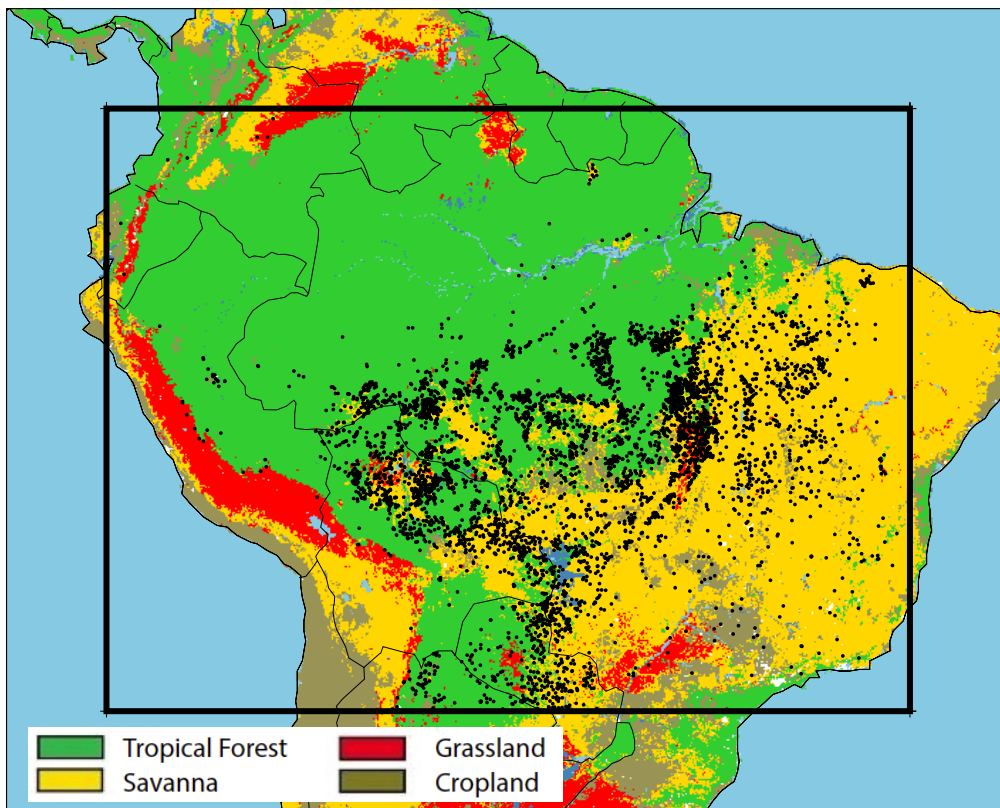


Figure 3.2: Locations of the MISR plumes analysed (black dots) over the four main biomes considered in the study. The black square represents the Amazon domain.

Throughout the study period, we find significant variability in smoke plume height, with altitudes ranging from a few meters (essentially near-surface) to 5 km, depending on the biome (Figure 3.3). Smoke plumes over cropland fires are scarce compared to the other fire types, as these fires are small and tend to be under-

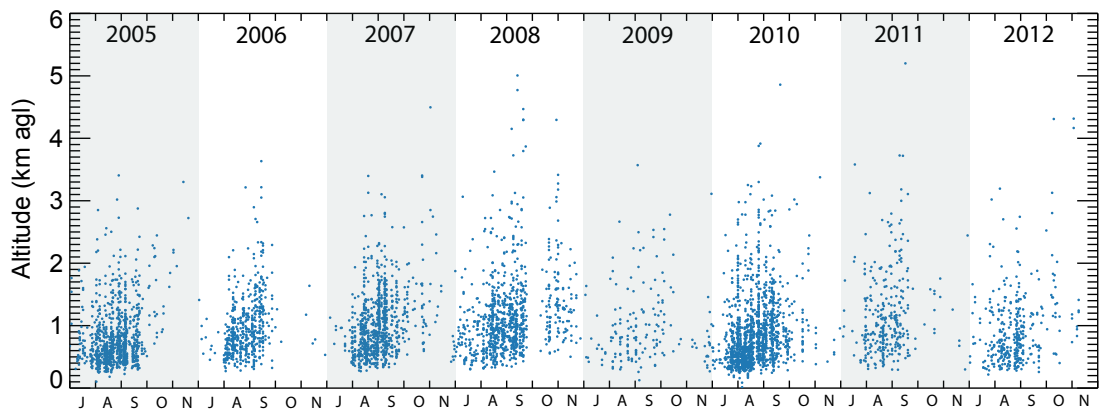


Figure 3.3: Time series of the 2005–2012 MISR Amazon smoke-plume-height climatology, covering the July–November burning season for each year. Each blue dot represents the maximum smoke height above ground level (agl) for one plume.

detected by MISR (Nelson et al., 2013). We summarise in Table 3.3 the statistical parameters of the smoke plumes for all observations except the cropland cases. Over the Amazon, the vertical distribution of smoke varies by biome. Statistically, the highest smoke altitudes averaged by biome are detected over grasslands, with median and maximum heights of 794 m and 1120 m, respectively, whereas the lowest heights are detected over tropical forest (601 and 845 m, respectively). In all the biomes, more than 85% of the smoke is located at altitudes below 2 km (Figure A2).

Table 3.3: Statistical summary for main smoke plume parameters and atmospheric conditions^a.

	Tropical Forest	Savanna	Grassland
Median Height (m)	601 ± 339	743 ± 422	794 ± 471
Max Height (m)	845 ± 499	1040 ± 585	1120 ± 653
MODIS FRP (MW)	209 ± 537	360 ± 658	421 ± 614
AOD (unitless)	0.51 ± 0.34	0.33 ± 0.28	0.35 ± 0.29
Atm Stab (K/km)	4.21 ± 2.97	3.16 ± 3.16	2.52 ± 2.50
BL Height (m)	1270 ± 514	1490 ± 507	1620 ± 530
Plumes in FT (%) ^b	3–15	4–17	5–19
Number	1744	2084	166

^aReported the average±SD and number of observations

^bReported range from more and less conservative definition of plume in the FT (see text for explanation).

Similar altitudes and distributions have been found across comparable fires in

other parts of the world. For example, altitudes between of 700–750 m were detected over the tropical forest in central America and Indonesia (Val Martin et al., 2010, Tosca et al., 2011). In contrast, smoke plume heights over the Amazon are substantially lower than smoke plumes observed over the boreal biomes (960–1040 m) (Kahn et al., 2008, Val Martin et al., 2010). There are several factors that influence smoke altitudes and contribute to the differences between biomes, such as fire intensity, availability of fuel, combustion efficiency, atmospheric stability, and entrainment (e.g., Lavoué et al., 2000, Trentmann et al., 2006, Luderer et al., 2006, Kahn et al., 2007, 2008, Val Martin et al., 2012). We assess some of these factors for our Amazon dataset next.

3.3.2 Effect of atmospheric and fire conditions on smoke plumes

We explore the relationship between smoke plume height, fire characteristics (i.e., MODIS FRP and AOD) and atmospheric conditions derived in the vicinity of the fires throughout the burning season, across the major biomes in the Amazon except cropland. For atmospheric conditions, we focus both on how smoke plume height relates to boundary layer height and on the effect of atmospheric stability on plume rise. We consider atmospheric stability conditions above our fires as the average of the atmospheric stability over the atmospheric column (K/km; Section 3.2.4) from the surface, at the origin of the fire, to the maximum altitude that smoke reached in the atmosphere. We add a buffer of 10% to the maximum altitude to account for any potential influence that the atmosphere above the plume might have over the column. We include in Table 3.3 a summary of these main parameters.

Consistent with previous studies (e.g., Val Martin et al., 2010, 2012, Sofiev et al., 2009, Amiridis et al., 2010), we find that the highest-altitude smoke plumes tend to be associated with highest MODIS FRP values, though there is significant variability in the relationship in all the biomes ($r^2=0.2$; Figure A3). Smoke plumes detected

over tropical forest fires have the lowest FRP (209 MW) and largest AOD values (0.51) (Table 3.3). The other two main biomes (savanna and grassland) have FRP and AOD values similar to each other (360–421 MW and 0.33–0.35, respectively). Tropical forest has deeper root systems, which allows fires to access deeper soil layers (Nepstad et al., 2008) that can maintain higher moisture content and lower oxygen availability than other biomes, such as grasslands. High fuel moisture content and low oxygen availability favour smouldering rather than flaming fires, which in turn tends to produce greater smoke emission but lower radiant emissivity (Kauffman et al., 1995). Therefore, the low FRP and high AOD in tropical forest fires are consistent with these conditions, in which smouldering fires predominate, whereas high FRP and low AOD are typical with dryer, less dense fuels, eg, savanna and grassland, that tend to produce flaming fires (Giglio et al., 2006). In addition, high smoke opacity and tree canopy obscuring the fire-emitted 4-micron radiance as viewed by MODIS, as well as low radiant emissivity, rather than just low radiative total fire intensity, probably contribute to these differences (Kahn et al., 2008).

The atmospheric stability structure affects the vertical motion of smoke and is a key factor in plume rise, either enhancing or suppressing the lifting. Some studies have shown the important role that atmospheric stability plays in plume rise (e.g., Kahn et al., 2007, 2008, Val Martin et al., 2010, Amiridis et al., 2010), and the quantitative representation of this factor still remains an open question in plume-rise model parametrisations. For instance, Val Martin et al. (2012) showed that, in North America, fires that inject smoke to high altitudes tend to be associated with higher FRP and weaker atmospheric stability conditions than those that inject smoke at low altitudes, in which smoke tends to be trapped within the boundary layer. Similar results were found for agricultural fires over eastern Europe (Amiridis et al., 2010).

To analyse the influence of atmospheric stability over Amazon fires qualitatively, we divide our plume dataset into two groups that we define as having weak and strong atmospheric stability conditions based on MERRA-2 reanalysis. Over the

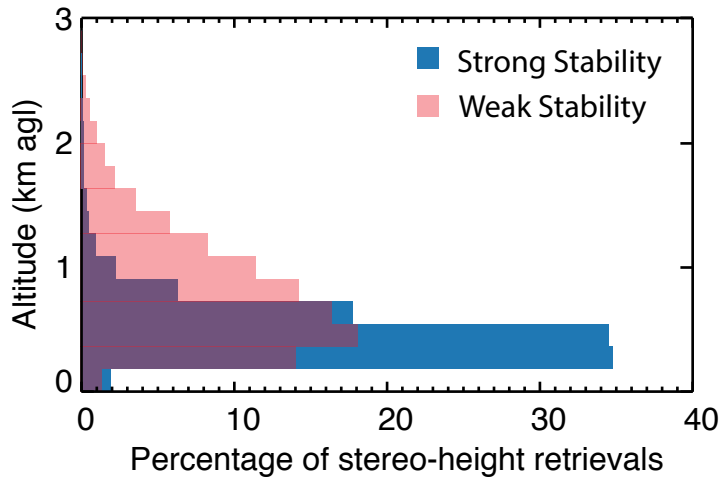


Figure 3.4: Vertical distribution of MISR stereo-height retrievals for all the plumes analysed, under strong (blue) and weak (pink) atmospheric stability conditions.

Amazon, and at the locations and times studied, atmospheric stability ranges from -3 to 23 K/km. We designate atmospheric stability < 2 K/km as 'weak', and atmospheric stability > 4 K/km as 'strong'. Each group contains about 30% of plumes in the database. Figure 3.4 shows the vertical distribution of smoke stereo-height retrievals for the plumes classified under weak and strong atmospheric stability conditions. Our comparison supports previous observations that plumes under weak atmospheric conditions tend to inject smoke to higher altitudes than those encountering strong stability, with maximum plume heights of 1150 m and 654 m, respectively. A similar pattern is found for the median plume heights (821 and 482 m, respectively). Weak atmospheric stability conditions are also associated with deeper PBLs (~ 1500 m) than strong stability conditions (~ 1200 m) (not shown).

Atmospheric conditions also correlate with biome type. We find that tropical forest fires tend to be associated with more stable atmospheric conditions than grassland fires (4.2 versus 2.5 K/km). Shallower PBLs are also observed over tropical forest (1270 m) compared to grassland (1620 m). Tropical forests typically have higher relative humidity conditions and more constant temperatures than grasslands, which favours more stable conditions and lower PBL heights (Fisch et al., 2004). We note that our dataset was all acquired at Terra overpass time, which occurs

between about 10–11 am LT. This might produce a bias toward the more stable atmospheric conditions that occur preferentially during the morning; later in the afternoon convection tends to become more important (Itterly et al., 2016).

3.3.3 Seasonality of smoke plumes heights

Figure 3.5 shows the seasonal cycle of maximum plume height with FRP, AOD, and atmospheric conditions over the major Amazon biomes. We further disaggregate these observations by biome, season and dry/wet years in Table A1. For these biomes, we find minimum plume heights of 600–750 m in July and maximum plume heights of 900–1400 m in October and November. Similarly, over tropical forest and grassland, MODIS FRP values follow the plume-height patterns, with maximum values toward the end of the burning season (180–200 MW), compared to the early season (90 MW). For savanna fires, MODIS FRP remains mostly constant throughout the season (\sim 150–200 MW). Savannas are known to be fire-adapted, and combustion efficiency typically remains constant throughout the season (Van der Werf et al., 2010). All these patterns are similar in wet and dry years, although larger MODIS FRP values are observed over savanna and grassland fires in dry years (Table A1).

Some previous studies show the seasonal peak in MODIS FRP over the Amazon earlier, in August–September (Tang and Arellano, 2017). However, their work relies on the maximum MODIS FRP detected by the Terra and Aqua satellites (four times/day) over the Amazon, whereas our seasonality shows the monthly median MODIS FRP observed by Terra, collocated with the MISR smoke plume observations (once/day). In addition, the MISR swath is substantially narrower than MODIS (380 versus 2330 km), and many fires detected by MODIS are not observed by MISR. Our seasonality thus captures the fire intensity that drives the smoke plumes detected specifically by MISR, i.e., only at about 10:30 AM local time, and the seasonal differences provide at least some indication of possible bias introduced

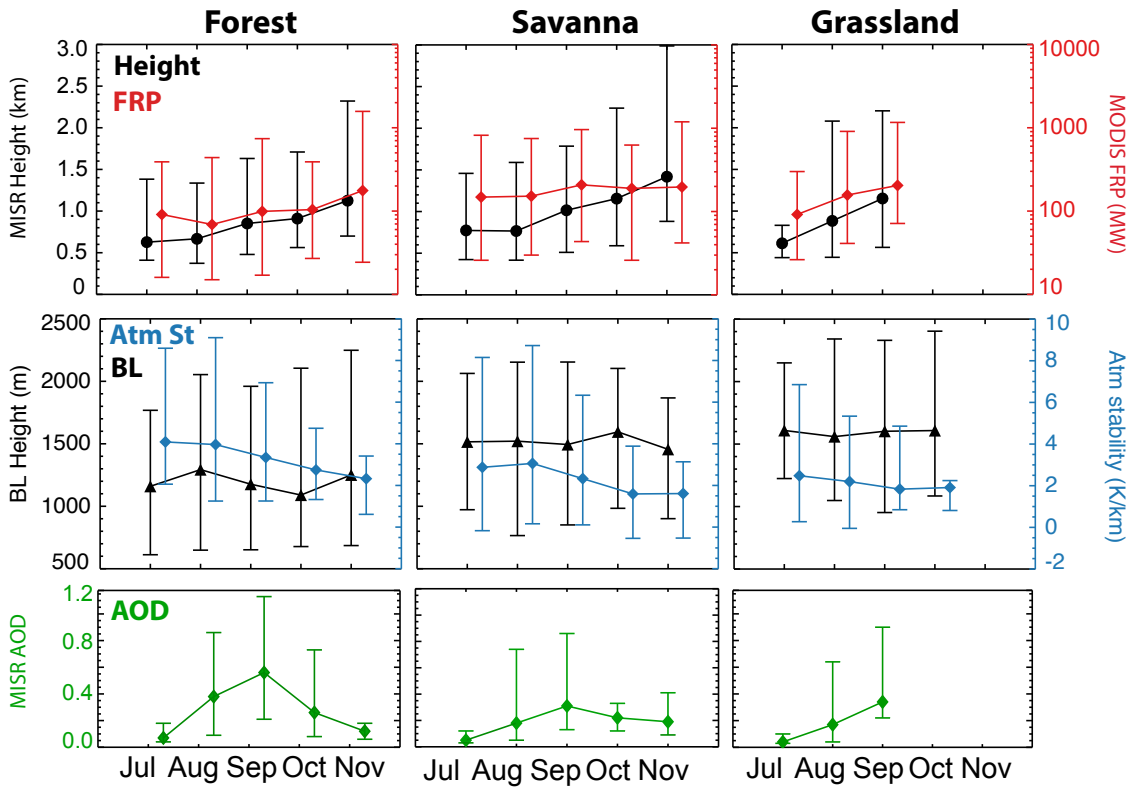


Figure 3.5: Seasonal cycle of MISR smoke plume maximum height above the terrain (black circles), MODIS FRP (red diamonds), PBL heights (black triangles), atmospheric stability (blue diamonds) and MISR AOD (green diamonds). Monthly median values are shown for tropical forest, savanna and grassland biomes. Vertical bars indicate the 10th and 90th percentile. Distributions with fewer than 10 observations are omitted and all years are included

by the MISR sampling of fires.

In contrast to the seasonality of plume heights and fire intensity, the peak monthly AOD occurs in September across the major biomes, with median AOD of 0.6 in tropical forest and 0.3 in savanna and grasslands, compared to AOD values of 0.04–0.1 in July and November. Over the Amazon, total AOD correlates well with the number of fires, and both tend to peak during September each year (Mishra et al., 2015). Baars et al. (2012) reported optical depths in the polluted biomass burning season (July–November) six times larger (on average) than in the pristine wet season (December–June), with highest values in September and October, for a site in the central Amazon near Manaus. In our dataset, September, together with August, are the months when the largest number of plumes were de-

tected (Figure A1). However, our monthly statistics might be influenced by the number of observations in each month. For example, the number of fires in August is driven by year 2010, in which an unusually large number of fires were observed, compared to the other August months. In addition, the large monthly median values in November are based on fewest numbers of plumes (Figure A1), although the few fires detected by MISR for those months were large and intense.

Boundary layer heights and atmospheric stability conditions may also vary by biome and throughout the season, influencing plume-rise spatial and temporal distributions. On a seasonal basis, the PBL height does not follow a clear cycle in any of our biomes, but higher PBL heights are observed over grassland fires (Table 3.3) and across all the biomes during dry years (Table A1 and Figure A1). More stable atmospheric conditions are found at the beginning (3.6 K/km in July) compared to the end of the burning season (1.9 K/km in November).

Previous studies have shown that a substantial fraction of smoke is injected above the boundary layer (i.e., into the FT), although this fraction varies depending on biome and fire type. For tropical fires over central America and Indonesia, smoke from about 4–6% of fires is reported to reach the FT (Val Martin et al., 2010, Tosca et al., 2011). This fraction is larger for boreal fires (>16%), where fires are more intense and the PBL is typically lower than in tropical regions (Val Martin et al., 2010, Kahn et al., 2008, Val Martin et al., 2018a). Following these studies, we consider that smoke reaches the FT when the median height of the plume is at least 500 m above the PBL height. This is a conservative definition that takes into account uncertainties in MINX and MERRA (e.g., Kahn et al., 2008, Val Martin et al., 2010, Tosca et al., 2011). Because fires over the Amazon tend to be smaller in size than those in boreal forests, we also consider a less conservative definition. We assume a plume is injected into the FT when the maximum plume height is at least 250 m above the PBL height. We understand that this is an upper limit, but it provides a bracket to our results. We include in Table 3.3 the percentage of the smoke plumes injected into the FT for both definitions, and present in Figure 3.6

the seasonality of these percentages. Our analysis shows that fires at the end of the burning season are more likely to inject smoke in the FT, with 15–40% in November versus 2–10% in July, and 5–22% at the peak of the burning season (August–September). This pattern seems to be related to a combination of more intense fires and less stable atmospheric conditions. We find no influence of the monthly PBL depth variability, although deeper PBL heights are found across the Amazon in drier conditions (i.e., over grassland fires and/or dry years). Interestingly, our analysis also shows a slightly larger percentage of fires injecting smoke into the FT over grassland (5–19%) compared to tropical forest (3–15%). As mentioned above, grassland fires are associated with high PBL heights, but also with large FRP values, suggesting that these fires are energetic enough to produce the buoyancy needed for the smoke to reach the FT.

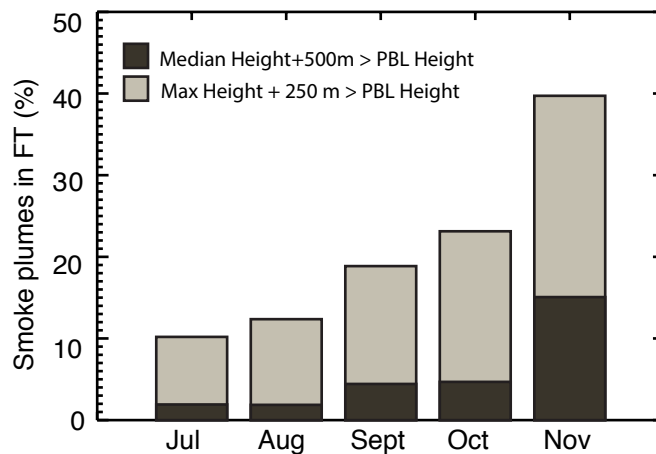


Figure 3.6: Seasonal variation of Amazon plume injection above the PBL (percent). Bar plots indicate the average of [Median Plume–PBL Height] > 0.5 km (dark grey) and [Maximum Plume–PBL Height] > 0.25 km (light grey) (see text for explanation).

3.3.4 Interannual variability of smoke plumes and drought conditions

We use MODIS DSI to assess the effect of drought conditions on smoke plume rise and the extent that these conditions control the interannual variability of smoke

plumes across the region. We present the interannual variability of MISR plume heights, MODIS FRP and MISR AOD in Figure 3.7, and summarise the annual averages of MODIS DSI, atmospheric stability, PBL height and percentage of smoke plumes in the FT in Table 3.4. In addition, we include the annual relationship of MISR plume heights, MODIS FRP and MISR AOD with MODIS DSI, and the percentage of plumes in the FT per drought level in Figure 3.8. In our dataset, 76% of plumes are recorded under extreme-mild drought conditions versus 7% plumes in wet conditions, as discussed in Section 3.3.1. During drought years (2005, 2007 and 2010), smoke plumes register the lowest MODIS DSI annual averages values (-0.89, -0.91 and -1.50, respectively), compared to the other years in the climatology (-0.63–0.18). Note that DSI is higher in wetter years.

Table 3.4: Summary of the main atmospheric parameters calculated at the location of the plumes per year^a.

Year	Number	BL height (m)	Atm. Stab (K/km)	% in FT ^c
2005 ^b	927	1370 ± 546	4.32 ± 3.01	3–13
2006	513	1210 ± 518	3.50 ± 2.89	6–25
2007 ^b	858	1380 ± 539	3.96 ± 3.30	3–18
2008	889	1480 ± 558	3.02 ± 2.28	4–23
2009	150	1100 ± 377	3.22 ± 2.60	4–27
2010 ^b	1373	1550 ± 498	3.69 ± 3.53	2–7
2011	320	1150 ± 296	2.73 ± 2.38	8–28
2012	363	1330 ± 453	3.20 ± 3.29	4–13

^aReported the average±SD

^bDrought years

^c Reported as percentage of plumes where [Median Plume–BL Height]> 0.5 km–[Maximum Plume–BL Height]> 0.25 km (see text for explanation).

We find a significant positive relationship between MISR maximum plume heights and MODIS DSI ($r=0.7$; $p<0.01$) in tropical forest and savanna fires, with higher maximum plume heights in normal and/or wetter than normal (1000–1100 m) than severe drought conditions (750–900 m) (Figure 3.8). Consistently, on an annual basis, these two biomes show the lowest smoke plume heights during dry years (Figure A1). Smoke plume heights in grassland fires, however, do not show any strong

relationship with DSI ($r=0.1$) or a clear interannual variability driven by droughts (Figure A1). In general, lowest median smoke heights are observed in our dataset

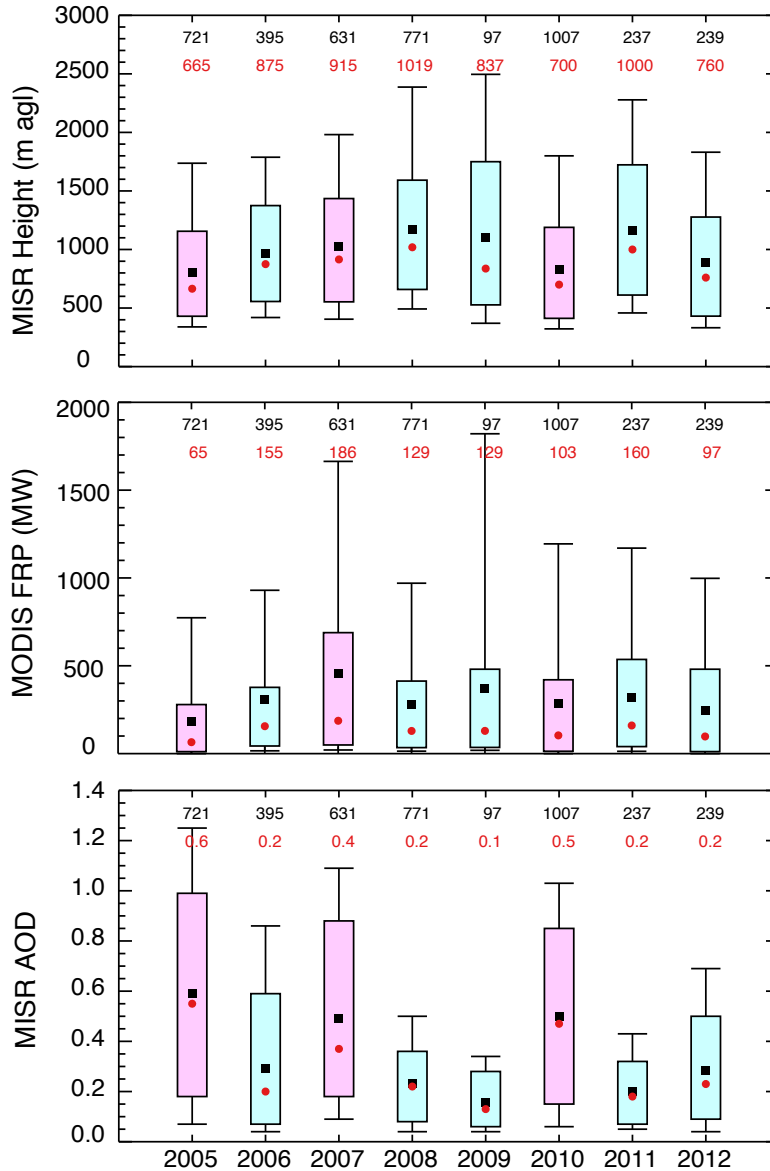


Figure 3.7: Interannual variability of MISR maximum plume heights above the terrain, MODIS FRP and MISR AOD, for the aggregate of tropical forest, savanna and grassland. Bar plots indicate the distribution of the data for each year. The medians (red circles) and the means (black squares) are shown along with the central 67% (box) and the central 90% (thin black whiskers). The number of observations (in black) and the median values (in red) included in each distribution are given at the top of the plot. Drought years are in pink and non-drought years in light blue. The same data, stratified by biome type, are plotted in Figure A4.

during the drought years of 2005 and 2010 (Figure 3.7), which are driven by tropical forest observations as they are the dominant biomes (Figure A1).

The relationship between MODIS FRP and drought levels over the Amazon is not straightforward on an annual basis as we do not observe any clear interannual variability of FRP driven by drought in Figure 3.7. However, our analysis shows some patterns when we subdivide the data by biome (Figures 3.8 and Figure A4). For example, we find a significant positive relationship between MODIS FRP and DSI ($r=0.6$; $p<0.01$) in tropical forest, with lower FRP in extreme dry than normal-wet conditions (170 versus ~ 250 MW; Figure 3.8). Contrariwise, savanna and grassland

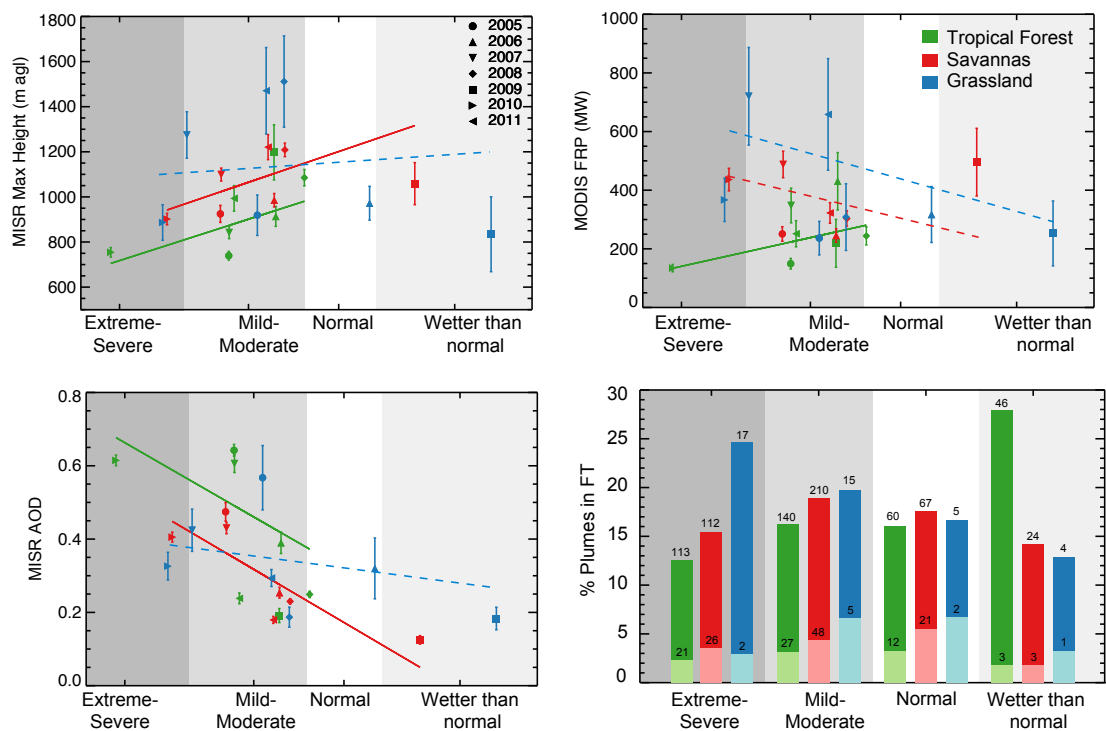


Figure 3.8: Relationship between MODIS DSI at the location of the plumes and MISR maximum plume height, MODIS FRP and MISR AOD annually averaged, for tropical forest (green), savanna (blue) and grassland (red). Symbols represent the annual average and bars the standard error of the mean. Regression lines are weighted by the number of plumes in each year; relationships with absolute $r < 0.4$ are plotted in dashed lines. Also included percentage of smoke plumes in the FT in each biome and by drought condition. Bar plots indicate the average of [Median Plume–PBL Height] > 0.5 km (light colour) and [Maximum Plume–PBL Height] > 0.25 km (dark colour), based on MERRA-2 PBL heights (see text for explanation).

fires have higher FRP in extreme and mild dry than in wet conditions (~ 500 MW versus 250 MW), although the relationship is weak ($r=-0.4$; $p<0.01$). As mentioned above, interpretation of FRP can be complicated by factors such as overlying smoke opacity and fire emissivity (Kahn et al., 2008).

The relationship between smoke plume height, FRP and drought conditions over the Amazon is somewhat complex. Drought conditions over the Amazon increase fuel flammability and the number of fires, but not necessarily increase smoke elevation. Drought also decreases fuel load, i.e., fuel available to burn, especially over grassland. Tang and Arellano (2017) reported that drought in the Amazon favours understory fires for tropical forest, which are dominated by smouldering combustion and are linked to low altitude smoke plumes. In addition, spatial changes in drought location can influence the type of biome affected and hence the type of fire regime in a given year. For example, drought in 2005 was located at the northeastern and central regions, and the large majority of the plumes recorded by MISR (65%; Figure A1) were from tropical forest fires, i.e., related to smouldering and fires that inject smoke to lower altitudes. In 2007, drought shifted to the southeastern region, and the majority of the plumes (60%; Figure A1) were from savanna and grassland fires associated with more flaming burning conditions, i.e., higher FRP and smoke plume altitudes. Our analysis supports this observation. In 2005, a drought year, smallest MODIS FRP (150 MW) and lowest smoke plume heights (750 m) were recorded over tropical forest (Figure 3.8), whereas in 2007, another drought year, larger FRP (500 and 750 MW), associated with higher smoke plume heights (1100 and 1300 m), were recorded over savanna and grassland fires, respectively.

In addition to the influence of drought in controlling the type of fires, drought can also affect atmospheric conditions. We find that during drought years, PBL heights tend to be about 200 m deeper than in wet years (Table 3.4). However, on an annual basis, atmospheric stability does not vary significantly, with values of $\sim 3-4$ K/km, across the Amazon for the averaged biomass burning season (Table 3.4). We also observe that a lower percentage of fires inject smoke plumes into the FT

in drought compared to non-drought years (2–18% versus 4–28%; Table 3.4). On a biome basis, tropical forest fires inject a larger percentage of smoke plumes into the FT in wet than extreme-dry conditions (27 versus 12%, Figure 3.8), and shallower PBL heights may partially explain the larger percentage of MISR plumes detected in the FT during non-drought years. Contrariwise, grassland fires, although with fewer observations, inject more smoke plumes into the FT during extreme dry than wet conditions (25% versus 13%, Figure 3.8). These fires are associated with high FRP values in dry conditions and this extra fire energy may be enough to produce the buoyancy needed to lift smoke directly into the FT, regardless of the PBL height. Note that in Figure 3.8 (right bottom), we present the data only subdivided by MODIS DSI and biome, regardless of the year, as in the rest of the panels in Figure 3.8.

Consistent with previous studies that have shown significant positive relationships between drought conditions and aerosol loading (e.g., Reddington et al., 2015, Tang and Arellano, 2017), we find a significant relationship between MISR AOD and MODIS DSI on an annual basis in tropical forest and savanna fires ($r=-0.7$ and $p<0.01$; Figure 3.8). Years with drier conditions have almost a factor of three greater AOD compared with years with wet conditions. Larger aerosol loading in drought periods is likely due to increases in the number and size of fires (e.g., Aragao et al., 2014) and subsequent increases in aerosol emissions. In addition, MISR AOD shows significant interannual variability, with the largest AOD values recorded in 2005, 2007 and 2010 (0.4–0.6; Figure 3.7), and in particular over tropical forest fires (0.6, Figure A4). Our results suggest that fires during drought periods might significantly degrade regional air quality, as they are associated with low smoke altitude and high aerosol loading.

3.3.5 CALIOP smoke plume observations

To further investigate smoke rise over the Amazon, we develop a climatology of smoke plume heights using CALIOP extinction profiles (section 3.2.6). We identify a total of 1600 CALIOP smoke plumes linked to active fires from July–November, 2006–2012 (Figure A5). Although the CALIOP climatology is 1/3 in size of the MISR climatology, these datasets agree well with respect to the temporal and spatial distributions. Similar to MISR, the largest number of plumes corresponds to years 2007 and 2010 (22 and 29%), whereas the lowest records are in 2009 and 2011 (4 and 7%). Most of the CALIOP plumes are also recorded at the peak of the biomass burning season (September; 51%) and over savanna and tropical forest (37 and 57%, respectively) compared to grassland.

Figure 3.9 displays the time series of derived median and maximum heights, for day and night-time observations. We include both daytime and night-time CALIOP observations to assess any day-night differences in smoke plume rise. Similar to the MISR climatology, we find large variability in the CALIOP smoke plume heights; the median heights range from 0.8–4.4 km (daytime) and 1.1–4.5 km (night-time). Maximum smoke plume heights are obviously higher, typically spanning 1.8–5 km (daytime) and 2.4–5.8 km (night-time). About 18 maximum plume height observations fell above 6 km (shown saturated at 6 km in Figure 3.9). Here we examine the vertical distribution of aerosol plumes individually. Ten cases show high altitude smoke (> 6 km) in a layer that extends through the column to near-surface (Figure A6, right panel), implying that smoke from the active fire below was lifted by fire-induced buoyancy, atmospheric processes, and/or both. The remaining cases show that high-altitude smoke was disconnected from the surface smoke layer (Figure A6, left panel), and we suggest that this smoke could be residual smoke from older fires, smoke transported from the source and concentrated in an elevated layer, aerosol that was wrongly classified as smoke by the CALIOP algorithm, and/or the result of CALIOP not being able to detect lower-level aerosol due to thick smoke aloft or the presence of clouds in the column. We include these observations in our

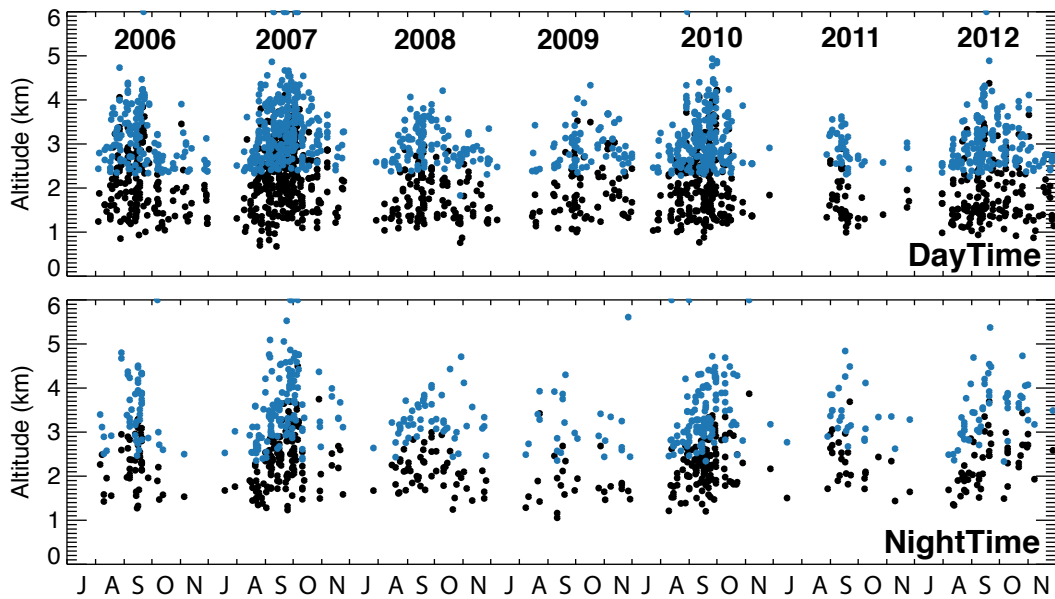


Figure 3.9: Time series of the CALIOP smoke plumes (2006–2012) for daytime and night-time observations. Each dot represents the maximum (blue) and median (black) smoke plume height above the terrain. Eighteen points for which the CALIOP height exceeds 6 km are plotted at the top of the charts.

analysis, but note that they represent only 1% of the total observations within the climatology and do not significantly impact the overall statistics shown here.

Figure 3.10 summarises the median and maximum heights for the CALIOP smoke plumes per biome, season and wet/dry years. Night-time plume heights are on average ~ 250 m higher than daytime plume heights (Figure 3.9). Differences between day and night-time CALIOP observations have been attributed in the past to a low bias in the daytime retrievals due to noise from scattered solar radiation (e.g., Winker et al., 2009, Huang et al., 2015). Therefore, our observed difference in day and night-time CALIOP plume heights might result from differences in data quality rather than reflecting smoke diurnal variability. We combine day and night-time CALIOP observations in Figure 3.10 and include the MISR plume heights for comparison. Average CALIOP median plume heights range from 2.1 km (tropical forest and savanna) to 2.3 km (grassland). Maximum plume heights are similar across all biomes (~ 3.2 km). Similar to MISR, CALIOP detects higher smoke plumes

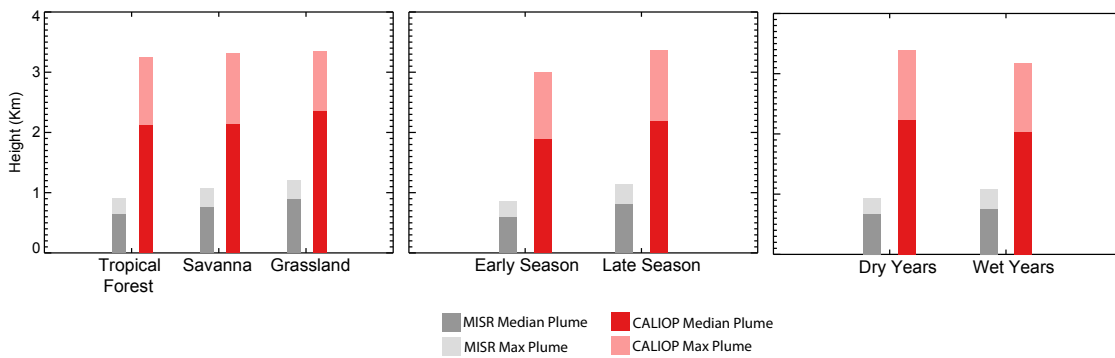


Figure 3.10: Average CALIOP and MISR plume heights per biome, time of the season and dry/wet years. The burning season is divided into early (July–August–September) and later (October–November) periods, and dry years (2007, 2010) and wet years (2006, 2008, 2009, 2011). Bars represent MISR plume heights (grey), and combined day and night-time CALIOP plume heights (red).

during the late burning season (2.1 and 3.3 km, for the median and maximum plume heights, respectively) than the early season (1.9 and 3.0 km). In contrast, CALIOP observes smoke at higher altitudes during dry (2.2 and 3.4 km) than wet years (2.0 and 3.2 km). In contrast, CALIOP observes smoke at higher altitudes during dry (2.2 and 3.4 km) than wet years (2.0 and 3.2 km). As discussed above, for the time and location of the MISR observations, a deeper PBL is observed in dry compared to wet years. Likewise, PBL heights at the CALIOP smoke plumes are 2.4 and 2.6 km in wet and dry years, respectively, and thus a deeper PBL during drought conditions explain the higher altitudes observed by CALIOP under drier conditions.

Smoke plume height values over the Amazon similar to ours were reported in other studies for CALIOP (Huang et al., 2015) and surface-based lidar measurements (Baars et al., 2012). Using the CALIOP vertical feature mask and AOD profiles, Huang et al. (2015) reported an average for the most probable smoke height of 1.6–2.5 km for September fires. Their definition is comparable to our CALIOP median plume height, which produced a value of 2.3 ± 0.7 km for the September months. Over Manaus in 2008, Baars et al. (2012) reported biomass burning layers at 3–5 km elevation, with most of the smoke trapped below 2 km. Other CALIOP smoke plume heights have been reported over eastern Europe (1.7–6 km) and several

regions and biomes across Asia (0.8–5.3 km)([Amiridis et al., 2010](#), [Labonne et al., 2007](#), [Tosca et al., 2011](#), [Vadrevu et al., 2015](#)).

In our study, CALIOP observes smoke at systematically higher altitudes than MISR, with median plume heights up to 1.4 km higher (2.2 km for the maximum plume heights). However, CALIOP still shows that the majority of the smoke is located at altitudes below 2.5 km above ground, consistent with previous observations from lidar measurements ([Baars et al., 2012](#)). Differences between MISR and CALIOP smoke plume heights are consistent with deeper PBL heights at the time of the CALIOP observation, as PBL is expected to grow further later in the day, and fires might also increase in intensity. We find that PBL height at the location/time of the CALIOP daytime smoke plumes is on average about 1.4 km higher than for MISR smoke plumes, specifically 2.7 km for CALIOP and 1.3 km for MISR.

[Tosca et al. \(2011\)](#) found similar differences between CALIOP and MISR (1–2.8 km) in peatland fires over southeastern Asia. In addition, CALIOP height retrievals are more sensitive to thin aerosol layers than MISR stereo analysis, so CALIOP is more likely to detect low-density smoke at plume-top ([Kahn et al., 2008](#)); this would include smoke that might have been lifted later in the day by convection, air mass advection or fire buoyancy ([Kahn et al., 2008](#), [Tosca et al., 2011](#)). Although we only select CALIOP plumes that are directly linked to active fires with some confidence, fires can burn for several days (and even weeks); in particular, deforestation fires can leave residual smoke layers over the region for many days or even weeks. As such, our CALIOP plume heights may include low-density smoke at higher altitudes, possibly from old fires.

Some previous studies with MISR smoke plume height have also analysed the altitude of 'smoke clouds', that is, dispersed smoke not easily associated with a particular fire ([Val Martin et al., 2010](#), [Tosca et al., 2011](#)). Smoke clouds tend to occur at higher altitudes than smoke plumes; they typically represent fire plumes at a later stage of evolution. Over Borneo peatland fires, [Tosca et al. \(2011\)](#) show that MISR smoke clouds and CALIOP smoke plumes had similar altitudes during their

period of study. The analysis of smoke clouds over the Amazon may support the expectation that plume heights tend to grow even larger than observed by MISR later in the afternoon. In addition, transported smoke is more likely to have stayed aloft longer than near-source smoke, and would therefore have more opportunity to mix upward.

3.4 Conclusions

A climatology of smoke plumes from MISR and CALIOP observations is used to characterise the magnitude and variability of smoke altitude across the Amazon during eight biomass burning seasons. Biome type, fire and smoke properties (FRP and AOD), atmospheric conditions (PBL height and atmospheric stability) and regional drought state are included in the analysis, to explore the degree to which each contributes to the observed variability.

Analysis of the smoke plume climatology shows large differences in smoke-plume elevation over the main biomes in the Amazon, with heights ranging a few hundred meters to 5.2 km above ground level. Smoke from plumes observed by MISR (10:00-11:00 LT) is mainly concentrated at altitudes below 1.5 km. As expected, smoke plume elevations are higher in our CALIOP climatology, ranging from 0.8 to 6 km during daytime (14:00-15:00 LT), although the majority are concentrated below 2.5 km. We find that CALIOP smoke plume heights are about 1.4–2.2 km higher than MISR smoke plumes, due to a deeper PBL later in the day, possibly more energetic afternoon fires and CALIOP’s greater sensitivity to very thin aerosol layers (Kahn et al., 2008, Flower and Kahn, 2017). Thus, our CALIOP plume climatology includes fresh smoke from active fires and low-density smoke at higher altitudes, some of which might be from old fires. Our results show that over the Amazon, and similar to other fire regions studied previously, on average, smoke plume heights tend to increase later in the afternoon due to greater near-surface convection, greater fire intensity, and possibly self-lofting. Direct injection of smoke to altitudes higher than

6 km (middle to upper troposphere) did not seem to be significant over the Amazon during our study period.

For our main biomes in the Amazon, smoke plume heights are substantially lower over moist tropical forest fires (0.8 km, maximum plume height definition) than grassland fires (1.1 km), although grassland smoke fire plumes represent a small fraction (4%) of cases in the climatology. The MISR and CALIOP Amazon plume climatologies show a well-defined plume height seasonal cycle in the main biomes, with larger heights toward the end of the burning season. Using MODIS FRP and MERRA-2-estimated atmospheric stability conditions, we determine that higher smoke-plume elevations in October–November are the result of the combination of more intense fires and a less stable atmosphere. Less than 5% of the fires inject smoke into the FT (i.e., Median Plume–PBL height > 500 m) using a conservative criterion, although an additional 15–19% of the fires may inject some smoke based on a looser criterion (i.e., Maximum Plume–PBL height > 250 m). This fraction increases throughout the burning season, with about 15–40% of the fires injecting smoke above the FT in November.

Previous studies have shown a direct connection between drought, large-scale climate processes (e.g., ENSO) and the number of fire occurrences (e.g., [Alencar et al., 2006](#), [Inness et al., 2015](#)). We find a negative relationship between MISR plume heights and drought conditions in tropical forest fires, as wet years show smoke plume altitudes 300 m higher than dry years. [Tang and Arellano \(2017\)](#) reported that drought conditions over the Amazon favour understory fires, for which smouldering combustion dominates, favouring lower smoke injection heights. In addition to low-altitude smoke, we find that drought conditions are also related to deeper PBL heights, which can reduce the frequency with which smoke is able to reach the FT.

A relationship between fire intensity (as approximated by FRP) and drought conditions is not clear in our study. We detect the highest FRP values in grassland fires during dry periods, and the lowest FRP values for tropical forest fires under

similar dry conditions, but without a significant relationship between FRP and DSI, nor any interannual variability of FRP driven by droughts. This lack of relationship may be due to the different locations of drought in different years, the type of fires recorded by MISR in a given year, and/or the low performance of MODIS FRP under dense smoke conditions.

Consistent with previous observations, we find larger MISR AOD during drought compared to non-drought periods. Our analysis confirms the important effect that biomass burning has on smoke aerosol loading over the region, from the surface to the lower free troposphere. Strong land management policies to control fires over the Amazon may become crucial as increases in drought frequency are projected in a future climate (Malhi et al., 2008); this would have important consequences for fire activity and thus air quality.

A variety of smoke injection height schemes are used to represent fire emissions over the Amazon, from fire emissions injected below 3 km (Reddington et al., 2016) or into the model-defined PBL (Zhu et al., 2018) to complex plume rise models, in which a significant fraction of emissions are in some conditions injected above 6 km (Freitas et al., 2007). Recent efforts have shown the value of using MISR-derived smoke plume heights to initialise model fire emission injection (Vernon et al., 2018, Zhu et al., 2018). Over the Amazon, Zhu et al. (2018) show that a new injection scheme based on MISR plume-height observations, which included vertical smoke profiles used in this study (Val Martin et al., 2018a), provide a better representation of CO observations over the region. With a very narrow swath but sensitivity to sub-visible aerosol, CALIOP tends to sample aerosol layers downwind, providing information complementary to the near-source mapping offered by MISR (Kahn et al., 2008). Thus, observations from both CALIOP and MISR provide a way to study smoke plume heights across the Amazon during the biomass burning season. Ultimately, this information will help improve the representation of biomass burning emissions in Earth system atmospheric models, and should aid our understanding of the feedbacks between drought, terrestrial ecosystems and atmospheric composition

over the region.

A next step in our work includes the evaluation of the influence of smoke plume height on the atmospheric composition over the southern hemisphere, based on insights from the analysis of the smoke plume climatology across the Amazon, and further application of this approach to other geographic regions.

Chapter 4

Biomass burning influence on CO and ozone over the Amazon: sensitivity to vertical smoke distribution and source contributions †

4.1 Introduction

Across the Amazon basin, with an area of 6,300,000 km² and a population of 25 million people ([Davidson et al., 2012](#)) distributed in eight countries, millions of hectares burn every year. Biomass burning in the Amazon is an important global source of emissions, which contributes by 15% to the global total fire emissions ([Van der Werf et al., 2010](#)) and drives the interannual variability in the southern

†This chapter will be submitted with some modifications to the Atmospheric Chemistry and Physics journal (ACP) as Gonzalez-Alonso, L., Val Martin, M., Deeter, M., Gaubert, B., Emons, L., Tilmes, S.: Biomass burning influence on CO and ozone over the Amazon: sensitivity to vertical smoke distribution and source contributions.

hemisphere (SH) atmospheric composition (Thompson et al., 2001, Edwards et al., 2003, 2006). Emissions from biomass burning include large amounts of aerosols, greenhouse gases and reactive trace gases, i.e., precursors of ozone to the atmosphere, such as CO and NO_x (Andreae and Merlet, 2001). Moreover, biomass burning is believed to be the most important source of CO and NO_x in the tropics (Chameides et al., 1992, Crutzen and Carmichael, 1993), which can lead to enhancements in global tropospheric ozone of around 3–5% (Ziemke et al., 2009). Specifically across the Amazon, biomass burning is responsible for increases in surface ozone of around 30–40% during the fire season (Galanter et al., 2000).

Tropospheric O₃ is a secondary product from biomass burning, an important greenhouse gas (IPCC, 2007) and air pollutant, harmful to human health (e.g., Levy et al., 2001, Ito et al., 2005, Bell et al., 2006) and detrimental to crops and plants (e.g., Sitch et al., 2007, Van Dingenen et al., 2009a). Inhalation of elevated levels of ozone can decrease lung function, aggravate asthma, cause higher susceptibility to respiratory infections and premature death (e.g., Bell et al., 2004, 2006, Kheirbek et al., 2013, Liu et al., 2018). High and long exposure to ozone concentrations can also damage leaf tissue, decrease net productivity of plants and reduce crop yields (e.g., Reich and Amundson, 1985, Avnery et al., 2011, Ghude et al., 2014, Yue and Unger, 2018). Ozone forms as a result of photochemical reactions of many combustion products in the atmosphere, i.e., carbon monoxide (CO), volatile organic compounds (VOC) and nitrogen oxides (NO_x=NO+NO₂). These reactions take place within a few tens of minutes after released (Goode et al., 2000, Yokelson et al., 2003, Jaffe and Wigder, 2012). The Amazon is strongly impacted by emissions of these products, from biomass burning and vegetation (Galanter et al., 2000, Edwards et al., 2006, Gloudemans et al., 2006, Williams et al., 2013), particularly during the burning season.

During the Amazon burning season, previous studies have reported high ozone mixing ratios (60–80 ppb) in the middle and upper troposphere over the region (e.g., Andreae et al., 1988, Kirchhoff et al., 1992, Fishman et al., 1996b, Betts et al.,

2002). Important enhancements on surface ozone (>20 – 40 ppb), with daily maxima of 100 ppb have also been reported (e.g., [Kirchhoff et al., 1992](#), [Kirkman et al., 2002](#), [Artaxo et al., 2005](#), [Bela et al., 2015](#)). Furthermore, high O_3 enhancements have been generally observed particularly in tropical/subtropical aged plumes, as a result of a more efficient O_3 production due to the greater flux of solar radiation and higher temperatures ([Andreae et al., 1994](#), [Jaffe and Wigder, 2012](#)). With a lifetime of several weeks, O_3 can be transported long-range downwind or be produced downwind after long-range transport of its precursors ([Jaffe et al., 2004](#), [Real et al., 2007](#), [Nassar et al., 2009](#)), which can produce exceedances of the O_3 air quality standards in metropolitan areas far from the fires ([Jaffe et al., 2008](#), [Pfister et al., 2008](#), [Chalbot et al., 2013](#), [Rubio et al., 2015](#), [Brey and Fischer, 2016](#)). Despite the high O_3 levels found every year across the Amazon region, little is known about the impact on air quality. For instance, [Pacífico et al. \(2015\)](#) modelled the impact of fire-induced O_3 damage on the Amazonian forest, and estimated mean reductions in net productivity of 15% and up to 60% at certain grids. However, models over the Amazon, including the one used in [Pacífico et al. \(2015\)](#), tend to overestimate O_3 levels within the boundary layer, specifically under clean air conditions, and underestimate elevated O_3 ([Pacífico et al., 2015](#), [Bela et al., 2015](#)), as a result of poor representation of biomass burning and the altitude to which biomass burning emissions are injected in the atmosphere i.e., the injection height ([Andreae et al., 2012](#)), among other factors.

The injection height is one of the main sources of uncertainty in chemical transport models (CTM). It determines the lifetime and downwind transport of pollutants, and thus, the magnitude of their impact ([Paugam et al., 2016](#)). Most large-scale CTMs used a simple approach to represent smoke injection heights: some models release all biomass burning emissions at the surface, others distributed evenly within the boundary layer ([Bey et al., 2001](#)) or homogeneously distributed from the surface to a prescribed height ([Dentener et al., 2006](#)). Results from models that inject a certain fraction of smoke in the free troposphere (FT) have shown improvements in

their estimates of surface and total column CO downwind of the fires (Leung et al., 2007, Turquety et al., 2007). Some modelling studies have used complex dynamical parametrisations based on thermal convective approaches for pyroconvection embedded on CTMs (Freitas et al., 2007, Rio et al., 2010). They showed that injecting fire emissions in the FT has a large impact on CO concentrations downwind (Freitas et al., 2006, 2007), but showed little agreement with observations for the elevated numerical cost (Val Martin et al., 2012) and complexity that can result in errors (Ichoku et al., 2012). Over the Amazon, results obtained using complex dynamical parametrisations tend to overestimate smoke plume heights (Freitas et al., 2007, Archer-Nicholls et al., 2015).

The injection height is highly variable and depends on the climatic zone, the season, the type of biome burned, the size and intensity of the fire and the atmospheric conditions (e.g., Amiridis et al., 2010, Val Martin et al., 2010, 2018b). Specifically over the Amazon, Gonzalez-Alonso et al. (2019), based on a comprehensive 8-year climatology of smoke plume heights derived from satellite observations from MISR and CALIOP, reported large variability on smoke plume heights, from a few meters to 6 km, with most smoke concentrated below 2.5 km. Their results agree well with previous studies across the region (Baars et al., 2012, Marenco et al., 2016). However, those studies were limited to a specific location or flight tracks. Gonzalez-Alonso et al. (2019) also showed the importance of drought conditions on the injection heights and aerosol loading over the region. Drought tends to favour smouldering fires, which are associated with low smoke injection heights and larger smoke emissions, and this, in turn, has important implications for air quality. Recently, results from a modelling study that applied a novel global injection height scheme derived from MISR observations (Val Martin et al., 2018b), which included smoke plume heights from Gonzalez-Alonso et al. (2019), showed an improvement in near-source surface concentrations and vertical profiles of CO over the Amazon (Zhu et al., 2018).

Future warming climate is expected to enhance frequency of droughts and fire

activity (Aragao et al., 2008, Li et al., 2008, Spracklen et al., 2009, Cochrane and Barber, 2009), as well as intensify biogenic emissions (Heald et al., 2008), which may result in an increase in O_3 precursor emissions. This, in combination with rapid urbanization, could pose a potential risk for millions of people’s health and vegetation across the Amazon. Given the large contribution of Amazonian biomass burning emissions to O_3 levels, it is important to understand the distribution of fire pollution across the region, as well as its impacts on surface O_3 levels. Here, we aim at improving the representation on the vertical distribution of biomass burning emissions in the Amazon and assessing the impacts on surface ozone levels across the region, with implications for air quality. To our knowledge, this is the first time that a study uses an improved representation of smoke injection height across the Amazon to address the relative impact of fire pollution on O_3 air quality. We use a global earth system model (ESM) with the Val Martin et al. (2018b) injection height parametrisation, which includes observations of Amazonian smoke plume heights, and evaluate the simulation with ozonesondes, satellite observations, and ground-based and aircraft measurements. Then, we assess the impact of biomass burning emissions from the Amazon on surface ozone, with focus on the associated exceedances of the ozone critical levels for air quality. Section 2 of this paper describes the global ESM and simulation experiments and Section 3 introduces the observational dataset used. Section 4 presents the model evaluation and Section 5 quantifies the impact of fire-induced O_3 on air quality.

4.2 Modelling Framework

To assess the performance of the updated representation of the vertical distribution of biomass burning emissions over the Amazon, and study the implication to simulated surface ozone, we use the Community Atmosphere Model with Chemistry (CAM6-Chem), a global atmospheric chemical transport model, which is part of the ESM Community Earth System Model (CESM). This section presents briefly the

model and describes the planned modelling simulations.

4.2.1 Model description

We use version 2 of the Community Earth System Model (CESM; [Lamarque et al. \(2012\)](#)) developed at the National Center for Atmospheric Research (NCAR). CESM is a fully coupled Earth system model (ESM), which consists of seven geophysical model components, the Community Atmosphere Model Version 6 (CAM6; [Bogenschutz et al. \(2018\)](#)), the Community Land Model Version 5.0 (CLM5; [Lawrence et al. \(2018\)](#)), and the river, ocean-wave, ocean, land-ice and sea-ice components. In this study, we run CESM2 with only the atmosphere component with chemistry (CAM6-chem) coupled with CLM5, and with prescribed sea-surface temperatures (SST) and sea-ice fractions ([Hurrell et al., 2008](#)). This setting allows for instantaneous flux exchanges between the land and the atmosphere, including biogenic emissions and dry deposition of gases and aerosols ([Oleson et al., 2010](#)). We refer to the model as CAM6-chem hereafter. All simulations are performed at a horizontal resolution of 0.9° latitude x 1.25° longitude and vertical resolution of 56 hybrid vertical sigma levels (top around 40 km), with a time step of 30 minutes.

CAM6-Chem includes over 200 species and 400 reactions ([Tilmes et al., 2016](#)), based on MOZART-4 ([Emmons et al., 2010](#)). Aerosols treatment follows the four-mode version of the modal aerosol module (MAM4) parametrisation, which differs four modes of aerosols size and distribution: coarse, aitken, accumulation mode and primary carbon ([Liu et al., 2016](#)). We use prescribed meteorology from the Modern-Era Retrospective Analysis for Research and Applications (MERRA-2) ([Bosilovich et al., 2015](#)). Table 4.1 shows a summary of several key species emissions used in this work. Anthropogenic emissions are monthly averages and extracted from the Coupled Model Intercomparison Project Phase 6 (CMIP6) ([Eyring et al., 2016](#)), which uses the Community Emissions Data System (CEDS) ([Hoesly et al., 2018](#)). Biogenic emissions are interactively computed by the Model of Emissions and Aero-

sols from Nature (MEGAN), version 2.1 (Guenther et al., 2012), integrated into the CLM5. MEGAN 2.1 estimates volatile organic compounds based on emission factors, plant functional type, leaf area index (LAI), leaf age, soil moisture, light and temperature. We include emissions from volcanoes and aircraft vertically distributed, from Dentener et al. (2006) and Lamarque et al. (2010), respectively. Emissions of NO_x from lightning follow Emmons et al. (2010) approach, that uses the Price parametrisation (Price and Rind, 1992, Price et al., 1997). These emissions are scaled to a global annual rate of 3-4 Tg(N)/year and vertically distributed following DeCaria et al. (2005).

Table 4.1: Summary of the global and domain-based emissions from main sectors for 2012.

Global [Tg]	CO	NO_x	BC	OC	Isoprene
Anthropogenic	576.09	81.26	7.85	27.20	-
Biogenic	75.54	-	-	-	479.24
Biomass burning	373.04	18.46	2.05	31.19	0.79
Amazon [Tg]	CO	NO_x	BC	OC	Isoprene
Anthropogenic	38.32	4.47	0.42	1.72	-
Biogenic	28.04	-	-	-	236.35
Biomass burning	79.29	4.25	0.46	5.99	0.12

Biomass burning emissions are obtained from the Fire Inventory from NCAR version 1.5 (FINNv1.5; Wiedinmyer et al. (2011)), which provides global trace gases and particles emissions from biomass burning, at high temporal (daily) and spatial resolution (1 km) from January 2002. FINNv1.5 emissions are calculated via satellite observations of active fires and land cover, estimates of fuel loadings and emission factors for open burning compiled by Akagi et al. (2011) and Andreae and Merlet (2001).

4.2.2 Biomass burning injection height parametrisation

We include a novel global biomass burning injection height scheme (Val Martin et al., 2018b) to distribute FINN’s emissions in altitude. The scheme assigns fire emission fractions at different altitudes depending on land cover, fire region and season, from

0 to 8 km and at a vertical resolution of 250 m. The plume height parametrisation is based on a statistical analysis of global MISR smoke plume heights observations for 2008–2010, compiled as part of the MISR Plume Height Project2 (MPHP2) for the AeroCom multi-model biomass burning experiment. For a detailed description of the plume height parametrisation, see [Val Martin et al. \(2018b\)](#).

To vertically distribute FINN fire emissions into CAM6-Chem, we first identify the region and assign plant functional types per grid. For each grid, depending on the region that contains it, the fraction of plant functional types and month of the year, a specific emission profile is calculated and applied. As an example, Figure 4.1 shows the summertime vertical distribution of fire emissions across the main biomes in the Amazon. An overview of the MISR instrument, standard products and the MISR plume digitizing tool is given in Chapter 2. The MISR plume database can be found in [Val Martin et al. \(2018b\)](#).

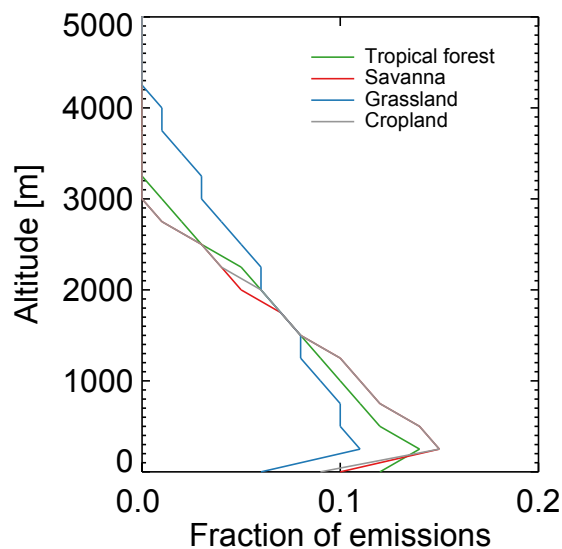


Figure 4.1: Vertical distribution of biomass burning emissions, in August, for the main biomes across the Amazon region.

4.2.3 Experimental setup

To assess the performance of the smoke injection height parametrisation over the Amazon, we conduct two simulations: a control simulation with biomass burning emissions released at the surface level (CAMsurf), and a simulation with biomass burning emissions vertically distributed following [Val Martin et al. \(2018b\)](#) scheme (CAMvert). Both simulations run from 2007-2012 with one year spin up. The simulated time frame coincides with recent aircraft campaigns over the region, which provide CO profiles to validate our results at high spatial and temporal resolution. In addition, we aim at investigating the contribution of biomass burning in the Amazon to surface ozone levels. For that, we perform an additional simulation for 2011-212 with the same configuration as CAMvert (i.e., biomass burning emissions vertically distributed) but with Amazon fire emissions set to zero (CAMzeroBB).

4.2.4 CO Tags

We introduce global tags of emitted CO associated with specific sources following the work of [Emmons et al. \(2010\)](#) and [Gaubert et al. \(2016\)](#). The CO tags allow us to assess the influence from a particular source, region or biome on the total CO levels and quantify the relative importance of each source. These CO tags are subject to the same reactions as the total CO ([Emmons et al., 2010](#), [Gaubert et al., 2016](#)) and include CO emitted by the main primary sources, i.e., anthropogenic, biomass burning, oceanic and biogenic. CO produced from chemical oxidation represents the secondary source of CO, and the sum of primary and secondary CO is the total CO. Additionally, we include CO tags for the main biomass burning regions across the globe, i.e., Europe, Boreal North America, Boreal Asia, Temperate North America, Central East-Asia, South East-Asia, Equatorial Asia, India, Australia, South America, Central America, North Africa, South Africa and Amazon (Figure B1 in Appendix B), and for the main biomes in the Amazon, i.e., tropical forest, savanna, grassland and cropland. For the latter, we associate FINN emissions to biome type

using MODIS MCD12C1 Land Cover product (Friedl et al., 2010) and select only the biome specific to the Amazon: tropical forest, savanna and others (agricultural and grassland).

4.3 Observational datasets for model evaluation

Simulations performed with CAM6-chem have been extensively evaluated against satellite, ozonesondes, aircraft and ground observations of key pollutants on a global and regional scale (e.g., Lamarque et al., 2012, Tilmes et al., 2015, Val Martin et al., 2015, Tilmes et al., 2016). Here we focus our evaluation on carbon monoxide (CO) and ozone (O_3) over the Amazon domain [90° – 10° W Longitude, 20° S– 10° N Latitude], using aircraft campaigns and CO retrievals from the Measurement of Pollution in the Troposphere (MOPITT), and ozonesondes and long-term surface measurements of O_3 .

4.3.1 CO Observations

CO is one of the main gases emitted by biomass burning and an important ozone precursor, whose relatively long lifetime (weeks to months) make it an excellent tracer for fire emissions (Edwards et al., 2006, Yurganov et al., 2010, Gatti et al., 2014).

We use CO vertical profiles measured from three aircraft campaigns to assess CAMvert versus CAMsurf performance. These aircraft campaigns include the Regional Carbon Balance in Amazonia (BARCA Balanco Atmosferico Regional de Carbono na Amazonia), the Gatti et al. (2014) flights and the South American Biomass Burning Analyses (SAMBBA). The dataset allows us to evaluate the impact of the smoke plume injection heights in different years and conditions. BARCA emerged as a combination of observations and analysis framework to quantify basin-scale carbon

fluxes with greenhouse gases and aerosols measurements over the Amazon ([Andreae et al., 2012](#)). BARCA was divided into two phases that represent the shift in the atmospheric conditions during the two seasons: BARCA–A, at the end of the dry season in 2008 (16 November–2 December), and BARCA–B, at the end of the wet season in 2009 (15–28 May). Flights in BARCA covered an altitude range from the surface to about 4500 m over most of the Amazon Basin. [Gatti et al. \(2014\)](#) used CO measurements as part of a sampling programme to observe climate sensitivity of the Amazon carbon pools during 2010 and 2011. The project consisted of bi-weekly vertical profiles of CO at four sites across the Amazon: Alta Floresta (ALF; 8.80°S, 56.75°W), Rio Branco (RBA; 9.38°S, 67.62°W), Santarem (SAN; 2.86°S, 54.95°W) and Tabatinga (TAB; 5.96°S, 70.06°W). Aircraft measurements were taken descending in spiral from approximately 4420 m to 30 m above sea level from 12:00 to 13:00 local time (LT). SAMBBA consisted of a combination of remote sensing, ground-based and aircraft measurements, which aimed to investigate the impacts of biomass burning pollution over South America ([Allan et al., 2014](#)). SAMBBA was conducted during the dry season of 2012 (14 September–3 October) and included 20 scientific flights sampling the Amazonian atmosphere from the surface up to almost 8 km.

MOPITT is a space-borne instrument aboard the NASA EOS Terra satellite designed to study the distribution, transport, sources, and sinks of CO in the troposphere. It uses gas correlation spectroscopy to retrieve measurements of the emitted and reflected radiance from the Earth in three spectral bands. The amount of energy absorbed into the sensor is correlated to the presence of CO in the atmosphere. MOPITT has a swath of 640 km and a spatial resolution of 22 km at nadir, and provides long record of global CO (since 2000) and global coverage every 3 days ([Deeter et al., 2003](#)).

We use daytime monthly joint retrievals (Thermal infra-red TIR and near infra-red NIR product) of the Level 3 Version 7, which provide total CO column and CO profiles in ten levels, from the surface to 100 hPa ([Deeter et al., 2003, 2014, 2018](#)). The use of combined TIR and NIR retrievals improves the sensitivity to CO in the

lower troposphere, particularly at daytime over land. To compare the MOPITT retrievals to our monthly CO simulations, we interpolate the model outputs to the ten-level pressure (surface-100 hPa) and horizontal $1^\circ \times 1^\circ$ MOPITT grid. Then, we apply the a priori and averaging kernels included in the MOPITT retrievals to account for the sensitivity of the retrieval to the truly observed profiles ([Morgenstern et al., 2012](#)).

4.3.2 Ozone Observations

We use ozonesonde observations compiled by [Tilmes et al. \(2012\)](#) to assess the performance of the simulated ozone vertical distributions. The dataset includes vertical ozone monthly profiles for 42 stations from 3 networks (World Ozone and Ultraviolet Data Center (WOUDC), the NOAA Earth System Research Laboratory (ESRL) and the Southern Hemisphere ADditional OZonesondes (SHADOZ)) for the period 1995–2011, and also regionally aggregated by similar ozone characteristics for their seasonal median and shape of pdfs. We focus on two regions: Equatorial Americas and Atlantic/Africa, which contain two and three stations, respectively (Figure B2 in Appendix B; [Tilmes et al. \(2012\)](#)). For the comparison, simulated ozone monthly outputs were first interpolated to the specific sondes locations and then aggregated and averaged by region and period.

In addition, we assess the ability of our simulation experiments to capture the spatial and temporal distribution of surface ozone. We evaluate our results with ground-based ozone measured at eight stations located within or close to the Amazon, from the Tropospheric Ozone Assessment Report (TOAR; [Schultz et al. \(2017\)](#)). These data are publicly available and free to download through [PANGAEA](#). We use a minimum of two-years monthly means of the records available and coincident with the simulations period (2007–2012). (Figure B2 and Table B1). Simulated monthly ozone mixing ratios at the surface are interpolated at the location of the stations and averaged for the run period.

4.4 Model performance with the smoke injection height parametrisation

We first compare results from CAMvert and CAMsurf to assess the impact of the biomass burning injection height distribution on the vertical distribution of CO and O₃ across the Amazon. We focus on differences between CAMvert and CAMsurf during March and September 2012, as these months represent wet versus dry conditions, and low (March) versus high (September) fire activity (Figure B3). Secondly, we evaluate simulated CO and O₃ from CAMsurf and CAMvert against observations to assess the performance of the simulations on representing CO and O₃ across the Amazon domain.

4.4.1 Impact of the smoke injection height scheme on simulated CO

Figure 4.2 shows the relative changes in the simulated CO mixing ratios between CAMvert and CAMsurf at the surface, 2 km, 6 km and the column from the surface to 8 km. Figure B4 shows the CO mixing ratios and column (0–8 km) value for these simulations. We choose 8 km as the top height in our analysis because smoke over the Amazon is rarely found above this altitude (Gonzalez-Alonso et al., 2019). Furthermore, the maximum altitude at which fire emissions are distributed over this region is typically 6 km (Val Martin et al., 2018b). As expected, the new injection scheme (CAMvert) decreases simulated CO mixing ratios at the surface, and increases them in the free troposphere, at 2 km and 6 km altitudes, especially near the fires in September. For example, simulated CO mixing ratios in CAMvert are reduced by around 70% (~800 ppb) at the surface, increased by 30% (~50 ppb) at 2 km, and by 7% (3 ppb) at 6 km above the fires, compared to CAMsurf in September. Small or negligible changes in simulated CO are found during the low fire active month of March. We find that the new injection height scheme

has important effects on the simulated CO column (0–8 km) on a regional scale (Figure 4.2b), especially at the peak of the biomass burning season in September. Simulated CO column is increased (5–10%) across the Peruvian coast, the Atlantic Ocean and the eastern Amazon, and decreased (10–15%) right above the fires at the arc of the deforestation. Previous studies have also shown that injecting fire emissions decreases CO in the source regions and increases it downwind, as CO lifetime is typically longer in the FT (Chen et al., 2009). Our results are consistent with the effect that injecting fire emissions at higher altitudes has on pollutant lifetime and downwind transport.

Evaluation of simulated CO with aircraft observations

We evaluate simulated CO from CAMvert and CAMsurf near the fire source with vertical profiles of CO from measurements gathered in 159 flights during three recent aircraft campaigns in the Amazon. We limit our comparison to the flights during the burning season (July-September) to maximize the differences in the simulated CO profiles in CAMvert and CAMsurf from the fire injection scheme. Figure 4.3 shows an example of simulated and observed CO from a flight during BARCA-A and SAMBBA, and the averaged CO observations in RBA site from Gatti et al. (2014) during 2010. We choose that SAMBBA flight and RBA site because they are highly influenced by biomass burning emissions (Brito et al., 2014, Gatti et al., 2014). For BARCA-A, we select a vertical profile where both simulations represent fairly well the CO vertical distribution, and focus on the differences from the injection height scheme. During BARCA-A aircraft measurements were only influenced by biomass burning during two days (Andreae et al., 2012) and our two simulations fail at capturing the observed high CO mixing ratios (400 ppb; Andreae et al. (2012)) at those two flights, due to underestimated CO emissions in FINN. Consistent with Section 4.4, our comparison for SAMBBA and RBA shows that CO mixing ratios in CAMvert are significantly reduced below 2 km (by up to 150 ppb) and enhanced from around 2–4 km (up to 40 ppb). In general, CAMvert matches better the

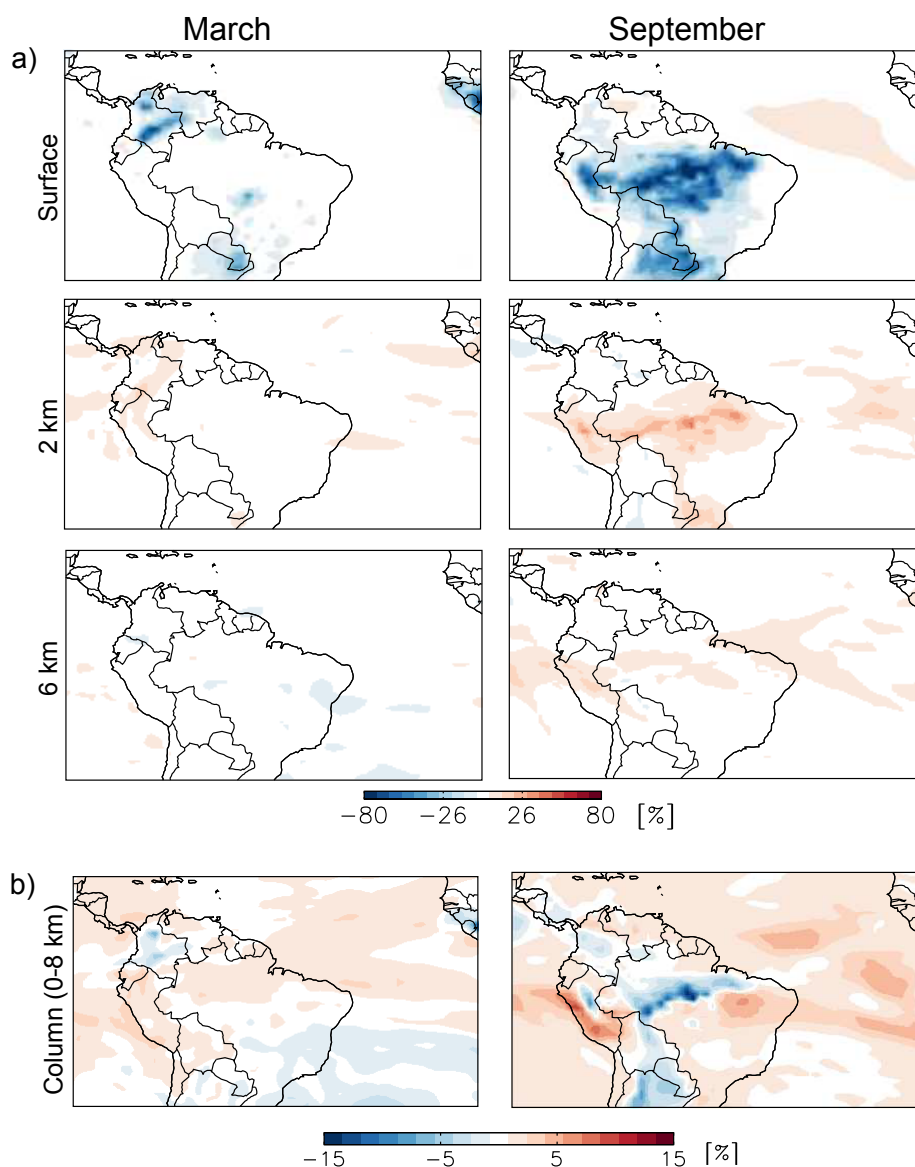


Figure 4.2: Relative differences (%) $[(\text{CAMvert} - \text{CAMsurf})/\text{CAMsurf}]$ in simulated CO mixing ratios between CAMvert and CAMsurf at three different levels: the surface, 2 km and 6 km (a), and the column (0-8 km) (b), for March and September 2012. Absolute mixing ratios (ppb) and column of CO (molec/cm²) are shown in Figure B4, in Appendix B.

observations at most levels during smoke-impacted conditions than CAMsurf. For the BARCA-A flight, CAMvert matches better the observations, specifically at 1–2 km, although this flight was hardly impacted by biomass burning compared to the SAMBBA and RBA site (averaged CO mixing ratio is 160 ppb, compared to

360 ppb at SAMBBA and 220 ppb at RBA site).

We also compare our simulated CO mixing ratio profiles from CAMvert and CAMsurf with other SAMBBA and BARCA flights and other [Gatti et al. \(2014\)](#) sites (TAB, ALF, and SAN), and the impact of new injection scheme on CO was low for some of them. Consistent with [Zhu et al. \(2018\)](#), we find that the evaluation of simulated CO against aircraft measurements is not that straightforward. Across the Amazon, fire emissions are highly variable and depend on many factors i.e., topography, type of vegetation burned, season, weather conditions and regional droughts on a particular year ([Van der Werf et al., 2010](#)). In general, FINN tends to overestimate fire emissions during the burning season across some regions in the Amazon ([Pereira et al., 2016](#)). In our analysis, a considerable number of simulated CO profiles had a poor agreement with the observations, as the model was not able to capture the extreme high CO resulting from high biomass burning influence or tended to overestimate CO under low biomass burning influence. Another aspect to consider is that the MISR injection height scheme may be biased low, as it is based on a statistical analysis of smoke plume heights observed during the early morning (10:00–11:00 LT) ([Val Martin et al., 2018b](#)). Most of the flights were performed in the afternoon ([Andreae et al., 2012](#), [Gatti et al., 2014](#)), when the PBL is fully developed and fires are more energetic, and thus, smoke heights are higher, as shown for the Amazon fires by [Gonzalez-Alonso et al. \(2019\)](#).

Evaluation of simulated CO with MOPITT

We use monthly CO retrievals from MOPITT to evaluate simulated CO from CAMvert and CAMsurf at a larger scale. Figure 4.4 presents CO total column from MOPITT, CAMvert and CAMsurf in September 2012 over our Amazon domain. CAMvert and CAMsurf simulations are convolved with the MOPITT a priori and averaging kernels for comparison. Absolute differences between simulated and MOPITT CO total column are also included in Figure 4.4. MOPITT shows high levels of CO across the arc of deforestation and efficient transport of CO from Africa

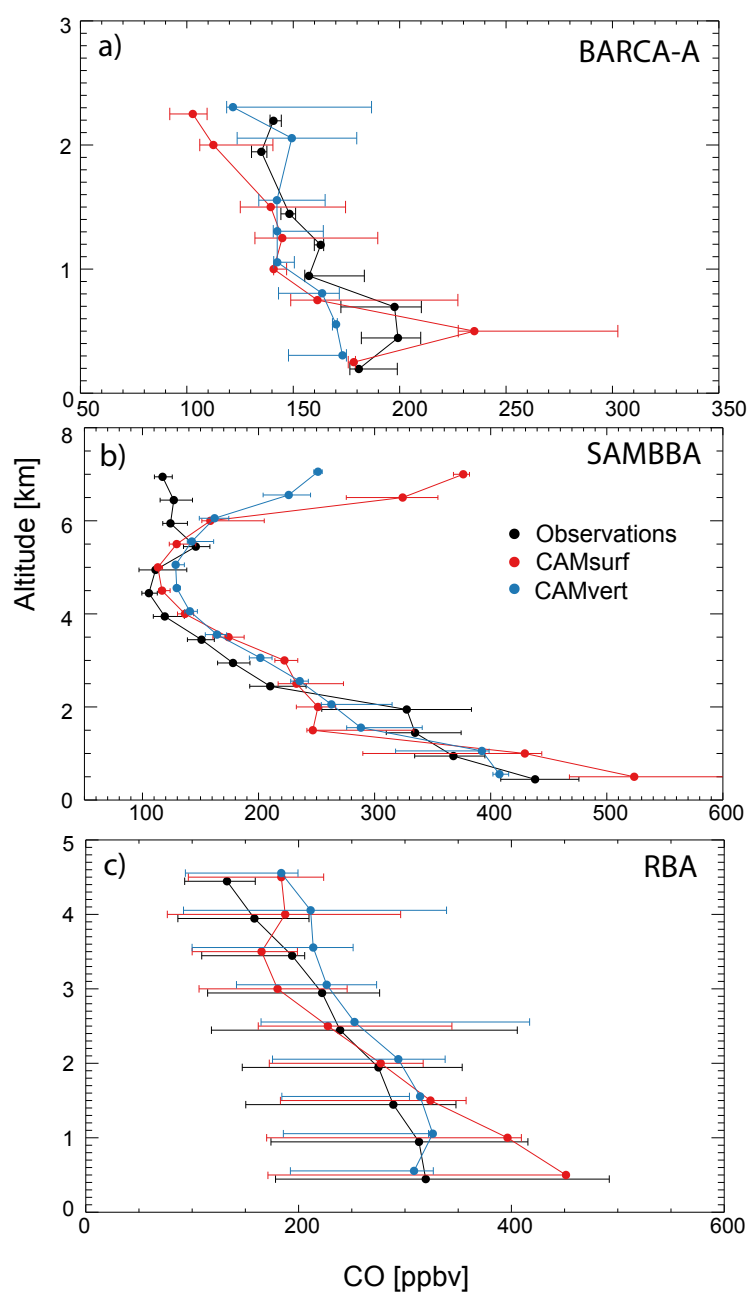


Figure 4.3: Examples of vertical profiles of CO mixing ratios from observations (black), simulated with CAM-vert (blue) and CAMsurf (red) for BARCA-A (a), SAMMBA (b) and RBA (c). Shown are median for SAMMBA and BARCA-A and average for RBA, with the horizontal bars indicating the 10th and 90th percentiles.

across the Atlantic, as reported by previous MOPITT studies ([Edwards et al., 2006](#)). Our comparison shows important biases between both CAM6-chem simulations and MOPITT. CAM6-chem misses the transport out of Africa, overestimates total CO column over western Amazon and along the Andes, and underestimates it over Eastern Amazon (by $\sim 30\%$). We notice a small difference between CAMvert and CAMsurf simulated CO total column with respect to MOPITT in this relatively large scale analysis, and compare them at two vertical levels in [Figure 4.5](#). We display the relative bias of simulated CO mixing ratios against MOPITT CO retrieved at 400 and 800 hPa (about 7 and 2 km altitude, respectively) for September 2012. [Figure B5](#) displays the comparison for March 2012. These two levels represent the lower troposphere (LT) and upper troposphere (UT) that include most of the information from the retrieval with the least contribution from the a priori ([Deeter et al., 2018](#)). We find that both CAMvert and CAMsurf overestimate mean CO mixing ratios, in particular at 800 hPa over western Amazon, with a relatively large bias up to 80–120% in March and September. Contrariwise, both simulations underestimate CO across the Eastern Amazon, in particular at 400 hPa with relative biases up to 60–80% in March and September.

[Deeter et al. \(2018\)](#) showed that MOPITT CO retrievals have a negative mean bias across the Amazon of about -16% and up to -27% due to the low sensitivity of MOPITT to the LT. This negative bias does not fully explain the positive bias we find in our comparison. Previous studies have also detected similar discrepancies between CAM6-chem and MOPITT (e.g., [Zeng et al., 2015](#)). They suggested that biases may be caused by poor representation of fire emissions, as well as model atmospheric processes (i.e., convection), which may result in accumulation of CO from fires along the Andes that act as a barrier during its transport by the easterly winds. The large bias between CAM6-chem and MOPITT makes it difficult to assess the large scale effect of including an injection height scheme in our model. Furthermore, most of the biomass burning emissions in CAMvert are released in the first 3 km, where MOPITT has the lowest sensitivity to CO, therefore, comparison

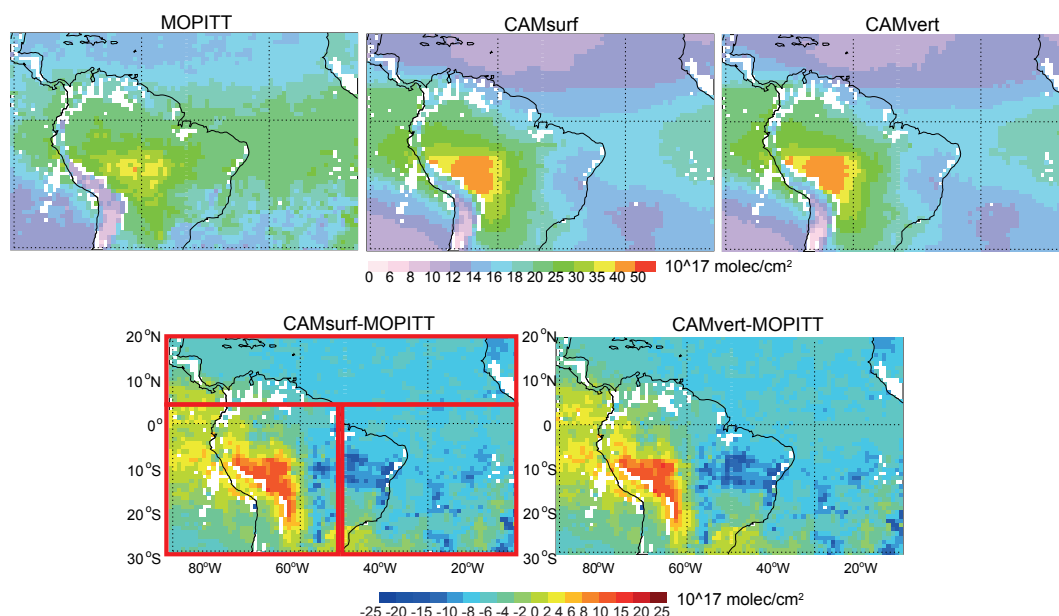


Figure 4.4: Mean MOPITT, CAMsurf and CAMvert CO total columns for September 2012 (top) and CAMsurf and CAMvert bias with respect to MOPITT (bottom). Red squares divide the domain in three fire regions North (90°–10°W Longitude, 5°–20°N Latitude), South-West (90°–50°W, 30°S–5°N) and South-East (50°–10°W, 30°S–5°N)(bottom left).

of CAMvert and CAMsurf differences against MOPITT does not provide much information. However, our analysis shows that during the burning season, the bias of CAMvert with respect to MOPITT is slightly higher than in CAMsurf at 800 hPa, where CAMvert injects most of the CO (12% versus 10%, respectively). Moreover, CAMvert improves somewhat the low bias observed at 400 hPa, being 17% versus 18% in CAMsurf.

To elucidate a regional and seasonal effect on our CAM-chem-MOPITT evaluation, Figure 4.6 compares monthly CO total column across three fire-influenced regions: north, southeast and southwest (depicted in Figure 4.4). We also include results from our simulation with Amazon biomass burning set to zero (CAMzerobb) to have a reference of the impact of biomass burning across these regions. This analysis confirms again the persistent low bias on the simulated CO across most of the Amazon, in particular north and southeast (15–20%), and positive bias during the biomass burning season in southwest ($\sim 5\%$). However, CAMvert and CAMsurf show an acceptable annual low bias of $\sim 15\%$ compared to MOPITT total CO column (not

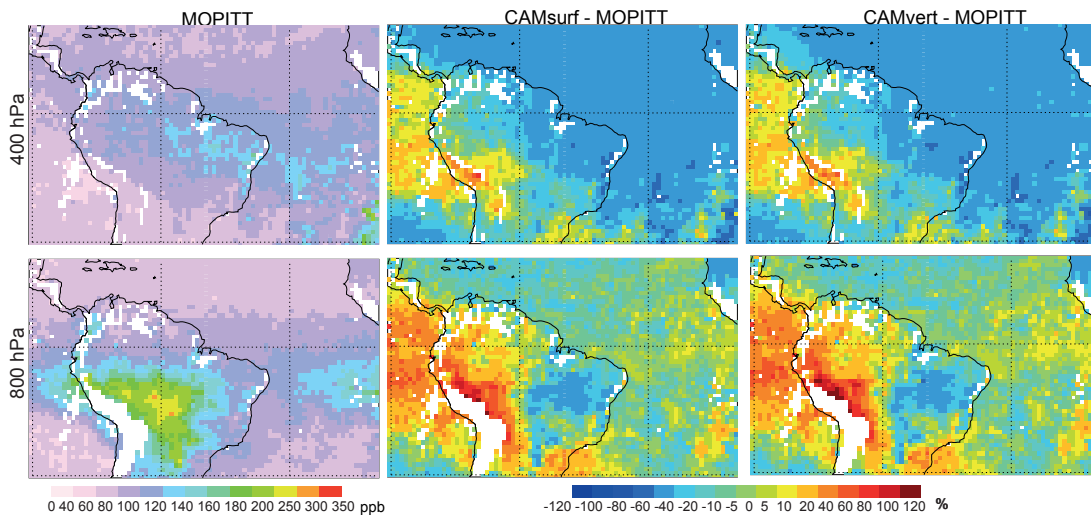


Figure 4.5: Averaged MOPITT CO mixing ratios and relative bias (in %) of CAMsurf and CAMvert with respect to MOPITT at 400 and 800 hPa for September 2012.

shown). Also, CAMvert slightly improves CO total column compared to MOPITT at the peak of the burning season (August-October) in the north and southeastern regions by 1-2%. Previous studies have also found small differences when comparing model simulations with and without injection heights against large-scale observations with low vertical information (e.g., MOPITT) (e.g., [Chen et al., 2009](#), [Zhu et al., 2018](#)). As in [Zhu et al. \(2018\)](#), we find better agreement in simulated CO with the improved vertical injection height scheme (CAMvert) when the model is compared to specific plumes from aircraft measurements and these improved simulations can have important implications for air quality.

4.4.2 Impact of smoke injection height scheme on simulated O_3

Figure 4.7 displays the relative changes in the simulated O_3 mixing ratios between CAMvert and CAMsurf at the surface, 2 km, 6 km and the column from the surface to 8 km. Figure B6 shows the simulated O_3 mixing ratios and column (0–8 km) values. Injecting O_3 precursors at higher altitudes leads to changes in the formation and vertical distribution of O_3 particularly near the source during the burning sea-

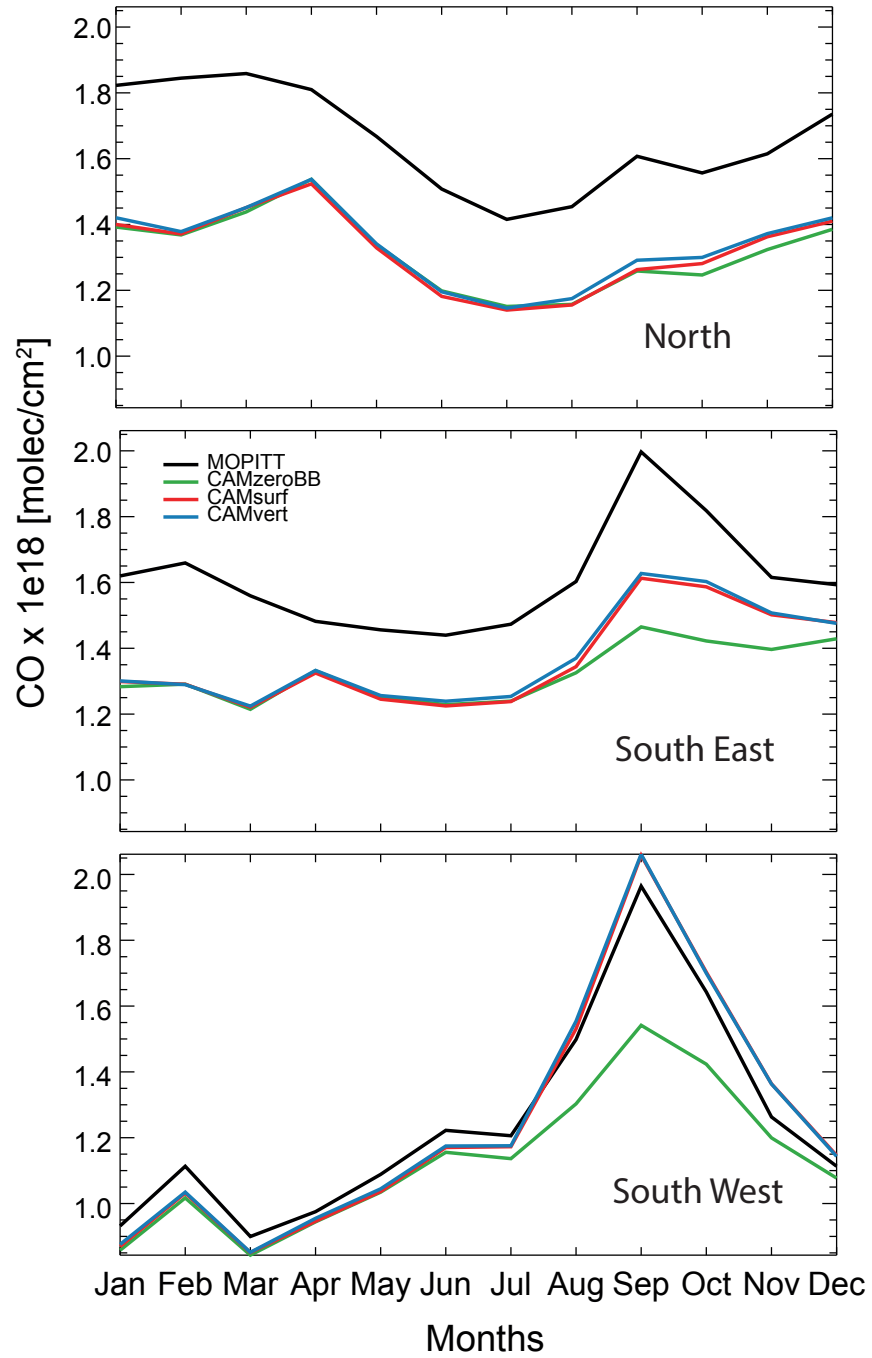


Figure 4.6: Monthly averages of CO total columns for MOPITT (black), CAMsurf (red), CAMvert (blue) and CAMzeroBB (green) for three major regions in our domain (see Figure 4.4) in 2012.

son. It decreases simulated O_3 mixing ratios at the surface, and increases them in the low-mid troposphere. For instance, in September, simulated O_3 mixing ratios in CAMvert are reduced by 40% (~ 25 ppb) at the surface and increased by 10% (~ 5 ppb) at 2 km above the fires. At 6 km, the sensitivity of O_3 to the injection height scheme above the fires is minimal. Also, we observe little change above the fires in March. On a regional scale, the new injection height scheme (CAMvert) decreases the simulated O_3 column (0–8 km) across the source regions i.e., the arc of deforestation (Figure 4.7b) ($\sim 5\%$) in September. O_3 formation is complex and many factors are involved i.e., availability of NO_x , the limiting factor in O_3 production in the Amazon. Moreover, we observe NO_x column reductions across the source regions (by 25%) (not shown) coincident with the O_3 reductions. In addition, reductions in CAMvert O_3 column may be partly caused because injecting biomass burning aerosols at higher altitudes, may decrease ozone formation via photolysis attenuation produced from scattering or absorbing solar radiation by aerosols (Reid et al., 2005, Real et al., 2007).

Evaluation of simulated O_3 with ozonesondes

We use monthly mean profiles from ozonesondes averaged in two regions to evaluate simulated O_3 from CAMvert and CAMsurf at a larger scale. Figure 4.8 shows the simulated and observed O_3 mixing ratios at 800, 600 and 400 hPa (~ 2 , 4 and 7 km) for the Equatorial and African/Atlantic regions. Overall, CAM6-chem captures increasing O_3 mixing ratios with height and represent quite well O_3 spatial and temporal distribution, particularly at 800 and 600 hPa. The simulated O_3 mixing ratios are in the uncertainty limits of the measurements, although we find some bias. CAM6-chem overestimates O_3 in the Equatorial region at 800 hPa (25%) and at 600 hPa ($< 10\%$) during the Amazon burning season, probably caused by poor representation of O_3 precursor emissions by FINN. Over the Atlantic, from July to December, CAM6-chem misses large O_3 mixing ratios ($\sim 35\%$) commonly found every year (Thompson et al., 2001). At 400 hPa, the CAM6-chem simulations show

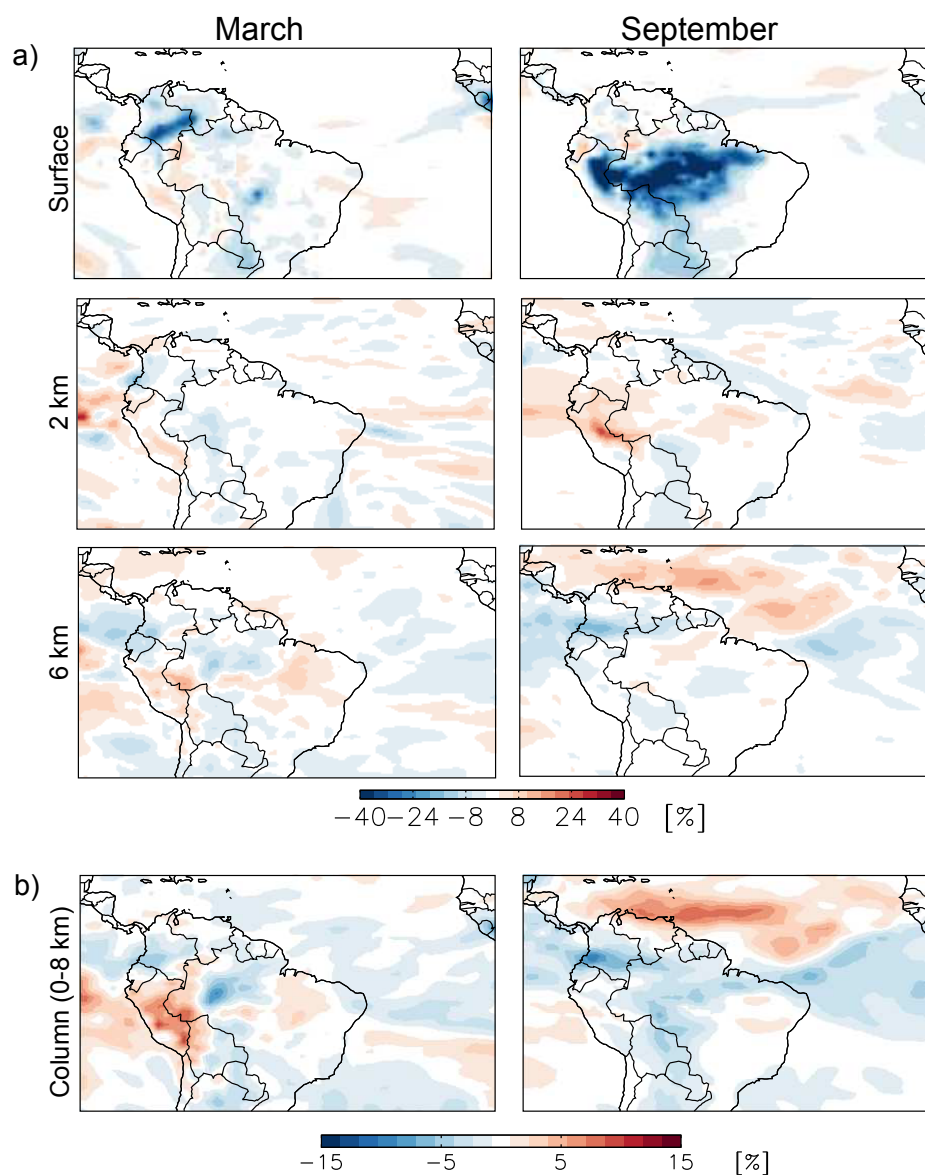


Figure 4.7: i

Relative differences (%) in simulated O_3 mixing ratios between CAMvert and CAMsurf at three different levels: the surface, 2 km and 6 km (a), and the column (0-8 km) (b), for March and September 2012. Absolute mixing ratios (ppb) and column of O_3 (DU) are shown in Figure B6.

a poorer representation of O_3 mixing ratios than at the rest of levels. Previous modelling studies reported a systematic low bias in the SH, particularly in the UT, and argued that it is associated with missing recirculated pollution from southeastern Brazil, biomass burning and/or lightning NO_x production (e.g., Bela et al., 2015,

Young et al., 2018, Ziemke et al., 2009).

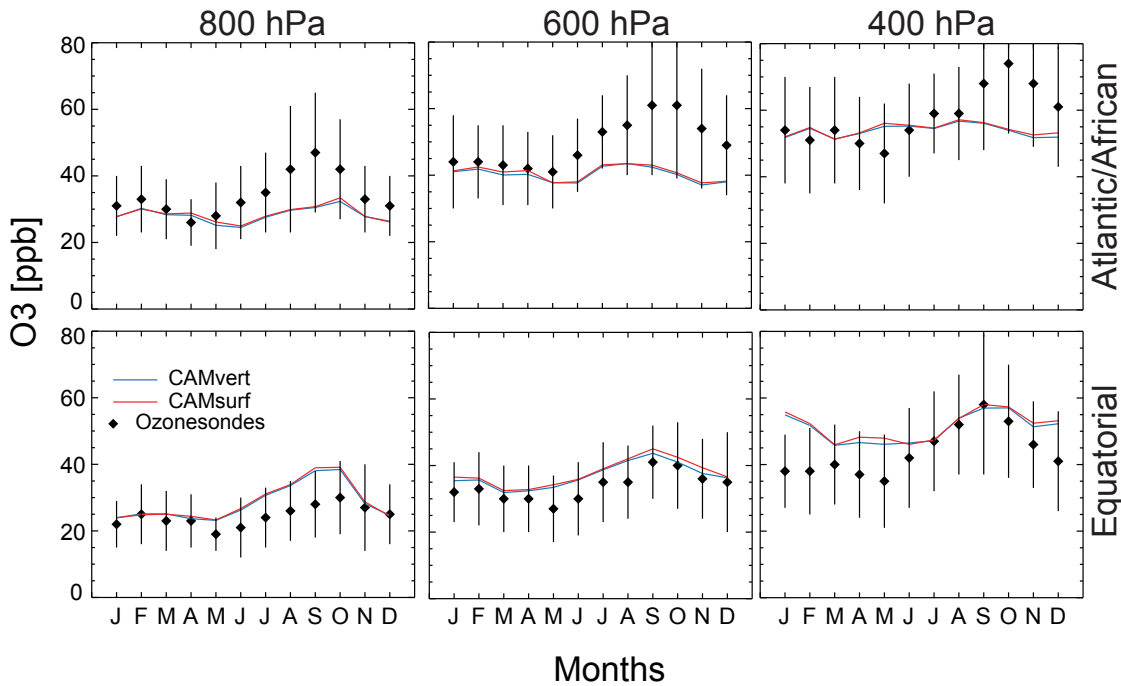


Figure 4.8: Monthly mean O_3 mixing ratios averaged across the Equatorial and Atlantic/African regions at 800, 600 and 400 hPa for ozonesonde observations (black), CAMsurf (red) and CAMvert (blue). Error bars show the standard deviation of the mean.

CAMvert slightly improves O_3 mixing ratios in the Equatorial region, particularly at 600 hPa and during the burning season. Over the Atlantic, CAMsurf gives slightly higher O_3 mixing ratios, and represents somehow better O_3 mixing ratios, where CAM6-chem shows a low bias. As in the evaluation with MOPITT, in Section 4.4.1, we notice small differences in the simulated O_3 mixing ratios between CAMsurf and CAMvert when compared against large-scale measurements with low vertical information. However, at smaller scales, injection heights can considerably impact surface O_3 levels. We investigate this below.

Evaluation of simulated O_3 with surface ozone measurements

We use long-term measurements from ground-based TOAR stations to evaluate CAMvert and CAMsurf performance at representing the spatial and temporal dis-

tribution of surface ozone. Figures 4.9 and B7 show the observed and simulated monthly mean surface O₃ mixing ratios from the TOAR stations, CAMvert, CAMsurf and CAMzerobb. We include CAMzeroBB as a reference to the total impact of biomass burning emissions on surface ozone. Observations of monthly mean surface O₃ range from few ppb to 40 ppb, depending on location and month. During the wet season, TOAR measurements in the Amazon basin (Amazon TT34 and Porto Velho), are lower than 10 ppb, evidencing the low influence of polluted air across the Amazon. However, during the burning season, O₃ mixing ratios at these stations increase up to almost 20 ppb. Surface O₃ levels in central Brazil can be 2–3 times higher than background concentrations during periods of intense burning (Kirchhoff et al., 1989). In general, the CAM6-chem captures well the seasonality of the simulated O₃ monthly means, although with some persistent high bias (6–16 ppb). Similar biases were previously documented across the Amazon (5–15 ppb), especially under clean air conditions, and were suggested to arise for many reasons i.e., model resolution, uncertainties in fire emissions, O₃ dry deposition scheme in the models, excessive sensitivity to NO_x emissions, lightning NO_x production and transport of O₃ and its precursors across the area (Pacífico et al., 2015, Bela et al., 2015).

Differences in the simulated surface O₃ mixing ratios among the three simulations are large at the sites impacted by biomass burning, as it is the case of Amazon TT34 and Porto Velho, from August to November. Therefore, we focus the evaluation at these stations (Figure 4.9). CAMvert reduces surface O₃ mixing ratios compared to CAMsurf. CAMvert reductions range from 1.16% during the wet season, to over 100% in August, with a mean reduction in surface O₃ of around 70% during the burning season (July–November). This is consistent with Section 4.4.2. The Amazon TT34 and Porto Velho stations are located in the arc of deforestation, where we observe the largest impact of the injection heights on surface O₃ in September, with up to 55% of reduction in CAMvert at certain grids (Figure 4.7). CAMvert improves surface O₃ mixing ratios with respect to TOAR measurements across the Amazon during the burning season, particularly at the Amazon TT34 station. At

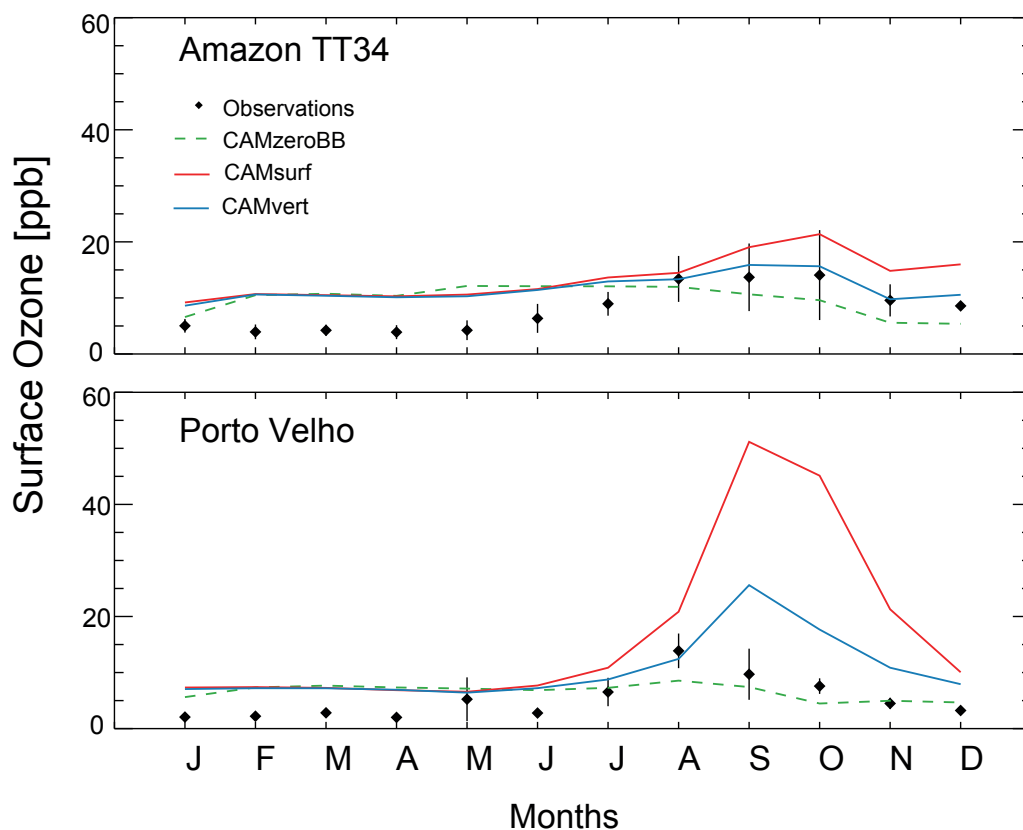


Figure 4.9: Monthly averages of O_3 mixing ratios at the Amazon TT34 and Porto Velho surface sites from TOAR observations (black), CAMvert (blue), CAMsurf (red) and CAMzeroBB (green). Vertical bars indicate the standard deviation of the mean.

Porto Velho, both simulations overestimate surface O_3 , which may be related to the uncertainty in the measurements because of the low availability of data at the site. However, CAMvert still matches significantly better the observations. The evaluation presented here demonstrates the large impact of the improved injection height scheme on surface O_3 when compared at a local scale, important for air quality assessment.

4.5 Large scale impacts of biomass burning on CO and O₃

In this section, we present an analysis of the impact of biomass burning on CO and O₃ with simulations from CAMvert.

4.5.1 Source attribution of CO

We use tags of emitted CO from different sources to quantify the contribution of biomass burning emissions to the total CO in the region and the relative importance of biomass burning compared to other sources. Figure 4.10 presents the monthly relative contributions of the CO tags in 2012 for major emission sources (i.e., anthropogenic, biomass burning, oceans and biogenic), for main biomass burning regions that may directly impact the Amazon (i.e., Amazon, NH Africa, SH Africa, Central America and South America), and for main biomass burning sources within the Amazon (i.e., tropical forest, savanna and other). Firstly, we estimate that primary sources contribute to about 37% of the total CO over the Amazon, and secondary sources, i.e. due to oxidation of biogenic products, contribute to about 67%. This estimate is consistent with previous studies that showed secondary production as the dominant source of CO in the SH (Zeng et al., 2015), mainly due to oxidation of isoprene (Stein et al., 2014), which is a major emission within our domain (Table 4.1).

For primary CO (Figure 4.10a), our analysis shows that anthropogenic emissions are the major source of CO from January to August (44–52%), whereas biomass burning dominates from September to December (48–65%), with its peak in October. On an annual basis, both sources contribute equally to the total CO, with an average of about 42%. Biogenic sources contribute about 8–15% and ocean emissions about 2–3%.

The main source of CO from biomass burning is local fire emissions from Septem-

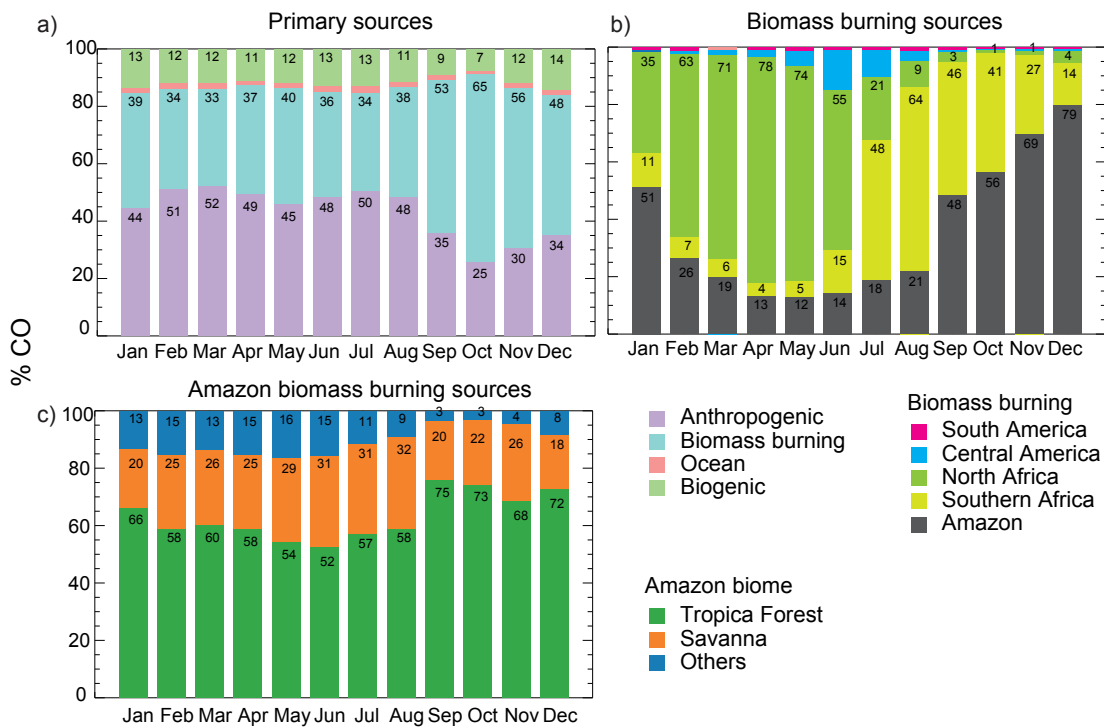


Figure 4.10: Monthly relative contributions to primary CO for major emission sources a), for main biomass burning regions b) and for main biomes in the Amazon c), for 2012.

ber to January (48–79%), whereas contributions from NH African fires are important from February to June (55–78%) and from SH African fires from July to September (46–64%). Central and South American fires have little influence (<15%) on the total CO from fires across our region. Overall, we find that contribution from African fires (24 and 35%) can be as significant as Amazonian fires (36%) in our domain. Biomass burning emissions in Africa are responsible for half of the global carbon emissions (Van der Werf et al., 2010) and long-range transport from biomass burning in Africa has been shown to have a strong influence over South America (Edwards et al., 2006). We also find some interannual variability in the relative contributions from the different biomass burning regions (not shown). For example, SH fires contributed slightly more to the total CO in September–October 2011 (51–64%) than in 2012 (41–46%).

With respect to the domestic biomass burning sources, our analysis shows that tropical forest fires in the Amazon represents the largest source (52–75%) of the

total Amazonian biomass burning CO, followed by savanna fires (18–32%) and other fires, such as grassland and cropland (3–16%) (Figure 4.10c). As in the case of biomass burning CO from fire regions, we also find some interannual variability in the relative contribution from a specific biome (not shown). For instance, tropical forest fires in November contributed more to the total biomass burning CO in 2011 (72%) than in 2012 (68%). As mentioned previously, fire emissions in the Amazon are highly variable (Van der Werf et al., 2010), and specific weather conditions in a year i.e., spatial changes in drought location, can affect the type of biome burning (Gonzalez-Alonso et al., 2019) and hence, its relative contribution to total CO.

4.5.2 Contribution of biomass burning in the Amazon to CO and O₃

We compare CAMvert and CAMzeroBB simulations to assess the impact of Amazonian biomass burning on CO and O₃ across the Amazon domain. Figure 4.11 presents the relative difference in the simulated CO and O₃ column (0–8 km) in CAMvert for September 2012, and Figure B8 for March. Biomass burning in the Amazon contributes an average of 1% and 1.5% (March), and 8.5% and 5% (September) to the CO and O₃ background throughout most of the troposphere. However, similar to previous studies (Ziemke et al., 2009), locally, contributions can be larger. For instance, in September biomass burning in the Amazon contributed up to 58% and 30% (17×10^{17} molec/cm² of CO and 9.2 DU of O₃), respectively to CO and O₃ columns. Largest impacts are located where most CO and O₃ precursors are produced and transported downwind, across the arc of deforestation, along the Andes and towards the Pacific, in September. In addition, both simulations capture high tropospheric O₃ levels in the tropical south Atlantic, particularly in September (~30 DU). These are likely lower limit levels if we consider the low bias across the Atlantic mentioned in Section 4.4.2. High tropospheric O₃ levels have been previously reported over the South Atlantic during the burning season (Fishman et al.,

1996b, Edwards et al., 2003), but there is lack of consensus about its origin, i.e., biomass burning from the Amazon and Africa or lightning (e.g., Mauzerall et al., 1998, Thompson et al., 1996, Moxim and Levy, 2000, Sauvage et al., 2007, Ziemke et al., 2009). Our results show no contribution from Amazonian biomass burning to the high tropospheric O₃ levels over the South Atlantic in September.

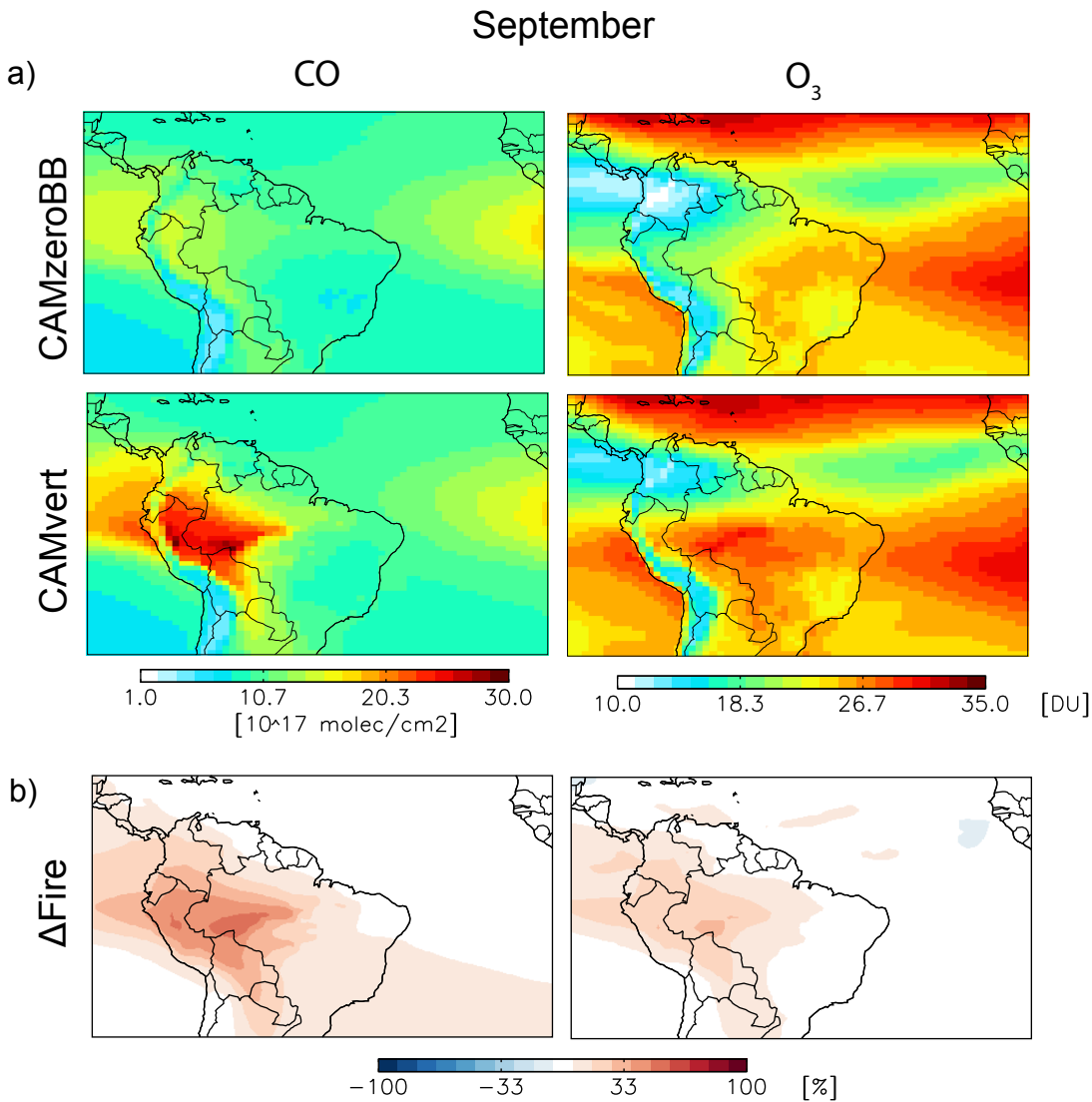


Figure 4.11: Simulated averaged CO and O₃ columns by CAMvert and CAMzeroBB (a) and relative changes (in %; (Δ Fire) between CAMvert and CAMzeroBB (b), in September 2012.

4.6 Impact of biomass burning in the Amazon on surface O₃ and air quality O₃ standards

Consistent with previous studies (Kirchhoff et al., 1992, Galanter et al., 2000), Amazonian fires contribute to increasing surface O₃ mixing ratios at the source regions, up to 34% (6 ppb), in March and up to 87.5% (31 ppb), in September. Here, we characterise the impact of biomass burning in the Amazon on surface ozone levels that can be harmful to human health and vegetation. To quantify the impact, we use CAMvert and CAMzeroBB simulated hourly surface ozone mixing ratios and calculate metrics commonly used for human health, i.e., MDA8, and vegetation protection, i.e. M12 and AOT40, and compare them.

The maximum daily 8 h average ozone concentration (MDA8) is the metric most commonly used in many world regions for regulatory purposes concerning human health protection (e.g., Pfister et al., 2008, Reidmiller et al., 2009, Fleming et al., 2018). AOT40 is the sum of the difference between the hourly mean ozone value and values above 40 ppb for all daylight hours, considered here as from 0800 to 1959 hours (LT), over a specified period, usually the growing season (Mills et al., 2007). The daily 12-h (0800–1959 h) mean ozone exposure metric, M12 (e.g., Van Dingenen et al., 2009a, Avnery et al., 2011, Hollaway et al., 2012) has been widely used to characterize crop exposures to establish crop-specific exposure–response relationships. Figure 4.12 presents simulated CAMvert MDA8, M12 and AOT40, and fire-induced changes (Δ Fire) i.e., difference with respect to CAMzeroBB during the burning season of 2012. CAMvert mean \pm standard deviation and maximum MDA8, M12 and AOT40 are 27.7 ± 6.99 ppb, 25.5 ± 6.63 ppb and 731 ± 1820 ppb h, and 53 ppb, 45 ppb and 15000 ppb h, respectively. Biomass burning in the Amazon contributes substantially to enhance these metrics. We observe maximum enhancements of 25 ppb, 20 ppb and 12000 ppb h, respectively for MDA8, M12 and AOT40, across the arc of deforestation, the Peruvian coast and Bolivia.

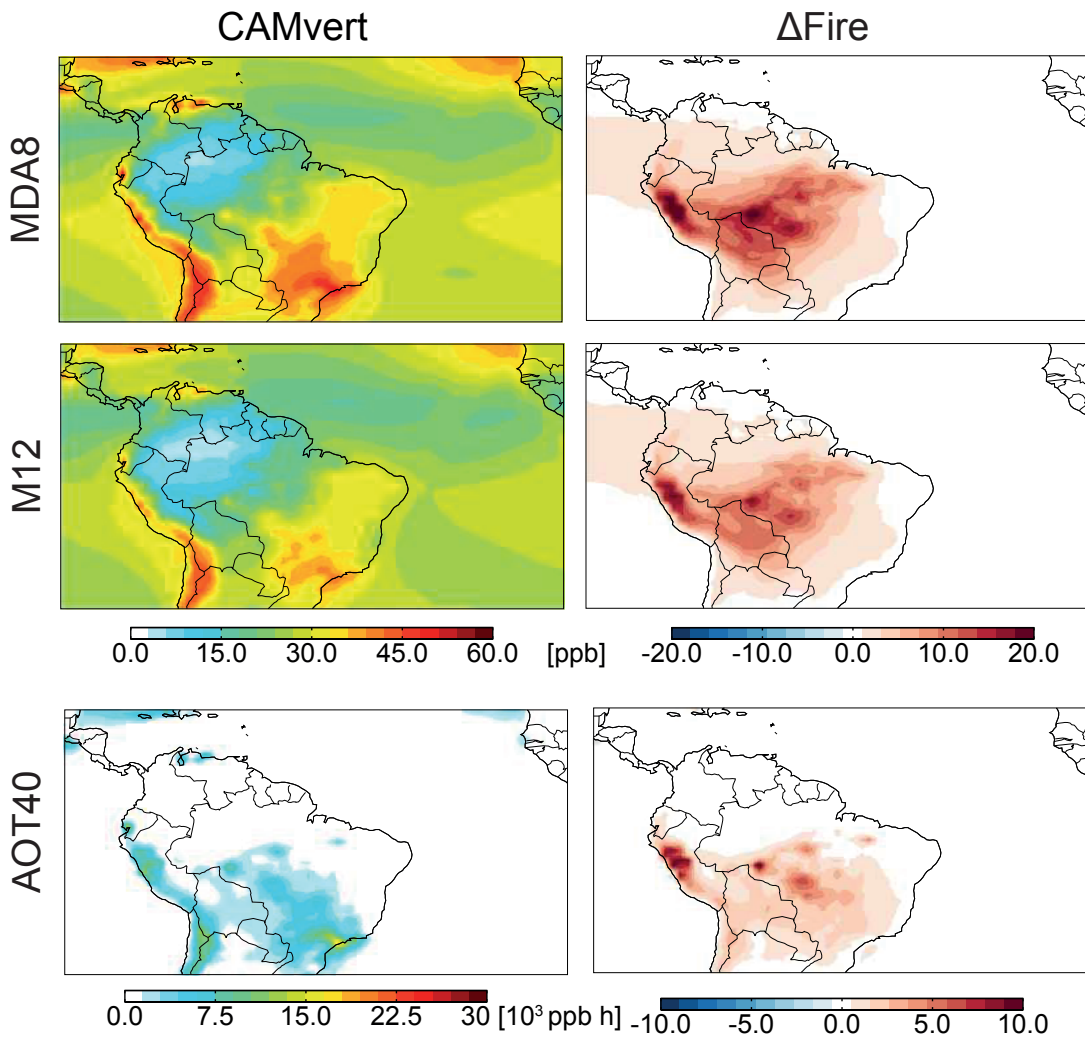


Figure 4.12: CAMvert simulated maximum daily 8 hour average (MDA8), daily 12-h (0800–1959 h) mean (M12) and sum of the difference between the hourly mean ozone (0800–1959 h) and values above 40 ppb (AOT40), and fire-induced changes (Δ Fire, i.e., CAMvert-CAMzeroBB), during the 2012 burning season (July–November).

Impacts of fire-induced ozone on human health

Ozone standards for human health protection are variable across the globe. According to Fleming et al. (2018), MDA8 standards across the Amazon region range from 40–80 ppb. We set the MDA8 standard to 50 ppb in the domain and apply a limit of maximum 25 days of exceedance in a year. Figure 4.12 shows that the estimated MDA8 standard is exceeded across some regions in the SE Brazil and along the Pacific coast, during the biomass burning of 2012. However, some of these exceedances are likely to be produced by anthropogenic sources rather than biomass burning. We present in Figure 4.13 the estimated number of days with fire-induced exceedances of MDA8 O₃ during 2012. We observe that the fire-induced estimated MDA8 exceeds the standard in more than 25 days across regions where some of the most populated cities are located.

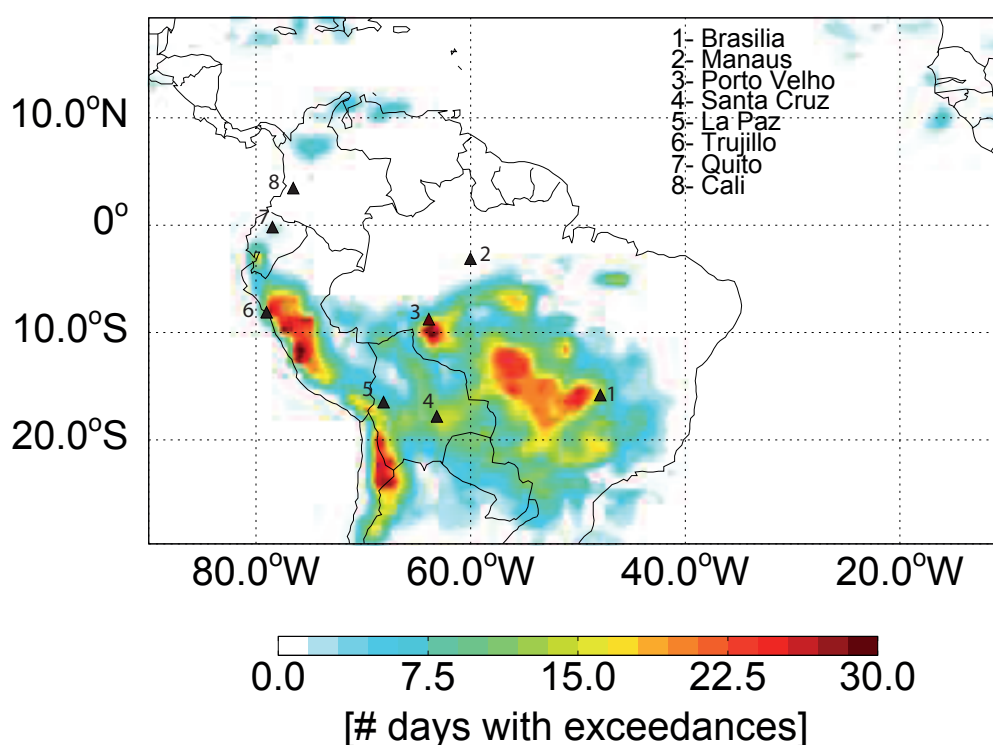


Figure 4.13: Number of days in which MDA8 O₃ was exceeded due to fire pollution (see text for more explanation). Main populated cities close to or within the exceedances regions are also represented.

Figure 4.14 depicts the cumulative probability distributions of the estimated O_3 MDA8 during the burning season of 2012, over some populated cities within or close to fire-induced O_3 impacted regions. We also include estimated O_3 MDA8 from CAMsurf to show the impact of the injection height scheme for air quality purposes. Over most of these cities, we find a decline in air quality due to Amazonian fires, for most polluted days during the biomass burning season, with MDA8 values above 50 ppb. Furthermore, the estimated fire-induced impact is significantly reduced when the improved injection height scheme is applied (CAMvert), which highlights the necessity of an enhanced vertical distribution of biomass burning emissions in air quality studies. Previous studies showed that biomass burning is responsible for thousands of people's premature death across the world due to unhealthy air quality conditions (Jacobson, 2014). Furthermore, Reddington et al. (2015) estimated that aerosols from biomass burning in the Amazon can cause thousands of premature deaths. Here, we show that biomass burning in the Amazon contributes to increasing O_3 levels above the standards safe for human health, with the potential to affect more than 14 million people's health across the Amazon.

Impacts of fire-induced ozone on vegetation

Figure 4.12 shows that biomass burning is responsible for substantial enhancements in M12 and AOT40 during the biomass burning season of 2012. To establish vegetation-specific fire-induced impact that can be related to a reduction in production across the Amazon (Van Dingenen et al., 2009a, Mills et al., 2018), we calculate M12 and AOT40 for each crop-specific growing season or vegetation-specific period of maximum sensitivity. We focus on major crops for food security (i.e., wheat, rice), commercial crops which contribute significantly to the economy (i.e., soybean, sugarcane, cotton, coffee, tobacco, cocoa, banana and quinoa), and the tropical forest. First, we characterise the areas of fire-induced damage for each type of vegetation. We use datasets of crop harvested area and yield from 2000, on a 5 min by 5 min latitude and longitude grid (Monfreda et al., 2008). This dataset

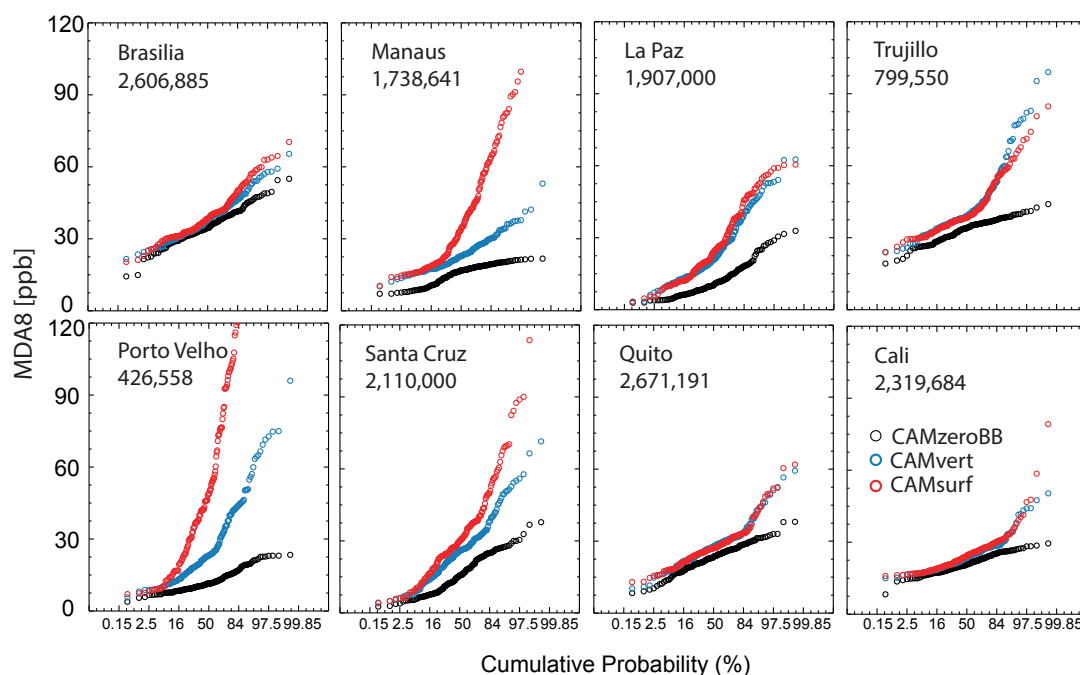


Figure 4.14: Cumulative probability distributions of simulated surface O₃ MDA8 at the cities close or within regions with the highest number of days exceedances for CAMvert (blue), CAMsurf (red) and CAMzeroBB (black). City and population are shown in the insert.

comprises 175 distinct crops across the world, including our selection of crops. It should be noted that agriculture has largely changed (e.g. spatial extent) between the year of the Monfreda et al. (2008) dataset and the year under consideration. In the case of tropical forest, we use MODIS MCD12C1 Land Cover product (Friedl et al., 2010). We set the accumulation period of maximum sensitivity to ozone for each crop, i.e., the start and duration of the growing season. This is complex to determine as it depends on many factors, i.e. precipitation and temperature, which can be highly variable for a specific year or region. We extracted these data from crop calendars for South America, created by the United States Department of Agriculture USDA (USDA, 2019) and the Food and Agriculture Organization FAO (FAO, 2019), and crop-specific information¹. However, for some crops, these

¹<https://www.fundesyam.info/biblioteca.php?id=4426>; <http://www.coffeeresearch.org/agriculture/environment.htm>; <http://www.agro20.com/>; <https://www.zipmec.com/en/south-america-season-for-fruits-and-vegetables.html>; <https://www.icco.org/faq/58-cocoa-harvesting/131-what-time-of-year-is-cocoa-harvested.html>; <http://www.soybeansandcorn.com/Brazil-Crop-Cycles>; <https://www.thebalance.com/>

data are missing or given as national-level averages in graphical format. Therefore, we assume the specific-crop growing season for the main productive country and applied it to the harvested area within the domain. This assumption can be a source of bias, but in general, countries where the same crops grow are usually close in distance and tend to have similar ambient conditions, and thus growing season period. In reality, planting dates vary within each region and crop and, during the last years, production of many crops has increased due to double-cropping (Brazilian National Supply Agency, [CONAB](#)), which adds more complexity to determine each crop growing season. For tropical forest, we set the accumulation period during the biomass burning season.

Table 4.2 summarises the estimated CAMvert and CAMzeroBB M12 and AOT40 statistics for our selection of vegetation and crops, and Figure 4.15 shows the estimated fire-induced M12 and AOT40 for vegetation with a potential risk of yield loss. We observe that quinoa, tobacco, wheat and the tropical forest are highly sensitive to fire-induced O_3 , with maximum enhancements of the AOT40 of 9930 ppb h for quinoa and tobacco, 9510 ppb h for wheat and 12400 ppb h for the tropical forest. These enhancements are above the vegetation-based critical levels of 3000 ppb h during 3 months for wheat, and 5000 ppb h during 6 months for quinoa, tobacco and tropical forest, and can lead to production losses of 5–10% ([Mills et al., 2018](#)). Consistent with [Pacífico et al. \(2015\)](#), we find that the Amazonian forest productivity can be reduced by 5–10%, as the enhancement on AOT40 is more than double the critical level known to produce 5% loss. The growing season established for wheat, tobacco and quinoa are coincident with the biomass burning season. These crops are also produced across areas of Peru, Bolivia, Southern Brazil, where a large impact of fires on AOT40 and M12 is observed (Figure 4.12). Our results suggest that any crops with a growing season coincident with the biomass burning season and spatially distributed across these regions may be susceptible to yield loss due to high fire-induced O_3 from biomass burning in the Amazon. Furthermore, we

corn-planting-and-harvest-seasons-809309; <http://esmiperu.blogspot.com/2007/08/principales-cultivos-agricolas-del-per.html>; last access 14/02/2019

Table 4.2: Vegetation-specific statistical summary of CAMzeroBB (no fire) and CAMvert (fire) estimated O_3 AOT40 and M12. O_3 sensitive vegetation with a potential risk of yield loss across the Amazon are bolded.

Crop	Growing season	AOT40						M12					
		No Fire			Fire			No Fire			Fire		
		Mean±SD	Maximum	Minimum	Mean±SD	Maximum	Minimum	Mean±SD	Maximum	Minimum	Mean±SD	Maximum	Minimum
Banana	Apr-Sep	1030±1450	9410	1640±1610	10100	23.50±8.09	39.0	25.40±7.14	38.9	19.40±9.70	43.2	20.30±9.31	43.0
Cocoa	Nov-Apr	1170±1840	9580	993±1730	9740	21.60±9.43	42.7	22.90±8.78	42.6	16.70±9.91	42.2	23.80±9.06	43.7
Coffee	Oct-Apr	1570±2680	25400	1440±2510	25500	22.10±8.94	43.2	22.80±8.53	43.0	22.40±9.22	42.2	25.40±7.85	43.7
Quinoa	May-Oct	1340±2690	15600	3170±3040	18500	23.80±7.98	44.2	24.30±7.66	44.5	22.10±8.94	43.2	22.80±8.53	43.0
Sugarcane	Nov-Apr	1320±2330	19400	1200±2200	19000	22.10±8.94	43.2	22.80±8.53	43.0	22.40±9.22	42.2	25.40±7.85	43.7
Tobacco	May-Oct	1340±2100	15600	2250±2620	18500	23.80±7.98	44.2	24.30±7.66	44.5	22.40±9.22	42.2	25.40±7.85	43.7
Cotton	Dec-Feb	484±988	10100	465±963	9880	22.10±8.64	44.5	22.70±8.32	44.5	23.80±7.98	44.2	24.30±7.66	44.5
Maize	Dec-feb	604±1300	10100	554±1230	9880	22.10±8.64	44.5	22.70±8.32	44.5	22.10±8.64	44.5	22.70±8.32	44.5
Rice	Dec-Feb	680±1390	10100	614±1310	9880	21.90±8.87	44.5	22.50±8.54	44.5	21.90±8.87	44.5	22.50±8.54	44.5
Soybean	Jan-Apr	911±1350	12800	899±1360	12800	23.10±8.25	40.7	23.50±8.07	40.8	23.10±8.25	40.7	23.50±8.07	40.8
Wheat	Jul-Sep	1090±1240	10400	2220±2060	13700	25.10±9.56	45.6	29.70±8.26	49.1	25.10±9.56	45.6	29.70±8.26	49.1
Forest	Jul-Nov	751±1540	11400	1480±1850	12400	11.70±7.66	38.9	16.90±7.96	39.0	11.70±7.66	38.9	16.90±7.96	39.0

attempt to estimate the relative yield loss (RYL) for wheat caused by fire-induced O_3 . We use Mills et al. (2007) concentration-response function and find a RYL of 5–23% for wheat, where regional fires may be responsible for 2–5% of the RYL. Most of the critical levels established by regulations are based on exposure-response studies for vegetation types and climate zones in the NH, mainly USA and Europe (Mills et al., 2007, 2018). Therefore, our results must be taken with caution. O_3 exposure-response functions specific to crops in the SH are necessary to allow for improved estimations on the O_3 impact and promote less sensitive O_3 crops across areas with a potential risk of exceedances of O_3 critical levels. We find that biomass burning in the Amazon can negatively impact the local economy through crops yield losses, which could be enhanced if fires increase, according to future projections.

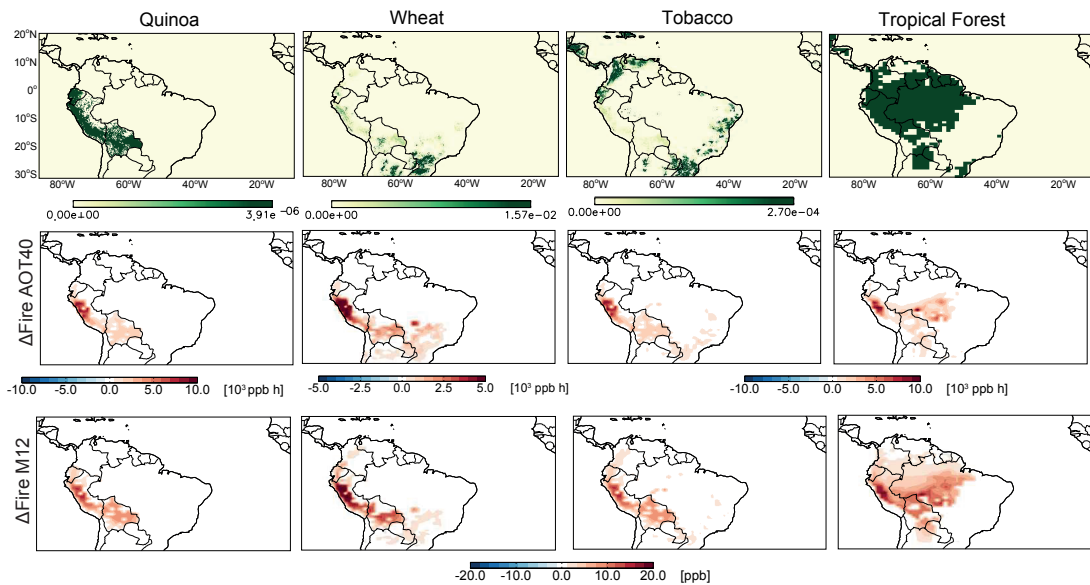


Figure 4.15: Distribution of the tropical forest and fraction of harvested area for quinoa, wheat and tobacco in the Amazon domain (top) and simulated fire-induced surface O_3 AOT40 and M12 for quinoa, wheat, tobacco and tropical forest (bottom).

4.7 Conclusions

We implement a global smoke plume injection height parametrisation in CESM, that includes smoke plumes observed in the Amazon, to assess the performance on

the vertical distribution of CO and O₃ across the Amazon. We conduct two multi-year simulations: with emissions released at the surface and vertically distributed following the injection height scheme. Results from the simulations are compared with CO and O₃ observations from satellite, aircraft, ozonesondes, and ground-based measurements. Similar to previous studies ([Jian and Fu, 2014](#), [Zhu et al., 2018](#)), the injection height scheme reduces CO and O₃ mixing ratios at the surface (70% and 40%), and enhances them in the free troposphere (30% and 10%) above the fires, especially during the peak of the burning season. On a regional scale, the injection height scheme produces overall CO column enhancement across downwind regions (5–10%) and reduction across the source regions (10–15%), which is consistent with the effect of injecting emissions at higher altitudes and the longer lifetime of CO in the FT, as argued previously ([Chen et al., 2009](#)). In the case of O₃, an overall reduction in O₃ column is observed across the source regions (~5%), coincident with NO_x column reduction, the main limiting factor in O₃ production in the Amazon. The injection height scheme leads to improvements in the representation of CO and O₃ in the model, particularly near the source, with important regional air quality implications. However, we find some discrepancies with observations probably due to poor representation of biomass burning emissions and atmospheric processes in the model, which results in an excess of pollutants in the LT, mainly across the arc of deforestation and along the Andes.

We assess the relative importance of biomass burning in the Amazon with respect to other sources during 2012. As previously reported ([Zeng et al., 2015](#)), most of the CO in the Amazon is produced by oxidation of biogenic products (63%), given the relatively low anthropogenic emissions and the dominance of biogenic emissions. Biomass burning is the main source of directly emitted CO, from September to December (48–53%), comparable to anthropogenic emissions (43%) on an annual basis. Fires in the Amazon are the main source of CO from biomass burning from September to January (48–79%), although annually, long-range transport of plumes from Africa contributes significantly to fire CO (24–35%), as previously found ([Ed-](#)

wards et al., 2006). Furthermore, most of the CO emissions from fires in the Amazon come from the tropical forest (52–75%) compared to other biomes. However, the contribution from biomass burning over a particular region or biome may change, as many factors are involved i.e., meteorological conditions or governmental policies (e.g., Reddington et al., 2015, Gonzalez-Alonso et al., 2019).

We conduct an additional simulation with fire emissions in the Amazon set to zero to assess the impact of domestic biomass burning on CO and O₃ during 2012. Consistent with previous studies (Galanter et al., 2000, Ziemke et al., 2009), biomass burning in the Amazon contributes significantly to enhancements of background CO (58%) and O₃ (30%) at the source regions. However, mean enhancements of CO are relatively small (8% in September) considering the large contribution from secondary production mentioned above. Fires in the Amazon are also responsible for important enhancements in surface O₃ (30 ppb) across the source and downwind regions, i.e., the arc of deforestation, along the Andes and towards the Pacific. We estimate the fire-induced O₃ impact on air quality with common metrics i.e., MDA8, M12 and AOT40. We find frequent exceedances of the O₃ standard for human health protection during 2012 and a decline in air quality over some of the most populated cities (1–2 million people) during the burning season. In addition, we find that fire-induced O₃ can lead to an estimated relative wheat yield loss of 2–5% and 5–10% of reduction in forest productivity, consistent with previous studies across the region (Pacífico et al., 2015). Moreover, any vegetation grown across the areas of major impact with a growing season coincident with the burning season may be at risk of production loss due to O₃ produced from biomass burning in the Amazon. Future projections suggest an increase in fires caused by climate change and anthropogenic activities, which may lead to higher ozone levels and degraded air quality across the region.

The results presented here show that biomass burning in the Amazon can considerably reduce O₃ air quality across the region, with negative consequences for health, ecosystems and local economy. Furthermore, we demonstrate the import-

ance of an improved representation of the vertical distribution of biomass burning in models for future air quality studies. Ultimately, the outcomes of this study can help to efficiently manage air quality across the region and promote policies to limit fire burns.

Chapter 5

Summary and Conclusions

This work produced several major results. First, it characterised the vertical distribution of smoke plume heights from satellite observations across the Amazon and determined the main drivers that govern smoke plume dynamics across the region. Then, it demonstrated an improved representation of biomass burning products across the Amazon via implementation of a smoke injection height parametrisation in an Earth system model. Finally, it revealed that biomass burning in the Amazon substantially impacted surface ozone levels and degraded air quality across the region, with important risk for vegetation and population's health. The main conclusions of this work are presented below in more detail, followed by a general summary and recommendations for future research.

5.1 Vertical distribution of biomass burning emissions over the Amazon

Observations from MISR and MODIS (2005–2012) and CALIOP (2006–2012), allowed to derive an extensive climatology of smoke plumes across the Amazon, during the biomass burning season (July–November).

The 8-year climatology showed larger number of smoke plumes during years with drought conditions, at the peak of the burning season (September), and over savanna and tropical forest, the dominant biomes in the region. The analysis on the vertical distribution of biomass burning emissions revealed that smoke plume heights exhibited large variability, from few hundred meters to 6 km, although most of the smoke was located below 2.5 km. In addition, smoke plume heights tended to be higher later in the afternoon, at CALIOP overpass, as a result of deeper PBL heights, possibly more energetic fires and CALIOP's greater sensitivity to very thin aerosol layers.

Finally, the Amazon climatology of smoke plumes demonstrated the value of combining observations from both instruments to constrain the vertical distribution of smoke from biomass burning over the Amazon.

5.2 Factors of variability on the vertical distribution of biomass burning over the Amazon

The 8-year climatology of smoke plumes across the Amazon combined with an extensive analysis on the main factors that drive smoke plume dynamics showed that smoke plume heights tended to be higher over biomes with dominant flaming combustion (i.e., grassland) compared to smouldering dominant biomes (i.e. tropical forest). Furthermore, a marked seasonal cycle on the smoke plume heights was noticed, where larger fire radiative power from the fire and more stable atmospheric conditions during the late burning season, increased the probability of fires to inject smoke in the FT, from 2–10%, in July to 15–40%, in November.

In addition, drought conditions increased fire activity and contributed significantly to the total aerosol loading across the region. Droughts were shown to favour understory fires and deeper PBL, where dominant smouldering combustion associ-

ated with low smoke injection heights, resulted in high smoke loading throughout the PBL, with important implications for regional air quality.

This work highlighted the importance of biome type, fire properties, atmospheric and, particularly drought conditions for plume dynamics and smoke loading in the Amazon.

5.3 Impacts of Amazonian biomass burning on surface ozone levels across the Amazon

The modelling experiments using the Community Earth System Model (CESM) with an updated smoke injection height scheme improved the representation of O₃ and CO in the model. The injection height scheme reduced O₃ and CO mixing ratios at the surface (40% and 70%) and enhanced them in the low-mid troposphere (10% and 30%) above the fires, which led to a better agreement with observations, particularly close to the source regions.

An analysis on the relative contribution from biomass burning to the total simulated CO across the Amazon domain during 2012 indicated that biomass burning was the main source of directly emitted CO from September to December, comparable to the contribution from anthropogenic sources on an annual basis. Furthermore, fires in the Amazon were the largest contributor to the total fire CO (36%) in 2012, although significant contribution from long-range transported plumes from Africa was evident (24–35%). Overall absolute contributions from biomass burning in the Amazon to total CO were considerably small (up to 8% in September) in the domain, where most of the CO was produced by oxidation of biogenic products (63%).

Results from the simulation showed that biomass burning in the Amazon was responsible for significant enhancements of surface ozone (30 ppb) in the peak burning season across the arc of deforestation, along the Andes and towards the Pacific, which could lead to unhealthy conditions. Particularly throughout 2012, estimated

fire-induced O_3 produced frequent exceedances of the target value for the protection of human health (50 ppb) and induced a decline in air quality across some largely populated cities during the burning season. In addition, fire-induced ozone levels could also produce considerable damages in vegetation across areas of Peru, Bolivia and central and southern Brazil during the burning season. Furthermore, fire-induced ozone levels led to an estimated relative wheat yield loss of 2–5%, with implications for the local economy, and reductions in the tropical forest productivity of 5–10%.

This work provided important insights on the necessity of accurately represent the vertical distribution of biomass burning emissions for air quality studies and the impacts of biomass burning emissions in the Amazon on air quality.

5.4 Summary of conclusions and future research

The evidence presented in this work benefits future assessment on the impact of biomass burning emissions in the Amazon on air quality and climate. This work results in an improvement of the understanding of the vertical distribution of biomass burning pollution across the Amazon and the main factors of variability in plume dynamics. This information is crucial to predict and mitigate the impacts of biomass burning. In addition, this work provides evidence of the impacts of Amazonian biomass burning on surface O_3 levels during the burning season and the benefit of using an improved injection height scheme for air quality studies. The results and analysis exhibited in this work motivate further investigation. Some opportunities for future research are presented below.

First, the climatology of smoke plume heights across the Amazon established a relationship between smoke plume heights, smoke loading and drought conditions. In view of more frequent droughts expected in the near future, an extended analysis of smoke plumes including 2015, associated to severe drought conditions induced by el Niño, is recommended to establish trends on plume dynamics across the region

and understand the impact of increased frequency of droughts.

Results from the simulation experiments evidenced an excess of biomass burning pollution within the boundary layer across the Amazon. To understand the role of an overestimation of biomass burning emissions or a poor representation of atmospheric processes in the model i.e., convection, a simulation with different biomass burning emission inventories, such as GFED, will help shed light on this discrepancy.

Appendix A

Supplementary information

This document includes supplementary tables, figures and results used for the analysis discussed in Chapter 3 of this work.

Table A1: Statistical summary for main smoke plume and plume rise controlling parameters^a.

	Tropical Forest				Savanna				Grassland			
	Dry Years ^b		Wet Years ^b		Dry Years		Wet Years		Dry Years		Wet Years	
	Early ^c	Late ^c	Early	Late	Early	Late	Early	Late	Early	Late	Early	Late
Smoke Height (m)	698 ± 407	898 ± 451	906 ± 418	1180 ± 693	795 ± 462	1110 ± 589	984 ± 473	1250 ± 653	881 ± 508	1160 ± 474	1280 ± 971	1350 ± 728
FRP (MW)	182 ± 408	245 ± 613	369 ± 813	369 ± 813	352 ± 744	503 ± 828	269 ± 456	330 ± 537	390 ± 480	567 ± 838	148 ± 152	529 ± 654
AOD (unitless)	0.53 ± 0.29	0.73 ± 0.37	0.21 ± 0.17	0.33 ± 0.21	0.37 ± 0.30	0.46 ± 0.32	0.14 ± 0.12	0.28 ± 0.18	0.29 ± 0.26	0.38 ± 0.35	0.1 ± 0.07	0.30 ± 0.15
Stability (K/km)	5.27 ± 3.64	4.28 ± 2.82	3.93 ± 2.17	3.11 ± 1.76	4.17 ± 3.72	2.92 ± 2.95	3.44 ± 3.24	2.47 ± 2.26	2.45 ± 3.07	2.32 ± 1.92	3.15 ± 3.65	2.07 ± 1.53
PBL Height (m)	1330 ± 535	1290 ± 551	1150 ± 487	1220 ± 486	1580 ± 509	1510 ± 482	1350 ± 522	1480 ± 543	1760 ± 525	1770 ± 534	1360 ± 443	1380 ± 316
Number	536	438	238	271	434	575	353	516	51	43	17	38

^aReported the average ± SD for smoke plumes with valid values for all the parameters

^bDry years are 2005, 2007 and 2010 and wet years are 2006, 2008, 2009, 2011 and 2012

^cEarly season is defined as July–August and late season as September–November

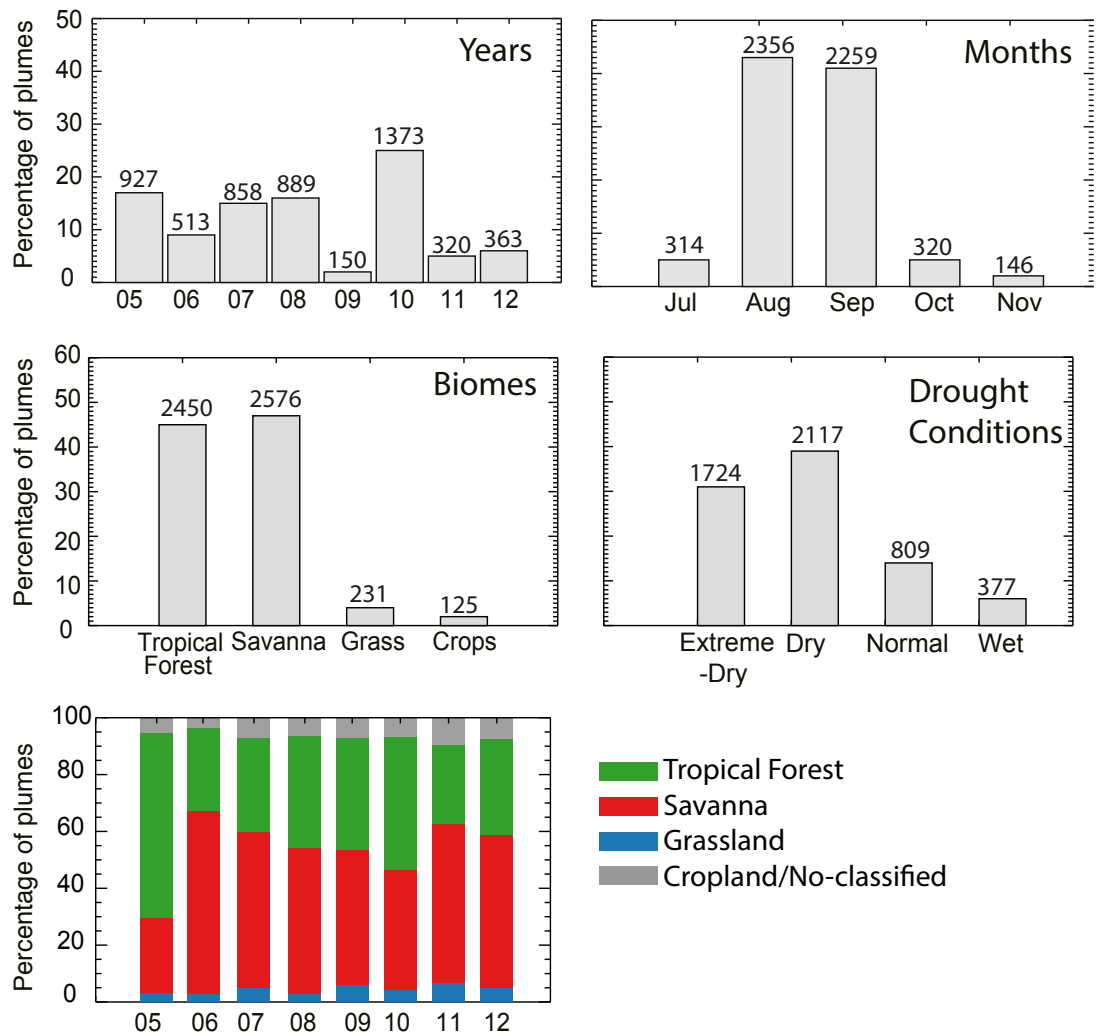


Figure A1: Percentage of MISR plumes in the climatology classified by year, month, biome and drought conditions. Absolute values in each distribution are included above the bars. Percentage of MISR plumes classified by biome and year are also shown, as tropical forest (green), savanna (red), grassland (blue), and cropland and not classified (grey).

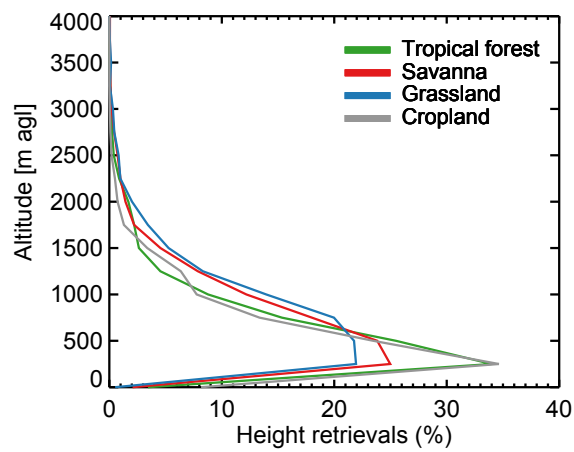


Figure A2: Vertical distribution of individual MISR stereo-height retrievals, averaged over all plumes in the eight-year of the study and stratified by biome.

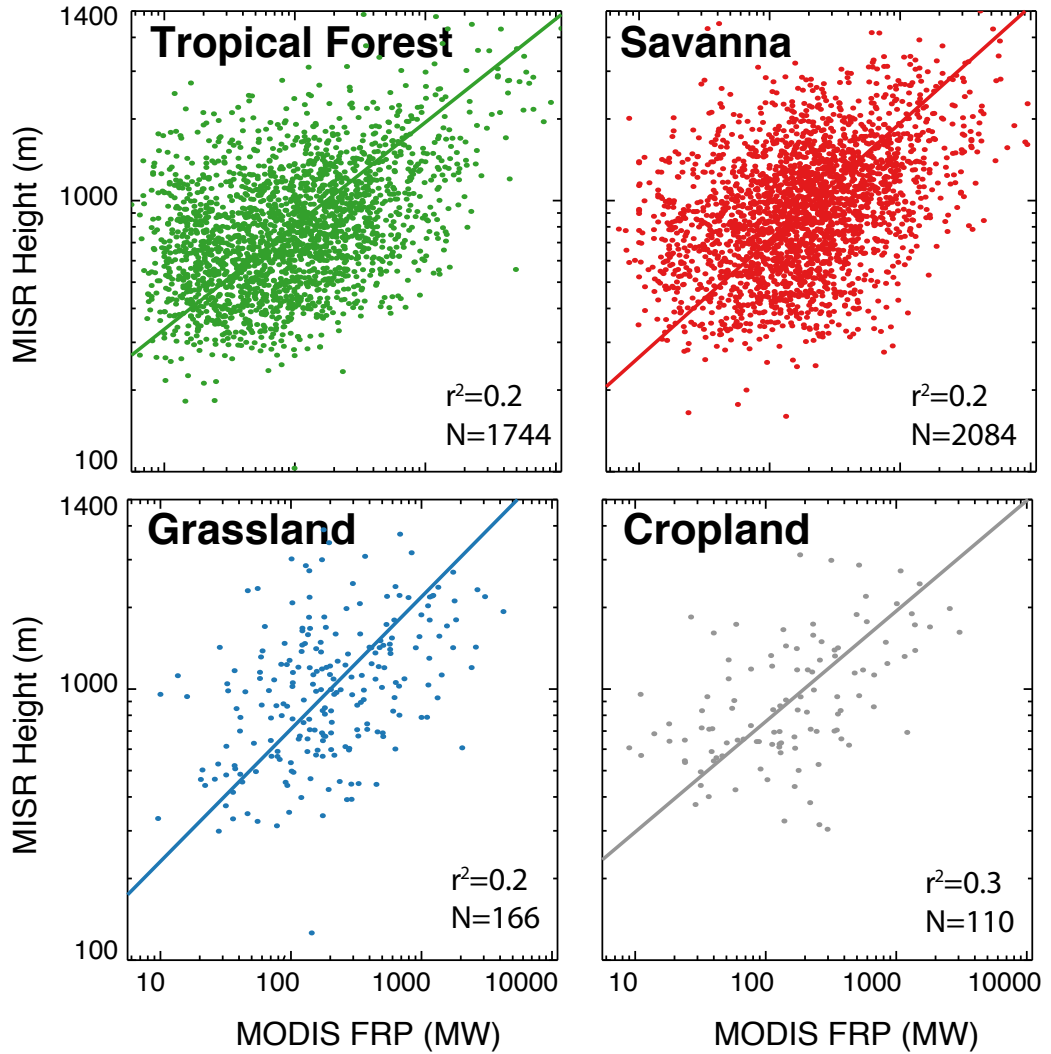


Figure A3: Relationship between MISR maximum plume heights and MODIS total fire radiative power (FRP) for the 8-year data set. Data are colour-coded per biome as tropical forest (green), savanna (red), grassland (blue), and cropland (grey). Total number of observations and r^2 are given in the annotation of each panel.

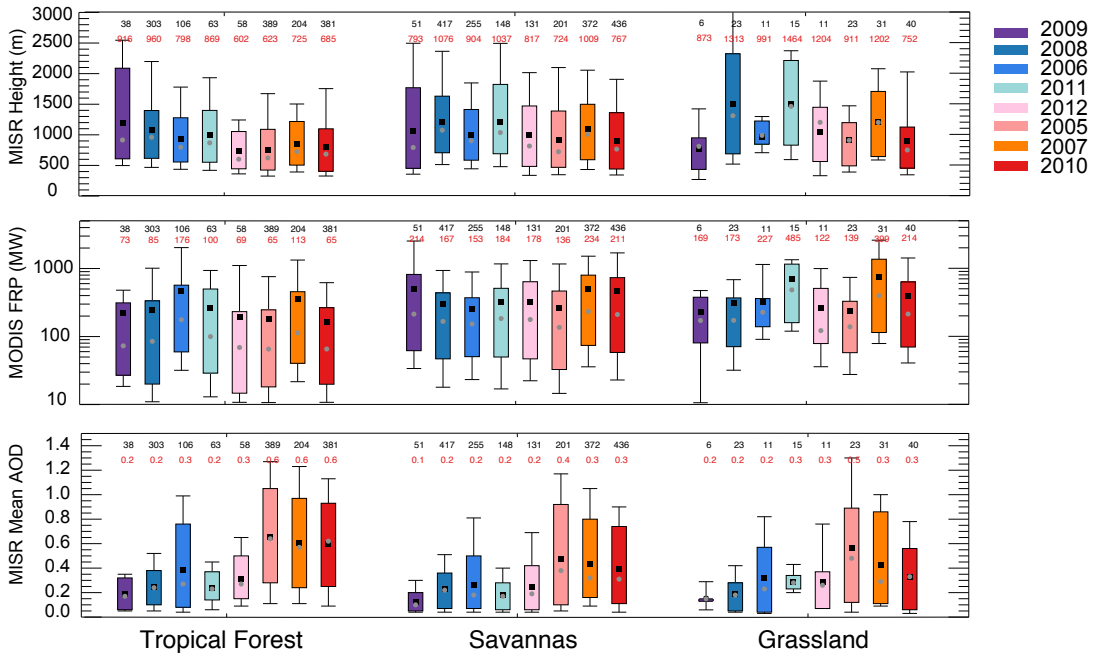


Figure A4: Interannual variability of MISR plume maximum heights above the terrain, MODIS FRP and MISR AOD by biome. Bar plots indicate the distribution of the data for each year. Bars in this figure are ordered based on DSI (Table 3) rather than chronologically. The medians (grey circles) and the means (black squares) are shown along with the central 67% (box) and the central 90% (thin black lines). Distributions are colour-coded based on drought conditions (Table 3). Note that, although no MODIS DSI data are available for year 2012, this year is plotted in the middle as it is defined as dry year by Erfanian et al., (2017). The number of observations (in black) and the median values (in red) included in each distribution are given at the top of the plot.

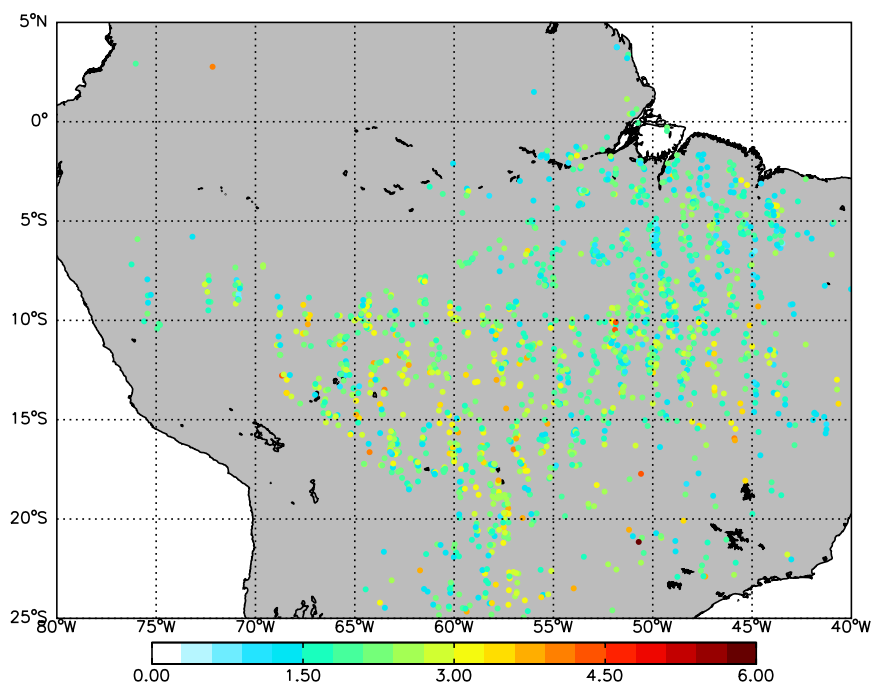


Figure A5: Location of the CALIOP plumes analysed with the median smoke plume height over the Amazon domain.

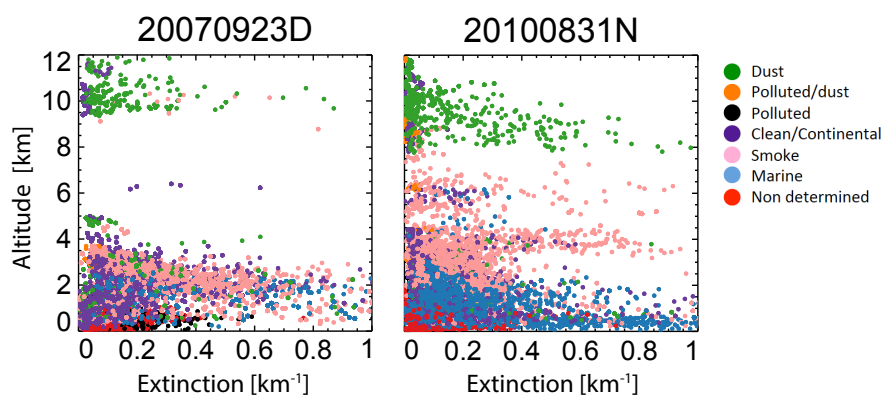


Figure A6: Examples of CALIOP vertical extinction profiles with smoke aerosols above 6 km. Values are coloured by classified aerosol types. Profile 20070923D represents a case where high altitude smoke is disconnected from low altitude smoke and profile 20100831N gives an example of smoke gradually distributed from low to high altitudes.

Appendix B

Supplementary information

This document includes supplementary tables, figures and results used for the analysis discussed in Chapter 4 of this work.

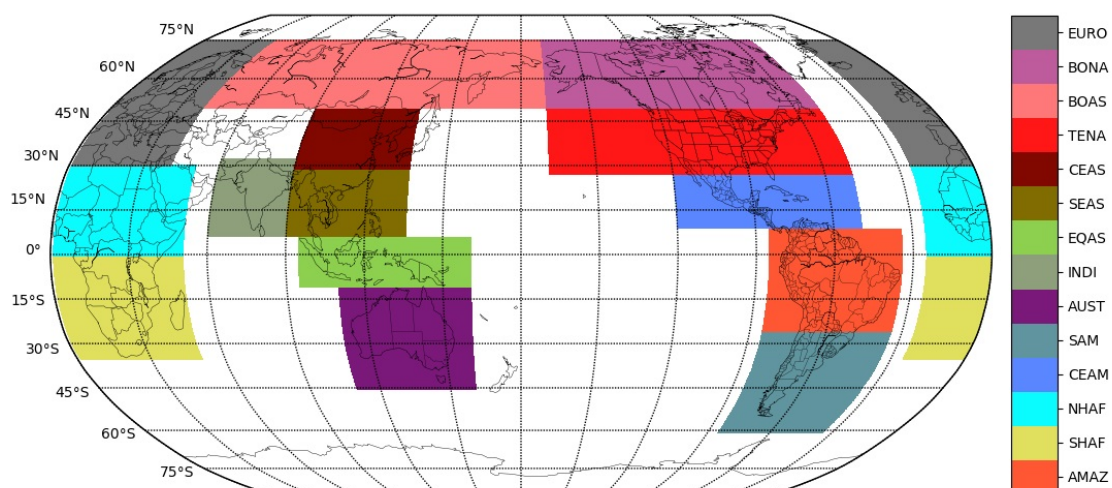


Figure B1: Fire regions of tagged CO across the globe used. EURO: Europe, BONA: Boreal North America, BOAS: Boreal Asia, TENA: Temperate North America, CEAS: Central East-Asia, SEAS: South East-Asia, EQAS: Equatoria-Asia, INDI: India, AUST: Australia, SAM: South America, CEAM: Central America, NHAF: North Africa, SHAF: South Africa, AMAZ: Amazon.

Table B1: Summary of the TOAR stations for surface ozone evaluation.

Name	Station type	Area type	Country	Longitude	Latitude	Altitude
Porto Velho	background	rural	Brazil	-63.86	-8.68	84
Ragged Point	other-marine	rural	Barbados	-59.43	13.16	15
Amazon TT34	background	remote	Brazil	-60.209	-2.594	150
Cayenne	background	urban	French Guiana	-52.33	4.93	4
Cape Verde	background	remote	Cape Verde	-24.87	16.84	10
San Lorenzo	background	remote	Paraguay	-57.55	-25.36	133
Tololo	background	remote	Chile	-30.17	-70.79	2220

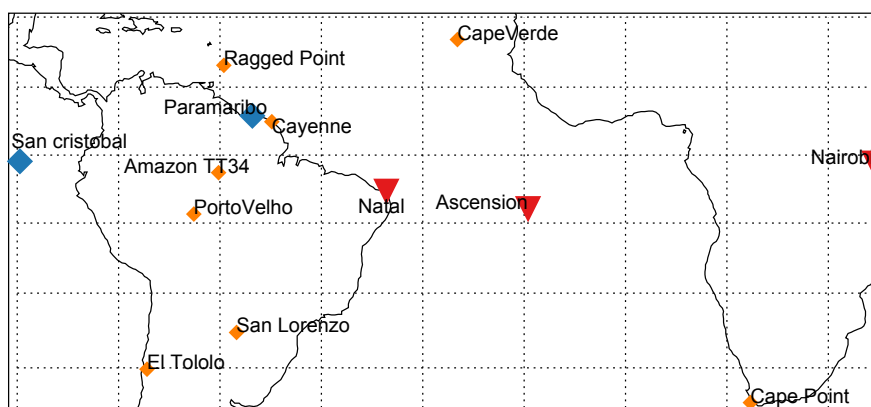


Figure B2: Location of the ozone observational dataset used in our model evaluation. TOAR stations with surface ozone measurements (orange square), ozonesondes in the Equatorial region (blue square) and ozonesondes in the Atlantic/African region (red upside down triangle).

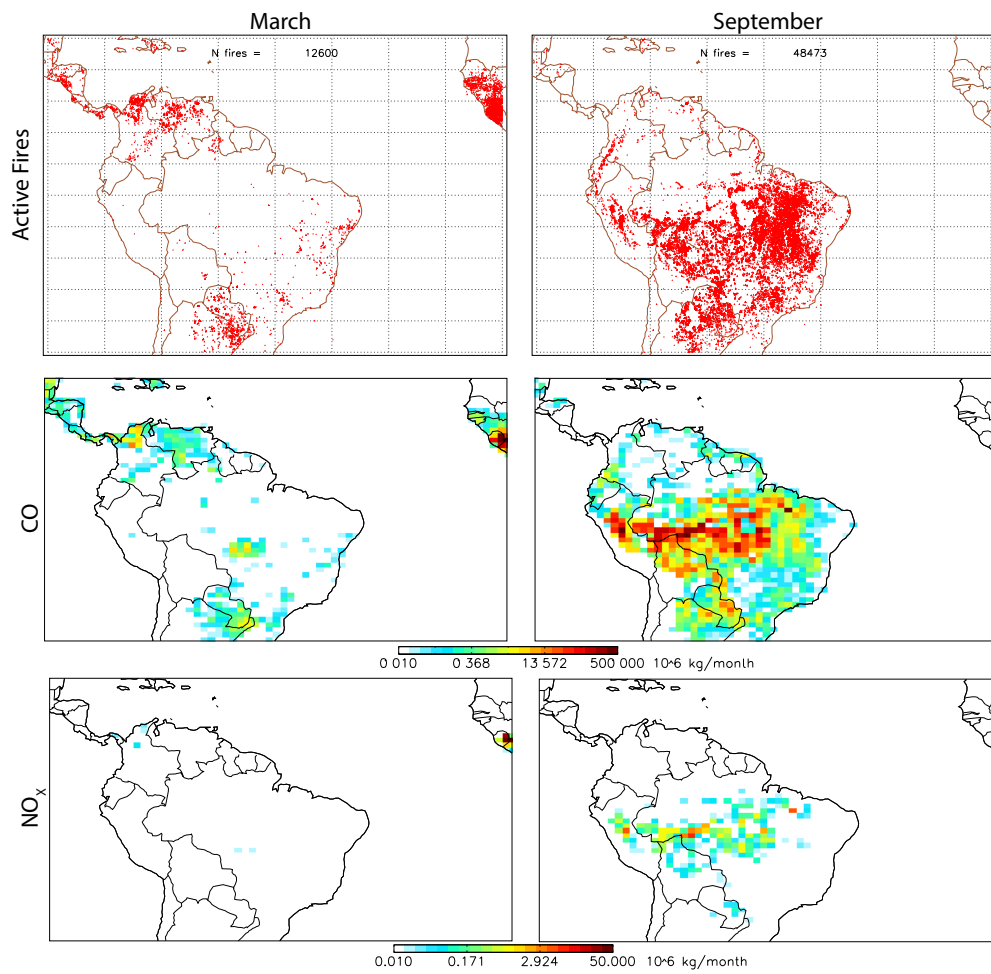


Figure B3: MODIS active fires and FINNv1.5 CO and NO_x emissions in March and September 2012.

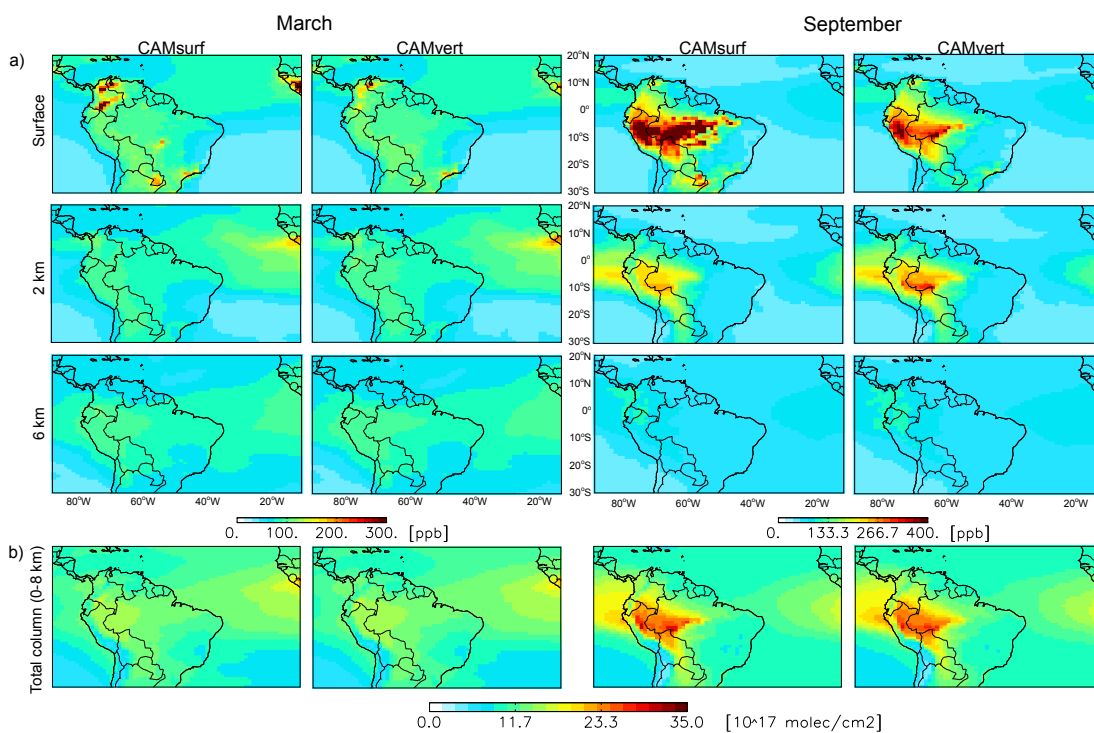


Figure B4: CAMsurf and CAMvert simulated CO mixing ratios (ppb) at three different levels: the surface, 2 km and 6 km (a), and the column (0–8 km) (molec/cm²) for March and September 2012.

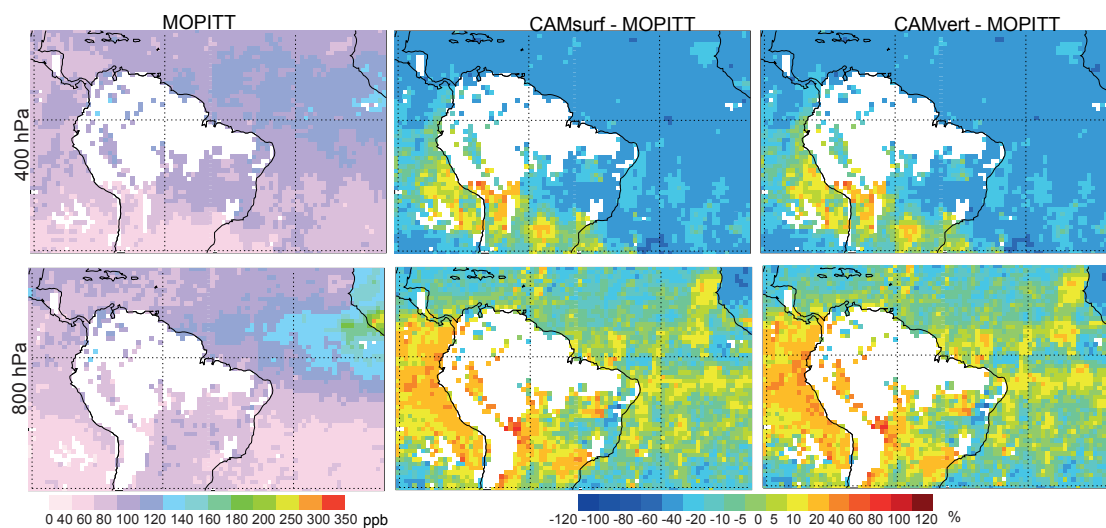


Figure B5: Averaged MOPITT CO mixing ratios and relative bias (in %) of CAMsurf and CAMvert with respect to MOPITT at 400 and 800 hPa for March 2012.

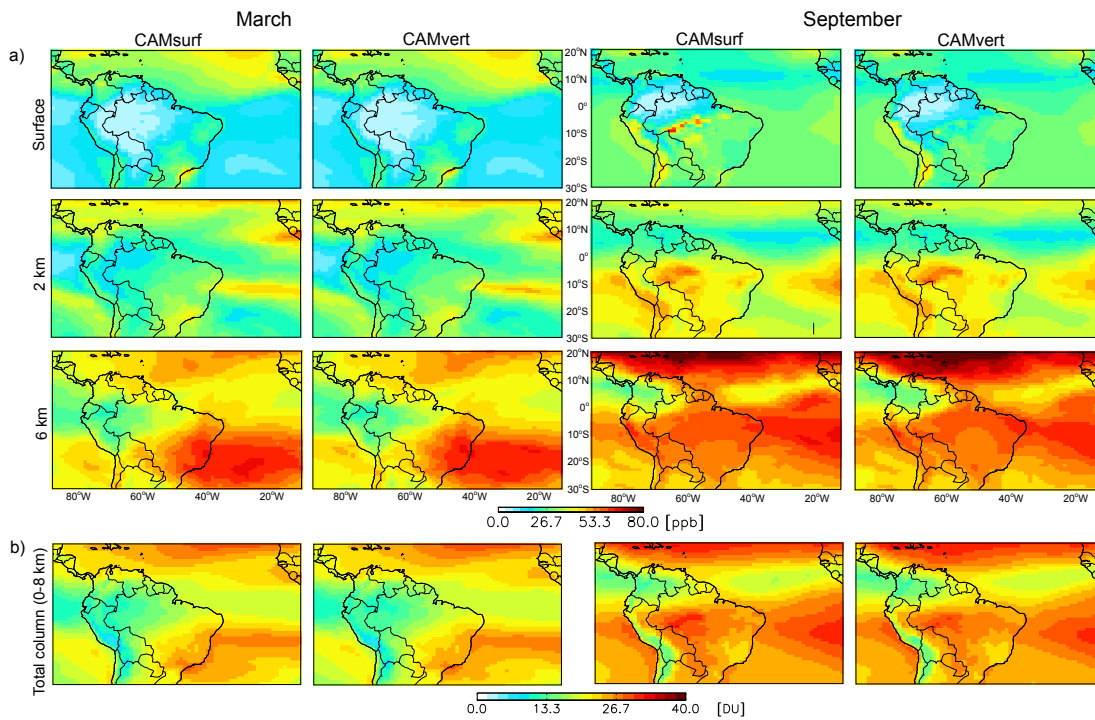


Figure B6: CAMsurf and CAMvert simulated O₃ mixing ratios (ppb) at three different levels: the surface, 2 km and 6 km (a), and the column (0–8 km) (DU) for March and September 2012.

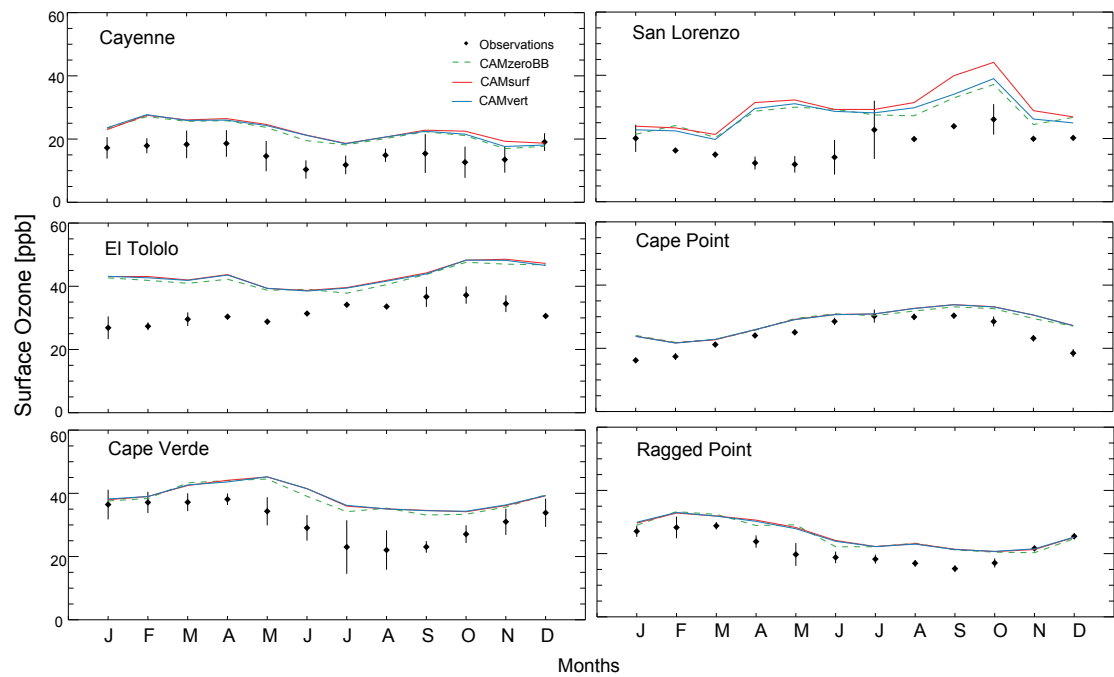


Figure B7: Monthly averages of O_3 mixing ratios from TOAR observations (black), CAMvert (blue), CAMsurf (red) and CAMzeroBB (green). Vertical bars indicate the standard deviation of the mean.

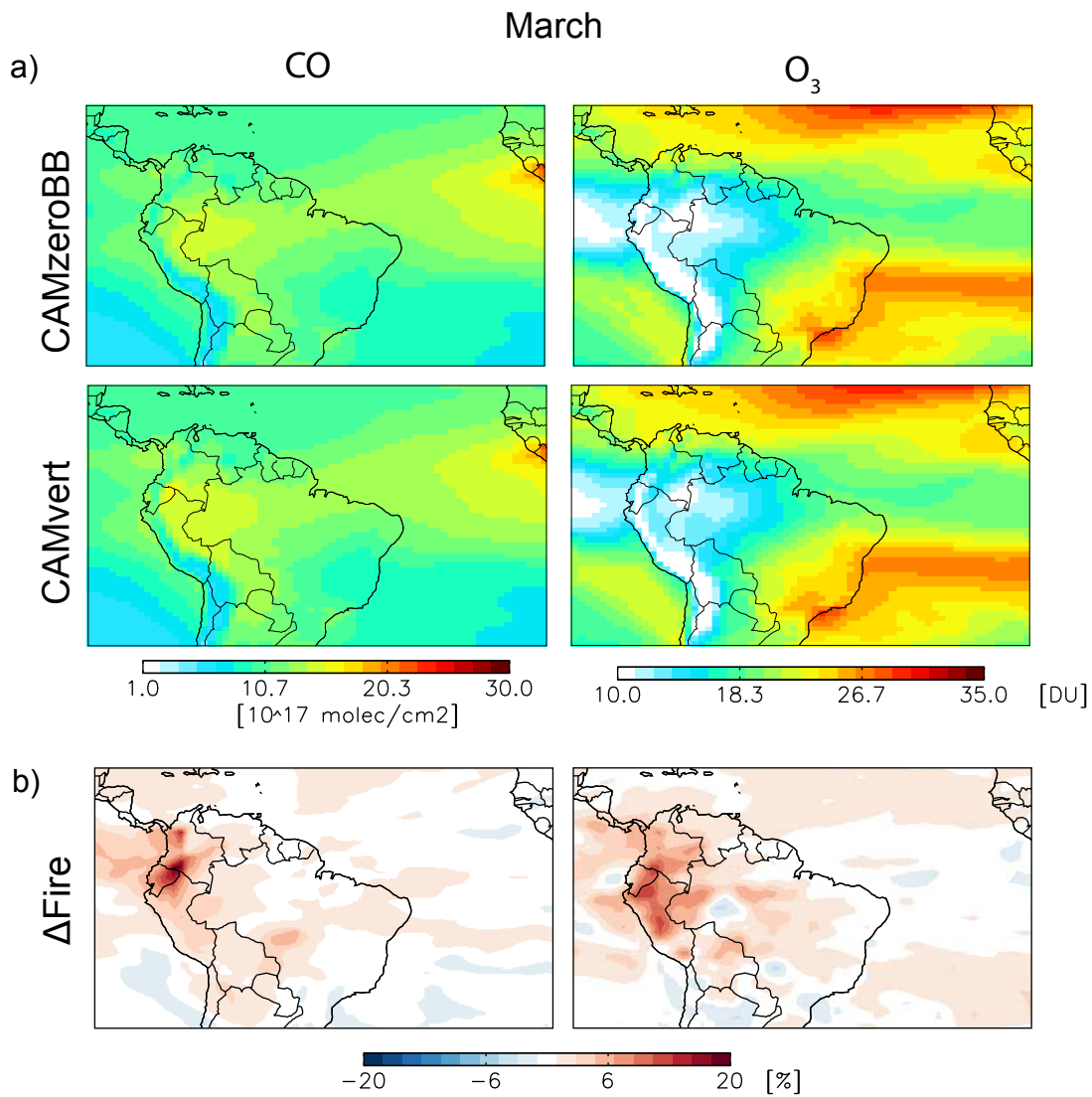


Figure B8: Simulated averaged CO and O_3 columns by CAMvert and CAMzeroBB (a) and relative changes (in %; (Δ Fire) between CAMvert and CAMzeroBB (b), in March 2012.

Appendix C

Contributions and co-authors

Table C1: Summary of contributions and co-authors.

Chapter	Contribution
1	My own work.
2	My own work.
3	<p>This chapter was published on February 8th, 2019 in the Atmospheric Chemistry and Physics journal (ACP) with the following co-authors: Maria Val Martin and Ralph A. Kahn.</p> <p>I carried out the study, developed the climatology, analysed the data, and drafted the manuscript. Maria Val Martin was the principal investigator of the study, and supervised my analysis and manuscript writing. Ralph A. Kahn contributed to the interpretation of results and assisted on writing.</p>
4	<p>This chapter is prepared to be submitted with some modifications to ACP journal with the following co-authors: Maria Val Martin, Merritt N. Deeter, Benjamin Gaubert, Louisa K. Emmons and Simone Tilmes.</p> <p>I carried out the study, prepared the modelling experiments, analysed the results and drafted the manuscript. Maria Val Martin gave me advice and guidance on the study, and supervised my analysis and manuscript writing. Merritt N. Deeter provided MOPITT data and expertise guidance on MOPITT products. Benjamin Gaubert provided expertise guidance on CESM and helped me to prepare the modelling experiments and the CO tag experiment. Louisa K. Emmons provided the emission files at CESM grid and expertise guidance on CESM. Simone Tilmes provided the MERRA-2 meteorological fields at CESM grid, the ozonesondes dataset and expertise guidance on CESM.</p>
5	My own work.

Bibliography

- Ainsworth, E. A., Yendrek, C. R., Sitch, S., Collins, W. J., and Emberson, L. D. The effects of tropospheric ozone on net primary productivity and implications for climate change. *Annual review of plant biology*, 63:637–661, 2012. Cited on pages 2 and 12.
- Akagi, S., Yokelson, R. J., Wiedinmyer, C., Alvarado, M., Reid, J., Karl, T., Crouse, J., and Wennberg, P. Emission factors for open and domestic biomass burning for use in atmospheric models. *Atmospheric Chemistry and Physics*, 11(9):4039–4072, 2011. Cited on pages 1, 5, and 95.
- Albrecht, B. A. Aerosols, cloud microphysics, and fractional cloudiness. *Science*, 245(4923):1227–1230, 1989. ISSN 0036–8075. doi: 10.1126/science.245.4923.1227. URL <http://science.sciencemag.org/content/245/4923/1227>. Cited on page 2.
- Alencar, A., Nepstad, D., and Diaz, M. C. V. Forest understory fire in the brazilian amazon in enso and non-enso years: area burned and committed carbon emissions. *Earth Interactions*, 10(6):1–17, 2006. Cited on page 85.
- Alencar, A., Asner, G. P., Knapp, D., and Zarin, D. Temporal variability of forest fires in eastern amazonia. *Ecological Applications*, 21(7):2397–2412, 2011. Cited on page 52.
- Allan, J. D., Morgan, W. T., Darbyshire, E., Flynn, M. J., Williams, P. I., Oram, D. E., Artaxo, P., Brito, J., Lee, J. D., and Coe, H. Airborne observations of ieopox-derived isoprene soa in the amazon during sambba. *Atmospheric Chemistry and Physics*, 14(20):11393–11407, 2014. Cited on pages 12, 53, and 99.
- Alvarado, M., Logan, J., Mao, J., Apel, E., Riemer, D., Blake, D., Cohen, R., Min, K.-E., Perring, A., Browne, E., et al. Nitrogen oxides and pan in plumes from boreal fires during arctas-b and their impact on ozone: an integrated analysis of aircraft and satellite observations. *Atmospheric Chemistry and Physics*, 10(20):9739–9760, 2010. Cited on pages 1 and 5.
- Amiridis, V., Giannakaki, E., Balis, D. S., Gerasopoulos, E., Pytharoulis, I., Zanis, P., Kazadzis, S., Melas, D., and Zerefos, C. Smoke injection heights from agricultural burning in eastern europe as seen by calipso. *Atmospheric Chemistry and Physics*, 10(23):11567–11576, 2010. doi: 10.5194/acp-10-11567-2010. URL <https://www.atmos-chem-phys.net/10/11567/2010/>. Cited on pages 6, 8, 18, 63, 68, 69, 83, and 92.
- Andreae, M., Anderson, B., Blake, D., Bradshaw, J., Collins, J., Gregory, G., Sachse, G., and Shipham, M. Influence of plumes from biomass burning on atmospheric chemistry over the equatorial and tropical south atlantic during cite 3. *Journal of Geophysical Research: Atmospheres*, 99(D6):12793–12808, 1994. Cited on page 91.

- Andreae, M., Artaxo, P., Beck, V., Bela, M., Freitas, S., Gerbig, C., Longo, K., Munger, J., Wiedemann, K., and Wofsy, S. Carbon monoxide and related trace gases and aerosols over the amazon basin during the wet and dry seasons. *Atmospheric Chemistry and Physics*, 12(13):6041–6065, 2012. Cited on pages 10, 12, 13, 53, 91, 99, 102, and 104.
- Andreae, M. O. Biomass burning-its history, use, and distribution and its impact on environmental quality and global climate. In *Global biomass burning-Atmospheric, climatic, and biospheric implications*. 1991. Cited on page 2.
- Andreae, M. O. and Merlet, P. Emission of trace gases and aerosols from biomass burning. *Global biogeochemical cycles*, 15(4):955–966, 2001. Cited on pages 1, 2, 5, 51, 90, and 95.
- Andreae, M. O., Browell, E. V., Garstang, M., Gregory, G., Harriss, R., Hill, G., Jacob, D. J., Pereira, M., Sachse, G., Setzer, A., et al. Biomass-burning emissions and associated haze layers over amazonia. *Journal of Geophysical Research: Atmospheres*, 93(D2):1509–1527, 1988. Cited on pages 11, 12, and 90.
- Aragao, L. E., Poulter, B., Barlow, J. B., Anderson, L. O., Malhi, Y., Saatchi, S., Phillips, O. L., and Gloor, E. Environmental change and the carbon balance of a mazonian forests. *Biological Reviews*, 89(4):913–931, 2014. Cited on pages 10, 51, and 79.
- Aragao, L. E. O., Malhi, Y., Barbier, N., Lima, A., Shimabukuro, Y., Anderson, L., and Saatchi, S. Interactions between rainfall, deforestation and fires during recent years in the brazilian amazonia. *Philosophical Transactions of the Royal Society of London B: Biological Sciences*, 363(1498):1779–1785, 2008. Cited on page 93.
- Archer-Nicholls, S., Lowe, D., Darbyshire, E., Morgan, W., Bela, M., Pereira, G., Trembath, J., Kaiser, J., Longo, K., Freitas, S., et al. Characterising brazilian biomass burning emissions using wrf-chem with mosaic sectional aerosol. *Geoscientific Model Development*, 8(3):549–577, 2015. Cited on pages 52, 53, and 92.
- Archer-Nicholls, S., Lowe, D., Schultz, D. M., and McFiggans, G. Aerosol–radiation–cloud interactions in a regional coupled model: the effects of convective parameterisation and resolution. *Atmospheric Chemistry and Physics*, 16(9):5573–5594, 2016. Cited on page 12.
- Artaxo, P., Martins, J. V., Yamasoe, M. A., Procópio, A. S., Pauliquevis, T. M., Andreae, M. O., Guyon, P., Gatti, L. V., and Leal, A. M. C. Physical and chemical properties of aerosols in the wet and dry seasons in rondônia, amazonia. *Journal of Geophysical Research: Atmospheres*, 107(D20):LBA–49, 2002. Cited on pages 10 and 12.
- Artaxo, P., Gatti, L. V., Leal, A. M. C., Longo, K. M., Freitas, S. R. d., Lara, L. L., Pauliquevis, T. M., Procópio, A. S., and Rizzo, L. V. Atmospheric chemistry in amazonia: the forest and the biomass burning emissions controlling the composition of the amazonian atmosphere. *Acta Amazonica*, 35(2):185–196, 2005. Cited on page 91.
- Ashmore, M. R. and Marshall, F. Ozone impacts on agriculture: an issue of global concern. In *Advances in Botanical Research*, volume 29, pages 31–52. Elsevier, 1998. Cited on page 3.
- Avnery, S., Mauzerall, D. L., Liu, J., and Horowitz, L. W. Global crop yield reductions due to surface ozone exposure: 2. year 2030 potential crop production losses and economic damage under two scenarios of o3 pollution. *Atmospheric Environment*, 45(13):2297–2309, 2011. Cited on pages 3, 9, 90, and 119.

- Baars, H., Ansmann, A., Althausen, D., Engelmann, R., Heese, B., Müller, D., Artaxo, P., Paixao, M., Pauliquevis, T., and Souza, R. Aerosol profiling with lidar in the amazon basin during the wet and dry season. *Journal of Geophysical Research: Atmospheres*, 117(D21), 2012. doi: 10.1029/2012JD018338. Cited on pages 8, 53, 72, 82, 83, and 92.
- Baylon, P., Jaffe, D., Wigder, N., Gao, H., and Hee, J. Ozone enhancement in western us wildfire plumes at the mt. bachelor observatory: The role of nox. *Atmospheric Environment*, 109:297–304, 2015. Cited on page 5.
- Baylon, P., Jaffe, D. A., Hall, S. R., Ullmann, K., Alvarado, M. J., and Lefer, B. L. Impact of biomass burning plumes on photolysis rates and ozone formation at the mount bachelor observatory. *Journal of Geophysical Research: Atmospheres*, 123(4): 2272–2284, 2018. doi: 10.1002/2017JD027341. Cited on page 5.
- Bela, M., Longo, K., Freitas, S., Moreira, D., Beck, V., Wofsy, S., Gerbig, C., Wiedemann, K., Andreae, M., and Artaxo, P. Ozone production and transport over the amazon basin during the dry-to-wet and wet-to-dry transition seasons. *Atmospheric Chemistry and Physics*, 15:757–782, 2015. Cited on pages 12, 13, 91, 111, and 113.
- Bell, M. L., McDermott, A., Zeger, S. L., Samet, J. M., and Dominici, F. Ozone and short-term mortality in 95 us urban communities, 1987-2000. *Jama*, 292(19):2372–2378, 2004. Cited on pages 3 and 90.
- Bell, M. L., Peng, R. D., and Dominici, F. The exposure–response curve for ozone and risk of mortality and the adequacy of current ozone regulations. *Environmental health perspectives*, 114(4):532–536, 2006. Cited on pages 3 and 90.
- Benkoussas, B., Consalvi, J.-L., Porterie, B., Sardoy, N., and Loraud, J.-C. Modelling thermal degradation of woody fuel particles. *International Journal of Thermal Sciences*, 46(4):319–327, 2007. Cited on page 5.
- Benton, J., Fuhrer, J., Gimeno, B., Skärby, L., Palmer-Brown, D., Ball, G., Roadknight, C., and Mills, G. An international cooperative programme indicates the widespread occurrence of ozone injury on crops. *Agriculture, ecosystems & environment*, 78(1): 19–30, 2000. Cited on page 3.
- Betts, A. K., Gatti, L. V., Cordova, A. M., Silva Dias, M. A. F., and Fuentes, J. D. Transport of ozone to the surface by convective downdrafts at night. *Journal of Geophysical Research: Atmospheres*, 107(D20):LBA 13–1–LBA 13–6, 2002. doi: 10.1029/2000JD000158. URL <https://agupubs.onlinelibrary.wiley.com/doi/abs/10.1029/2000JD000158>. Cited on page 90.
- Bey, I., Jacob, D. J., Yantosca, R. M., Logan, J. A., Field, B. D., Fiore, A. M., Li, Q., Liu, H. Y., Mickley, L. J., and Schultz, M. G. Global modeling of tropospheric chemistry with assimilated meteorology: Model description and evaluation. *Journal of Geophysical Research: Atmospheres*, 106(D19):23073–23095, 2001. Cited on page 91.
- Bogenschutz, P. A., Gettelman, A., Hannay, C., Larson, V. E., Neale, R. B., Craig, C., and Chen, C.-C. The path to cam6: coupled simulations with cam5.4 and cam5.5. *Geoscientific Model Development*, 11(1):235–255, 2018. doi: 10.5194/gmd-11-235-2018. URL <https://www.geosci-model-dev.net/11/235/2018/>. Cited on page 94.
- Bosilovich, M., Lucchesi, R., and Suarez, M. Merra-2: File specification. 2015. Cited on pages 55, 60, and 94.

- Bourgeois, Q., Ekman, A. M., and Krejci, R. Aerosol transport over the andes from the amazon basin to the remote pacific ocean: A multiyear caliop assessment. *Journal of Geophysical Research: Atmospheres*, 120(16):8411–8425, 2015. Cited on page 8.
- Bowman, D. M., Balch, J. K., Artaxo, P., Bond, W. J., Carlson, J. M., Cochrane, M. A., D’Antonio, C. M., DeFries, R. S., Doyle, J. C., Harrison, S. P., et al. Fire in the earth system. *science*, 324(5926):481–484, 2009. Cited on page 13.
- Brey, S. J. and Fischer, E. V. Smoke in the city: how often and where does smoke impact summertime ozone in the united states? *Environmental science & technology*, 50(3): 1288–1294, 2016. Cited on pages 7 and 91.
- Brito, J., Rizzo, L. V., Morgan, W. T., Coe, H., Johnson, B., Haywood, J., Longo, K., Freitas, S., Andreae, M. O., and Artaxo, P. Ground-based aerosol characterization during the south american biomass burning analysis (sambba) field experiment. *Atmospheric Chemistry and Physics*, 14(22):12069–12083, 2014. Cited on pages 10 and 102.
- Canadell, J. G., Le Quéré, C., Raupach, M. R., Field, C. B., Buitenhuis, E. T., Ciais, P., Conway, T. J., Gillett, N. P., Houghton, R., and Marland, G. Contributions to accelerating atmospheric co2 growth from economic activity, carbon intensity, and efficiency of natural sinks. *Proceedings of the national academy of sciences*, 104(47):18866–18870, 2007. Cited on page 11.
- Chalbot, M.-C., Kavouras, I. G., and Dubois, D. W. Assessment of the contribution of wildfires to ozone concentrations in the central us-mexico border region. *Aerosol Air Qual. Res*, 13:838–848, 2013. Cited on pages 7 and 91.
- Chameides, W., Fehsenfeld, F., Rodgers, M., Cardelino, C., Martinez, J., Parrish, D., Lonneman, W., Lawson, D., Rasmussen, R., Zimmerman, P., et al. Ozone precursor relationships in the ambient atmosphere. *Journal of Geophysical Research: Atmospheres*, 97(D5):6037–6055, 1992. Cited on page 90.
- Chen, Q. Airborne lidar data processing and information extraction. *Photogrammetric engineering and remote sensing*, 73(2):109, 2007. Cited on page 5.
- Chen, Y., Li, Q., Randerson, J. T., Lyons, E. A., Kahn, R. A., Nelson, D. L., and Diner, D. J. The sensitivity of co and aerosol transport to the temporal and vertical distribution of north american boreal fire emissions. *Atmospheric Chemistry and Physics*, 9(17): 6559–6580, 2009. Cited on pages 102, 108, and 127.
- Chen, Y., Randerson, J. T., Morton, D. C., DeFries, R. S., Collatz, G. J., Kasibhatla, P. S., Giglio, L., Jin, Y., and Marlier, M. E. Forecasting fire season severity in south america using sea surface temperature anomalies. *Science*, 334(6057):787–791, 2011. Cited on page 59.
- CLRTAP. *Forest Condition in Europe: 2017 Technical Report of ICP Forests. Report under the UNECE Convention on Long-Range Transboundary Air Pollution (CLRTAP)*. 12 2017. doi: 10.13140/RG.2.2.17808.30720. Cited on pages 9 and 10.
- Cochrane, M. A. Fire science for rainforests. *Nature*, 421(6926):913, 2003. Cited on page 51.
- Cochrane, M. A. and Barber, C. P. Climate change, human land use and future fires in the amazon. *Global Change Biology*, 15(3):601–612, 2009. Cited on pages 13 and 93.

- CONAB. Brazilian national supply agency. <https://www.conab.gov.br/info-agro>; last accessed on 5 March 2019. Cited on page 124.
- Crippa, P., Castruccio, S., Archer-Nicholls, S., Lebron, G., Kuwata, M., Thota, A., Sumin, S., Butt, E., Wiedinmyer, C., and Spracklen, D. Population exposure to hazardous air quality due to the 2015 fires in equatorial asia. *Scientific reports*, 6:37074, 2016. doi: 10.1038/srep37074. Cited on page 7.
- Crutzen, P. A discussion of the chemistry of some minor constituents in the stratosphere and troposphere. *Pure and Applied Geophysics*, 106(1):1385–1399, 1973. Cited on page 2.
- Crutzen, P. and Carmichael, G. Modeling the influence of fires on atmospheric chemistry. *Fire in the environment: the ecological, atmospheric, and climatic importance of vegetation fires*. New York: Wiley, pages 89–105, 1993. Cited on page 90.
- Crutzen, P. J. and Andreae, M. O. Biomass burning in the tropics: Impact on atmospheric chemistry and biogeochemical cycles. *Science*, 250(4988):1669–1678, 1990. Cited on page 1.
- Davidson, E. A., de Araújo, A. C., Artaxo, P., Balch, J. K., Brown, I. F., Bustamante, M. M., Coe, M. T., DeFries, R. S., Keller, M., Longo, M., et al. The amazon basin in transition. *Nature*, 481(7381):321, 2012. Cited on pages 10, 11, 14, and 89.
- Davies, R., Horváth, Á., Moroney, C., Zhang, B., and Zhu, Y. Cloud motion vectors from misr using sub-pixel enhancements. *Remote sensing of environment*, 107(1-2):194–199, 2007. Cited on pages 22 and 41.
- de Andrade Filho, V. S., Artaxo, P., Hacon, S., Carmo, C. N. d., and Cirino, G. Aerosols from biomass burning and respiratory diseases in children, manaus, northern brazil. *Revista de Saúde Pública*, 47(2):239–247, 2013. Cited on page 12.
- de Oliveira Alves, N., Brito, J., Caumo, S., Arana, A., de Souza Hacon, S., Artaxo, P., Hillamo, R., Teinilä, K., de Medeiros, S. R. B., and de Castro Vasconcellos, P. Biomass burning in the amazon region: Aerosol source apportionment and associated health risk assessment. *Atmospheric Environment*, 120:277–285, 2015. Cited on page 12.
- DeCaria, A. J., Pickering, K. E., Stenchikov, G. L., and Ott, L. E. Lightning-generated nox and its impact on tropospheric ozone production: A three-dimensional modeling study of a stratosphere-troposphere experiment: Radiation, aerosols and ozone (sterao-a) thunderstorm. *Journal of Geophysical Research: Atmospheres*, 110(D14), 2005. Cited on page 95.
- Deeter, M., Martínez-Alonso, S., Andreae, M. O., and Schlager, H. Satellite-based analysis of co seasonal and interannual variability over the amazon basin. *Journal of Geophysical Research: Atmospheres*, 123(10):5641–5656, 2018. Cited on pages 12, 99, and 106.
- Deeter, M. N., Emmons, L. K., Francis, G. L., Edwards, D. P., Gille, J. C., Warner, J. X., Khattatov, B., Ziskin, D., Lamarque, J.-F., Ho, S.-P., Yudin, V., Attie, J.-L., Packman, D., Chen, J., Mao, D., and Drummond, J. R. Operational carbon monoxide retrieval algorithm and selected results for the mopitt instrument. *Journal of Geophysical Research: Atmospheres*, 108(D14), 2003. doi: 10.1029/2002JD003186. URL <https://agupubs.onlinelibrary.wiley.com/doi/abs/10.1029/2002JD003186>. Cited on page 99.

- Deeter, M. N., Martínez-Alonso, S., Edwards, D. P., Emmons, L. K., Gille, J. C., Worden, H. M., Sweeney, C., Pittman, J. V., Daube, B. C., and Wofsy, S. C. The mopitt version 6 product: algorithm enhancements and validation. *Atmospheric Measurement Techniques*, 7(11):3623–3632, 2014. doi: 10.5194/amt-7-3623-2014. URL <https://www.atmos-meas-tech.net/7/3623/2014/>. Cited on page 99.
- Denman, K., Brasseur, G., Chidthaisong, A., Ciais, P., Cox, P., and Dickinson, R. Coauthors, 2007: Couplings between changes in the climate system and biogeochemistry, 2007. Cited on page 1.
- Dentener, F., Kinne, S., Bond, T., Boucher, O., Cofala, J., Generoso, S., Ginoux, P., Gong, S., Hoelzemann, J., Ito, A., et al. Emissions of primary aerosol and precursor gases in the years 2000 and 1750 prescribed data-sets for aerocom. *Atmospheric Chemistry and Physics*, 6(12):4321–4344, 2006. Cited on pages 91 and 95.
- Diner, D. J., Beckert, J. C., Reilly, T. H., Bruegge, C. J., Conel, J. E., Kahn, R. A., Martonchik, J. V., Ackerman, T. P., Davies, R., Gerstl, S. A., et al. Multi-angle imaging spectroradiometer (misr) instrument description and experiment overview. *IEEE Transactions on Geoscience and Remote Sensing*, 36(4):1072–1087, 1998. Cited on pages 17, 19, 20, 30, 55, and 56.
- Dozier, J. A method for satellite identification of surface temperature fields of subpixel resolution. *Remote Sensing of environment*, 11:221–229, 1981. Cited on page 22.
- Edwards, D., Lamarque, J.-F., Attié, J.-L., Emmons, L., Richter, A., Cammas, J.-P., Gille, J., Francis, G., Deeter, M., Warner, J., et al. Tropospheric ozone over the tropical atlantic: A satellite perspective. *Journal of Geophysical Research: Atmospheres*, 108(D8), 2003. doi: 10.1029/2002JD002927. Cited on pages 90 and 118.
- Edwards, D., Emmons, L., Gille, J., Chu, A., Attié, J.-L., Giglio, L., Wood, S., Haywood, J., Deeter, M., Massie, S., et al. Satellite-observed pollution from southern hemisphere biomass burning. *Journal of Geophysical Research: Atmospheres*, 111(D14), 2006. doi: 10.1029/2005JD006655. Cited on pages 12, 90, 98, 106, 116, and 127.
- Emmons, L. K., Walters, S., Hess, P. G., Lamarque, J.-F., Pfister, G. G., Fillmore, D., Granier, C., Guenther, A., Kinnison, D., Laepple, T., Orlando, J., Tie, X., Tyndall, G., Wiedinmyer, C., Baughcum, S. L., and Kloster, S. Description and evaluation of the model for ozone and related chemical tracers, version 4 (mozart-4). *Geoscientific Model Development*, 3(1):43–67, 2010. doi: 10.5194/gmd-3-43-2010. URL <https://www.geosci-model-dev.net/3/43/2010/>. Cited on pages 94, 95, and 97.
- EPA, U. Naaqs table. 2016. Cited on page 9.
- Eyring, V., Bony, S., Meehl, G. A., Senior, C. A., Stevens, B., Stouffer, R. J., and Taylor, K. E. Overview of the coupled model intercomparison project phase 6 (cmip6) experimental design and organization. *Geoscientific Model Development*, 9(5):1937–1958, 2016. doi: 10.5194/gmd-9-1937-2016. URL <https://www.geosci-model-dev.net/9/1937/2016/>. Cited on page 94.
- FAO. <http://www.fao.org/faostat/en/#home>, 2019. Online; last accessed on 7 January 2019. Cited on page 123.
- Felzer, B. S., Cronin, T., Reilly, J. M., Melillo, J. M., and Wang, X. Impacts of ozone on trees and crops. *Comptes Rendus Geoscience*, 339(11-12):784–798, 2007. Cited on pages 2 and 7.

- Fisch, G., Tota, J., Machado, L., Silva Dias, M. d., da F. Lyra, R., Nobre, C., Dolman, A., and Gash, J. The convective boundary layer over pasture and forest in amazonia. *Theoretical and Applied Climatology*, 78(1):47–59, 2004. Cited on page 70.
- Fiscus, E. L., Booker, F. L., and Burkey, K. O. Crop responses to ozone: uptake, modes of action, carbon assimilation and partitioning. *Plant, Cell & Environment*, 28(8): 997–1011, 2005. Cited on page 2.
- Fishman, J., Brackett, V. G., Browell, E. V., and Grant, W. B. Tropospheric ozone derived from toms/sbuw measurements during trace a. *Journal of Geophysical Research: Atmospheres*, 101(D19):24069–24082, 1996a. Cited on page 12.
- Fishman, J., Hoell Jr, J. M., Bendura, R. D., McNeal, R. J., and Kirchhoff, V. W. Nasa trace a experiment (september–october 1992): overview. *Journal of Geophysical Research: Atmospheres*, 101(D19):23865–23879, 1996b. Cited on pages 12, 90, and 117.
- Fleming, Z. L., Doherty, R. M., Von Schneidmesser, E., Malley, C., Cooper, O. R., Pinto, J. P., Colette, A., Xu, X., Simpson, D., Schultz, M. G., et al. Tropospheric ozone assessment report: Present-day ozone distribution and trends relevant to human health. *Elementa: Science of the Anthropocene*, 2018. doi: 10.1525/elementa.273. Cited on pages 7, 9, 119, and 121.
- Flower, V. J. and Kahn, R. A. Assessing the altitude and dispersion of volcanic plumes using misr multi-angle imaging from space: Sixteen years of volcanic activity in the kamchatka peninsula, russia. *Journal of Volcanology and Geothermal Research*, 337: 1–15, 2017. Cited on pages 45, 57, and 84.
- Ford, B. and Heald, C. L. An a-train and model perspective on the vertical distribution of aerosols and co in the northern hemisphere. *Journal of Geophysical Research: Atmospheres*, 117(D6), 2012. Cited on page 62.
- Freitas, S., Longo, K., and Andreae, M. Impact of including the plume rise of vegetation fires in numerical simulations of associated atmospheric pollutants. *Geophysical Research Letters*, 33(17), 2006. doi: 10.1029/2006GL026608. Cited on pages 6 and 92.
- Freitas, S. R., Longo, K. M., Chatfield, R., Latham, D., Silva Dias, M., Andreae, M., Prins, E., Santos, J., Gielow, R., and Carvalho Jr, J. Including the sub-grid scale plume rise of vegetation fires in low resolution atmospheric transport models. *Atmospheric Chemistry and Physics*, 7(13):3385–3398, 2007. Cited on pages 52, 86, and 92.
- Friedl, M. A., Sulla-Menashe, D., Tan, B., Schneider, A., Ramankutty, N., Sibley, A., and Huang, X. Modis collection 5 global land cover: Algorithm refinements and characterization of new datasets. *Remote sensing of Environment*, 114(1):168–182, 2010. Cited on pages 23, 55, 60, 98, and 123.
- Fromm, M., Bevilacqua, R., Stocks, B., and Servranckx, R. New directions: Eruptive transport to the stratosphere: Add fire-convection to volcanoes. *Atmospheric Environment*, 38:163–165, 2004. Cited on page 6.
- Fromm, M., Lindsey, D. T., Servranckx, R., Yue, G., Trickl, T., Sica, R., Doucet, P., and Godin-Beekmann, S. The untold story of pyrocumulonimbus. *Bulletin of the American Meteorological Society*, 91(9):1193–1210, 2010. Cited on page 6.
- Fuehrer, J. and Achermann, B. Critical levels for ozone, a un-ee workshop report. 1994. Cited on page 3.

- Fumagalli, I., Gimeno, B. S., Velissariou, D., De Temmerman, L., and Mills, G. Evidence of ozone-induced adverse effects on crops in the mediterranean region. *Atmospheric Environment*, 35(14):2583–2587, 2001. Cited on page 3.
- Galanter, M., Levy, H., and Carmichael, G. R. Impacts of biomass burning on tropospheric co, no x, and o3. *Journal of Geophysical Research: Atmospheres*, 105(D5):6633–6653, 2000. Cited on pages 12, 90, 119, and 128.
- Gatti, L., Gloor, M., Miller, J., Doughty, C., Malhi, Y., Domingues, L., Basso, L., Martinewski, A., Correia, C., Borges, V., et al. Drought sensitivity of amazonian carbon balance revealed by atmospheric measurements. *Nature*, 506(7486):76, 2014. doi: <https://doi.org/10.1038/nature12957>. Cited on pages 98, 99, 102, and 104.
- Gaubert, B., Arellano Jr., A. F., Barre, J., Worden, H. M., Emmons, L. K., Tilmes, S., Buchholz, R. R., Vitt, F., Raeder, K., Collins, N., Anderson, J. L., Wiedinmyer, C., Martinez Alonso, S., Edwards, D. P., Andreae, M. O., Hannigan, J. W., Petri, C., Strong, K., and Jones, N. Toward a chemical reanalysis in a coupled chemistry-climate model: An evaluation of mopitt co assimilation and its impact on tropospheric composition. *Journal of Geophysical Research: Atmospheres*, 121(12):7310–7343, 2016. doi: 10.1002/2016JD024863. Cited on page 97.
- Ghude, S. D., Jena, C., Chate, D., Beig, G., Pfister, G., Kumar, R., and Ramanathan, V. Reductions in india’s crop yield due to ozone. *Geophysical Research Letters*, 41(15): 5685–5691, 2014. Cited on pages 3 and 90.
- Giangrande, S. E., Feng, Z., Jensen, M. P., Comstock, J. M., Johnson, K. L., Toto, T., Wang, M., Burleyson, C., Bharadwaj, N., Mei, F., Machado, L. A. T., Manzi, A. O., Xie, S., Tang, S., Silva Dias, M. A. F., de Souza, R. A. F., Schumacher, C., and Martin, S. T. Cloud characteristics, thermodynamic controls and radiative impacts during the observations and modeling of the green ocean amazon (goamazon2014/5) experiment. *Atmospheric Chemistry and Physics*, 17(23):14519–14541, 2017. Cited on page 12.
- Giglio, L., Descloitres, J., Justice, C. O., and Kaufman, Y. J. An enhanced contextual fire detection algorithm for modis. *Remote Sensing of Environment*, 87(2):273–282, 2003. ISSN 0034–4257. URL <http://www.sciencedirect.com/science/article/pii/S0034425703001846>. Cited on pages 19, 22, 56, and 63.
- Giglio, L., Van der Werf, G., Randerson, J., Collatz, G., and Kasibhatla, P. Global estimation of burned area using modis active fire observations. *Atmospheric Chemistry and Physics*, 6(4):957–974, 2006. Cited on pages 55 and 69.
- Giglio, L., Randerson, J., Van der Werf, G., Kasibhatla, P., Collatz, G., Morton, D., and DeFries, R. Assessing variability and long-term trends in burned area by merging multiple satellite fire products. *Biogeosciences*, 7(3):1171–1186, 2010. URL <https://www.biogeosciences.net/7/1171/2010/>. Cited on page 1.
- Gloude-mans, A., Krol, M., Meirink, J., De Laat, A., Van der Werf, G., Schrijver, H., Van den Broek, M., and Aben, I. Evidence for long-range transport of carbon monoxide in the southern hemisphere from sciamachy observations. *Geophysical research letters*, 33(16), 2006. Cited on page 90.
- Gonzalez-Alonso, L., Val Martin, M., and Kahn, R. A. Biomass-burning smoke heights over the amazon observed from space. *Atmospheric Chemistry and Physics*, 19(3): 1685–1702, 2019. URL <https://www.atmos-chem-phys.net/19/1685/2019/>. Cited on pages 10, 19, 41, 92, 101, 104, 117, and 128.

- Gonzi, S. and Palmer, P. I. Vertical transport of surface fire emissions observed from space. *Journal of Geophysical Research: Atmospheres*, 115(D2), 2010. Cited on pages 8 and 53.
- Goode, J. G., Yokelson, R. J., Ward, D. E., Susott, R. A., Babbitt, R. E., Davies, M. A., and Hao, W. M. Measurements of excess o₃, co₂, co, ch₄, c₂h₄, c₂h₂, hcn, no, nh₃, hcooh, ch₃cooh, hcho, and ch₃oh in 1997 alaskan biomass burning plumes by airborne fourier transform infrared spectroscopy (aftir). *Journal of Geophysical Research: Atmospheres*, 105(D17):22147–22166, 2000. Cited on pages 1, 5, and 90.
- Guan, H., Esswein, R., Lopez, J., Bergstrom, R., Warnock, A., Follette-Cook, M., Fromm, M., and Iraci, L. T. A multi-decadal history of biomass burning plume heights identified using aerosol index measurements. *Atmospheric Chemistry and Physics*, 10(14):6461–6469, 2010. URL <https://www.atmos-chem-phys.net/10/6461/2010/>. Cited on pages 8 and 53.
- Guenther, A. B., Jiang, X., Heald, C. L., Sakulyanontvittaya, T., Duhl, T., Emmons, L. K., and Wang, X. The model of emissions of gases and aerosols from nature version 2.1 (megan2.1): an extended and updated framework for modeling biogenic emissions. *Geoscientific Model Development*, 5(6):1471–1492, 2012. doi: 10.5194/gmd-5-1471-2012. URL <https://www.geosci-model-dev.net/5/1471/2012/>. Cited on page 95.
- Haikerwal, A., Akram, M., Sim, M. R., Meyer, M., Abramson, M. J., and Dennekamp, M. Fine particulate matter (pm 2.5) exposure during a prolonged wildfire period and emergency department visits for asthma. *Respirology*, 21(1):88–94, 2016. Cited on page 7.
- Harriss, R., Wofsy, S., Garstang, M., Browell, E., Molion, L., McNeal, R., Hoell, J., Bendura, R., Beck, S., Navarro, R., et al. The amazon boundary layer experiment (able 2a): Dry season 1985. *Journal of Geophysical Research: Atmospheres*, 93(D2): 1351–1360, 1988. Cited on page 12.
- Heald, C., Henze, D., Horowitz, L., Feddema, J., Lamarque, J.-F., Guenther, A., Hess, P., Vitt, F., Seinfeld, J., Goldstein, A., et al. Predicted change in global secondary organic aerosol concentrations in response to future climate, emissions, and land use change. *Journal of Geophysical Research: Atmospheres*, 113(D5), 2008. Cited on page 93.
- Hoell Jr, J. M., Davis, D. D., Gregory, G. L., McNeal, R. J., Bendura, R. J., Drewry, J. W., Barrick, J. D., Kirchhoff, V. W., Motta, A. G., Navarro, R. L., et al. Operational overview of the nasa gte/cite 3 airborne instrument intercomparisons for sulfur dioxide, hydrogen sulfide, carbonyl sulfide, dimethyl sulfide, and carbon disulfide. *Journal of Geophysical Research: Atmospheres*, 98(D12):23291–23304, 1993. Cited on page 12.
- Hoesly, R. M., Smith, S. J., Feng, L., Klimont, Z., Janssens-Maenhout, G., Pitkanen, T., Seibert, J. J., Vu, L., Andres, R. J., Bolt, R. M., et al. Historical (1750–2014) anthropogenic emissions of reactive gases and aerosols from the community emissions data system (ceds). *Geoscientific Model Development (Online)*, 11(PNNL-SA-123932), 2018. Cited on page 94.
- Hollaway, M. J., Arnold, S., Challinor, A. J., and Emberson, L. Intercontinental trans-boundary contributions to ozone-induced crop yield losses in the northern hemisphere. *Biogeosciences*, 9(1):271–292, 2012. Cited on page 119.

- Huang, J., Guo, J., Wang, F., Liu, Z., Jeong, M.-J., Yu, H., and Zhang, Z. Calipso inferred most probable heights of global dust and smoke layers. *Journal of Geophysical Research: Atmospheres*, 120(10):5085–5100, 2015. Cited on pages 8, 18, 53, 63, 64, 81, and 82.
- Huete, A., Didan, K., Miura, T., Rodriguez, E. P., Gao, X., and Ferreira, L. G. Overview of the radiometric and biophysical performance of the modis vegetation indices. *Remote sensing of environment*, 83(1):195–213, 2002. Cited on page 61.
- Hurrell, J. W., Hack, J. J., Shea, D., Caron, J. M., and Rosinski, J. A new sea surface temperature and sea ice boundary dataset for the community atmosphere model. *Journal of Climate*, 21(19):5145–5153, 2008. doi: 10.1175/2008JCLI2292.1. URL <https://doi.org/10.1175/2008JCLI2292.1>. Cited on page 94.
- Ichoku, C., Kahn, R., and Chin, M. Satellite contributions to the quantitative characterization of biomass burning for climate modeling. *Atmospheric Research*, 111:1–28, 2012. Cited on page 92.
- Ignotti, E., Valente, J. G., Longo, K. M., Freitas, S. R., Hacon, S. d. S., and Artaxo Netto, P. Impact on human health of particulate matter emitted from burnings in the brazilian amazon region. *Revista de saude publica*, 44:121–130, 2010. Cited on page 12.
- Inness, A., Benedetti, A., Flemming, J., Huijnen, V., Kaiser, J., Parrington, M., and Remy, S. The enso signal in atmospheric composition fields: emission-driven versus dynamically induced changes. *Atmospheric Chemistry and Physics*, 15(15):9083–9097, 2015. Cited on page 85.
- INPE. Prodes—monitoramento da floresta amazônica brasileira por satélite (são José dos campos, sp). 2016. Cited on page 13.
- IPCC, I. P. o. C. C. *Fourth Assessment Report: Climate Change 2007: The AR4 Synthesis Report*. Geneva: IPCC, 2007. URL <http://www.ipcc.ch/ipccreports/ar4-wg1.htm>. Cited on pages 2 and 90.
- Ito, A. and Penner, J. E. Global estimates of biomass burning emissions based on satellite imagery for the year 2000. *Journal of Geophysical Research: Atmospheres*, 109(D14), 2004. doi: 10.1029/2003JD004423. Cited on page 1.
- Ito, K., De Leon, S. F., and Lippmann, M. Associations between ozone and daily mortality: analysis and meta-analysis. *Epidemiology*, pages 446–457, 2005. Cited on page 90.
- Itterly, K. F., Taylor, P. C., Dodson, J. B., and Tawfik, A. B. On the sensitivity of the diurnal cycle in the amazon to convective intensity. *Journal of Geophysical Research: Atmospheres*, 121(14):8186–8208, 2016. Cited on page 71.
- Jacobson, M. Z. Effects of biomass burning on climate, accounting for heat and moisture fluxes, black and brown carbon, and cloud absorption effects. *Journal of Geophysical Research: Atmospheres*, 119(14):8980–9002, 2014. doi: 10.1002/2014JD021861. URL <https://agupubs.onlinelibrary.wiley.com/doi/abs/10.1002/2014JD021861>. Cited on pages 2 and 122.
- Jaeglé, L., Steinberger, L., Martin, R. V., and Chance, K. Global partitioning of no x sources using satellite observations: Relative roles of fossil fuel combustion, biomass burning and soil emissions. *Faraday discussions*, 130:407–423, 2005. Cited on page 3.

- Jaffe, D., Bertschi, I., Jaeglé, L., Novelli, P., Reid, J. S., Tanimoto, H., Vingarzan, R., and Westphal, D. L. Long-range transport of siberian biomass burning emissions and impact on surface ozone in western north america. *Geophysical Research Letters*, 31(16), 2004. doi: 10.1029/2004GL020093. URL <https://agupubs.onlinelibrary.wiley.com/doi/abs/10.1029/2004GL020093>. Cited on page 91.
- Jaffe, D., Chand, D., Hafner, W., Westerling, A., and Spracklen, D. Influence of fires on o₃ concentrations in the western us. *Environmental science & technology*, 42(16): 5885–5891, 2008. Cited on pages 2, 7, and 91.
- Jaffe, D. A. and Wigder, N. L. Ozone production from wildfires: A critical review. *Atmospheric Environment*, 51:1–10, 2012. Cited on pages 1, 2, 4, 90, and 91.
- Jian, Y. and Fu, T.-M. Injection heights of springtime biomass-burning plumes over peninsular southeast asia and their impacts on long-range pollutant transport. *Atmospheric Chemistry and Physics*, 14(8):3977–3989, 2014. Cited on pages 8, 18, 52, 57, and 127.
- Johnston, F. H., Henderson, S. B., Chen, Y., Randerson, J. T., Marlier, M., DeFries, R. S., Kinney, P., Bowman, D. M., and Brauer, M. Estimated global mortality attributable to smoke from landscape fires. *Environmental health perspectives*, 120(5):695, 2012. Cited on page 52.
- Jonson, J., Simpson, D., Fagerli, H., and Solberg, S. Can we explain the trends in european ozone levels? *Atmospheric Chemistry and Physics*, 6(1):51–66, 2006. Cited on page 3.
- Jovanovic, V., Moroney, C., and Nelson, D. Multi-angle geometric processing for globally geo-located and co-registered misr image data. *Remote Sensing of Environment*, 107(1–2):22–32, 2007. Cited on page 41.
- Jovanovic, V. M., Smyth, M. M., Zong, J., Ando, R., and Bothwell, G. W. Misr photogrammetric data reduction for geophysical retrievals. *IEEE Transactions on Geoscience and Remote Sensing*, 36(4):1290–1301, 1998. Cited on page 24.
- Kahn, R. A. and Gaitley, B. J. An analysis of global aerosol type as retrieved by misr. *Journal of Geophysical Research: Atmospheres*, 120(9):4248–4281, 2015. Cited on page 56.
- Kahn, R. A. and Limbacher, J. Eyjafjallajökull volcano plume particle-type characterization from space-based multi-angle imaging. *Atmospheric Chemistry & Physics Discussions*, 12(7):9459–9477, 2012. Cited on page 24.
- Kahn, R. A., Garay, M. J., Nelson, D. L., Yau, K. K., Bull, M. A., Gaitley, B. J., Martonchik, J. V., and Levy, R. C. Satellite-derived aerosol optical depth over dark water from misr and modis: Comparisons with aeronet and implications for climatological studies. *Journal of Geophysical Research: Atmospheres*, 112(D18), 2007. doi: 10.1029/2006JD008175. Cited on pages 6, 22, 39, 52, 57, 60, 62, 68, and 69.
- Kahn, R. A., Chen, Y., Nelson, D. L., Leung, F.-Y., Li, Q., Diner, D. J., and Logan, J. A. Wildfire smoke injection heights: Two perspectives from space. *Geophysical Research Letters*, 35(4), 2008. doi: 10.1029/2007GL032165. Cited on pages 6, 8, 52, 56, 57, 65, 68, 69, 73, 78, 83, 84, and 86.
- Kalashnikova, O. V. and Kahn, R. A. Mineral dust plume evolution over the atlantic from misr and modis aerosol retrievals. *Journal of Geophysical Research: Atmospheres*, 113(D24), 2008. doi: 10.1029/2008JD010083. Cited on pages 24 and 45.

- Kauffman, J. B., Cummings, D., Ward, D., and Babbitt, R. Fire in the brazilian amazon: 1. biomass, nutrient pools, and losses in slashed primary forests. *Oecologia*, 104(4): 397–408, 1995. Cited on page 69.
- Kheirbek, I., Wheeler, K., Walters, S., Kass, D., and Matte, T. Pm 2.5 and ozone health impacts and disparities in new york city: sensitivity to spatial and temporal resolution. *Air Quality, Atmosphere & Health*, 6(2):473–486, 2013. Cited on pages 3 and 90.
- Kirchhoff, V. and Rasmussen, R. Time variations of co and o3 concentrations in a region subject to biomass burning. *Journal of Geophysical Research: Atmospheres*, 95(D6): 7521–7532, 1990. Cited on page 12.
- Kirchhoff, V., Setzer, A., and Pereira, M. Biomass burning in amazonia: Seasonal effects on atmospheric o3 and co. *Geophysical Research Letters*, 16(5):469–472, 1989. Cited on pages 11 and 113.
- Kirchhoff, V., Nakamura, Y., Marinho, E., and Mariano, M. Excess ozone production in amazonia from large scale burnings. *Journal of atmospheric and terrestrial physics*, 54(5):583–588, 1992. Cited on pages 90, 91, and 119.
- Kirkman, G., Gut, A., Ammann, C., Gatti, L., Cordova, A., Moura, M., Andreae, M., and Meixner, F. Surface exchange of nitric oxide, nitrogen dioxide, and ozone at a cattle pasture in rondonia, brazil. *Journal of Geophysical Research: Atmospheres*, 107(D20), 2002. Cited on pages 12 and 91.
- Kolusu, S. R., Marsham, J. H., Mulcahy, J., Johnson, B., Dunning, C., Bush, M., and Spracklen, D. V. Impacts of amazonia biomass burning aerosols assessed from short-range weather forecasts. *Atmospheric Chemistry and Physics*, 15(21):12251–12266, 2015. Cited on pages 12 and 53.
- Labonne, M., Bréon, F.-M., and Chevallier, F. Injection height of biomass burning aerosols as seen from a spaceborne lidar. *Geophysical Research Letters*, 34(11), 2007. Cited on pages 8, 53, and 83.
- Lamarque, J.-F., Bond, T. C., Eyring, V., Granier, C., Heil, A., Klimont, Z., Lee, D., Liousse, C., Mieville, A., Owen, B., Schultz, M. G., Shindell, D., Smith, S. J., Stehfest, E., Van Aardenne, J., Cooper, O. R., Kainuma, M., Mahowald, N., McConnell, J. R., Naik, V., Riahi, K., and van Vuuren, D. P. Historical (1850–2000) gridded anthropogenic and biomass burning emissions of reactive gases and aerosols: Methodology and application. *Atmospheric Chemistry and Physics*, 10(15):7017–7039, 2010. doi: 10.5194/acp-10-7017-2010. URL <https://www.atmos-chem-phys.net/10/7017/2010/>. Cited on page 95.
- Lamarque, J.-F., Emmons, L. K., Hess, P. G., Kinnison, D. E., Tilmes, S., Vitt, F., Heald, C. L., Holland, E. A., Lauritzen, P. H., Neu, J., Orlando, J. J., Rasch, P. J., and Tyndall, G. K. Cam-chem: description and evaluation of interactive atmospheric chemistry in the community earth system model. *Geoscientific Model Development*, 5(2):369–411, 2012. doi: 10.5194/gmd-5-369-2012. URL <https://www.geosci-model-dev.net/5/369/2012/>. Cited on pages 94 and 98.
- Langmann, B., Duncan, B., Textor, C., Trentmann, J., and van der Werf, G. R. Vegetation fire emissions and their impact on air pollution and climate. *Atmospheric Environment*, 43(1):107–116, 2009. ISSN 1352-2310. doi: <https://doi.org/10.1016/j.atmosenv.2008.09.047>. URL <http://www.sciencedirect.com/science/article/pii/S135223100800900X>. Cited on page 2.

- Lapina, K., Honrath, R., Owen, R., Val Martin, M., and Pfister, G. Evidence of significant large-scale impacts of boreal fires on ozone levels in the midlatitude northern hemisphere free troposphere. *Geophysical Research Letters*, 33(10), 2006. doi: 10.1029/2006GL025878. Cited on page 1.
- Laurance, W. F., Cochrane, M. A., Bergen, S., Fearnside, P. M., Delamônica, P., Barber, C., D'angelo, S., and Fernandes, T. The future of the brazilian amazon. *Science*, 291(5503):438–439, 2001. Cited on page 10.
- Lavoué, D., Lioussé, C., Cachier, H., Stocks, B. J., and Goldammer, J. G. Modeling of carbonaceous particles emitted by boreal and temperate wildfires at northern latitudes. *Journal of Geophysical Research: Atmospheres*, 105(D22):26871–26890, 2000. Cited on page 68.
- Lawrence, D., Fisher, R., and Koven, C. The community land model version 5: Description of new features, benchmarking, and impact of forcing uncertainty. *Journal Advanced Model Earth System*, 2018. Cited on page 94.
- Lerdau, M., Guenther, A., and Monson, R. Plant production and emission of volatile organic compounds. *Bioscience*, 47(6):373–383, 1997. Cited on page 3.
- Leung, F.-Y. T., Logan, J. A., Park, R., Hyer, E., Kasischke, E., Streets, D., and Yurganov, L. Impacts of enhanced biomass burning in the boreal forests in 1998 on tropospheric chemistry and the sensitivity of model results to the injection height of emissions. *Journal of Geophysical Research: Atmospheres*, 112(D10), 2007. Cited on page 92.
- Levy, H. Normal atmosphere: Large radical and formaldehyde concentrations predicted. *Science*, 173(3992):141–143, 1971. Cited on page 2.
- Levy, J. I., Carrothers, T. J., Tuomisto, J. T., Hammitt, J. K., and Evans, J. S. Assessing the public health benefits of reduced ozone concentrations. *Environmental health perspectives*, 109(12):1215–1226, 2001. Cited on page 90.
- Li, L. and Sokolik, I. Analysis of dust aerosol retrievals using satellite data in central asia. *Atmosphere*, 9(8):288, 2018. ISSN 2073–4433. Cited on page 45.
- Li, W., Fu, R., Juarez, R. I. N., and Fernandes, K. Observed change of the standardized precipitation index, its potential cause and implications to future climate change in the amazon region. *Philosophical Transactions of the Royal Society B: Biological Sciences*, 363(1498):1767–1772, 2008. Cited on page 93.
- Lippmann, M. Health effects of tropospheric ozone: review of recent research findings and their implications to ambient air quality standards. *Journal of exposure analysis and environmental epidemiology*, 3(1):103–129, 1993. Cited on page 2.
- Liu, H., Liu, S., Xue, B., Lv, Z., Meng, Z., Yang, X., Xue, T., Yu, Q., and He, K. Ground-level ozone pollution and its health impacts in china. *Atmospheric Environment*, 173: 223–230, 2018. Cited on pages 3 and 90.
- Liu, X., Ma, P. L., Wang, H., Tilmes, S., Singh, B., Easter, R. C., Ghan, S. J., and Rasch, P. J. Description and evaluation of a new four-mode version of the modal aerosol module (mam4) within version 5.3 of the community atmosphere model. *Geoscientific Model Development (Online)*, 9(2), 2 2016. doi: 10.5194/gmd-9-505-2016. Cited on page 94.

- Liu, Z., Vaughan, M., Winker, D., Kittaka, C., Getzewich, B., Kuehn, R., Omar, A., Powell, K., Treppe, C., and Hostetler, C. The calipso lidar cloud and aerosol discrimination: Version 2 algorithm and initial assessment of performance. *Journal of Atmospheric and Oceanic Technology*, 26(7):1198–1213, 2009. Cited on page 61.
- Lobert, J. M. and Warnatz, J. Emissions from the combustion process in vegetation. *Fire in the Environment*, 13:15–37, 1993. Cited on page 5.
- Lobert, J. M., Scharffe, D. H., Weimin, H., Kuhlbusch, T. A., Seuwen, R., Warneck, P., and Crutzen, P. J. Experimental evaluation of biomass burning emissions: Nitrogen and carbon containing compounds. In *Global biomass burning. Atmospheric, climatic, and biospheric implications*, volume 23. 1991. Cited on page 5.
- Logan, J. A., Prather, M. J., Wofsy, S. C., and McElroy, M. B. Tropospheric chemistry: A global perspective. *Journal of Geophysical Research: Oceans*, 86(C8):7210–7254, 1981. Cited on page 2.
- Luderer, G., Trentmann, J., Winterrath, T., Textor, C., Herzog, M., Graf, H., and Andreae, M. Modeling of biomass smoke injection into the lower stratosphere by a large forest fire (part ii): sensitivity studies. *Atmospheric Chemistry and Physics*, 6(12):5261–5277, 2006. Cited on page 68.
- Malhi, Y., Wood, D., Baker, T. R., Wright, J., Phillips, O. L., Cochrane, T., Meir, P., Chave, J., Almeida, S., Arroyo, L., et al. The regional variation of aboveground live biomass in old-growth amazonian forests. *Global Change Biology*, 12(7):1107–1138, 2006. Cited on page 10.
- Malhi, Y., Roberts, J. T., Betts, R. A., Killeen, T. J., Li, W., and Nobre, C. A. Climate change, deforestation, and the fate of the amazon. *Science*, 319(5860):169–172, 2008. ISSN 0036-8075. doi: 10.1126/science.1146961. URL <http://science.sciencemag.org/content/319/5860/169>. Cited on pages 10, 51, and 86.
- Marais, E. A., Jacob, D. J., Wecht, K., Lerot, C., Zhang, L., Yu, K., Kurosu, T., Chance, K., and Sauvage, B. Anthropogenic emissions in nigeria and implications for atmospheric ozone pollution: A view from space. *Atmospheric environment*, 99:32–40, 2014. Cited on page 2.
- Marengo, F., Johnson, B., Langridge, J. M., Mulcahy, J., Benedetti, A., Remy, S., Jones, L., Szpek, K., Haywood, J., Longo, K., et al. On the vertical distribution of smoke in the amazonian atmosphere during the dry season. 2016. doi: 10.5194/acpd-15-31739-2015. Cited on pages 8, 53, and 92.
- Marengo, J. A. and Espinoza, J. Extreme seasonal droughts and floods in amazonia: causes, trends and impacts. *International Journal of Climatology*, 36(3):1033–1050, 2016. Cited on page 10.
- Marengo, J. A. and Nobre, C. A. to the global climate system. *The Biogeochemistry of the Amazon Basin*, page 17, 2001. Cited on page 14.
- Marengo, J. A., Alves, L. M., Soares, W. R., Rodriguez, D. A., Camargo, H., Riveros, M. P., and Pabló, A. D. Two contrasting severe seasonal extremes in tropical south america in 2012: flood in amazonia and drought in northeast brazil. *Journal of climate*, 26(22):9137–9154, 2013. Cited on page 59.

- Marengo, J. A., Alves, L. M., Alvala, R., Cunha, A. P., Brito, S., and Moraes, O. L. Climatic characteristics of the 2010–2016 drought in the semiarid northeast brazil region. *Anais da Academia Brasileira de Ciências*, 90(2):1973–1985, 2018. Cited on page 11.
- Martin, S., Artaxo, P., Machado, L., Manzi, A., Souza, R., Schumacher, C., Wang, J., Andreae, M., Barbosa, H., Fan, J., et al. Introduction: Observations and modeling of the green ocean amazon (goamazon2014/5). *Atmospheric Chemistry and Physics*, 16(8), 2016. Cited on pages 12 and 53.
- Martonchik, J. V., Kahn, R. A., and Diner, D. J. Retrieval of aerosol properties over land using misr observations. In *Satellite Aerosol Remote Sensing Over Land*, pages 267–293. Springer, 2009. Cited on page 56.
- Matson, M. and Dozier, J. Identification of subresolution high temperature sources using a thermal ir sensor. *Photogrammetric Engineering and Remote Sensing*, 47(9):1311–1318, 1981. Cited on page 22.
- Mauzerall, D. L., Logan, J. A., Jacob, D. J., Anderson, B. E., Blake, D. R., Bradshaw, J. D., Heikes, B., Sachse, G. W., Singh, H., and Talbot, B. Photochemistry in biomass burning plumes and implications for tropospheric ozone over the tropical south atlantic. *Journal of Geophysical Research: Atmospheres*, 103(D7):8401–8423, 1998. Cited on page 118.
- Mazzoni, D., Logan, J. A., Diner, D., Kahn, R., Tong, L., and Li, Q. A data-mining approach to associating misr smoke plume heights with modis fire measurements. *Remote Sensing of Environment*, 107(1-2):138–148, 2007. Cited on page 8.
- Mickley, L. J., Murti, P., Jacob, D. J., Logan, J. A., Koch, D., and Rind, D. Radiative forcing from tropospheric ozone calculated with a unified chemistry-climate model. *Journal of Geophysical Research: Atmospheres*, 104(D23):30153–30172, 1999. Cited on page 2.
- Mills, G., Buse, A., Gimeno, B., Bermejo, V., Holland, M., Emberson, L., and Pleijel, H. A synthesis of aot40-based response functions and critical levels of ozone for agricultural and horticultural crops. *Atmospheric Environment*, 41(12):2630–2643, 2007. Cited on pages 119 and 126.
- Mills, G., Pleijel, H., Malley, C., Sinha, B., Cooper, O., Schultz, M., Neufeld, H., Simpson, D., Sharps, K., Feng, Z., et al. Tropospheric ozone assessment report: present day tropospheric ozone distribution and trends relevant to vegetation. *elem sci anth* 6: 47, 2018. Cited on pages 10, 122, 124, and 126.
- Mims, S. R., Kahn, R. A., Moroney, C. M., Gaitley, B. J., Nelson, D. L., and Garay, M. J. Misr stereo heights of grassland fire smoke plumes in australia. *IEEE Transactions on Geoscience and Remote Sensing*, 48(1):25–35, 2010. Cited on pages 8, 18, 24, 31, and 52.
- Mishra, A. K., Lehahn, Y., Rudich, Y., and Koren, I. Co-variability of smoke and fire in the amazon basin. *Atmospheric Environment*, 109:97–104, 2015. Cited on pages 9 and 72.
- Monfreda, C., Ramankutty, N., and Foley, J. A. Farming the planet: 2. geographic distribution of crop areas, yields, physiological types, and net primary production in the year 2000. *Global biogeochemical cycles*, 22(1), 2008. Cited on pages 122 and 123.

- Morgenstern, O., Zeng, G., Wood, S. W., Robinson, J., Smale, D., Paton-Walsh, C., Jones, N. B., and Griffith, D. W. T. Long-range correlations in fourier transform infrared, satellite, and modeled co in the southern hemisphere. *Journal of Geophysical Research: Atmospheres*, 117(D11), 2012. doi: 10.1029/2012JD017639. URL <https://agupubs.onlinelibrary.wiley.com/doi/abs/10.1029/2012JD017639>. Cited on page 100.
- Moroney, C., Davies, R., and Muller, J.-P. Operational retrieval of cloud-top heights using misr data. *IEEE Transactions on Geoscience and Remote Sensing*, 40(7):1532–1540, 2002a. Cited on pages 21, 22, 28, and 56.
- Moroney, C., Horváth, Á., and Davies, R. Use of stereo-matching to coregister multiangle data from misr. *IEEE transactions on geoscience and remote sensing*, 40(7):1541–1546, 2002b. Cited on page 28.
- Moxim, W. and Levy, H. A model analysis of the tropical south atlantic ocean tropospheric ozone maximum: The interaction of transport and chemistry. *Journal of Geophysical Research: Atmospheres*, 105(D13):17393–17415, 2000. Cited on page 118.
- MPHP2. Misr plume height project 2. <https://misr.jpl.nasa.gov/getData/accessData/MisrMinxPlumes2>; last accessed on 11 February 2019. Cited on page 96.
- Mu, Q., Heinsch, F. A., Zhao, M., and Running, S. W. Development of a global evapotranspiration algorithm based on modis and global meteorology data. *Remote sensing of Environment*, 111(4):519–536, 2007. Cited on page 61.
- Mu, Q., Zhao, M., and Running, S. W. Modis global terrestrial evapotranspiration (et) product (nasa mod16a2/a3). *Algorithm Theoretical Basis Document, Collection*, 5, 2013. Cited on pages 55 and 61.
- Muller, J.-P., Mandanayake, A., Moroney, C., Davies, R., Diner, D. J., and Paradise, S. Misr stereoscopic image matchers: Techniques and results. *IEEE Transactions on Geoscience and Remote Sensing*, 40(7):1547–1559, 2002. Cited on pages 21 and 56.
- Nassar, R., Logan, J. A., Megretskaia, I. A., Murray, L. T., Zhang, L., and Jones, D. Analysis of tropical tropospheric ozone, carbon monoxide, and water vapor during the 2006 el niño using tes observations and the geos-chem model. *Journal of Geophysical Research: Atmospheres*, 114(D17), 2009. Cited on page 91.
- Nelson, D., Averill, C., Boland, S., Morford, R., Garay, M., Thompson, C., Hall, J., Diner, D., and Camphell, H. Misr interactive explorer (minx) v1.0 user's guide. *Jet Propulsion Laboratory*, 480, 2008a. Cited on page 41.
- Nelson, D., Chen, Y., Kahn, R., J. Diner, D., and Mazzoni, D. Example applications of the misr interactive explorer (minx) software tool to wildfire smoke plume analyses. *Proc SPIE*, 7089:708909, 03 2008b. doi: 10.1117/12.795087. Cited on pages 19, 24, and 32.
- Nelson, D. L., Garay, M. J., Kahn, R. A., and Dunst, B. A. Stereoscopic height and wind retrievals for aerosol plumes with the misr interactive explorer (minx). *Remote Sensing*, 5(9):4593–4628, 2013. ISSN 2072–4292. doi: 10.3390/rs5094593. Cited on pages 19, 24, 40, 45, 47, 48, 54, 57, 58, and 67.

- Nepstad, D., Schwartzman, S., Bamberger, B., Santilli, M., Ray, D., Schlesinger, P., Lefebvre, P., Alencar, A., Prinz, E., Fiske, G., et al. Inhibition of amazon deforestation and fire by parks and indigenous lands. *Conservation Biology*, 20(1):65–73, 2006. Cited on pages 52 and 59.
- Nepstad, D. C., Stickler, C. M., Soares-Filho, B., and Merry, F. Interactions among amazon land use, forests and climate: prospects for a near-term forest tipping point. *Philosophical Transactions of the Royal Society of London B: Biological Sciences*, 363(1498):1737–1746, 2008. Cited on page 69.
- Nobre, C. A., Sellers, P. J., and Shukla, J. Amazonian deforestation and regional climate change. *Journal of climate*, 4(10):957–988, 1991. Cited on page 14.
- Nobre, C. A., Sampaio, G., Borma, L. S., Castilla-Rubio, J. C., Silva, J. S., and Cardoso, M. Land-use and climate change risks in the amazon and the need of a novel sustainable development paradigm. *Proceedings of the National Academy of Sciences*, 113(39): 10759–10768, 2016. Cited on pages 10 and 11.
- Novelli, P., Masarie, K., and Lang, P. Distributions and recent changes of carbon monoxide in the lower troposphere. *Journal of Geophysical Research: Atmospheres*, 103(D15): 19015–19033, 1998. Cited on page 2.
- Oleson, K. W., Lawrence, D. M., B, G., Flanner, M. G., Kluzek, E., J, P., Levis, S., Swenson, S. C., Thornton, E., Feddema, J., Heald, C. L., francois Lamarque, J., yue Niu, G., Qian, T., Running, S., Sakaguchi, K., Yang, L., Zeng, X., Zeng, X., and Decker, M. Technical description of version 4.0 of the community land model (clm). *NCAR TECHNICAL NOTE*, 2010. Cited on page 94.
- Omar, A. H., Winker, D. M., Vaughan, M. A., Hu, Y., Treppe, C. R., Ferrare, R. A., Lee, K.-P., Hostetler, C. A., Kittaka, C., Rogers, R. R., et al. The calipso automated aerosol classification and lidar ratio selection algorithm. *Journal of Atmospheric and Oceanic Technology*, 26(10):1994–2014, 2009. Cited on page 61.
- Pacifico, F., Folberth, G., Sitch, S., Haywood, J., Rizzo, L., Malavelle, F., and Artaxo, P. Biomass burning related ozone damage on vegetation over the amazon forest: a model sensitivity study. *Atmospheric Chemistry and Physics*, 15(5):2791–2804, 2015. Cited on pages 13, 52, 91, 113, 124, and 128.
- PANGAEA. <https://doi.pangaea.de/10.1594/PANGAEA.876108>, last accessed on 15 December 2018. Cited on page 100.
- Paugam, R., Wooster, M., Freitas, S., and Val Martin, M. A review of approaches to estimate wildfire plume injection height within large-scale atmospheric chemical transport models. *Atmospheric Chemistry and Physics*, 16(2):907–925, 2016. Cited on pages 6, 7, 52, and 91.
- Pereira, G., Siqueira, R., Rosário, N. E., Longo, K. L., Freitas, S. R., Cardozo, F. S., Kaiser, J. W., and Wooster, M. J. Assessment of fire emission inventories during the south american biomass burning analysis (sambba) experiment. *Atmospheric Chemistry and Physics*, 16(11):6961–6975, 2016. Cited on page 104.
- Pfister, G., Wiedinmyer, C., and Emmons, L. Impacts of the fall 2007 california wildfires on surface ozone: Integrating local observations with global model simulations. *Geophysical Research Letters*, 35(19), 2008. Cited on pages 7, 91, and 119.

- Price, C. and Rind, D. A simple lightning parameterization for calculating global lightning distributions. *Journal of Geophysical Research: Atmospheres*, 97(D9):9919–9933, 1992. Cited on page [95](#).
- Price, C., Penner, J., and Prather, M. Nox from lightning: 2. constraints from the global atmospheric electric circuit. *Journal of Geophysical Research: Atmospheres*, 102(D5): 5943–5951, 1997. Cited on page [95](#).
- Radke, L. F., Hegg, D. A., Hobbs, P. V., Nance, J. D., Lyons, J. H., Laursen, K. K., Weiss, R. E., Riggan, P. J., and Ward, D. E. Particulate and trace gas emissions from large biomass fires in north america. *Global biomass burning: Atmospheric, climatic, and biospheric implications*, pages 209–224, 1991. Cited on page [5](#).
- Ramanathan, V. and Carmichael, G. Global and regional climate changes due to black carbon. *Nature geoscience*, 1(4):221–227, 2008. Cited on page [2](#).
- Ramanathan, V., Crutzen, P., Kiehl, J., and Rosenfeld, D. Aerosols, climate, and the hydrological cycle. *science*, 294(5549):2119–2124, 2001. Cited on pages [2](#) and [52](#).
- Real, E., Law, K., Weinzierl, B., Fiebig, M., Petzold, A., Wild, O., Methven, J., Arnold, S., Stohl, A., Huntrieser, H., et al. Processes influencing ozone levels in alaskan forest fire plumes during long-range transport over the north atlantic. *Journal of Geophysical Research: Atmospheres*, 112(D10), 2007. Cited on pages [91](#) and [110](#).
- Reddington, C., Butt, E., Ridley, D., Artaxo, P., Morgan, W., Coe, H., and Spracklen, D. Air quality and human health improvements from reductions in deforestation-related fire in brazil. *Nature Geoscience*, 8(10):768, 2015. Cited on pages [2](#), [12](#), [52](#), [79](#), [122](#), and [128](#).
- Reddington, C. L., Spracklen, D. V., Artaxo, P., Ridley, D. A., Rizzo, L. V., and Arana, A. Analysis of particulate emissions from tropical biomass burning using a global aerosol model and long-term surface observations. *Atmospheric Chemistry and Physics*, 16(17): 11083–11106, 2016. Cited on page [86](#).
- Register, U. F. National ambient air quality standards for ozone. 40 CFR(Part 50, 51, 52, 53, and 58):65292—65468, 2015. Cited on page [10](#).
- Reich, P. B. and Amundson, R. G. Ambient levels of ozone reduce net photosynthesis in tree and crop species. *Science*, 230(4725):566–570, 1985. Cited on page [90](#).
- Reichle, H. G., Connors, V. S., Holland, J. A., Hypes, W. D., Wallio, H. A., Casas, J. C., Gormsen, B. B., Saylor, M. S., and Hesketh, W. D. Middle and upper tropospheric carbon monoxide mixing ratios as measured by a satellite-borne remote sensor during november 1981. *Journal of Geophysical Research: Atmospheres*, 91(D10):10865–10887, 1986. Cited on page [12](#).
- Reid, J., Koppmann, R., Eck, T., and Eleuterio, D. A review of biomass burning emissions part ii: intensive physical properties of biomass burning particles. *Atmospheric Chemistry and Physics*, 5(3):799–825, 2005. Cited on pages [5](#) and [110](#).
- Reidmiller, D., Fiore, A. M., Jaffe, D., Bergmann, D., Cuvelier, C., Dentener, F., Duncan, B. N., Folberth, G., Gauss, M., Gong, S., et al. The influence of foreign vs. north american emissions on surface ozone in the us. *Atmospheric Chemistry and Physics*, 9 (14):5027–5042, 2009. Cited on page [119](#).

- Rein, G. Smoldering combustion. In *SFPE Handbook of Fire Protection Engineering*, pages 581–603. Springer, 2016. Cited on pages 5 and 6.
- Rémy, S., Veira, A., Paugam, R., Sofiev, M., Kaiser, J. W., Marengo, F., Burton, S. P., Benedetti, A., Engelen, R. J., Ferrare, R., and Hair, J. W. Two global data sets of daily fire emission injection heights since 2003. *Atmospheric Chemistry and Physics*, 17(4):2921–2942, 2017. doi: 10.5194/acp-17-2921-2017. URL <https://www.atmos-chem-phys.net/17/2921/2017/>. Cited on page 7.
- Rio, C., Hourdin, F., and Chédin, A. Numerical simulation of tropospheric injection of biomass burning products by pyro-thermal plumes. *Atmospheric Chemistry and Physics*, 10(8):3463–3478, 2010. Cited on page 92.
- Rogers, R. R., Hostetler, C. A., Hair, J. W., Ferrare, R. A., Liu, Z., Obland, M. D., Harper, D. B., Cook, A. L., Powell, K. A., Vaughan, M. A., et al. Assessment of the calipso lidar 532 nm attenuated backscatter calibration using the nasa larc airborne high spectral resolution lidar. *Atmospheric Chemistry and Physics*, 11(3):1295–1311, 2011. Cited on page 62.
- Rubio, M., Lissi, E., Gramsch, E., and Garreaud, R. Effect of nearby forest fires on ground level ozone concentrations in santiago, chile. *Atmosphere*, 6(12):1926–1938, 2015. Cited on pages 7 and 91.
- Saatchi, S. S., Harris, N. L., Brown, S., Lefsky, M., Mitchard, E. T., Salas, W., Zutta, B. R., Buermann, W., Lewis, S. L., Hagen, S., et al. Benchmark map of forest carbon stocks in tropical regions across three continents. *Proceedings of the national academy of sciences*, 108(24):9899–9904, 2011. Cited on page 10.
- Sauvage, B., Martin, R. V., Van Donkelaar, A., and Ziemke, J. Quantification of the factors controlling tropical tropospheric ozone and the south atlantic maximum. *Journal of Geophysical Research: Atmospheres*, 112(D11), 2007. Cited on page 118.
- Schultz, M. G., Schröder, S., Lyapina, O., Cooper, O., Galbally, I., Petropavlovskikh, I., Von Schneidmesser, E., Tanimoto, H., Elshorbany, Y., Naja, M., et al. Tropospheric ozone assessment report: Database and metrics data of global surface ozone observations. 2017. doi: 10.1525/elementa.244. Cited on page 100.
- Schweizer, D. and Cisneros, R. Forest fire policy: change conventional thinking of smoke management to prioritize long-term air quality and public health. *Air Quality, Atmosphere & Health*, 10(1):33–36, 2017. Cited on page 7.
- Scollo, S., Kahn, R., Nelson, D., Coltelli, M., Diner, D., Garay, M., and Realmuto, V. Misr observations of etna volcanic plumes. *Journal of Geophysical Research: Atmospheres*, 117(D6), 2012. doi: 10.1029/2011JD016625. Cited on pages 24, 45, and 46.
- Seinfeld, J. H. and Pandis, S. N. From air pollution to climate change. *Atmospheric Chemistry and Physics*, page 1326, 1998. Cited on pages 2 and 3.
- Sillman, S. The relation between ozone, nox and hydrocarbons in urban and polluted rural environments. *Atmospheric Environment*, 33(12):1821–1845, 1999. Cited on page 4.
- Simpson, I. J., Rowland, F. S., Meinardi, S., and Blake, D. R. Influence of biomass burning during recent fluctuations in the slow growth of global tropospheric methane. *Geophysical Research Letters*, 33(22), 2006. doi: 10.1029/2006GL027330. Cited on page 1.

- Singh, H., Anderson, B., Brune, W., Cai, C., Cohen, R., Crawford, J., Cubison, M., Czech, E., Emmons, L., Fuelberg, H., et al. Pollution influences on atmospheric composition and chemistry at high northern latitudes: Boreal and california forest fire emissions. *Atmospheric Environment*, 44(36):4553–4564, 2010. Cited on page 5.
- Sitch, S., Cox, P., Collins, W., and Huntingford, C. Indirect radiative forcing of climate change through ozone effects on the land-carbon sink. *Nature*, 448(7155):791, 2007. Cited on pages 2 and 90.
- Sofiev, M., Vankevich, R., Lotjonen, M., Prank, M., Petukhov, V., Ermakova, T., Koskinen, J., and Kukkonen, J. An operational system for the assimilation of the satellite information on wild-land fires for the needs of air quality modelling and forecasting. *Atmospheric Chemistry and Physics*, 9(18):6833–6847, 2009. Cited on page 68.
- Sofiev, M., Vankevich, R., Ermakova, T., and Hakkarainen, J. Global mapping of maximum emission heights and resulting vertical profiles of wildfire emissions. *Atmospheric Chemistry and Physics*, 13(14):7039–7052, 2013. Cited on page 52.
- Spracklen, D. and Garcia-Carreras, L. The impact of amazonian deforestation on amazon basin rainfall. *Geophysical Research Letters*, 42(21):9546–9552, 2015. Cited on page 11.
- Spracklen, D. V., Mickley, L. J., Logan, J. A., Hudman, R. C., Yevich, R., Flannigan, M. D., and Westerling, A. L. Impacts of climate change from 2000 to 2050 on wildfire activity and carbonaceous aerosol concentrations in the western united states. *Journal of Geophysical Research: Atmospheres*, 114(D20), 2009. Cited on page 93.
- Stein, O., Schultz, M., Bouarar, I., Clark, H., Huijnen, V., Gaudel, A., George, M., and Clerbaux, C. On the wintertime low bias of northern hemisphere carbon monoxide found in global model simulations. *Atmospheric chemistry and physics*, 14(17):9295–9316, 2014. Cited on page 115.
- Tai, A. P., Martin, M. V., and Heald, C. L. Threat to future global food security from climate change and ozone air pollution. *Nature Climate Change*, 4(9):817, 2014. Cited on page 9.
- Tang, W. and Arellano, A. Investigating dominant characteristics of fires across the amazon during 2005–2014 through satellite data synthesis of combustion signatures. *Journal of Geophysical Research: Atmospheres*, 122(2):1224–1245, 2017. Cited on pages 71, 78, 79, and 85.
- Thompson, A., Diab, R., Bodeker, G., Zunckel, M., Coetzee, G., Archer, C., McNamara, D., Pickering, K., Combrink, J., Fishman, J., et al. Ozone over southern africa during safari-92/trace a. *Journal of Geophysical Research: Atmospheres*, 101(D19):23793–23807, 1996. Cited on page 118.
- Thompson, A. M., Witte, J. C., Hudson, R. D., Guo, H., Herman, J. R., and Fujiwara, M. Tropical tropospheric ozone and biomass burning. *Science*, 291(5511):2128–2132, 2001. Cited on pages 12, 90, and 110.
- Thornhill, G. D., Ryder, C. L., Highwood, E. J., Shaffrey, L. C., and Johnson, B. T. The effect of south american biomass burning aerosol emissions on the regional climate. *Atmospheric Chemistry and Physics Discussions*, 2017:1–34, 2017. doi: 10.5194/acp-2017-953. URL <https://www.atmos-chem-phys-discuss.net/acp-2017-953/>. Cited on page 53.

- Tilmes, S., Lamarque, J.-F., Emmons, L. K., Conley, A., Schultz, M. G., Saunio, M., Thouret, V., Thompson, A. M., Oltmans, S. J., Johnson, B., and Tarasick, D. Technical note: Ozone-sonde climatology between 1995 and 2011: description, evaluation and applications. *Atmospheric Chemistry and Physics*, 12(16):7475–7497, 2012. doi: 10.5194/acp-12-7475-2012. URL <https://www.atmos-chem-phys.net/12/7475/2012/>. Cited on page 100.
- Tilmes, S., Lamarque, J.-F., Emmons, L. K., Kinnison, D. E., Ma, P.-L., Liu, X., Ghan, S., Bardeen, C., Arnold, S., Deeter, M., Vitt, F., Ryerson, T., Elkins, J. W., Moore, F., Spackman, J. R., and Val Martin, M. Description and evaluation of tropospheric chemistry and aerosols in the community earth system model (cesm1.2). *Geoscientific Model Development*, 8(5):1395–1426, 2015. doi: 10.5194/gmd-8-1395-2015. URL <https://www.geosci-model-dev.net/8/1395/2015/>. Cited on page 98.
- Tilmes, S., Lamarque, J.-F., Emmons, L. K., Kinnison, D. E., Marsh, D., Garcia, R. R., Smith, A. K., Neely, R. R., Conley, A., Vitt, F., Val Martin, M., Tanimoto, H., Simpson, I., Blake, D. R., and Blake, N. Representation of the community earth system model (cesm1) cam4-chem within the chemistry-climate model initiative (ccmi). *Geoscientific Model Development*, 9(5):1853–1890, 2016. doi: 10.5194/gmd-9-1853-2016. URL <https://www.geosci-model-dev.net/9/1853/2016/>. Cited on pages 94 and 98.
- Tosca, M., Randerson, J., Zender, C., Nelson, D., Diner, D., and Logan, J. Dynamics of fire plumes and smoke clouds associated with peat and deforestation fires in indonesia. *Journal of Geophysical Research: Atmospheres*, 116(D8), 2011. doi: 10.1029/2010JD015148. Cited on pages 8, 18, 24, 52, 57, 63, 65, 68, 73, and 83.
- Trentmann, J., Andreae, M., Graf, H.-F., Hobbs, P., Ottmar, R., and Trautmann, T. Simulation of a biomass-burning plume: Comparison of model results with observations. *Journal of Geophysical Research: Atmospheres*, 107(D2), 2002. doi: 10.1029/2001JD000410. Cited on page 6.
- Trentmann, J., Luderer, G., Winterrath, T., Fromm, M., Servranckx, R., Textor, C., Herzog, M., Graf, H.-F., and Andreae, M. Modeling of biomass smoke injection into the lower stratosphere by a large forest fire (part i): reference simulation. *Atmospheric Chemistry and Physics*, 6(12):5247–5260, 2006. Cited on page 68.
- Turquety, S., Logan, J. A., Jacob, D. J., Hudman, R. C., Leung, F. Y., Heald, C. L., Yantosca, R. M., Wu, S., Emmons, L. K., Edwards, D. P., et al. Inventory of boreal fire emissions for north america in 2004: Importance of peat burning and pyroconvective injection. *Journal of Geophysical Research: Atmospheres*, 112(D12), 2007. Cited on page 92.
- Twomey, S. The influence of pollution on the shortwave albedo of clouds. *Journal of the atmospheric sciences*, 34(7):1149–1152, 1977. Cited on page 2.
- USDA. https://ipad.fas.usda.gov/rssiws/al/crop_calendar/nsa.aspx, 2019. Online; last accessed on 2 January 2019. Cited on page 123.
- Vadrevu, K. P., Lasko, K., Giglio, L., and Justice, C. Vegetation fires, absorbing aerosols and smoke plume characteristics in diverse biomass burning regions of asia. *Environmental Research Letters*, 10(10):105003, 2015. Cited on pages 8 and 83.
- Val Martin, M., Honrath, R., Owen, R. C., Pfister, G., Fialho, P., and Barata, F. Significant enhancements of nitrogen oxides, black carbon, and ozone in the north atlantic

- lower free troposphere resulting from north american boreal wildfires. *Journal of Geophysical Research: Atmospheres*, 111(D23), 2006. doi: 10.1029/2006JD007530. Cited on page 1.
- Val Martin, M., Logan, J., Kahn, R., Leung, F.-Y., Nelson, D., and Diner, D. Smoke injection heights from fires in north america: analysis of 5 years of satellite observations. *Atmospheric Chemistry & Physics*, 10(4):1491–1510, 2010. Cited on pages 6, 8, 18, 24, 27, 52, 57, 60, 62, 68, 69, 73, 83, and 92.
- Val Martin, M., Kahn, R. A., Logan, J. A., Paugam, R., Wooster, M., and Ichoku, C. Space-based observational constraints for 1-d fire smoke plume-rise models. *Journal of Geophysical Research: Atmospheres*, 117(D22), 2012. doi: 10.1029/2012JD018370. Cited on pages 7, 52, 68, 69, and 92.
- Val Martin, M., Heald, C., Lamarque, J.-F., Tilmes, S., Emmons, L., and Schichtel, B. How emissions, climate, and land use change will impact mid-century air quality over the united states: a focus on effects at national parks. *Atmospheric Chemistry and Physics*, 15(5):2805–2823, 2015. Cited on page 98.
- Val Martin, M., Kahn, R., and Tosca, M. A global analysis of wildfire smoke injection heights derived from space-based multi-angle imaging. *Remote Sensing*, 10(10):1609, 2018a. Cited on pages 58, 73, and 86.
- Val Martin, M., Kahn, R. A., and Tosca, M. G. A global analysis of wildfire smoke injection heights derived from space-based multi-angle imaging. *Remote Sensing*, 10(10), 2018b. ISSN 2072–4292. doi: 10.3390/rs10101609. Cited on pages 8, 92, 93, 95, 96, 97, 101, and 104.
- van der Werf, G. R., Randerson, J. T., Giglio, L., Collatz, G. J., Kasibhatla, P. S., and Arellano Jr, A. F. Interannual variability in global biomass burning emissions from 1997 to 2004. *Atmospheric Chemistry and Physics*, 6(11):3423–3441, 2006. Cited on page 1.
- Van der Werf, G. R., Randerson, J. T., Giglio, L., Collatz, G., Mu, M., Kasibhatla, P. S., Morton, D. C., DeFries, R., Jin, Y. v., and van Leeuwen, T. T. Global fire emissions and the contribution of deforestation, savanna, forest, agricultural, and peat fires (1997–2009). *Atmospheric chemistry and physics*, 10(23):11707–11735, 2010. Cited on pages 9, 18, 52, 71, 89, 104, 116, and 117.
- Van Dingenen, R., Dentener, F. J., Raes, F., Krol, M. C., Emberson, L., and Cofala, J. The global impact of ozone on agricultural crop yields under current and future air quality legislation. *Atmospheric Environment*, 43(3):604–618, 2009a. Cited on pages 90, 119, and 122.
- Van Dingenen, R., Dentener, F. J., Raes, F., Krol, M. C., Emberson, L., and Cofala, J. The global impact of ozone on agricultural crop yields under current and future air quality legislation. *Atmospheric Environment*, 43(3):604–618, 2009b. Cited on pages 3 and 9.
- Vaughan, M. A., Young, S. A., Winker, D. M., Powell, K. A., Omar, A. H., Liu, Z., Hu, Y., and Hostetler, C. A. Fully automated analysis of space-based lidar data: An overview of the calipso retrieval algorithms and data products. In *Laser radar techniques for atmospheric sensing*, volume 5575, pages 16–31. International Society for Optics and Photonics, 2004. Cited on page 61.

- Verma, S., Worden, J., Pierce, B., Jones, D. B. A., Al-Saadi, J., Boersma, F., Bowman, K., Eldering, A., Fisher, B., Jourdain, L., Kulawik, S., and Worden, H. Ozone production in boreal fire smoke plumes using observations from the tropospheric emission spectrometer and the ozone monitoring instrument. *Journal of Geophysical Research: Atmospheres*, 114(D2), 2009. doi: 10.1029/2008JD010108. Cited on page 5.
- Vernon, C. J., Bolt, R., Canty, T., and Kahn, R. A. The impact of misr-derived injection height initialization on wildfire and volcanic plume dispersion in the hysplit model. *Atmospheric Measurement Techniques*, 11(11):6289–6307, 2018. Cited on page 86.
- Watson, C. E., Fishman, J., and Reichle, H. G. The significance of biomass burning as a source of carbon monoxide and ozone in the southern hemisphere tropics: A satellite analysis. *Journal of Geophysical Research: Atmospheres*, 95(D10):16443–16450, 1990. Cited on page 12.
- Wegesser, T. C., Pinkerton, K. E., and Last, J. A. California wildfires of 2008: coarse and fine particulate matter toxicity. *Environmental health perspectives*, 117(6):893–897, 2009. Cited on page 7.
- Werth, D. and Avissar, R. The local and global effects of amazon deforestation. *Journal of Geophysical Research: Atmospheres*, 107(D20):LBA–55, 2002. Cited on page 14.
- WHO. *Health risks of ozone from long-range transboundary air pollution*. WHO Regional Office Europe, 2008. Cited on page 9.
- Wiedinmyer, C., Akagi, S., Yokelson, R., Emmons, L., Al-Saadi, J., Orlando, J., and Soja, A. The fire inventory from near (finn)—a high resolution global model to estimate the emissions from open burning. *Geosci. Model Dev. Discuss*, 3:2439–2476, 2010. Cited on page 1.
- Wiedinmyer, C., Akagi, S., Yokelson, R. J., Emmons, L., Al-Saadi, J., Orlando, J., and Soja, A. The fire inventory from near (finn): A high resolution global model to estimate the emissions from open burning. *Geoscientific Model Development*, 4(3):625, 2011. doi: 10.5194/gmd-4-625-2011. Cited on page 95.
- Williams, J., Van Velthoven, P., and Brenninkmeijer, C. Quantifying the uncertainty in simulating global tropospheric composition due to the variability in global emission estimates of biogenic volatile organic compounds. *Atmospheric Chemistry and Physics*, 13(5):2857–2891, 2013. Cited on page 90.
- Winker, D., Tackett, J., Getzewich, B., Liu, Z., Vaughan, M., and Rogers, R. The global 3-d distribution of tropospheric aerosols as characterized by caliop. *Atmospheric Chemistry and Physics*, 13(6):3345–3361, 2013. Cited on pages 55 and 61.
- Winker, D. M., Vaughan, M. A., Omar, A., Hu, Y., Powell, K. A., Liu, Z., Hunt, W. H., and Young, S. A. Overview of the calipso mission and caliop data processing algorithms. *Journal of Atmospheric and Oceanic Technology*, 26(11):2310–2323, 2009. doi: 10.1175/2009JTECHA1281.1. URL <https://doi.org/10.1175/2009JTECHA1281.1>. Cited on pages 18, 62, and 81.
- Xing, J., Wang, J., Mathur, R., Wang, S., Sarwar, G., Pleim, J., Hogrefe, C., Zhang, Y., Jiang, J., Wong, D. C., et al. Impacts of aerosol direct effects on tropospheric ozone through changes in atmospheric dynamics and photolysis rates. *Atmospheric chemistry and physics*, 17(16):9869–9883, 2017. Cited on page 5.

- Yokelson, R. J., Susott, R., Ward, D. E., Reardon, J., and Griffith, D. W. Emissions from smoldering combustion of biomass measured by open-path fourier transform infrared spectroscopy. *Journal of Geophysical Research: Atmospheres*, 102(D15):18865–18877, 1997. Cited on page 5.
- Yokelson, R. J., Bertschi, I. T., Christian, T. J., Hobbs, P. V., Ward, D. E., and Hao, W. M. Trace gas measurements in nascent, aged, and cloud-processed smoke from african savanna fires by airborne fourier transform infrared spectroscopy (aftir). *Journal of Geophysical Research: Atmospheres*, 108(D13), 2003. Cited on page 90.
- Young, P. J., Naik, V., Fiore, A. M., Gaudel, A., Guo, J., Lin, M., Neu, J., Parrish, D., Reider, H., Schnell, J., et al. Tropospheric ozone assessment report: Assessment of global-scale model performance for global and regional ozone distributions, variability, and trends. *Elementa: Science of the Anthropocene*, 6(1), 2018. Cited on page 112.
- Yue, X. and Unger, N. Fire air pollution reduces global terrestrial productivity. *Nature communications*, 9(1):5413, 2018. Cited on pages 3 and 90.
- Yurganov, L., Duchatelet, P., Dzhola, A., Edwards, D., Hase, F., Kramer, I., Mahieu, E., Mellqvist, J., Notholt, J., Novelli, P., et al. Increased northern hemispheric carbon monoxide burden in the troposphere in 2002 and 2003 detected from the ground and from space. *Atmospheric Chemistry and Physics Discussions*, 4(5):4999–5017, 2004. Cited on pages 1 and 2.
- Yurganov, L., McMillan, W., Grechko, E., and Dzhola, A. Analysis of global and regional co burdens measured from space between 2000 and 2009 and validated by ground-based solar tracking spectrometers. *Atmospheric Chemistry and Physics*, 10(8):3479–3494, 2010. doi: 10.5194/acp-10-3479-2010. URL <https://www.atmos-chem-phys.net/10/3479/2010/>. Cited on page 98.
- Zemp, D., Schleussner, C.-F., Barbosa, H., Van der Ent, R., Donges, J. F., Heinke, J., Sampaio, G., and Rammig, A. On the importance of cascading moisture recycling in south america. *Atmospheric Chemistry and Physics*, 14(23):13337–13359, 2014. Cited on page 11.
- Zeng, G., Williams, J. E., Fisher, J. A., Emmons, L. K., Jones, N. B., Morgenstern, O., Robinson, J., Smale, D., Paton-Walsh, C., and Griffith, D. W. T. Multi-model simulation of co and hcho in the southern hemisphere: comparison with observations and impact of biogenic emissions. *Atmospheric Chemistry and Physics*, 15(13):7217–7245, 2015. Cited on pages 106, 115, and 127.
- Zhang, Y., Fu, R., Yu, H., Dickinson, R. E., Juarez, R. N., Chin, M., and Wang, H. A regional climate model study of how biomass burning aerosol impacts land-atmosphere interactions over the amazon. *Journal of Geophysical Research: Atmospheres*, 113(D14), 2008. Cited on page 12.
- Zhu, L., Val Martin, M., Gatti, L. V., Kahn, R., Hecobian, A., and Fischer, E. V. Development and implementation of a new biomass burning emissions injection height scheme (bbeh v1. 0) for the geos-chem model (v9-01-01). *Geoscientific Model Development*, 11(10):4103–4116, 2018. Cited on pages 52, 86, 92, 104, 108, and 127.
- Ziemke, J., Chandra, S., Duncan, B., Schoeberl, M., Torres, O., Damon, M., and Bhartia, P. Recent biomass burning in the tropics and related changes in tropospheric ozone. *Geophysical Research Letters*, 36(15), 2009. Cited on pages 90, 112, 117, 118, and 128.

Zong, J., Davies, R., Muller, J.-P., and Diner, D. J. Photogrammetric retrieval of cloud advection and top height from the multi-angle imaging spectroradiometer (misr). *Photogrammetric Engineering and Remote Sensing*, 68(8):821–829, 2002. Cited on pages [28](#) and [41](#).